Gas Content and Transport in Cold First Year Sea Ice

By

Odile Crabeck

A thesis submitted to the Faculty of Graduate Studies of
The University of Manitoba
in partial fulfilment of the degree of

Doctor of Philosophy

Department of Geology
University of Manitoba
Winnipeg, Manitoba, Canada

Gas Content and Transport in Cold First Year Sea Ice

By

Odile Crabeck

A thesis submitted to the Faculty of Graduate Studies of
The University of Manitoba
in partial fulfilment of the degree of

Doctor of Philosophy

Department of Geology
University of Manitoba
Winnipeg, Manitoba, Canada

Abstract

Past and recent literature have highlighted that sea ice might play a crucial role in controlling and contributing to the exchange of significant climatically active biogases between the ocean and the atmosphere in polar areas. However, the formation of air inclusions and the transport of gases within sea ice cover are still poorly understood.

Thanks to development of a new fast and non-destructive X-ray computed tomography (CT) technique to quantify the air volume fraction and the characterization of gas concentration profiles (Ar, O_2, N_2, CH_4 and pCO_2) in natural (Kapisillit fjord, Greenland) and artificial (Sea Ice Research Facility, Winnipeg, Canada) cold sea ice, we revealed some key properteies of gas content and transport in sea ice.

We concluded that gases are incorporated in dissolved phase in the brine during ice growth. Nucleation further happened in the brine inclusions at rate depending of the gas saturation factor and the brine volume. Nucleation exerts a strong control on gas content and transport because at any given time when bubbles form in the brine, they are segregated from the transport pathway of dissolved salts and dissolved gas. Due to their low density, bubbles will not drain out of the ice by convection. Instead, nucleation leads to the forced buoyant upward transport and an accumulation of gas in sea ice. In addition, we show that the gas content of air bubbles can be exchanged with the brine medium and diffuse within the brine network at a comparable rate (10^{-5} cm^2 s^{-1}) than aqueous diffusivities.

In addition, CT-X-ray results showed that air volume fraction was <2% in most of the internal layers and systematically > 5% at the ice-atmosphere interface (top 2 cm). The evidence of air volume fraction over 5% in granular top layers with the presence of macro bubbles introduces new challenges for the interpretation of sea ice atmosphere gas exchange. Substantiation of air porosity in columnar internal layers and granular top layers questions the current sea ice mathematical description in which the air volume fraction is currently neglected.

Acknowledgments

Firstly, I would like to express my sincere gratitude to my advisor Dr. Soren Rysgaard for the continuous support of my Ph.D. study and related research, for his patience, motivation, and immense knowledge. His guidance helped me in all the time of research and writing of this thesis. Also I would like to thank him for letting me find my own way, in spite of my rather disperse character and multiplicity of interests. Our conversations on very diverse topics have been a source of inspiration and insight. The joy and enthusiasm you have for the research is contagious and motivational.

I would like to especially thank you my co-supervisor Dr. Ryan Galley. Ryan thank you for your patience and endless availability. You have played a very important role in this broad and exciting intellectual journey. You are a great mentor, and thanks to your teaching, and especially your perfectionism, I became a better scientist. I will always remember one of your advice: “Do it right in the first place, or you will have to do it twice”. I look forward to build new collaboration with you.

Besides my advisor, I would like to thank the rest of my thesis committee: Dr.Tim Papakyriakou for his guidance and counseling, particularly in the difficult moments. Dr. Feiyue Wang for having his door open and his advices in chemistry, and Dr. Jens Ehn, for his encouragements.

A very special acknowledgement to the two persons who have iniated me to science research and left profound teachings; Dr. Jean-Louis Tison and Dr. Bruno Delille. Jean-Louis et Bruno, tout d’abord merci pour m’avoir initié à la

recherche scientifique durant mon master à l'ULB et de m'avoir encouragé à poursuivre dans cette voix. Je suis très heureuse que malgré une expatriation au Canada, vous avez continué à jouer votre rôle de mentor. Notre collaboration est précieuse à mes yeux. Jean-Louis, merci ton spécialement pour ton enseignement de la rigueur et le partage de ton savoir. Bruno, merci de ton accessibilité et disponibilité pendant ces quatre années et tout particulièrement durant les moments de doutes de cette fin de thèses.

My sincere gratitude also goes to CEOS Research team. Especially Brent, you always gave precious advices and insightful comments during the redaction of my manuscripts, you are example of success. Thank you to Claire, Heather, Jack, Karley and Tonya for their support at end of this thesis. Thank you to Nix who introduced me to fieldwork. Thank you to Marcos, for his constant help in the lab and to Linda who made sure that my administrative papers were in order. Thank you to Kunuk and Ivaly for making field season awesome. Especially, Ivaly who introduced me to ice-fishing. I feel incredibly lucky to have traveled the Arctic and look for more adventures in the near futures.

I would like to thank my family: my parents and to my sister (Stephanie) for supporting me spiritually throughout writing this thesis and my life in general. I strongly believe that being a parent it is one of the most challenging job, with no doubt, mom and dad, you succeeded at it ☺. Stephanie, thank you to being there during the last 10 years, I am lucky and grateful to have you as a sister, love you. I would also like to thank my partner in life Franck. You have helped me see, think

and feel in ways that I had never experienced before. After three years of building a partnership, I look forward to keep walking side by side with you.

Last but not the least, I would thank you all my friends from Belgium and Canada, for their endless support and encouragements.

Table of Contents

List of Tables

List of Figures

Use of Copyright

Manuscripts:

Chapter IV of this thesis is reproduced with minor modifications from Crabeck et al. (2014a, First ‘‘in situ’’ determination of gas transport coefficients (DO_2, DAr, and DN_2) from bulk gas concentration measurements (O_2, N_2, Ar) in natural sea ice, J. Geophys. Res. Oceans, 119, 6655–6668 doi: 10.1002/2014JC009849), with permission from the American Geophysical Union.

Chapter V of this thesis is reproduced with minor modifications from Crabeck et al. (2014b, CO_2 and CH_4 in sea ice from a subarctic fjord under influence of riverine input, Biogeosciences, 11, 6525-6538, doi:10.5194/bg-11-6525-2014), with permission from Copernicus Publications on behalf of the European Geosciences Union (EGU) in the journal Biogeosciences.

Chapter VI of this thesis is reproduced with minor modifications from Crabeck et al.(2016, Imaging air volume fraction in sea ice using non-destructive X-ray tomography, The Cryosphere, 10, 1125-1145, doi:10.5194/tc-10-1125-2016), with permission from Copernicus Publications on behalf of the European Geosciences Union (EGU) in the journal The Cryosphere.

Figures:

Figure II-1 from Weeks and Ackley (1986) used with copyright permission.

Figure II-2 from Weeks and Ackey (1986) used with copyright permission.

Figure II-4b from Perey and Pounder (1958) used with copyright permission.

Figure II-5 from Petrich and Eicken (2010) used copyright permission.

Figure II-6 from Cox and Weeks (1975) used copyright permission.

Figure II-8 from Vancoppenolle (2013) used with copyright permission.

Figure II-9 from Pringle et al, (2009) used copyright permission.

Figure II-10a from Golden et al, (1998) used copyright permission.

Figure II-10b from Golden et al, (2007) used copyright permission.

Figure II-12 from Niedrauer and Martin (1979) and Lake and Lewis (1970) used with copyright permission.

Figure II-15 from Perovich and Polashenski (2012) used copyright permission.

Figure II-18 from Rysgaard et al, (2014) used copyright permission.

Figure II-20 from Cole et al, (2004) used copyright permission.

Figure II-21 from Zhou et al, (2013) used copyright permission.

Figure II-22 from Zhou et al, (2014) used copyright permission.

Figure II-24 from Geilfus et al, (2014) used copyright permission.

Figure II-25 from Delille et al, (2014) used copyright permission.

Figure III-1 from SRI instrument Europe (2012) used copyright permission.

Figure VII-2 from Rysgaard et al, (2007) used copyright permission.

Figure VII-5 from Werge and Erbin (1995) used copyright permission.

.

Chapter-I-Introduction

I-1 Motivation

In it is pure form sea ice is a multi-phase system formed by the freezing of seawater, which consists of ice, salt precipitates, liquid brine, and air bubbles (WMO, 1970). The mixed solid-liquid sea ice environment is distinctly different from the fluid pelagic regime. Sea ice formation raises the ocean surface albedo (Cox and Weeks, 1988b; Perovich, 1996), and reduces the exchange of heat, moisture and momentum between the ocean surface and the atmosphere (Untersteiner, 1961; Maykut and Untersteiner, 1971; Cox and Weeks, 1988). Furthermore, sea ice formation leads to the rejection of brine into the upper layers of the ocean, thereby inducing deep-water formation (Aggard and Carmack,1989; Rysgaard et al., 2011). Conversely, sea ice melt enhances water mass stratification, isolating the seawater below the halocline from the atmosphere (Agaard and Carmack, 1989; Visbeck et al., 1995). Sea ice also impacts the primary production of the polar oceans, increasing the food source to higher trophic-level species in winter and early spring (Kottmeier et al., 1987; Smith, 1991; Niebauer et al., 1995). Since sea ice is one of the largest biomes on earth, cyclically covering 10% of the global ocean, sea ice play a key role for the earth climate system (Comiso et al., 2010).

Recent evidence has suggested that sea ice play potentially a role in controlling and contributing to the ocean-atmosphere exchange of significant

climatically active biogases (Semiletov et al., 2004; Zemmelink et al., 2006; Delille et al., 2007; Rysgaard et al., 2007; Zhou et al., 2014; Damm et al., 2015). Rysgaard et al. (2011) estimated that the seasonal CO_2 uptake in the sea ice zone might equal half of the annual CO_2 uptake of ice-free polar seas (>62°N latitude and >50°S latitude). Delille et al. (2014) reported that the Antarctic sea ice cover is a net sink of atmospheric CO_2 during the spring and summer, contributing to 58% of the annual uptake from the Southern Ocean. Active gas sources and sinks in sea ice, as well as dynamic gas transport through the sea ice brine network, have been observed (e.g. Mock et al., 2002; Tison et al., 2002; Papadimitriou et al., 2004; Rysgaard and Glud, 2004; Semiletov et al., 2004; Delille et al., 2007; Loose et al., 2011; Geilfus et al., 2012). In a recent modeling study, Moreau et al. (2014) concluded that the partitioning between dissolved and gaseous phases can play a critical role in gas transport in sea ice, since the transport of gas in air bubbles might be decoupled from brine motion. However, the current understanding of the fate of gas – including its entrapment, transformation, transport, and exchange – is still insufficient for accurate interpretations and modeling of physical and biogeochemical sea ice processes. Consequently, computations of sea ice physical proprieties, such as brine volume fraction and permeability, neglect the air phase in sea ice by assuming that most of the gas is dissolved in the brine and that the air volume fraction is negligible. Similarly, recent mathematical formulation of physical sea ice processes using "mushy layer theory" (Taylor and Feltham, 2004; Notz and Worster, 2009) predict the transport of heat and solute transport during sea ice growth and decay. However, it assumes that first year sea ice is a two-phase

medium made of brine (liquid porosity) and solid pure ice, neglecting the presence of air bubbles (air porosity). For similar reasons, the role of sea ice on CO_2 dynamics in the polar oceans has also been poorly represented in global earth system models, since they rely on the assumptions that sea ice cover is chemically and biologically inactive, and physically impermeable to gas (Yager et al., 1995; Orr et al., 2001; Bates and Mathis, 2009). Only one study by Moreau et al. (2016) simulated the impact of sea ice growth and decay on global marine carbon cycles in a global ocean circulation model (NEMO-LIM-PISCES), with the assumptions that sea ice is chemically and biologically active and physically permeable to gas.

Historical and on-going climatic changes are amplified in the circumpolar regions (Holland et al., 2006). The Arctic is losing multiyear (thick) sea ice cover at a rate of 15% per decade, and being replaced by thinner, more porous, seasonal (first year) sea ice, which forms in winter and completely melts in the summer (Vaughan et al., 2013). Future changes in the polar seas and continued melt of multiyear sea ice will affect future marine biogeochemistry (Arzel et al., 2006), resulting in positive feedback cycles on the climate system and consequences for marine ecosystems, some of which have already been observed (e.g. Fabry et al., 2009; Wassmann et al., 2011). In the face of these rapid changes, efforts are being made to model future changes in the circumpolar Arctic; however, observational data of the pertinent processes are still missing to design more accurate models.

This study aims to document gas dynamics, including the characterization of air volume fraction and controlling factors for gas entrapment and transport in partially impermeable (i.e. V_b <5% in some ice layers) Arctic first year sea ice.

Results from this work are a valuable addition to limited studies available on gas content dynamics in sea ice, and provides a new methodology for the interpretation and characterization of sea ice porosity as well as new knowledge for sea ice modeling.

I-2 Thesis Objectives

This research aims to increase our understanding of the dynamics of major atmospheric gases (Ar, O_2 and N_2), and document the concentrations of greenhouse gases (CO_2 and CH_4) in impermeable first year Arctic sea ice. Particular attention is paid to processes governing: (i) the gas entrapment at the ice-seawater and ice-atmosphere interface; (ii) the transport pathways modulating the exchange of gases through the sea ice cover between the ocean and atmosphere; and (iii) the physical state of the gas, from its dissolved phase in brine to its gaseous phase in air bubbles (air porosity). This study will cover three key objectives: firstly, to examine bulk ice profiles of the most abundant natural gas species (Ar, O_2 and N_2) in naturally occurring sea ice. These gases represent 99.9 % of the gas in the Earth's atmosphere and the gas dissolved in the ocean, are easily detectable, and are representative of most of the ocean-atmosphere gas exchange processes. Ar is an inert gas and N_2 is, for the most part inert; therefore, they can be used as natural tracers to highlight physical constraints and processes. Secondly, this study will compare inert gas profiles with greenhouse gas profiles to highlight key physical and biogeochemical processes that may play a role in the dynamics of greenhouse gases within the sea ice cover. Thirdly, this thesis research will focus on the development of a

methodology to visualize and estimate the vertical distribution of air volume fraction (i.e. air porosity) in sea ice. These three objectives correspond, respectively, to the following scientific questions:

1. **What physical processes control the transport of major atmospheric gases (Ar, O_2, and N_2) in sea ice?**

For this first scientific question, focused on major atmospheric gases profiles, we aim to: (i) theoretically estimate how gas is distributed between the dissolved phase in the brine and gaseous phase in air bubbles; and (ii) evaluate how gas diffusion processes affect mass transport of gas across and within sea ice.

2. **How does sea ice affect the uptake and emissions of greenhouse gases (CO_2 and CH_4)?**

Knowing the basic physical frames for the major atmospheric gases, this second scientific question focused on the greenhouse gas content of sea ice using the same spatial and temporal scale as in objective 1. We aim to: (i) quantify CH_4 concentrations in bulk sea ice in order to gain key information on the effect of sea ice cover on CH_4 emissions; and (ii) measure bulk ice pCO_2 to investigate the pCO_2 dynamics in an ice covered fjord.

3. **What is the vertical distribution of air volume fraction?**

Since theoretical estimations of the physical state of gas (dissolved in brine versus gaseous in air bubbles) suggest that gases are mostly contained in bubbles instead of being dissolved in brine, it challenges the assumption that the air volume fraction is negligible in first year sea ice. Therefore, we aim to: (i) develop a reliable

methodology for the estimation of the air volume fraction at high resolution; and (ii) compare the air volume fraction profile to major atmospheric gas profiles.

To meet these objectives, I closely collaborated with the laboratory of Glaciology, Free University of Bruxelles, Belgium, which has long-term specialized expertise in ice gas extraction and analysis. I also collaborated with the INRS-Ete (Institut National pour la Recherche Scientifique) in Québec, where I benefited from new and innovative instrumentation.

I-3 Thesis outline

This thesis includes seven chapters. In chapter II, I introduce background on: (i) the physical processes governing the vertical thermohaline structure of first year sea ice during ice growth and decay, and (ii) the gas content, composition and transport in first year sea ice. As a preface to the three scientific questions, chapter III focuses on the development of an analytical methodology for the detection of major atmospheric gases (O_2, N_2 and Ar) and greenhouse gases (CO_2, CH_4 and N_2O) on a custom made Gas Chromatograph (GC). Chapters IV, V, and VI address scientific questions 1, 2, and 3 respectively; they also contain three separate original full-length research papers, each of which has been published in a peer-review journal (Table I-1).

As this study deals exclusively with first year sea ice, all future mentions of "sea ice" will refer to first year ice. In previous works, sea ice air volume fraction is ubiquitously neglected, so historically, sea ice porosity refers to the brine volume fraction. In the context of this document, the terms brine inclusions and brine

volume fraction (V_b %) refers to liquid porosity and air volume fraction refers to the air porosity (V_a %). The terms "bubbles" and "air inclusions" interchangeably denote gas phase inclusions in sea ice.

Table I-1: Contribution to the scientific literature as first author.

Scientific questions	**Contribution to literature as first author**
1 - Chapter IV	Crabeck, O., Delille, B., Rysgaard, S., Thomas, D. N., Geilfus, N. -X., Else, B., and Tison, J.-L.: First "in situ" determination of gas transport coefficients (DO_2, DAr, and DN_2) from bulk gas concentration measurements (O_2, N_2, Ar) in natural sea ice, Journal of Geophysical Research: Oceans, 119, 6655-6668, doi: 10.1002/2014JC009849, 2014a.
2 - Chapter V	Crabeck, O., Delille, B., Thomas, D., Geilfus, N. -X., Rysgaard, S., and Tison, J.-L.: CO_2 and CH_4 in sea ice from a subarctic fjord under influence of riverine input, Biogeosciences, 11, 6525-6538, doi: 10.5194/bg-11-6525-2014, 2014b.
3 - Chapter VI	Crabeck, O., Galley, R., Delille, B., Else, B., Geilfus, N.-X., Lemes, M., Des Roches, M., Francus, P., Tison, J.-L., and Rysgaard, S.: Imaging air volume fraction in sea ice using non-destructive X-ray tomography, The Cryosphere, 10, 1125-1145, doi:10.5194/tc-10-1125-2016, 2016.

In order to address scientific question 1 and the knowledge gap in the literature regarding physical processes regulating the physical state of gas (dissolved in brine versus gaseous in bubbles) and transport within the sea ice, chapter IV reports bulk ice profiles of Ar, O_2 and N_2 and total gas content, in landfast subarctic sea ice (Godthåbsfjord, Greenland). Firstly, based on solubility law and bulk ice gas profiles, chapter IV estimates the air volume fraction (V_a) and the fraction of the gas residing in air bubbles. Secondly, chapter IV discusses potential transport processes by diffusion in cold impermeable sea ice (V_b< 5%; Golden et al., 1998). Unlike previous studies, which have used artificial gas tracers or artificial sea ice (e.g. Gosink et al., 1976; Loose et al., 2011), this study used measurements of natural gas tracers (Ar, O_2 and N_2) in natural sea ice samples.

Since no study has reported such measurements of major atmospheric gases in natural sea ice, the findings of this research significantly enhance the scientific understanding of physical gas processes and transport in sea ice. Chapter IV is published in the following peer-reviewed paper:

1. Crabeck, O., Delille, B., Rysgaard, S., Thomas, D. N., Geilfus, N.-X., Else, B., and Tison, J.-L.: First ‘‘in situ’’ determination of gas transport coefficients (D_{O2}, D_{Ar}, and D_{N2}) from bulk gas concentration measurements (O_2, N_2, Ar) in natural sea ice, J. Geophys. Res. Oceans, 119, 6655–6668, doi:10.1002/2014JC009849, 2014a.

Chapter V investigates bulk ice greenhouse gas content (CO_2 and CH_4) since there is an urgent need to specify the role of sea ice in the exchange and emission of greenhouse gases. Because greenhouse gases have multiple sources and sinks, sea ice should be considered part of a larger coupled ecosystem. Chapter V documents the interaction between landfast sea ice and the water column, riverine input, and gas dynamics. While CH_4 concentrations within sea ice cover have been poorly documented, CO_2 has more recently been the focus of numerous studies; however, the fate of CO_2 in ice-covered areas is still uncertain (Delille et al., 2014, Geilfus et al., 2016). Since greenhouse gases are involved in biogeochemical cycles, it is important to first discriminate physical processes, which are common to all gas species (chapter IV), from the biogeochemical processes which relate to CO_2 and CH_4. In order to highlight the processes specific to CO_2 and CH_4, chapter V uses the same physical, spatial, and temporal scale as in chapter IV, and compares major atmospheric gas content to greenhouse gas content. This work adds to the very few existing studies of CO_2 in sea ice, and is particularly valuable to modelers

when evaluating the role of coastal Arctic sea ice in the carbon cycle. This study represents a fundamental step for the understanding of how sea ice can affect CH_4 flux in ice cover area, as it reports the second measurements of bulk ice methane concentration (the first originating from Zhou et al., 2014). Chapter V is addressed in the following peer-reviewed publication:

2. Crabeck O., Delille B., Thomas D., Geilfus N.-X, Rysgaard S. and Tison J.-L.: CO_2 and CH_4 in sea ice from a subarctic fjord under influence of riverine input, Biogeosciences, 11, 6525-6538, doi:10.5194/bg-11-6525-2014, 2014b.

Chapters IV and V both suggest that a significant amount of gases (Ar, O_2, N_2 and CH_4) reside potentially in bubbles instead of being dissolved in brine. These findings highlight the importance of documenting bubble distribution in sea ice and accurately estimating the air volume fraction to enhance our understanding of the physical processes regulating the gas phase. Our current understanding of the morphology and connectivity of air inclusions in sea ice is inadequate (Moreau et al., 2014). Precise interpretation of sea ice data is imperative for future use in regional and large-scale climate models, highlighting the need for more concerted research efforts in gas exchange processes. Since the lack of detailed descriptions of sea ice air porosity presents several methodological challenges, chapter VI is dedicated to the development of a new methodology allowing an accurate high-resolution characterization and visualization of sea ice air porosity. The constraints associated with thin section microscopy incited the development of a non-destructive methodology based on computed tomography (CT X-ray). The research in chapter VI compares and combines both traditional (chapter IV) and new sea ice

analytical techniques, and presents the resulting issues of these techniques. The findings of this research contribute to the field of sea ice physics as they provide the first suitable technique to quantify air volume fraction and make detailed air volume fraction profiles with extremely high vertical resolution. Chapter VI is published in the following peer-reviewed manuscript:

3. Crabeck, O., Galley, R., Delille, B., Else, B., Geilfus, N.-X., Lemes, M., Des Roches, M., Francus, P., Tison, J.-L., and Rysgaard, S.: Imaging air volume fraction in sea ice using non-destructive X-ray tomography, The Cryosphere, 10, 1125-1145, doi:10.5194/tc-10-1125-2016, 2016.

Lastly, chapter VII synthesizes the findings of this PhD thesis and provides concluding comments and insights on how current gas dynamics within sea ice are likely to evolve in the future.

REFERENCES

Aagaard, K., and Carmack, E. C.: The role of fresh water in ocean circulation and climate, Journal of Geophysical Research, 94, 14485-14498, 10.1029/JC094iC10p14485, 1989.

Arzel, O., Fichefet, T., and Goosse, H.: Sea ice evolution over the 20th and 21st centuries as simulated by current AOGCMs, Ocean Modelling, 12, 401-415, 2006.

Bates, N. R., Cai, W. J., and Mathis, J. T.: The ocean carbon cycle in the western Arctic Ocean: Distributions and air-sea fluxes of carbon dioxide, Oceanography, 24, 186-201, 10.5670/oceanog.2011.71, 2011.

Comiso, J. C.: Variability and trends of the global sea ice cover, in: Sea Ice, second edition, edited by: Thomas, D. N., and Dieckmann, G. S., Wiley- Blackwell, Oxford, 205-246, 2010.

Cox, G., and Weeks, W.: Numerical simulations of the profile properties of undeformed first-year sea ice during the growth season, Journal of Geophysical Research: Oceans, 93, 12449-12460, 1988.

Damm, E., Rudels, B., Schauer, U., Mau, S., and Dieckmann, G.: Methane excess in Arctic surface water triggered by sea ice formation and melting, Scientific Reports, 5, 16179, 10.1038/srep16179, 2015.

Delille, B., Jourdain, B., Borges, A. V., Tison, J.-L., and Delille, D.: Biogas (CO_2, O_2, dimethylsulfide) dynamics in spring Antarctic fast ice, Limnology and Oceanography, 52, 1367-1379, 10.4319/lo.2007.52.4.1367, 2007.

Delille, B., Vancoppenolle, M., Geilfus, N.-X., Tilbrook, B., Lannuzel, D., Schoemann, V., Becquevort, S., Carnat, G., Delille, D., Lancelot, C., Chou, L., Dieckmann, G. S., and Tison, J.-L.: Southern Ocean CO2 sink: The contribution of the sea ice, Journal of Geophysical Research: Oceans, 119, 6340-6355, 10.1002/2014JC009941, 2014.

Fabry, V. J., McClintock, J. B., Mathis, J. T., and Grebmeier, J. M.: Ocean acidification at high latitudes: the bellweather, Oceanography, 22, 160-171, 2009.

Geilfus, N.-X., Galley, R. J., Else, B. G., Campbell, K., Papakyriakou, T., Crabeck, O., Lemes, M., Delille, B., and Rysgaard, S.: Estimates of ikaite export from sea ice to the underlying seawater in a sea ice-seawater mesocosm, The Cryosphere, 10, 2173, 10.5194/tc-10-2173-2016, 2016.

Geilfus, N. X., Carnat, G., Papakyriakou, T., Tison, J. L., Else, B., Thomas, H., Shadwick, E., and Delille, B.: Dynamics of pCO2 and related air-ice CO2 fluxes in the Arctic coastal zone (Amundsen Gulf, Beaufort Sea), Journal of Geophysical Research: Oceans, 117, 1-15, 10.1029/2011JC007118, 2012.

Golden, K. M., Ackley, S. F., and Lytle, V. I.: The percolation phase transition in sea ice, Science, 282, 2238-2241, 10.1126/science.282.5397.2238, 1998.

Gosink, T. A., Pearson, J. G., and Kelly, J. J.: Gas movement through sea ice, Nature, 263, 41 - 42, 1976.

Holland, M. M., Bitz, C. M., and Tremblay, B.: Future abrupt reductions in the summer Arctic sea ice, Geophysical Research Letters, 33, 10.1029/2006GL028024, 2006.

Kottmeier, S. T., and Sullivan, C. W.: Late winter primary production and bacterial production in sea ice and seawater west of the Antarctic Peninsula, Mar Ecol Prog Ser, 36, 287-298, 1987.

Loose, B., Miller, L. A., Elliot, S., and Papakyriakou, T.: Sea ice biogeochemistry and material transport accros the frozen interface, Oceanography, 24, 202-218, 10.5670/oceanorg.2011.72., 2011.

Maykut, G. A., and Untersteiner, N.: Some results from a time-dependent thermodynamic model of sea ice, Journal of Geophysical Research, 76, 1550, 10.1029/JC076i006p01550, 1971.

Mock, T., Dieckmann, G. S., Haas, C., Krell, A., Tison, J. L., Belem, A. L., Papadimitriou, S., and Thomas, D. N.: Micro-optodes in sea ice: A new approach to investigate oxygen dynamics during sea ice formation, Aquatic Microbial Ecology, 29, 297-306, 10.3354/ame029297, 2002.

Moreau, S., Vancoppenolle, M., Zhou, J., Tison, J. L., Delille, B., and Goosse, H.: Modelling argon dynamics in first-year sea ice, Ocean Modelling, 73, 1-18, 10.1016/j.ocemod.2013.10.004, 2014.

Moreau, S., Vancoppenolle, M., Bopp, L., Aumont, O., Madec, G., Delille, B., Tison, J.-L., Barriat, P.-Y., and Goosse, H.: Assessment of the sea-ice carbon pump: Insights from a three-dimensional ocean-sea-ice biogeochemical model (NEMO-LIM-PISCES), Elementa: Science of the Anthropocene, 4, 000122, 10.12952/journal.elementa.000122, 2016.

Niebauer, H. J., Alexander, V., and Henrichs, S. M.: A time-series study of the spring bloom at the Bering Sea ice edge I. Physical processes, chlorophyll and nutrient chemistry, Continental Shelf Research, 15, 1859-1877, 10.1016/0278-4343(94)00097-7, 1995.

World Meteorological Organization.: WMO Sea-ice Nomenclature. Vol. 145, Secretariat of the World Meteorological Organization, Geneva, Switzerland, 1970.

Notz, D., and Worster, M. G.: Desalination processes of sea ice revisited, Journal of Geophysical Research: Oceans, 114, 1-10, 10.1029/2008JC004885, 2009.

Orr, J. C., Maier-Reimer, E., Mikolajewicz, U., Monfray, P., Sarmiento, J. L., Toggweiler, J., Taylor, N. K., Palmer, J., Gruber, N., and Sabine, C. L.: Estimates of anthropogenic carbon uptake from four three-dimensional global ocean models, Global Biogeochemical Cycles, 15, 43-60, 2001.

Papadimitriou, S., Kennedy, H., Kattner, G., Dieckmann, G. S., and Thomas, D. N.: Experimental evidence for carbonate precipitation and CO_2 degassing during sea ice formation, Geochimica et Cosmochimica Acta, 68, 1749-1761, 2004.

Perovich, D. K., and Gow, A. J.: A quantitative description of sea ice inclusions, Journal of Geophysical Research-Oceans, 101, 18327-18343, 1996.

Rysgaard, S., and Glud, R. N.: Anaerobic N_2 production in Arctic sea ice, Limnology and Oceanography, 49, 86-94, 10.4319/lo.2004.49.1.0086, 2004.

Rysgaard, S., Glud, R. N., Sejr, M. K., Bendtsen, J., and Christensen, P. B.: Inorganic carbon transport during sea ice growth and decay: A carbon pump in polar seas, Journal of Geophysical Research: Oceans, 112, 1-8, 10.1029/2006JC003572, 2007.

Rysgaard, S., Bendtsen, J., Delille, B., Dieckmann, G. S., Glud, R. N., Kennedy, H., Mortensen, J., Papadimitriou, S., Thomas, D. N., and Tison, J. L.: Sea ice contribution to the air-sea CO(2) exchange in the Arctic and Southern Oceans, Tellus Series B-Chemical and Physical Meteorology, 63, 823-830, 10.1111/j.1600-0889.2011.00571.x, 2011.

Semiletov, I., Makshtas, A., Akasofu, S. I., and Andreas, E. L.: Atmospheric CO_2 balance: The role of Arctic sea ice, Geophysical Research Letters, 31, L05121-doi:05110.01029/02003GL017996, 10.1029/2003GL017996, 2004.

Smith, W. O.: Nutrient distributions and new production in polar regions: parallels and contrasts between the Arctic and Antarctic, Marine Chemistry, 35, 245-257, 10.1016/S0304-4203(09)90020-2, 1991.

Taylor, P. D., and Feltham, D. L.: A model of melt pond evolution on sea ice, Journal of Geophysical Research-Oceans, 109, 10.1029/2004jc002361, 2004.

Tison, J. L., Haas, C., Gowing, M. M., Sleewaegen, S., and Bernard, A.: Tank study of physico-chemical controls on gas content and composition during growth of young sea ice, Journal of Glaciology, 48, 177-191, 2002.

Untersteiner, N.: On the mass and heat budget of Arctic sea ice, Archiv für Meteorologie, Geophysik und Bioklimatologie, Serie A, 12, 151-182, 1961.

Vaughan, D. G., Comiso, J. C., Allison, I., Carrasco, J., Kaser, G., Kwok, R., Mote, P., Murray, T., Paul, F., and Ren, J.: Observations: cryosphere, in Climate Change 2013: The Physical Science Basis. Contribution of Working Group I to the Fifth Assessment Report of the Intergovernmental Panel on Climate Change Climate change, Cambridge Univ. Press, Cambridge, 317-382, 2013.

Visbeck, M., Fischer, J., and Schott, F.: Preconditioning the Greenland Sea for deep convection: Ice formation and ice drift, Journal of Geophysical Research: Oceans, 100, 18489-18502, 1995.

Wassmann, P., Duarte, C. M., Agusti, S., and Sejr, M. K.: Footprints of climate change in the Arctic marine ecosystem, Global Change Biology, 17, 1235-1249, 2011.

Yager, P. L., Wallace, D. W., Johnson, K. M., Smith, W., Minnett, P. J., and Deming, J.: The Northeast Water Polynya as an atmospheric CO_2 sink, Journal of Geophysical Research, 100, 4389-4398, 1995.

Zemmelink, H. J., Delille, B., Tison, J. L., Hintsa, E. J., Houghton, L., and Dacey, J. W. H.: CO_2 deposition over the multi-year ice of the western Weddell Sea, Geophysical Research Letters, 33, 10.1029/2006GL026320, 2006.

Zhou, J. Y., Tison, J. L., Carnat, G., Geilfus, N. X., and Delille, B.: Physical controls on the storage of methane in landfast sea ice, The Cryosphere, 8, 1019-1029, 10.5194/tc-8-1019-2014, 2014.

Chapter-II-Background

II-1 Open structure of the ice crystal

At the Earth's surface (1 atmosphere and 0°C) water crystallizes in the hexagonal crystal system (Ih structure), as illustrated in Figure II-1 (Bragg, 1922; Owstom, 1958; Weeks and Ackley, 1986). The water molecules (H_2O) are arranged tetrahedrally around each other, resulting in an open crystal structure. This crystal system is characterized by four axes: three equivalent a-axes and one optical c-axis, used to define the exact orientation of a crystal (Langway, 1958). The fastest growth occurs in the plane of the a-axes as it consumes less energy to add molecules to the present plane as compared to build a new one (Hobbs, 1974) .

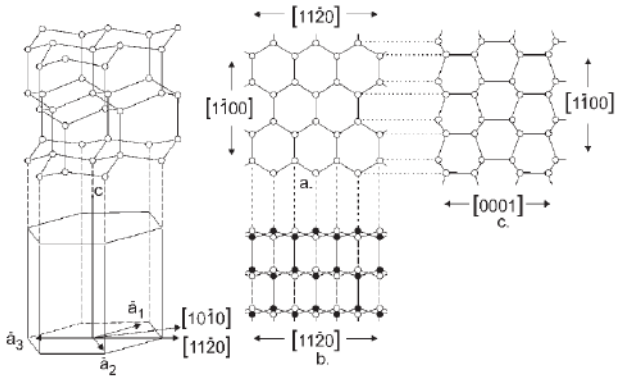

Figure II-1: Crystal structure of sea ice on the left. The central panel presents the arrangement of oxygen atoms along (top) and perpendicular (bottom) to the c-axis. The 3 a-axes are lying within the basal plane (left panel) from Weeks and Ackley (1986).

The open spaces in the structure explain the low density of ice compared to that of water. Fresh water is 1.00 g/m³ at 4 °C, but evolves toward lower density as ice crystals appear to reach 0.9167 g/m^3 at 0°C. Despite the open structure of the

ice crystal, most of the impurities existing in seawater (e.g. Na^+, Cl^-, K^+, Ca^{2+}, Mg^{2+}, SO_4^{2-}, CO_3^{2-}) are rejected from the ice matrix ahead of the advancing freezing front (Hobbs, 1974; Weeks and Gow,1978; Weeks and Ackley, 1986).

II-2 Transition from open-ocean to sea ice cover

In the Arctic, during autumn and winter, the cold atmosphere in contact with the ocean cools the surface layer. This layer consequently becomes denser than the underlying water since the temperature of maximum density of seawater ($t_{\rho max}$=-1.33°C at a global average salinity of 34) is below the freezing point (t_g=-1.86°C for a salinity of 34) (Figure II-2).

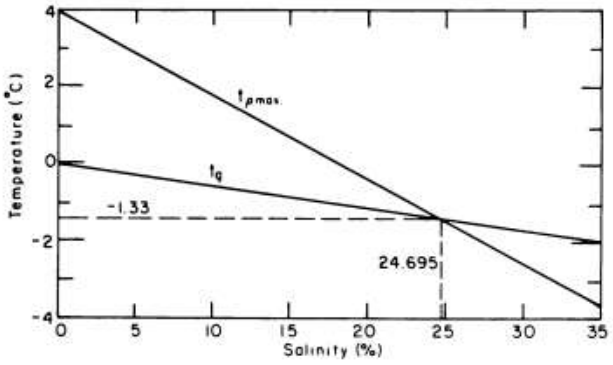

Figure II-2: Evolution of the maximum density temperature ($t_{\rho max}$) and of the freezing point (t_g) in function of the salinity, from Weeks and Ackley (1986).

This unstable vertical density distribution induces convective mixing, during which the colder surface water sinks and is replaced by warmer underlying seawater.

Once the surface mixed layer reaches the freezing point, small, unconsolidated frazil ice crystals form and aggregate at the ocean's surface (Martin, 1981). Realistically, frazil ice crystals may form before the entire mixed layer has reached the freezing point, because particulate materials in supercooled seawater may serve as nucleation sites (Weeks and Ackley,1986). Due to turbulence, these first crystals are small (mm to cm range), randomly shaped, and arbitrarily oriented (Figure II-3), This texture in fully formed sea ice is referred to as granular ice (Weeks and Ackley, 1986).

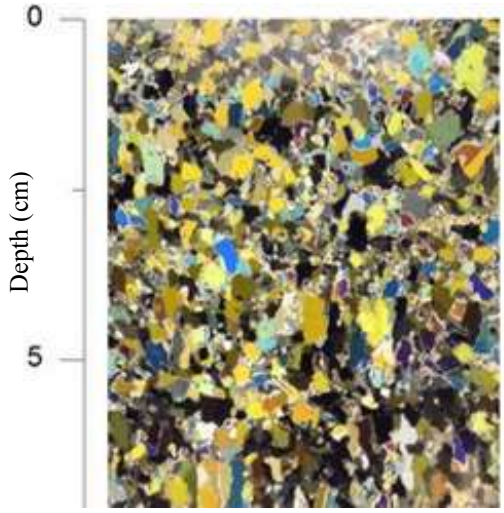

Figure II-3: Picture of frazil ice with granular ice texture taken in cross-polarized light from the top of a first year ice core, Young Sound, Greenland, in May 2014.

Once the ocean surface is covered by a thin layer of frazil ice, the frazil layer thickens from its base by the formation of congelation ice (Maykut and Untersteiner, 1971, Weeks and Akley,1986). Since there is no more direct heat exchanged between the ocean surface and the atmosphere, the growth of the ice sheet depends of latent heat conductivity through the sea ice cover (Weeks and Ackley, 1986). Since crystals with horizontal c-axes display a maximum rate of

growth in the vertical direction (vertical a-axes), they will outgrow those with c-axes off the horizontal (this is the so-called "geometric selection" (Figure II-4 a, b) (Perey and Pounder, 1958; Weeks and Gow, 1980; Weeks and Ackley, 1986). As a result, congelation ice is comprised of large vertically oriented crystals with basal planes (a-axes) parallel to the temperature gradient. This particular oriantion of the basal planes favors the conduction of heat accros the sea ice cover. This texture is referred to as columnar ice (Figure II-4c).

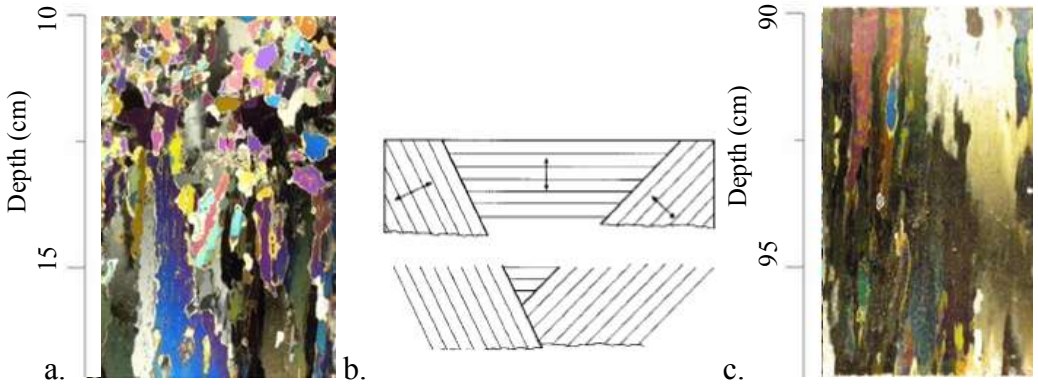

Figure II-4: (a) Picture of the transition between frazil and congelation ice, marked by a change in ice texture from randomly shaped granular crystal to vertically elongated columnar ice crystal. Picture was taken in cross-polarized light from a first year ice core at 10 cm depth,Young Sound, May 2014. (b) A schematic diagram showing the geometric selection in sea ice from Perey and Pounder, (1958), the lines within the crystals represent the orientaion of the a-axes in the basal planes. (c) Picture of congelation ice with vertically elongated ice crystals forming the so-called columnar texture. Picture was taken in cross-polarized light fom the bottom of a first year ice core, Young Sound, May 2014.

As the columnar crystals grow downward, salt is being rejected into a thin layer at the ice-seawater interface. As a result, the salt is transported by diffusion from the interface (saltier) toward the bulk ocean (less salty) (Weeks and Akley, 1986). Simultaneously, heat is transferred by diffusion from the bulk ocean

(warmer) toward the ice interface (colder). Since the transport of salt away from the interface is an order magnitude slower as the transfer of heat toward the sea ice interface (Weeks and Ackley, 1986), a thin layer is cooled below its theoretical freezing point but not yet salinized, exists below the interface. This layer is described as supercooled water (Figure II-5).

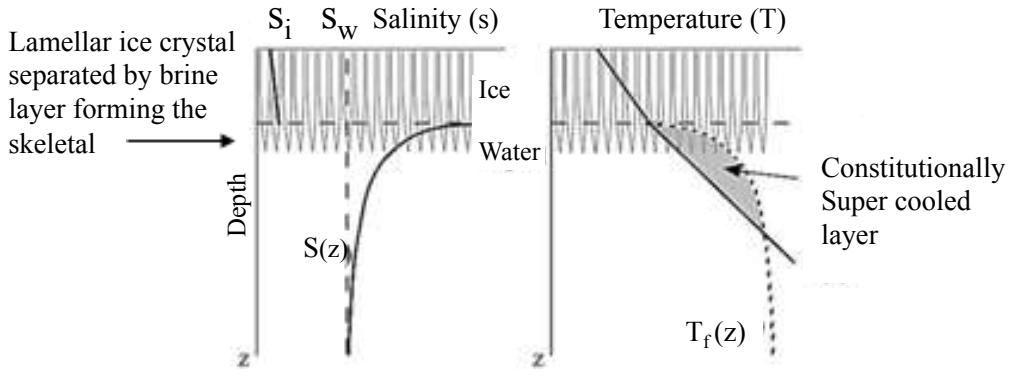

Figure II-5: Schematic representation of the skeletal ice layer, consisting of lamellar ice crystals separated by layers of brine, and of the changes of salinity (left) and temperature (right) below the ice-seawater interface (dashed horizontal line). $T_f(z)$ is the freezing temperature for the actual salinity (S(z)). The shaded area, where (T(z)) is below the $T_f(z)$, represents the constitutionally supercooled layer. Figure adapted from Petrich and Eicken (2010).

In this constitutionally supercooled layer, any growing crystals have a thermodynamic growth advantage, because supercooled water acts as an 'extra' heat sink, which extracts more heat as compared to the part of the crystals above the constitutionally supercooled layer. Where ice crystals with horizontal c-axes growing vertically are considered, the salt rejected contributes to reduce the brine freezing point along the crystal boundaries in the constitutionally supercooled layer. As such, each crystal side is surrounded by brine. These features sustain the development of thin vertical lamellar blades of ice crystals separated by films of

brine (termed "brine layers") (Figure II-5). Within this interfacial lamellar structure, referred to as the "skeletal layer", the brine volume can exceed the ice volume (ice volume fraction varies from 0 to 30 %) (Weeks and Ackley, 1986).

As the skeletal layer grows downward, the ice temperature decreases in the upper part of the skeletal layer. This causes the water in brine to freeze, adding ice to the existing lamellae and reducing the brine volume fraction. Eventually, the ice lamellae join to form the pure ice crystal matrix, within which isolated liquid brine inclusions concentrate almost all the impurities in ice (Weeks and Ackley, 1986; Wettlaufer et al., 1997). Field measurements have shown a strong correlation between ice growth rate and salt retention (Nakawo and Sinha, 1981). A reduction in growth velocity closely corresponds to an increase in brine layer spacing, lowering the amount of salt trapped in the ice matrix. Usually, the amount of salt trapped increases while the growth rate increases, because salts have less time to diffuse and/or convect into the underlying seawater. The presence of currents at the growing interface also influences the lamellar substructure and brine spacing, and usually enhances salt transport away from the ice (Weeks and Gow, 1978, 1980). Strong tidal currents could produce a pressure difference in the lower part of the brine network and enhance brine rejection, as suggested by theoretical and experimental studies (Neufeld, 2008). Forced convection may bring in and redistribute salt, nutrients, and gases in sea ice. However, further studies are warranted to evaluate that exact contribution.

According to the "Stagnant Boundary-Layer" diffusion model (Cox and Weeks, 1975, 1988; Eicken, 1998), which refers to the "Burton-Prim Slichter" model (Burton et al., 1953), the fractionation between a solid and a liquid phase leads to direct segregation of the components present in the liquid and solid phase. This fractionation is described by the effective distribution coefficient K_{eff}:

$$K_{eff} = {}^{S_{ice}}/_{S_{sw}} \quad \text{(Eq. II-1)}$$

Where S_{ice} is the bulk ice salinity and S_{sw} is the seawater salinity.

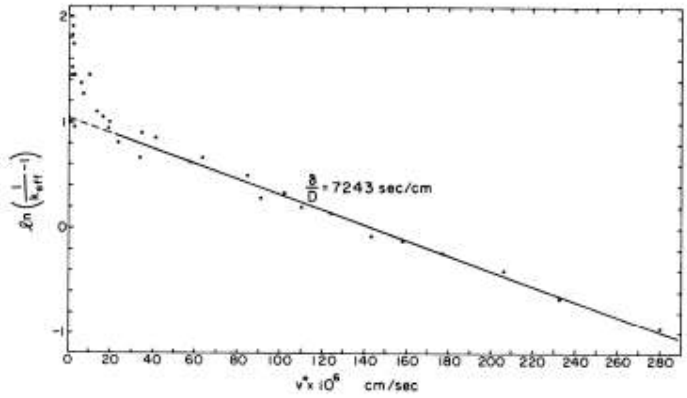

Figure II-6: Relationship between the effective salt segregation coefficient K_{eff} ($\ln(1/K_{eff} - 1)$) and the growing rate of the ice V (Cox and Weeks, 1975).

Following a simplification of the salt entrapment similar to solid solutions ("Burton-Prim Slichter") and implicitly assuming a planar rather than lamellar ice-seawater interface, Cox and Weeks (1975,1988) computed the relationship between K_{eff} and the ice growing rate V_i from laboratory experiments (Figure II-6).

This work was later completed by Eicken (1998) based on field work by Nakawo and Sinha (1981) and isotope measurements:

$$K_{eff} = \frac{0.26}{0.26 + 0.74e^{-7243V_i}} \qquad \text{for } V_i > 3.6\ 10^{-5}\text{cm s}^{-1}$$

$$K_{eff} = 0.8925 + 0.0568\ \ln(V_i) \quad \text{for } 3.6\ 10^{-5}\text{cm s}^{-1} \geq V_i 2.0\ 6\ \text{cm s}^{-1}$$

$$K_{eff} = 0.12 \qquad \text{for } V_i < 2.0\ 6\ \text{cm s}^{-1}$$

(Eq. II-2)

The differences between a derived salinity profile using the growing rate dependency (Eq.II-2) and an *in situ* salinity profile can be explained by further brine transport taking place in the ice cover: brine migration, brine expulsion, brine drainage, and flushing, which redistributes salt within the ice and exports salt out of the ice. Fluid transport through the ice is controlled by the vertical thermohaline structure of sea ice, which determines both the vertical stability of the brine network and its connectivity (Vancoppenolle et al., 2013).

II-3 Thermodynamic equilibrium within sea ice

Once a horizon of ice comprised of pure ice crystals and brine inclusions is formed, its physical structure is subject to change due to temperature variability, resulting from atmospheric (i.e. air temperature and snow precipitation) and/or ocean forcing.

The extreme change of incident solar radiation between winter and summer in the Arctic produces a great range of air temperatures from -40°C to above 0°C (Figure II-7). These atmospheric seasonal changes drive the onset of ice growth and decay, but also a myriad of changes in ice physical properties. For instance, any

variation of temperature has significant effects on the physical structure (volume and distribution) and chemical composition of the brine.

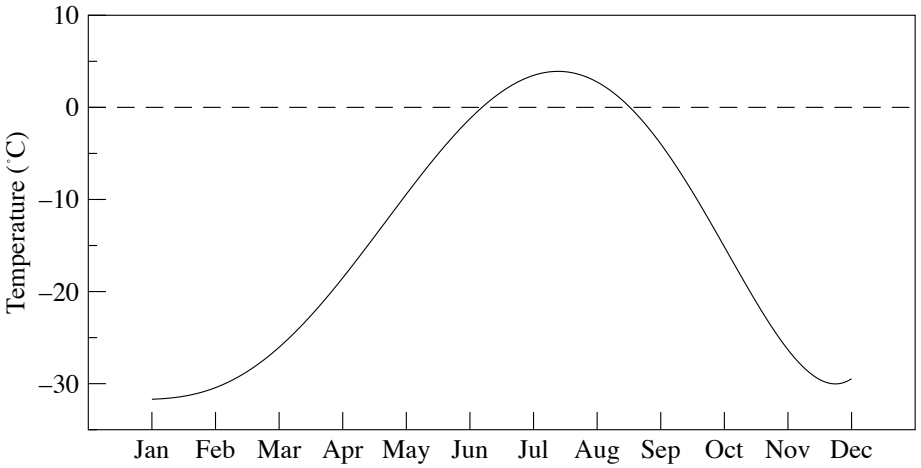

Figure II-7: Average daily (24h) temperature per month for 2015 in Resolute Bay, Nunavut, Canada (data from Almanac-Environment Canada, http://climate.weather.gc.ca/climate_data/almanac_e.htmlStationID=53060).

II.3.1 Phase equilibrium

Since brine inclusions are at the thermodynamic equilibrium with the ice matrix enclosing them, vertical and seasonal changes of temperature control the volume and salinity of the brine. Because the liquid brine is always at its salinity-based freezing point and increasing brine salinity decreases the brine freezing point, brine salinity increases as a function of decreasing temperature (concentration effect), and conversely decreases as a function of increasing temperature (dilution effect).

Under cooling conditions, each brine inclusion shrinks in size until the internal salinity of the inclusion is high enough to compensate further cooling. Even at extremely low temperatures observed in sea ice (around -30°C), a portion of the brine stay liquid (Assur, 1958). In these smallest inclusions, the concentration of

salts as well as others solutes (e.g. gases, dissolved inorganic carbon) can increase to a point where the solution is supersaturated, resulting in the onset of bubble nucleation (see section II.10.3 Nucleation processes and air volume fraction) and carbonate and salts precipitation (see section II.12.1 The CO_2 and the carbonate system). When liquid water in brine freezes, the increase of pure ice volume may fracture the ice along the crystal boundaries or lines of natural weakness, resulting in brine expulsion along cracks (Bennington, 1963). The brine expulsion process is typically characterized by the presence of brine skim and high salinity in frost flowers, (Untersteiner, 1968; Lake and Lewis, 1970; Niedrauer and Martin, 1979; Galley et al., 2015). The upward expulsion of brine is a source of salt for the top granular layer.

Also, in cooling condition, the top of a brine cell is colder than its bottom. The pocket freezes at its colder top, increasing the internal salinity, which produces the melt of the inclusion bottom and a downward migration of the brine inclusion (Whitman 1926; Niedrauer and Martin, 1979). Recurrence of this process during ice growth leads to a slow downward migration of brine inclusions, which eventually can be expelled from the base of the ice cover.

Conversely, if the temperature of the ice cover increases under warming conditions, some of the pure ice along the inclusion walls melts, expanding the brine inclusions and diluting the brine, which lowers the brine salinity and increases its freezing point in order to maintain phase equilibrium. During internal ice melting, brine dilution may dissolve precipitated salts and nucleated bubbles. Also, because pure ice is less dense than brine, pure ice melt inevitably causes the

formation of voids above the freeboard, which will rapidly be filled with water vapor and air (Tsurikov, 1979; Perovich and Gow, 1996).

II.3.2 Brine salinity and brine volume temperature dependent relationships

The seawater freezing point (T_f) is a function of salinity (S_{sw}) and pressure (P) as determined by UNESCO, (1978):

$$T_f = a_0 S_{sw} + a_1 S_{sw}^{3/2} + a_2 S_{sw}^2 + bP \qquad \text{(Eq. II-3)}$$

Where a_0, a_1, a_2 and b are the coefficients listed in Table II-1.

Table II-1: Coefficient for the computation of the seawater freezing point for a valid range of salinity from 4 to 40 at atmospheric pressure by UNESCO (1978).

a_0	a_1	a_2	b
-0.0575	$1.710523\ 10^{-3}$	$-2.154996\ 10^{-4}$	$-7.53\ 10^{-4}$

Brine salinity (S_{br}) is solely a function of temperature and can be calculated from the *in situ* sea ice temperature. Notz (2005) determined an empirical function for S_{br} as a function of the ice temperature (T) based on the data of Assur (1958):

$$S_{br} = -1.2 - 21.8T - 0.919T^2 - 0.0178T^3 \qquad \text{(Eq. II-4)}$$

According to Vancoppenolle et al. (2013a), a simpler, linear relationship between brine salinity and *in situ* temperature can be used, based on the linearized freezing point relationship of seawater:

$$S_{br} = -T / 0.054 \quad \text{(Eq. II-5)}$$

However, this simpler computation renders significantly different results from -5°C to low temperatures compared to equations II-3 and II-4, (Figure II-8). Hence, especially for cold sea ice, it is recommended to use equations II-3 and II-4, rather than equation II-5 (Vancoppenolle et al., 2013a).

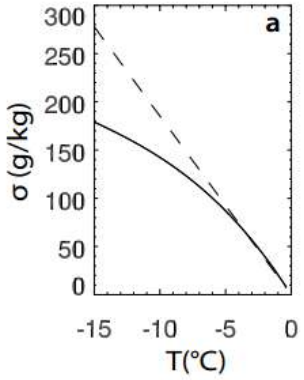

Figure II-8:. Brine salinity S_{br} (T) from 3-order (Eq. II-4, solid) and linear expressions (Eq. II-5, dash) (Vancoppenolle et al., 2013).

Light et al. (2003) showed a clear dependency between the physical structure of the brine porosity (volume, shape, size, abundance) and the sea ice temperature. Toward low temperatures, brine inclusions are small and have high number density while toward high temperatures, brine cells enlarge and have low number density. According to Light et al. (2003) the cross-sectional area of brine increases drastically while the ice temperature reaches -5°C. Eicken et al. (2000) and Pringle et al. (2009) described the microstructural evolution of brine inclusions

as a function of temperature using magnetic resonance imaging (MRI) and X-ray tomography, respectively. Studies revealed that under warming conditions the brine volume increases, and the size, morphology, and connectivity of the inclusions evolve. Above -6°C, the studies showed that isolated liquid inclusions started to connect to each other's (Eicken et al., 2000; Pringle et al., 2009). This process of interconnection under warming condition is of great importance for the vertical transport of heat and mass in sea ice, controlling the thermal conductivity and permeability of the ice cover (Figure II-9) (see section II-4 Critical vertical permeability threshold).

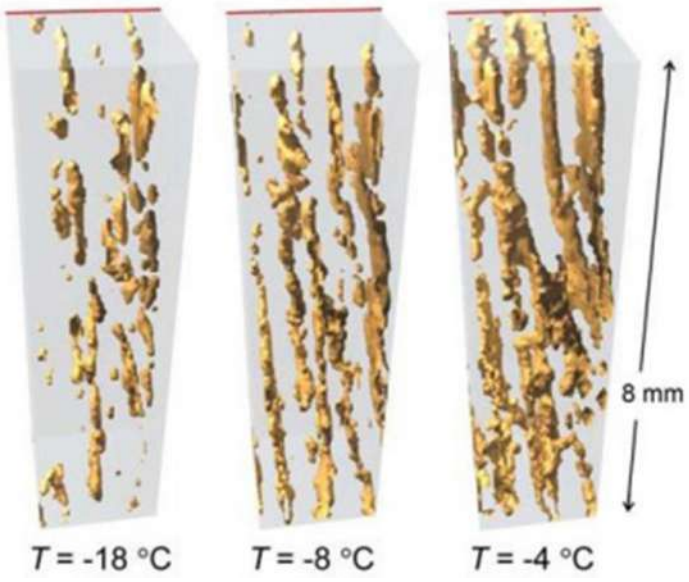

Figure II-9: Evolution of the brine pore space with increasing temperatures as assessed by X-ray computed tomography; with increasing temperatures, the brine inclusions become larger and more connected to each other (Pringle et al., 2009).

Based on data compiled in the phase diagram of Assur (1958), Cox and Weeks (1983) computed a series of empirical equations to derive the brine volume fraction (V_b) from the bulk ice temperature (T) and bulk ice salinity (S_{ice}):

$$V_b = \left(1 - \frac{V_a}{V}\right) \frac{\left(\frac{\rho_i}{1000}\right) S_{ice}}{F1(T) - \left(\frac{\rho_i}{1000}\right) S_{ice} F2(T)} \quad \text{(Eq. II-6)}$$

Where V, V_b, V_a represent the volumes of ice, brine, and air, respectively; $F1(T)$ and $F2(T)$ are empirical polynomial temperature dependent functions ($Fi(T) = a_i + b_i T + c_i T + d_i T$). The coefficients for temperature ranged from -2°C to -30°C and from 0°C to -2°C are shown in Table II-2. S_{ice} is the bulk ice salinity and ρ_i is the density of pure ice (in kg m^{-3}), which according to Pounder (1965) is given as:

$$\rho_i = 917 - 0.1403T \quad \text{(Eq. II-7)}$$

with T in °C. In equation II-7, V_a/V is generaly neglected in the calculation of brine volume fraction, because it is typically much smaller than V_b in first-year ice. Moreover, a reliable methodology to assess V_a is currently missing in the literature.

Note that "*The Intergovernmental Oceanographic Commission (IOC) of the United Nations Educational, Scientific, and Cultural Organization (UNESCO), the Scientific Committee on Oceanic Research (SCOR), the International Association for the Physical Sciences of the Oceans (IAPSO), and the International Association for the Properties of Water and Steam (IAPWS) have all endorsed the new thermodynamic approach for ocean modeling, TEOS-10*". *TEOS is a new method of analyzing seawater which provides mutually consistent expressions for density, potential temperature, entropy, enthalpy, sound speed, chemical potential, as well*

as other seawater properties — and provides an update to the Equation of State of Seawater, which UNESCO endorsed in 1980 (referred to as EOS-80). Unlike the previous equation, however, the thermodynamic approach is also applicable to freshwater, ice, and water vapor." (UNESCO/IOC et al., 2011).

Table II-2: Petrich and Eicken (2010)'s compilation of the coefficients for F1(T) and F2(T) for different temperature intervals, based on Cox and Weeks (1983) -2 > T°C > -30) and Leppäranta and Manninen (1988) (for 0 > T°C > -2).

F1(T) °C	a_i	b_i	c_i	d_i
0 >T°C > -2	-0.041221	-18.407	0.58404	0.215
-2 > T > -22.9	-4.732	-22.45	-0.6397	-0.01074
-22.9 > T > -30	9899	1309	55.27	0.716
F2(T) °C	a_i	b_i	c_i	d_i
0 > T°C > -2	0.0903	-0.0161	0.00123	0.00036
-2 > T > -22.9	0.08903	-0.01763	-0.000533	-0.000008801
-22.9 > T > -30	8.547	1.089	0.04518	0.0005819

II-4 Critical vertical permeability threshold

Sea ice permeability is a crucial parameter for quantifying the fluid flow through sea ice. Once ice forms, further exchanges with seawater and/or atmosphere are modulated by brine and gas transport through the ice sheet. Brine transport has been extensively discussed in the literature (Untersteiner, 1968; Lake and Lewis, 1970; Cox and Weeks, 1975; Eide and Martin, 1975; Niedrauer and Martin, 1979; Weeks and Ackley, 1986; Oertling and Watts, 2004; Vancoppenolle et al., 2007; Notz and Worster, 2009) and some concepts for describing the transport of gases are directly derived from those established for the transport of brine (Tsurikov, 1979).

According to percolation theory, porous media (e.g. soils, rocks, sea ice) have a critical porosity threshold above which their permeability increases exponentially and the inclusions become sufficiently connected for a fluid to percolate through the pore network (e.g. Golden et al., 1998). Golden et al. (1998, 2007) estimated this threshold to be at 5% V_b in columnar sea ice with a model based on the pore structure of compressed powder. This theory is commonly referred to as "the law of fives", because V_b typically reaches 5% when the ice temperature is -5°C for a typical bulk ice salinity of 5 psu (Golden et al., 1998) (Figure II-10). According to Golden et al. (1998), the percolation threshold for granular sea ice could be higher than in columnar ice due to the random arrangement of brine inclusions as compared to columnar ice.

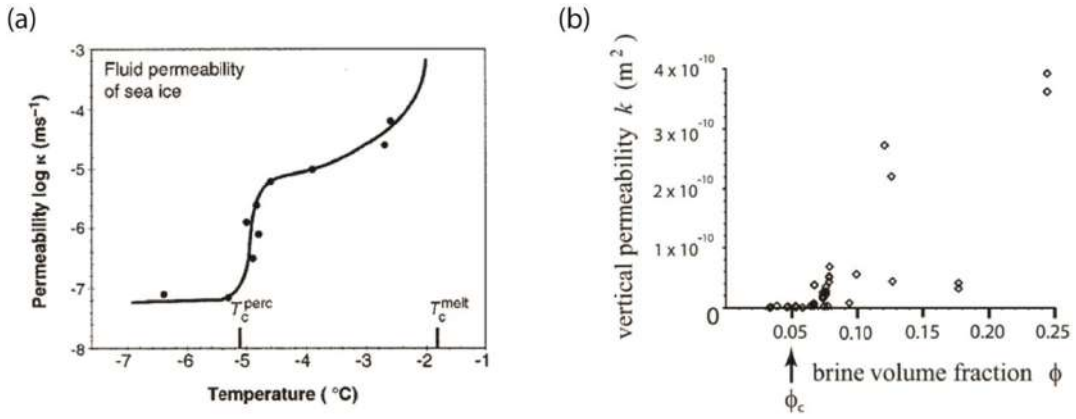

Figure II-10: (a) Changes in permeability as a function of the ice temperature adapted from Golden et al. (1998), and (b) changes in vertical permeability as a function of brine volume fraction, Φc is the critical percolation threshold, V_b = 5 %, adapted from Golden et al. (2007).

II-5 Seasonal evolution of brine dynamics in sea ice

The temperature dependence of brine volume produces vertical and seasonal heterogeneity in the distribution, structure, concentration, and

connectivity of brine inclusions, implicitly controlling sea ice permeability and transport processes.

II.5.1 Sea ice growth

During the ice growth period, the ice-seawater interface is always close to the seawater freezing point (-1.8°C), whereas the ice-atmosphere interface is colder and near above air temperature (Figure II-11). As a result, heat is transported in the upward direction and the temperature gradient between top and bottom of the sea ice cover can easily be around 15 °C m^{-1}; this thermal regime is referred to as "cold ice" (winter profile).

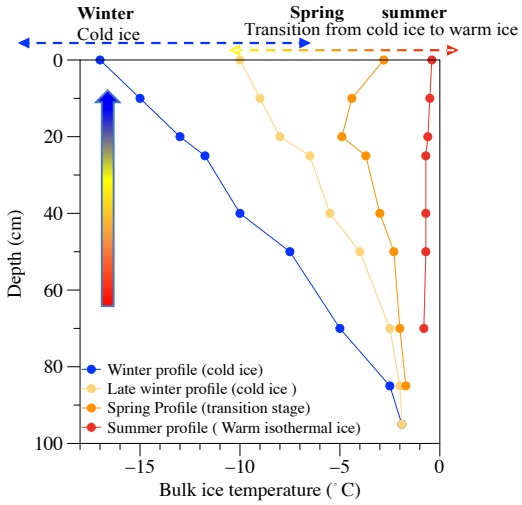

Figure II-11: Seasonal evolution of the bulk ice temperature profile, the arrow indicates the direction of heat flux in cold ice during winter.

As a result of the temperature gradient between the very cold top and relatively warm sea ice bottom, the brine inclusions are small, concentrated (saltier and denser), and isolated toward the top, and larger toward the bottom, where they

appear as connected channels, within which the brine is diluted (fresher and less dense) (Figure II-12).

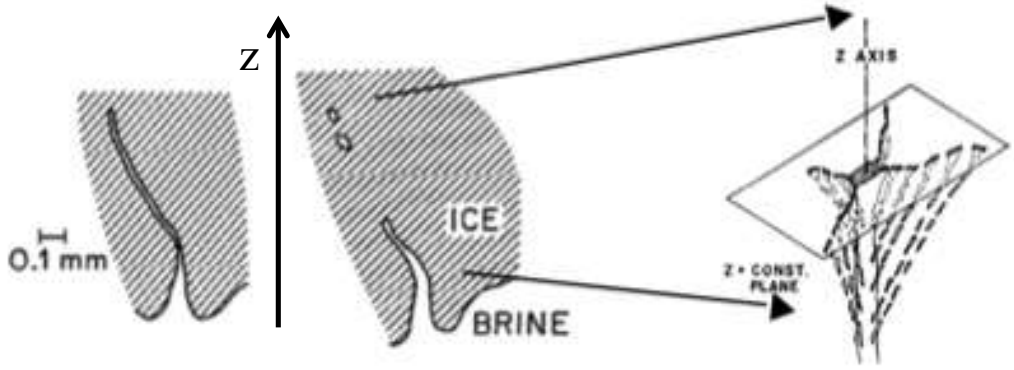

Figure II-12: Illustration of a brine channel pinching off into smaller and more concentrated brine pockets, while the brine is displaced from the warm seawater interface during ice growth (figure from Niedrauer and Martin, 1979).On the far right, an established brine channel and its feeder arms, made of smaller pockets (figure from Lake and Lewis, 1970).

Wakatsuchi and Kawamura (1987) and Cottier et al. (1999) show that brine channel structures within the relatively warm bottom are associated with localized increased salinity below them in the underlying water, with significant brine depletion in the ice surrounding these channels, thereby showing that the brine channels are a key path for salt rejection in growing sea ice (Middleton et al., 2016).

According to Eide and Martin (1975), the salt exported by brine drainage occurs in brine channels. Brine drainage refers to the natural convection leading to the replacement of salty, dense brine by less dense underlying brine or seawater in vertically permeable ice volumes (Hunke et al., 2011). Ultimately, this leads to an export of brine down and out of the ice into the underlying seawater. This process is referred to as gravity drainage, brine convection, or "Mushy-Layer Mode Convection" (Worster and Wettlaufer, 1997; Notz and Worster, 2009; Hunket al.,

2001). The Rayleigh number (Ra) is a parameter used to estimate the onset of brine convection. The Rayleigh number, following the definition of Wettlaufer et al. (1997) and Notz and Worster (2009) is calculated using:

$$Ra = \frac{gh\rho_w \beta_w \ \Delta S_{br-sw} \ \Pi(\overline{\phi_v})}{K_i \mu} \qquad \text{(Eq. II-8)}$$

Where g is the gravitational acceleration g=9.81 m s^{-2}, h is the ice thickness (m); ΔS_{br-sw} represents the salinity difference between the brine salinity determined by surface temperature and the seawater salinity at the ice-seawater interface; ρ_w and β_w are the density of pure water and the haline expansion coefficient of seawater, both taken at 0 °C from Fofonoff (1985). $\Pi(\overline{\phi_v})$ is the effective ice permeability (m^2) computed using the formula of Freitag (1999) as a function of the average solid volume in the ice cover (Notz and Worster, 2009). μ = 1.79x 10^{-3} (kg m^{-1} s^{-1}) is the dynamic viscosity of seawater at 0°C. Ki is the thermal diffusivity (m^2s^{-1}).

Ra is based on the competing effects of the energy available for convection ($gh\rho_w \beta_w \ \Delta S_{br-sw}$) and the energy dissipated ($K_i\mu/\Pi$) by internal friction and thermal diffusion during convection. Energy lost by internal friction depends of the ratio between the brine viscosity, μ and of the ice permeability, Π (μ/Π), while the energy dissipated through heat transfer depends of the thermal diffusivity coefficient, K_i (Hunke et al., 2011).

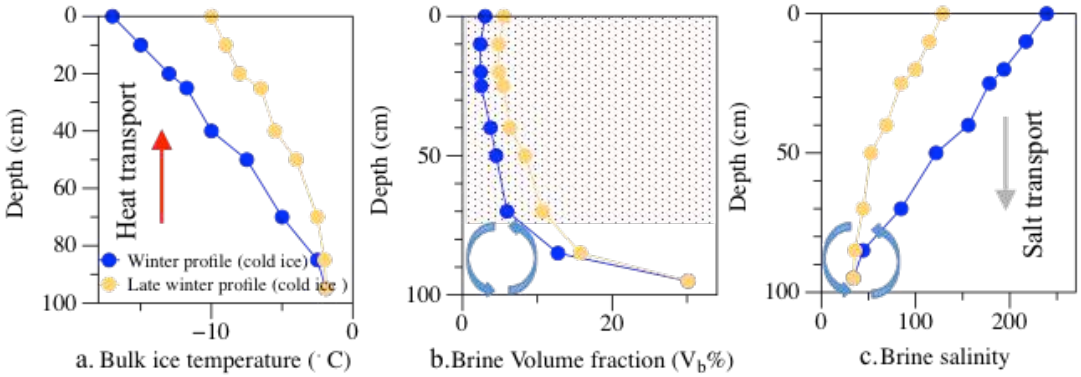

Figure II-13: (a) Vertical temperature gradient during winter, (b) brine volume fraction distribution, the shaded area highlights the impermeable ice layers due to the upward reduction of brine volume, (c) unstable vertical profile of brine salinity during winter, with saltier brine over fresher brine, blue arrows represent convective cells in (b) and (c).

Such convection occurs under conditions of unstable density distribution within the brine network in permeable ice layers (Figure II-13). These conditions are commonly found in the bottom layer of growing ice (Vancoppenolle et al., 2005; Notz and Worster, 2009) and/or episodically throughout the sea ice cover during warm periods in spring (Vancoppenolle et al., 2005, 2007; Jardon et al., 2013).

In winter, sea ice bulk salinity has a C-shaped profile with high salinity at the surface, low salinity at mid-depth, and high salinity at the bottom, which persists until late winter (Weeks and Ackley, 1986) (Figure II-14).

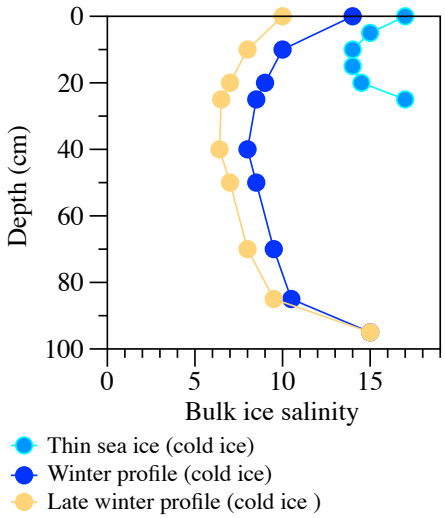

Figure II-14: Bulk ice salinity profile during winter Bulk ice salinity profiles are generally reasonably steady over the winter, as the ice grows thicker, the vertical extent of the lower salinity central zone increases and the average bulk salinity over the full ice thickness decreases, mainly due to brine drainage from the base of the ice sheet.

The internal low salinity layer of the ice cover results directly from brine convection occurring in drainage channels within the bottom layer (Figure II-13, blue convective cells). In winter, the 5% brine volume contour is about one third of the ice thickness of the ice-seawater interface, hence only the lowermost part of the ice is permeable (Vancoppenolle et al., 2007; Notz and Worster, 2009) (shaded area in Figure II-13). Therefore, brine drainage only occurs in that bottom layer. The high salinity in the surface layers result in a larger K_{eff} (i.e. $K_{eff} = S_{ice}/S_w$ (Eq.II-1)) for granular than for congelation ice. Several processes contribute to an increase in K_{eff}; the random arrangement of granular crystals creates more room for brine entrapment, and the misalignment of the brine inclusions induces incomplete drainage of the frazil layer. The salinity of the granular ice layers could also

increase over time due to flooding (see section II-6 Processes in presence of snow cover) and/or upward brine expulsion from internal columnar ice.

Bulk ice salinity profiles are generally reasonably steady over the winter. Nonetheless, brine convection occurring at the bottom of the ice cover is responsible for the decrease of the salinity minimum at mid depth and of the mean bulk salinity over the full ice thickness.

II.5.2 Sea ice melt

Sea ice starts to melt during summer, once the surface energy budget becomes positive. Excess energy penetrating the ice cover can be absorbed, heating the ice above the melting point, whereupon latent heating causes ice melt and surface ablation.Since the bulk ice ice temperature is below the fresh ice melting point (0 C°), the melting rate depends also of how fast the salts can diffused away. The surface energy budget resolves several energy sources, including: direct shortwave solar radiation, atmospheric long wave radiation, turbulent fluxes of sensible and latent heat, and the heat flux conducted through the ice cover to its surface (Maykut and Untersteiner, 1971). If the seawater underlying the ice is above the freezing point heat can be conducted or convected into the ice, in a mechanism known as the ocean heat flux. If the side of an ice floe is exposed, lateral melting can also occur. During lateral melting, meltwater which is more buoyant than seawater will be transported along the vertical ice-seawater interface, allowing new warm water to influence the ice (e.g. Steele, 1992; Tsamados et al., 2015).

After snow melt, the ice surface albedo shifts toward lower values due to the apparition of melt ponds with typical albedo values lower than snow (Figure II-15). As the melt pond surface increases, the ice surface albedo drops continuously, leading to further solar radiation absorption and to higher melt rates. This is known as the ice-albedo feedback (Curry et al., 1995).

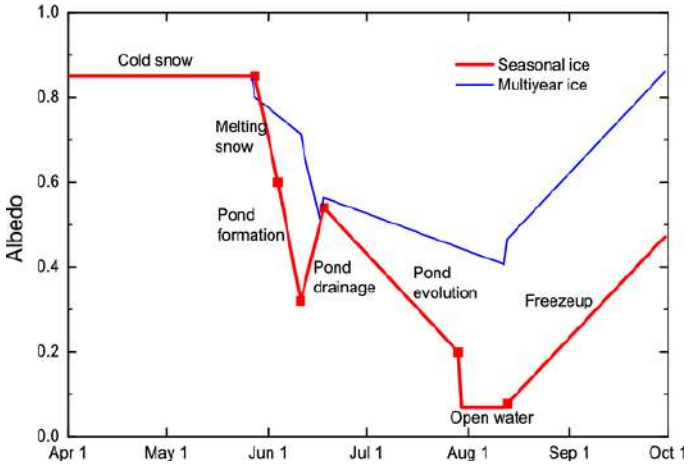

Figure II-15: Seasonal evolution of the ice surface albedo. The evolution of multiyear ice and seasonal ice albedo are plotted in blue and red, respectively. These particular time series assume melt onset on May 29th and freeze up on August 13th (Perovich and Polashenski, 2012).

In spring and summer, the heat flux is directed both downward and upward since the temperature at the ice-atmosphere interface and at the ice–seawater interface is often higher than that of the inner ice layers (Figure-II-16). This thermal regime is referred to as “warm ice” (summer profile).

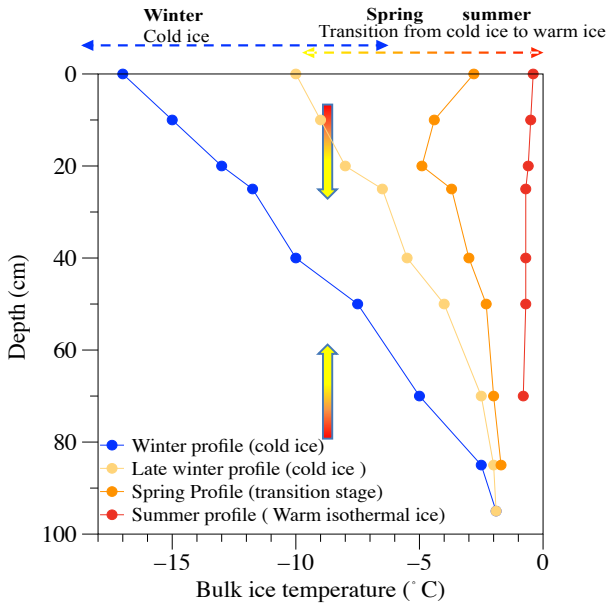

Figure II-16: Seasonal evolution of bulk ice temperature profile, the arrow indicates the direction of the heat flux in warm ice during spring and summer.

Under warming conditions in the spring, fresh water from internal melting increases the brine volume and lowers its salinity. The 5% brine volume contour modulating the permeability moves upwards in the ice due to warming. Full-depth connectivity occurs in spring once the ice is warm enough (Figure II-17, convective cell) (Vancoppenolle et al., 2005; Jardon et al., 2013). Then, transport processes (i.e. brine convection) previously confined at the warm ice-seawater interface can extend through the entire ice layer (Figure II-17a, transition from “cold ice” to “warm ice”: late winter profile to summer profile).

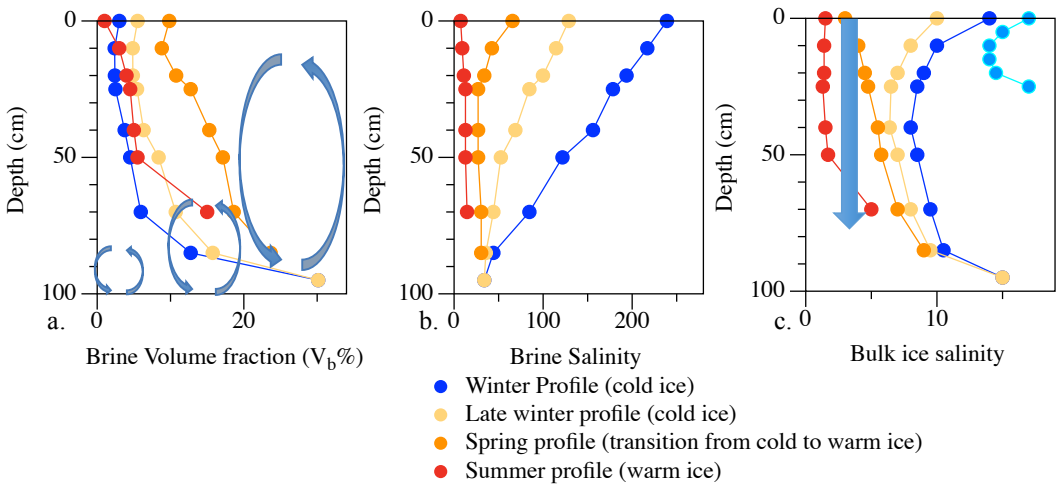

Figure II-17: (a) Seasonal evolution of brine volume fraction (%), the blue arrows represent the convective cells and (b) Seasonal evolution of brine salinity profiles, evolving from unstable to stable distribution. (c) Seasonal evolution of the bulk ice salinity profile, the blue arrow indicates flushing event.

An important consequence of meltwater pooling at the ice surface is that it can percolate downward through the connected brine network and drive out much of the brine (Notz and Worster, 2009). This process, known as flushing, is the most efficient and rapid form of brine drainage. It turns the salinity profile of late first year sea ice into one with a much lower salinity (Figure II-17c). Field measurements show that the onset of flushing corresponds to major desalination events in sea ice (Untersteiner, 1968; Cox and Weeks, 1974, 1975). The hydrostatic head of the surface meltwater provides the driving force, but as mentioned an interconnecting network of pores is necessary for the flushing process. During this time of the year, the inverse temperature gradient might cause the meltwater to refreeze in the ice, resulting in the formation of fresh impermeable ice layers (Eicken et al., 2004; Vancoppenolle et al., 2007; Polashenski et al., 2012; Landy et al., 2014).

Note that desalination could be slowed down due to the microbial production of EPS (extracellular polymeric substance) that alters the microstructure of the brine channels, reducing the pore spaces, and thus the permeability of the ice (Krembs et al., 2002, 2011).

II-6 Processes in presence of snow cover

Snow cover plays an important role in the thermodynamic evolution of sea ice (Eicken, 2003). Some properties of snow differ markedly from sea ice, mainly due to the high air content. For instance, the thermal conductivity of snow is one order of magnitude lower than the sea ice one (Andreas, 1987; Sturm and Massom, 1998). Thus, once snow accumulates at the ice surface in early winter, the snow cover slows the transfer of heat between the ocean surface, the sea ice and the atmosphere. Then, it acts as an insulator, decreasing bottom ice growth but also modulating internal ice temperature (Figure II-18) (Sturm and Massom, 1998). Since snow depth controls the thermal field, it influences brine volume fraction and sea ice permeability (intensity and depth of brine convection rates) (Maykut and Untersteuner,1971; Ledley, 1991; Notz and Worster, 2008). Moreover, the shortwave albedo of dry snow is above 0.9, which is much higher than the albedo of first year sea ice surface (about 0.52) (Grenfell and Maykut, 1977; Perovich et al., 2002). Increased albedo allows less solar radiation to penetrate the surface during spring and summer. Therefore, snow-covered sea ice and the underlying seawater receive less sunlight (Pedersen et al., 2009). Finally, snow my contributes

to the ice thickness by the development of superimposed-ice (e.g. Kawamura et al., 1997) or snow-ice (e.g. Leppäranta, 1983) at the snow-ice interface.

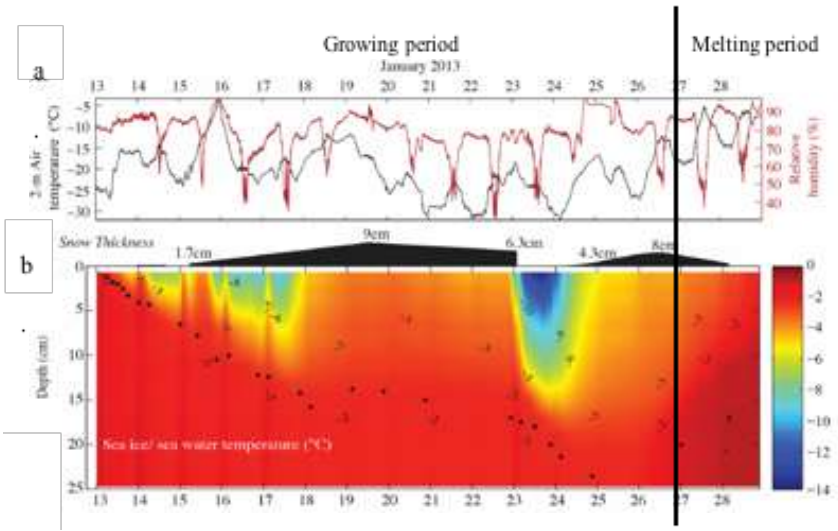

Figure II-18: Insulation effect of snow cover on sea ice from an outside tank experiment (SERF: Sea ice Research Facility, Manitoba, Canada). (a) Air temperature (black lines) and relative humidity (red lines), (b) Bulk ice and seawater thermal field in relation to snow cover (cm) (black horizontal bars), the black dots highlight the ice-seawater interface, adapted from Rysgaard et al. (2014).

Snow-ice forms as a result of refreezing of infiltrated seawater at the base of the snow pack, during flooding events (e.g. Eicken, 1994; Jeffries et al., 1994; Fichefet and Maqueda, 1999). Flooding occurs when the snow load is heavy enough to depress the ice surface below the water line (Eicken et al., 1995; Maksym and Jeffries, 2000). Seawater can then infiltrate the surface of sea ice from the edges of an ice floe and/or migrate upward through cracks, ridges, and brine channels (Maksym and Jeffries, 2000). During a flooding event, brine may be displaced upward due to hydrostatic adjustment (Hudier et al., 1995). In regions affected by heavy snowfall, flooding has the potential to significantly impact the vertical salinity distribution in sea ice by redistributing salt toward the surface

(Vancoppenolle et al., 2005, 2007). However, assessing the large-scale impact of flooding is difficult, because it requires an accurate computation of both the horizontal and vertical permeability, which is currently unavailable (Eicken et al., 2002, 2004).

Superimposed-ice forms when snow meltwater, percolating downward, refreezes deeper in the snow or at the snow-sea ice interface, where temperatures are lower than the freezing point (Digby, 1985; Onstott, 1992; Haas et al., 2001). When considering the time line, snow-ice appears most often at the beginning of the winter (Leppäranta, 1983), whereas superimposed-ice forms after the onset of surface melt at the beginning of the spring (Digby, 1985; Kawamura et al., 1997; Haas et al., 2001; Cheng et al., 2003; Nicolaus et al., 2003; Granskog et al., 2006; Wang et al., 215). During the formation of superimposed-ice, a thinner layer of ice with an appreciably higher thermal conductivity and lower albedo replaces a layer of snow (Haas et al., 2001; Nicolaus et al., 2003). Superimposed-ice forms an impermeable layer within the sea ice.

Ice formed in the presence of a snow cover (snow-ice and superimposed-ice) has a granular texture similar to that of frazil ice, but has a common negative $\delta^{18}O$[1] and δD[1] signature, caused by the significant contribution of $\delta^{18}O$ and δD-depleted snow crystals (Lange et al., 1990). For example, in Fram Strait (Meredith et al., 2001, Eicken et al., 2005), snow had a typical $\delta^{18}O$ of -21‰ while the Atlantic

[1] $\delta^{18}O$ and δD of a sample describes the relative abundance of the $^{18}O/^{16}O$ and $^{2}H/^{1}H$ ratio of the sample in comparison to that of the standard VSMO; Viena Mean Ocean, Water)

seawater had $\delta^{18}O$ of 0.3‰. In this case, the sea ice had a slightly more positive signature of 2.1‰. This can be explained by the fact that when seawater freezes, the solid phase (ice) is enriched in heavy isotopes in comparison to the parent seawater. By knowing the distinct $\delta^{18}O$ or δD of snow, ice, and seawater, the influence of snow meltwater in superimposed-ice and the influence of seawater in snow-ice formation can be elucidated (Eicken, 1998; Eicken et al., 2002, Eicken et al., 2005). In addition, the $\delta^{18}O$ and δD of sea ice depend on those of the parent water and the fractionation efficiency (which is partially a function of sea ice growth rate). Therefore, the $\delta^{18}O$ and δD of sea ice are useful for investigating under-ice water circulation and mixing in estuaries (Eicken et al., 2005), and for deducing ice growth rates (Souchez et al., 1987; Eicken, 1998).

II-7 The mushy layer model

The mushy-layer model approximates ice as a two-phase medium (ice and brine), with the important assumption that sea ice is free of gaseous inclusions (Notz and Worster, 2009). The mushy layer theory considers the solid pure ice matrix to be bathed in its impurity-rich melt (liquid brine), which can move in the gravity field as the solidification interface migrates away from the heat sink (Worster and Wettlaufer, 1997; Feltham et al., 2006; Hunke et al., 2011; Middleton et al., 2016). According to the mushy layer theory, there is no more necessity to differentiate the skeletal layer charactrezied by a relative high brine volume fraction from the internal ice layers containing a low brine volume fraction: both regions are “mushy”, since they consist of a mixture of solid and liguid (Hunke et al., 2011).

Mushy layer theory is typically expressed as a series of equations that relates the conservation of heat (Eq. II-9), mass, and solutes (Eq.II-10) (Worster, 1992; Feltham, 2006; Notz and Worster, 2006, 2009; Hunke et al., 2011). According to Notz and Worster (2009), the equation for the conservation of heat is formulated as follows:

$$c_m \frac{\partial T}{\partial t} + \rho_l c_l U \frac{\partial T}{\partial z} = \frac{\partial}{\partial z} \cdot \left(k_m \frac{\partial T}{\partial z} \right) + \rho_s L \frac{\partial \phi_v}{\partial t} + Q \quad \text{(Eq. II-9)}$$

Where the subscripts s and l represent the pure solid ice phase and pure liquid brine phase, respectively, T is the temperature, ϕ_v is the fraction of solid ice , U is the flux of moving brine with the velocity U_l as $U = (1-\phi_v)U_l$. (Notz and Worster, 2009). The heat conductivity and -capacity per specific ice volume, k_m and c_m , depends of the heat capacity of the brine and of the ice and their respective volumes, it is formulated as $X_m = \phi_v X_s + (1 - \phi_v)X_l$ where X is the respective property (Notz and Worster, 2009) . According to Notz and Worster (2009), L describes the local difference in enthalpy between the brine and the ice, is formulated as $L = L_0 \left(1 - \phi_v \, {\Delta\rho}/{\rho_m}\right)$ where L_0 is the constant latent heat at a reference temperature of 0 °C, ρ_m is the phase fraction weighted density, and $\Delta\rho = \rho_s - \rho_l$ is the difference between ice and brine density. Finally, Q is the solar radiation that enters into the ice. Hence, equation II-9 describes the transfer of heat and highlights that the major controlling factors of the sea ice temperature are the advection of heat with the moving brine, the diffusion of heat, the exchange of latent heat through internal phase changes, as well as the absorption of heat by the radiations (Q) (Hunke et al., 2011).

The second equation for the conservation of mass and solutes is given by Notz and Worster (2009) as:

$$(1-\phi_v)\frac{\partial S_{br}}{\partial t}+U\frac{\partial S_{br}}{\partial z}=\frac{\partial}{\partial z}\left(D_s\frac{\partial S_{br}}{\partial z}\right)+rS_{br}\frac{\partial \phi_v}{\partial t} \quad \text{(Eq. II-10)}$$

Where $r=\frac{\rho_s}{\rho_l}$ with ρ_s and ρ_l are the ice and brine density, respectively, and S_{br} is the brine salinity diffusing with an effective diffusivity D_s, $D_s=(1-\phi_v)D$, where D is the diffusion coefficient of salt in water (Notz and Worster, 2009). Hence, equation II-10 describes the transport of salt and shows that the total salt content of a control ice volume depends of the advection of salt associated to the moving brine (with velocity U), and of the transport of salt by aqueous diffusion in the brine (Hunke et al., 2011). Following the mushy layer, the advection of salt is regulated by buoyant fluxes as described in the Rayleigh number (Eq.II-8 and Eq.II-11) (Wettlaufer et al., 1997, 2000, Notz and Worster 2009).

The mushy layer equations represent an approximate mathematical framework to describe the transfer of heat through the porous structure of sea ice as well as the transport of salt including the development of brine channels (Feltham et al., 2006, Hunke et al., 2011; Jones et al., 2013). Past literatures (Untersteiner, 1968; Niedrauer and Martin, 1979; Weeks and Ackley, 1986) highlighted five processes leading to salt fluxes: salt segregation at the ice-seawater interface, brine inclusion migration, brine expulsion, gravity drainage, and flushing. Modeling work in mushy-layer-based simulations (Notz, 2005; Notz and Worster, 2006, 2008, 2009) introduced new perspectives on salt transport during sea ice growth.

II.7.1 Salt segregation at the freezing front versus mushy layer model

A long-standing idea suggests that salts are rejected at the growing ice-seawater interface. This release of salt was explained by the BPS model ("Burton-Prim Slichter" model, Burton et al., 1953) as in Cox and Weeks (1975, 1988) where empirical estimates of K_{eff} ($K_{eff} = S_{ice}/S_w$) were derived as a function of ice growth velocity (see section II-2 Transition from open-ocean to sea ice cover). Recent progress on the dynamics of mushy layers show that the BPS model initially developed to describe the evolution of single-crystal alloy, could not be directly applied to sea ice crystal formation (Notz and Worster, 2009). According to the mushy layer theory, there is no direct phase separation and salt segregation at the ice–seawater interface (Notz and Worster, 2008, 2009). In the absence of brine drainage, the solution of the mushy layer equations shows that the salinity in the skeletal layer is equal to the salinity of seawater at the ice interface, revealing that no salt is directly expelled at the advancing ice-seawater interface (Notz and Worster 2009; Hunke et al., 2011). Laboratory experiments from Wettlaufer et al. 1997 and Notz et al. 2005 revealed that all salt is initially trapped until it is rejected by brine drainage (i.e. brine convection) when the ice reaches a critical thickness. According to the mushy layer theory, the downward flux of brine is controlled by buoyant processes, regulated by the ice layer permeability (Worster, 1992; Wettlaufer et al., 1997; Notz and Worster, 2009). Notz and Worster (2009) explain that any effective segregation trying to capture the underlying physics of brine fluxes should then depend on the physical properties of the brine medium (density,

viscosity) and of the ice matrix (permeability, thermic capacity) and not solely on the ice growth rate. Cox and Weeks (1975, 1988) reported that higher bulk salinities coincided with higher ice growth rates based on measurements realized on really thin ice at the beginning of freezing process. Several Study (e.g. Notz and Worster, 2008, 2009; Worster and Jones, 2015) pinpointed that Ra has to reach a critical value (Ra_c) before the onset of the convection. For thin ice, the convection is probably very limited because the driving potential energy is insufficient to compensate the energy dissipated during the convection (thermal diffusion and friction linked to the brine viscosity). This delay of the convection increases salt and brine content of young growing sea ice (Notz and Worster, 2009).

The spatial extension of convective processes is most likely limited at the permeable ice layers in contact with the ice-seawater interface (Vancoppenolle et al., 2007; Notz and Worster, 2009). Hence, Notz and Worster (2009) recommend the use a local Rayleigh number, Ra_L described by :

$$Ra_L = \frac{g \Delta h_{br,z\text{-}sw} \rho_w \beta_w \Delta S_{br,z\text{-}sw} \Pi(\phi_{vmin})}{K_i \eta} \quad \text{(Eq. II-11)}$$

Where $\Delta h_{br,z\text{-}sw} \rho_w \beta_w \Delta S_{br,z\text{-}sw}$ refers to the density difference of seawater at the advancing interface and that of brine at level *z*, $\Pi(\phi_{vmin})$ represents the effective ice permeability considering the minimum ice volume fraction between level z and the seawater interface (Notz and Worster, 2009). Using the local Rayleigh number improves our understanding of the onset and delay of convective processes (see discussion Notz and Worster (2009) and Worster and Jones (2015)): After onset of convection, the release of salt lowers the bulk salinity and brine volume in the

convective area, which decreases the ice permeability. Hence, Ra can reach a subcritical stage leading to the offset of convection. The offset of convection leads to salt accumulation and higher permeability value in new formed sea ice just below the previously convective area. Salt content providing new potential energy increases until Ra becomes supercritical again and convection restarts (Notz and Worster 2009; Worster and Jones, 2015). Note that since the conduction of heat occurs at a faster rate than the diffusion of salt, it is the internal phase changes driven by temperature variations that control the brine salinity in the convective layer. Consequently, even though the driver of the convective process is by $\Delta S_{br\text{-}sw}$ (potential energy), the thermal diffusivity K_i is a stronger indicator to estimate of the onset and offset of the convection (Notz and Worster, 2009; Worster and Jones, 2015).

II.7.2 Brine inclusion migration and brine expulsion within the mushy layer

Previous estimations of brine inclusions migration relied on the phase equilibrium relationship and on the aqueous diffusivity of salt within a network of spherical isolated inclusions (Notz and Worster, 2009). Within the mushy layer framework, it is possible to compute the salt fluxes from the brine migration independently of the interstitial morphology of the brine pockets. Notz and Worster (2009) show that the contribution of brine migration to salt fluxes is insignificant both considering closed isolated brine inclusions or interconnected brine networks. According to Untersteiner (1968), the salt diffusion rate limits brine inclusion

migration to an estimated 3 μm h^{-1}, rendering this process negligible for the export of salt (Lake and Lewis, 1970; Niedrauer and Martin, 1979; Eicken, 2003).

Using the mushy layer framework to estimate brine expulsion (i.e. expulsion of brine along crystal boundaries as a result of the increase of pure ice volume during the freeze up of brine) shows that the rate of the downward expulsion of brine is constantly lower than the sea ice growth rate (Notz and Wortser, 2009; Hunke et al., 2011). Therefore, Notz and Worster (2009) and Vancoppenolle et al. (2005) reached the same conclusion as Cox and Weeks (1975), in that salt cannot be displaced beyond the advancing interface. According to Cox and Weeks (1975), the role of brine expulsion in desalination is limited to short periods of time, during which rapid ice growth produces strong temperature changes in every ice layer, inducing upward displacement of brine. This process can occasionally lead to the apparition of brine skim at the surface of the ice cover (Cox and Weeks, 1974, 1975; Eide and Martin, 1975).

II.7.3 Flushing

The salt fluxes from flushing events can be estimated with the mushy layer theory equations using Darcy's law. Darcy's law computes the downward motion of meltwater gathering at the top of the ice, using the permeability equations of Freitag (1999) (Notz and Worster, 2009). The main advantage of the thermodynamic mushy layer equation (Eq. II-9-10) is its ability to simulate the increase in temperature associated with the downward percolation of meltwater due to the brine velocity U, effect that is usually disregarded in existing sea ice models

(Notz and Worster, 2009). Results show that flushing is the most effective desalination process. According to the mushy layer model, the development of impermeable ice layers, which could reduce or interrupt the salt fluxes during flushing events, is unlikely (Notz and Worster, 2009). However, it has been argued that flushing events reduce sea ice permeability due to the decrease in brine volume and/or the formation of impermeable superimposed-ice (Vancoppenolle et al., 2007; Polashenski et al., 2012; Skyllingstad et al., 2015). Recent work shows that infiltration of fresh water into the pore structure of sea ice accounts for blocking percolation pathways within ice, sealing the ice against water percolation, and allowing water to pool above freeboard. (Vancoppenolle et al., 2007; Polashenski et al., 2012; Skyllingstad et al., 2015).

II.7.4 Synthesis of desalination processes

The mushy layer theory provides consistent formulations for heat and salt conservation in sea ice. Using the mushy layer theory, the sea ice heat conservation equations have been properly solved by Taylor and Feltham (2004) and Notz and Worster (2006, 2009) modeled both the heat and salt conservation equations using an enthalpy-based approach.

Recent advances in the mushy layer model highlighted that phase segregation at the growing interface is not a major desalination process. Simulation of the vertical changes of bulk ice salinity during ice growth by Notz and Worster (2009) showed that in the absence of brine drainage no meaningful rejection of salt occurs. Their results demonstrated that brine inclusion migration and brine

expulsion have the ability to redistribute salt, but are irrelevant for the large-scale of salt fluxes (Table II-3) (Untersteiner, 1968; Lake and Lewis, 1970; Eide and Martin, 1975; Niedrauer and Martin, 1979; Weeks and Ackley, 1986; Oertling and Watts, 2004; Notz and Worster, 2009).

The mushy layer model uses the Rayleigh number (Ra) as a proxy to describe the capacity of sea ice to exchange brine with underlying seawater by natural gravity drainage. Thus, V_b is only one parameter, among many others, to describe the propensity of sea ice for natural gravity drainage. As a result, any permeable ice layer would be able to exchange brine with the underlying seawater through convection according to percolation theory (e.g. Golden et al., 1998). However, according to mushy layer theory (Notz, 1992; Worster and Wettlaufer, 1997; Feltham et al., 2006), only permeable ice layers with sufficiently high Ra ($Ra > Ra_c$) are able to exchange fluid by brine convection.

Table II-3: Summary of desalination processes.

	Thermal regime	**Conditions**	**Impacts**
Brine drainage	-Cold ice -Transition from cold to warm ice	Connected brine network and unstable density distribution: $V_b > 5\%$, $Ra > Ra_c$	Export salt out of the ice => desalination process
Flushing	Warm ice	Connected brine network and meltwater on the ice surface above sea level	Export salt out the ice => desalination process
Flooding	Independent	Snow cover	Redistribute salt toward the surface
Brine inclusion migration	Cold ice	Temperature gradient across inclusions	Redistribute salt toward the bottom
Brine expulsion	Cold ice	High growing rate	Redistribute salt toward the surface and the bottom

II-8 Critical Threshold: 5% V_b and Ra_C

While V_b>5% and Ra_c are commonly used as criteria to discriminate between permeable and impermeable ice layers and underline the presence of convective processes, there are some important assumptions linked to these critical thresholds. These assumptions are discussed in details in Vancoppenolle et al. (2013) and Zhou (2014).

While V_b represents the total porosity (ft) of sea ice and it is used for calculating the vertical permeability however only a subsection of the pore spaces is integrated into an interconnected brine network and therefore available for fluid transport. The interconnected portion represents the effective porosity (fe) (e.g. Freitag, 1999; Petrich et al., 2006). According to percolation theory (Golden et al., 1998), fe is close to zero for V_b<5% and approaches V_b for V_b>9% (Petrich et al., 2006) so the difference between fe and ft (V_b) is only significant when V_b is between 5 and 9%. Consequently, it is more accurate to compute the vertical sea ice permeability as a function of fe, rather than V_b, at least while V_b is between 5 and 9% as in Freitag (1999).

Typically, different variable formulations and model representations used to simulate brine transport lead to different percolation thresholds. For example, Pringle et al. (2009) reported critical vertical percolation thresholds ranging from V_b 3.9 to 6.9 % while Zhu et al. (2006) and Golden et al (2007) found no percolation threshold). Secondly, V_b = 5% (according to Golden et al., 1998) is only valid to describe vertical permeability in columnar ice. Golden et al. (1998) suggested that the percolation threshold could be higher for granular ice due to the more random

arrangement of ice crystals and misalignment of brine inclusions. Pringle et al. (2009) showed that sea ice is an anisotropic medium, with a different horizontal than vertical permeability. Finally, if excluded volumes (i.e. non-brine inclusions) like precipitates (solid salts, e.g. ikaite), micro-organisms, as well as air bubbles are accounted in the brine volume fraction, the estimation of percolation threshold may be biaised (Pringle et al., 2009). Even though the 5%-V_b threshold is widely recognized as the criterion to differentiate permeable and impermeable ice layers, no obvious agreement exists in the literature.

Similarly, currently no consensus on the critical Ra_c values for convection is evident: Ra_c = 10 in Notz and Worster (2008), Ra_c = 7 in Notz and Worster (2009), Ra_c = 5 in Vancoppenolle et al. (2010), Ra_c =1±0.5 in Griewank and Notz (2013) and Ra_c = 3.2 to 7.1 in Griewank and Notz (2015). It is the divergence in variable formulations and model representations, which lead to a wide range of critical Ra_c values. Principally, different formulations for the thermal diffusivity (Pringle et al., 2007; Notz and Worster, 2009) and ice permeability (Freitag, 1999; Eicken et al., 2004; Petrich et al., 2006) coexist in the litterature. For instance, the effective permeability can be computed using the mean solid ice volume or as a function of either the minimum or maximum solid ice volume. Similarly, the linear relatiotionship between the temperature and brine salinity developed by Vancopenolle et al.(2013) (Eq.II-5-section II-3.2 Brine salinity and brine volume temperature dependent relationships) leads to brine salinity values different than the formulation of Notz (2005) or UNESCO (1978), which consequently affects the estimation of the critical Ra_c. In addition, the estimation of Ra can be biaised due

to errors and imprecisions on the measured temperature and salinity. If the measurments took place after the extraction of the ice core, a portion of the brine can be lost during the coring process, lowering the basal salanity and Ra value in the lowest section of the ice core volume (Vancoppenolle et al., 2013).

Finally, it would be more accurate to refer to brine porosity and brine permeability, because the ice is actually a three-phase rather than a two-phase medium as simplified in the theories discussed above. The true total porosity consists of liquid brine inclusions (brine porosity) and air bubbles (air porosity). While a description of air-porosity and -permeability is currently absent in the literature, the permeability and convection threshold (Ra_c) are repeatedly used as criterion in gas exchange studies as well (Zhou et al., 2013; Moreau et al., 2014). Processes of gas exchange and transport likely have different physical constraints compared to those of fluid transport; these thresholds should be used with care when extended to studies of gases in sea ice.

Brine transport and exchange processes definitely increase at high brine volumes, but the exact thresholds (V_b and Ra_c) above which brine transport starts are still under investigation. Vancoppenolle et al. (2013) call for interpreting data both qualitatively and relatively or combining multiple proxies and independent measurements to strengthen the use of V_b and Ra to indicate variations in sea ice permeability and brine convection localization (Jardon et al., 2013; Zhou et al., 2013).

II-9 Gas content and composition (Ar, O_2 and N_2)

Like salt, dissolved gases are incorporated in sea ice and concentrated into brine inclusions during ice formation (Matsuo and Miyake, 1966; Mock et al., 2003; Tison et al., 2002). Gas exists in sea ice in the dissolved state in brine and/or in the gaseous phase as air bubbles. The physical state of gas species is regulated by the salinity and temperature of the ice medium. Gas solubility in brine increases as temperatures drops, while an increase of salinity has the opposite effect. Solubility relationships have not been established for the range of temperatures and salinities in brine. However, if we assumed that the relationships established for seawater (i.e. for temperatures between 0 and 30°C and salinities between 0 and 34) still hold for brine, solubility in brine should decrease with decreasing temperature due to increasing salinity of brine during freezing (Zhou et al., 2013) (Figure II-19).

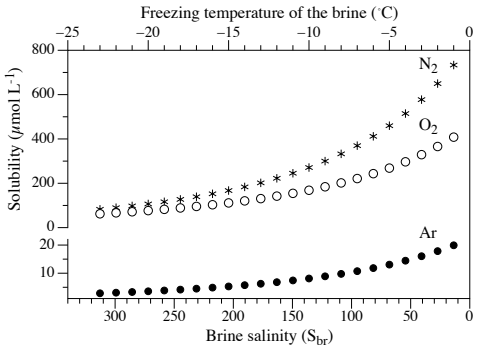

Figure II-19: Solubility of Ar, O_2 and N_2 (µmol L^{-1}). The brine freezing point is calculated after UNESCO, 1978 (Eq.II-3). Solubility is computed after Garcia and Gordon, (1992) for O_2 and Hamme and Emerson, (2004) for N_2 and Ar.

Only a few studies have documented total gas content (including the dissolved and gaseous fraction) within sea ice (Matsuo and Myake, 1966; Tison et

al., 2002). Bulk ice total gas content (mL L^{-1} ice) of sea ice is lower than in the seawater from which it formed. This is because gases in seawater are preferentially expelled from growing ice, along with salts (Cox and Weeks, 1983, 1988; Killawee et al., 1998; Tison et al., 2002; Loose et al., 2009, 2011a).The total gas content measurements reported for both natural (Matsuo and Miyake, 1966) and artificial sea ice (Tison et al., 2002) range from 2 to 22 mL STP kg^{-1} of ice (standard temperature and pressure) (Table II-4); lower values than expected from Instant Freezing of Seawater (IFSW ranging from 23 to 24 mL STP of air kg^{-1}, Cox and Weeks, (1983)).

Table II-4: Total gas content measurements and gas composition of sea ice.

Sea ice total gas content	**Min ml kg^{-1} of ice**				**Max ml kg^{-1} of ice**	
Cox et Weeks (1983)	< 23-24 IFSW					
Myake et Matsuo (1966)	2.2				22.2	
Tison et al. (2002)	3.8				18	
Gas composition (%)	**Ar**		**O_2**		**N_2**	
	Min	**Max**	**Min**	**Max**	**Min**	**Max**
Matsuo and Myake (1966)	0.9	1.1	20.6	29.0	54.2	76.8
Tison et al. (2002)	n/a	n/a	24.36	30.46	69.54	75.6
Sea water (t= 0°C, S=33)	1.69		34.84		61.14	
Atmospheric composition	0.93		20.95		78.08	

Bulk ice gas composition have been shown to span the interval between atmospheric and seawater composition, ~⅓ of O_2 and ~⅔of N_2 (Table II-4) (Matsuo and Myake, 1966; Tison et al., 2002). Ar and N_2 are considered as inert gases within sea ice, whose concentration depends only on physical processes such as: (i) the initial gas entrapment at the ice-seawater and ice-atmosphere interfaces; as well as (ii) the potential phase change (from dissolved in brine to gaseous in air bubbles) that may take place in the brine medium; and (iii) brine and bubble transport within

sea ice and across the ice-atmosphere and ice-seawater interfaces. Comparison of biogenic gases (such as O_2 and CO_2) with Ar and N_2 can be used as an indicator of primary production as respiration and photosynthesis will affect both O_2 and CO_2.

Greenhouse gases (CO_2, CH_4 and N_2O) have also been reported in sea ice at trace concentration from ppb to ppm depending on the gas species and the sea ice physical conditions (e.g. Geilfus et al., 2012a; Randall et al., 2012; Zhou et al., 2014b). The fate of these trace gases is differentiated from the abundant atmospheric gases (Ar, O_2 and N_2), because they are involved in chemical reactions and /or biochemical cycles. Therefore, they are treated separately in section II-12, which focuses on the specific case of the CO_2 (see section II.12.1The CO_2 and the carbonate system) and CH_4 (see section II.12.2 CH_4 in ice-covered area in the Arctic).

II-10 Gas entrapment and air porosity formation

II.10.1 Gas segregation at ice-water interface

Gas segregation at the growing ice-seawater interface refers to the processes by which most of the gas is rejected from the growing ice crystals because the crystal lattice can only accommodate limited amounts of impurities; for example, 45% to 61% of O_2 is rejected from the ice to the boundary layer, depending of the freezing rate (Loose et al., 2009). Rejection increases the gas concentration at the sea ice-seawater interface. The difference in concentration between the interfacial boundary layer and seawater reservoir drives gas transport toward the lower concentration in bulk seawater by gas diffusion and buoyancy-driven convection.

In an ice tank experiment, Loose et al. (2009) observed that gases are rejected more efficiently than salts, possibly by differential diffusion rates. Since gases have faster diffusion coefficient (Table II-5), they would diffuse away from the interface faster than salts and would then be incorporated in smaller quantities**.** Similar to salt, the freezing rate could play a determining role for gas entrapment, a lower freezing rate allows more time for gas diffusion across the boundary layer reducing gas build-up at the ice-seawater interface (Loose et al., 2009). Note that according to the emerging mushy layer theory the entrapment/rejection of solute at the ice interface is controlled by buoyant convection rather than by diffusion processes (Notz and Worster, 2009).

Table II-5: Diffusion coefficient of gases ($10^{-5} cm^2 s^{-1}$) and salts ($10^{-6} cm^2 s^{-1}$) in water.

	Wise and Houghton (1966)	**Broecker and Peng (1974)**	**Stauffer et al. (1985)**
T (°C)	10	0	0
Ar	1.7	0.88	n/a
O_2	1.7	1.17	2.08
N_2	1.8	0.95	1.61
CO_2	n/a	0.94	1.18
Na+ Cl-	D 10^{-6} $cm^2 s^{-1}$ (Loose et al., 2009)		

Killawee et al. (1998) and Tison et al. (2002) discuss the potential incorporation of gas by direct bubble entrapment in artificial sea ice tank experiments. Both observed that gas rejection from the consolidating ice matrix into the boundary layer increases the concentration of dissolved gases to the point they are supersaturated with respect to the atmosphere. Supersaturation is a state of a solution where the dissolved gas concentration (C) exceeds the saturation point

or solubility concentration ($C_{saturation}$). According to the sea ice tank experiments from Killawee et al. (1998) and Tison et al. (2002), supersaturation could lead to bubble nucleation and entrapment within the ice matrix. Supersaturation appears to be controlled by the thickness of the boundary layer at the interface, itself depending on the buoyancy-driven convection within the seawater reservoir (Killawee et al., 1998; Tison et al., 2002). Although direct observations of bubbles at the interface have yet to be reported, Killawee et al. (1998) documented the presence of air inclusions in the bottom layer of the ice matrix. Norris et al. (2011) reported measurements of bubble size spectra within the near-surface water of open leads in the central Arctic pack ice. During the onset of freezing of the leads, Norris et al. (2011) observed bubbles produced through thermodynamic processes rather than arising from wind generated wave-breaking processes. They suggested that, in the low turbulence environment of the open lead, loss of heat to the atmosphere cools the seawater surface layer below the bulk water temperature; increasing then the gas solubility and density of the surface layer. As the surface layer sinks due to buoyancy-driven convection and mixes with warmer water below, gas solubility will decrease resulting in local supersaturation and bubbles nucleation. The magnitude of the surface heat flux will affect both the depression of the surface temperature below the bulk water temperature and hence the attainable supersaturation, and the strength of buoyancy driven mixing.

In addition, the advancing freezing front can directly trap bubbles rising through a shallow water column. This is particularly true for methane, which is released at the seafloor from anoxic sediment and subsea-permafrost. Shakova et

al. (2010) observed large CH_4 bubbles enclosed in landfast sea ice growing above the East Siberian Arctic Shelf.

II.10.2 Gas entrapment at ice-atmosphere interface

The gas content is usually higher in the granular layer, near the ice-atmosphere interface (Grenfell, 1983; Perovich and Gow, 1996). The literature evokes several processes that could contribute to increase the gas content near the ice-atmosphere interface (e.g. Tsurikov, 1979; Perovich and Gow, 1996; Pustogvar and Kulyakhthtin, 2016). These processes could include (i) the capture of air during frazil, snow-ice, and superimposed-ice formation, (ii) the possible migration of air inclusions from the snow cover into the sea ice cover, (iii) accumulation of gases associated with the rapid freezing of snow meltwater and the replacement by air of the downward moving brine above the freeboard.

II.10.3 Nucleation processes and air volume fraction

In the vertical within a sea ice sheet, bottom columnar ice is usually depleted in air inclusions while top granular ice is described as bubbly with larger air inclusions (Figure II-20) (Grenfell, 1983; Perovich and Gow, 1996; Cole et al., 2004). The diameter of the bubbles scale from micrometer (Light et al., 2003) to several millimeters in first year sea ice (Grenfell, 1983; Perovich and Gow, 1996) (Table II-6).

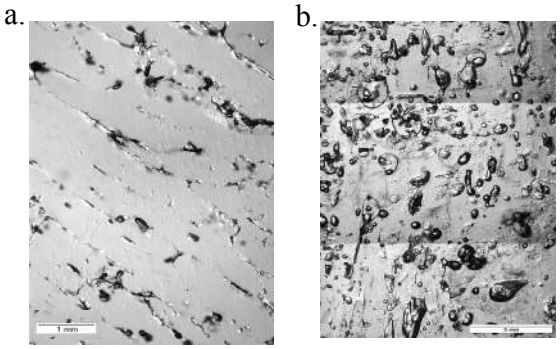

Figure II-20: Picture from the Chukchi Sea, April 2001 (a) obtained from a low-porosity band located in columnar sea ice, (b) obtained from a bubbly layer in fine-grained granular sea ice (Cole et al., 2004).

Table II-6: Bubble diameters reported from first year sea ice.

	Bubbles Ø (mm)	**Ice type**
Grenfell (1983)	0.2-4	First year sea ice
Perovich and Gow (1996)	0.64 (mean) 0.30 (mean) 0.64-1.30 (mean)	Granular first year ice (32 cm thick) Columnar first year sea ice (32 cm thick) Multi-year ice (>200 cm thick)
Light et al. (2003)	0.008-0.14	Columnar first year sea ice (175 cm thick)

Zhou et al. (2013, 2014a) reported that during the winter, bulk ice gas concentrations (Ar, O_2, N_2,) reached maximum supersaturation (2960%, 3180% and 7030%, respectively) where the brine volume fraction was the lowest (2%). These levels of supersaturation should induce bubbles formation within the brine system so that most of gas species would be in gas phase instead of being dissolved in the brine medium. Similarly, Glud et al. (2002) and Mock et al. (2002, 2003) suggested that most of O_2 contained in the ice was in gaseous phase in bubbles due to supersaturation resulting from increasing salinity in brine during the freezing process.

Current literature in the sea ice field (Zhou et al., 2013; Moreau et al., 2014) assumes that above the saturation concentration, gas starts to nucleate given that

the total partial pressure of all three major atmospheric gases is above the brine hydrostatic pressure (1 atm). The saturation concentration is given by Henry's Law which describes the gas solubility:

$$C_{isaturation}=P_i \times K_H \quad \text{(Eq. II-12)}$$

were P_i is the partial pressure of a given gas i just above the solution (in the gaseous phase), $C_{isaturation}$ is the concentration of the gas dissolved in the solution (the aqueous phase) in equilibrium with the partial pressure just above the solution, and K_H is the Henry's law constant, which is a function of the temperature and salinity.

The level of saturation (ΔC) compares the observed gas concentration in brine (C_{ibr}) with the gas solubility concentration in brine ($C_{isaturationbr}$); the expected gas concentration in brine assuming equilibrium with the atmosphere (see Eq.II-12):

$$\Delta C = C_{ibr} / C_{isaturationbr} \quad \text{(Eq. II-13)}$$

Gas supersaturation likely occurs during ice growth due to synergistic effects related to decreasing ice temperature. First, brine volume decreases, which increases dissolved gas concentration in brine (C_{ibr}) possibly above ($C_{isaturationbr}$). Secondly, decreasing ice temperature decreases gas solubility ($C_{isaturationbr}$) because the increasing brine salinity offsets the increase solubility due to cooling. Therefore, brine is typically supersaturated with gas and bubbles formation could occur if the sum of the partial pressures of all the dissolved gases is higher than the local hydrostatic pressure.

Conversely during spring, the solubility of gas in brine ($C_{isaturationbr}$) increases due to the decreasing brine salinity. In the same time, the gas concentration within the brine medium (C_{ibr}) also decreases by dilution associated with the input of freshwater from melting brine walls (i.e. the dilution effect). As a result, brine inclusions previously supersaturated during winter evolved toward their respective equilibrium solubility value (Figure II-21). Theoretically, internal melting also promotes air bubble formation; melting involves a 10% volume reduction due to the density difference caused by phase change (Perovich and Gow, 1996).

Since major gas concentrations (Ar, O_2 and N_2) are reported in bulk ice (Tison et al., 2002; Zhou et al., 2013), the temperature and salinity dependent solubility (i.e. saturation concentration) in brine is multiplied by the brine volume fraction to obtain the bulk ice gas solubility (bulk ice saturation concentration) (Zhou et al., 2013).

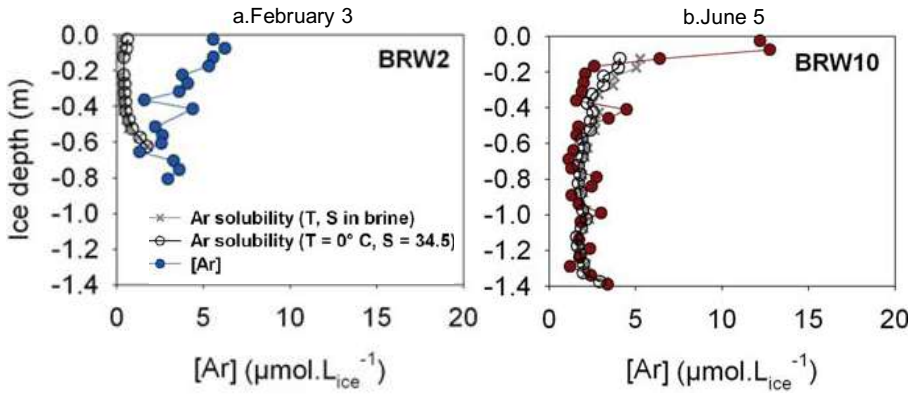

Figure II-21: Evolution of Ar concentration in bulk sea ice (dots) as compared to the bulk ice solubility limits (crosses). Deviation of [Ar] in bulk ice to the solubility limit indicates potential bubble content as in February (a), while [Ar] in bulk ice at the solubility limit indicates that the gas is dissolved in brine as in June (b), adapted from Zhou et al. (2013).

Because there is no analytical method to assess the partitioning of gases between dissolved and gaseous forms in sea ice brine, saturation state is commonly used as proxy to estimate the air volume fraction (Zhou et al., 2013, Moreau et al., 2014; Kotovitch et al., 2016). According to the reasoning therein, the air volume fraction should increase as temperature decreases due the concentration effect in winter. Reversely, the air volume fraction should decrease during melting season due to the dilution effect. However, according to the results of Light et al. (2003), cooling (-2°C to -25°C) sea ice caused inclusions to shrink in size including the disappearance of the smallest air inclusions, while warming (-25°C to -2°C) sea ice thin sections increased the size of existing air inclusions without forming new bubbles.

Cox and Weeks (1983) based on sea ice density measurements estimated that in first year sea ice the air volume fraction was inferior to 5% of the ice volume. Consequently, it is commonly assumed that air volume fraction is much lower than brine volume, which explains why it is usually ignored during brine volume calculations and sea ice permeability parameterizations.

II.10.4 Biological production

A final process to be considered is the formation of air inclusions produced through photosynthesis during the spring (Glud et al., 2002; Mock et al., 2002; Delille et al., 2007, 2014; Zhou et al., 2014a). While inert gas concentrations (Ar and N_2) reach their respective equilibrium solubility values during spring in warm ice (Figure II-21), O_2 concentration often stays above saturation in bottom sea ice

layers because biological O_2 production partly compensates for the dilution effect (Figure II-22). According to Zhou et al. (2014a), biological production could contribute to 29% of the O_2 supersaturation observed in sea ice during the spring and summer. Despite sea ice algal production, heterotrophic activities could result in a net consumption of O_2, which combines with the apparition of deoxygenated melted ice crystals (dilution effect), lead to potential local anoxic conditions within the brine micro-environment (Rysgaard and Glud, 2004).

In wintertime, while photosynthesis is mostly inhibited due to the absence of light, bacterial respiration could exert some control on O_2 concentrations within the ice and the underlying seawater (Moreau et al., 2015a,b; Zhou et al., 2014a).

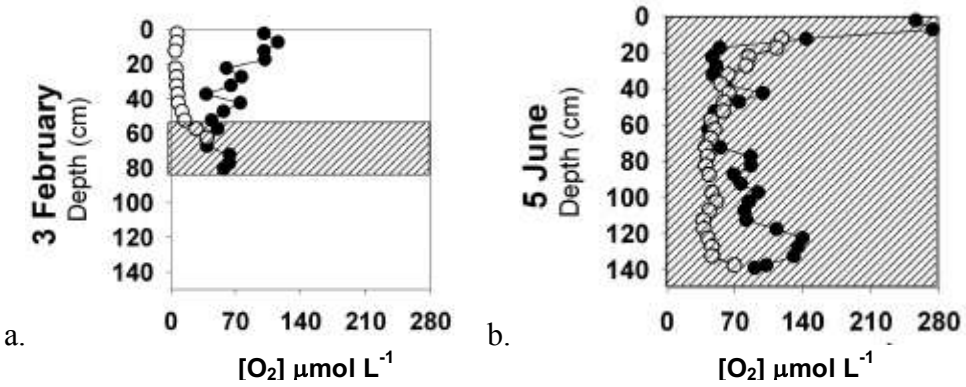

Figure II-22: Comparison of O_2 concentration (black dots) and its solubility (white dots) in bulk ice in winter (a) and spring (b), the dashed areas refer to permeable ice layers (i.e. V_b>5 %), in (b) the deviation of O_2 from the solubility limit indicates O_2 production by photosynthesis, adapted from Zhou et al. (2014a). For the same location and time, Figure II-21 showed that inert gas Ar reached solubility value in spring.

II-11 Potential gas transport and exchange

II.11.1 Transport of gas within the sea ice cover

Three main processes should be considered for gas transport within sea ice, all three of which require a certain level of permeability in the sea ice, which may differ depending on the process considered: 1) brine convection expelling dissolved salts and gas, 2) diffusion of dissolved gas along the concentration gradient in the brine network, and 3) upward buoyant transport of bubbles.

Gravity drainage, as defined by Eide and Martin (1975), refers to processes within the ice layer caused by the greater density of the brine relative to the seawater, driving the brine downward out of the ice into the underlying seawater. Observations of dissolved O_2 release into the underlying seawater both in rapidly growing sea ice and in steady sea ice (ice which is neither growing nor melting) show that brine drainage has the potential to carry dissolved gases to depth, removing them from exchange with the atmosphere. According to Else et al. (2015), intense brine convection events during rapid ice growth carry more dissolved O_2 out of the ice than at lower freezing rates, underlining again the role of the freezing rate in the gas segregation process. Brine drainage process has also been identified as a key process removing CO_2 from sea ice and sequestering it at depth, thereby prevent its release to the atmosphere (Rysgaard et al., 2007, 2011; Geilfus et al., 2016) (see section II.12.1 The CO_2 and the carbonate system).

At brine volume fractions below 5% no brine convection is expected to occur (Golden et al., 1998), and the ice cover is often considered impermeable to liquid exchange. Most dissolved gases are expected travel within the brine, so the

ice is often also considered impermeable to gas exchange at brine volume fractions below 5%. However it has been suggested that a permeability threshold for gas exchange might be different than for liquid exchange (Loose et al., 2011a,b). Past studies based on artificial sea ice have suggested that solute diffusion along a concentration gradient within brine is the major control on dissolved gas fluxes across sea ice while no liquid convection is occurring (Gosink et al., 1976; Loose et al., 2009, 2011a). Loose et al. (2011a) for example measured diffusion rates of 10^{-6} cm s^{-1} for O_2 and SF_6 in artificial columnar sea ice for brine volumes ranging from 4% to 6%.

A final transport process to consider is the upward migration of bubbles under buoyancy. According to Zhou et al. (2013) and Moreau et al. (2014), upward migration of bubbles could be the main vertical gas transport pathway at the beginning of spring when the brine network becomes sufficiently connected. A rapid release of gas out of the supersaturated sea ice, which combined with brine dilution and brine drainage, would bring gas concentrations to their equilibrium concentration relative to the atmosphere. In a recent model study, Kotovitch et al. (2016) inferred that the buoyant transport of bubbles is likely a significant contributor to air-ice gas flux in young growing sea ice. Even if this hypothesized gas transport pathway is plausible at this stage, it should still be subject to caution since it does not rely on direct process observations, but rather on inference from air-ice CO_2 flux (Kotovitch et al., 2016) and Ar content (Moreau et al., 2014) in a single sea ice model, and the authors called for more observations of air bubble dynamics and nucleation processes in sea ice.

II.11.2 Gas exchange at the ice-atmosphere interface

Air-ice gas exchange depends on the difference of partial pressure between brine and the atmosphere, wind speed and the diffusion coefficient (Wanninkhof, 1992). However, in contrast to air-sea exchange, the diffusion coefficient in sea ice is still poorly known. They have been described for only a few gas species (CO_2, SF_6, and O_2) in specific conditions in artificial sea ice. While air-sea gas exchange occurs through a free surface, air-ice gas exchange takes place across a rough and variably porous surface, therefore the amount of pore and their connectivity control also the magnitude of the exchange (Nomura et al., 2006; Moreau et al., 2015a; Kotovitch et al., 2016). The 5% -V_b threshold has been established for the percolation of brine in columnar sea ice only. Therefore, it is not applicable to the transport of air bubbles and it is not relevant for granular sea ice (Golden et al., 1998, 2007). Zhou et al. (2013) and model study from Moreau et al. (2014) show that buoyant transport of bubbles occurs potentially at higher brine volume fraction (V_b>10%).

The presence of snow cover above the ice modifies the nature of the ice-atmosphere interface; therefore, sea ice gas exchange depends also of the snow physical characteristics. Snow permeability evolves seasonally due to aging snow processes (i.e. metamorphism) and temperature gradient, which modify the grain radius and the snow density (e.g. Hardy an Albert, 1993) (Figure II-23). Although snow is generally more permeable than ice, snow cover can act as an intermediate reservoir (or buffer) in which gas are stored until wind speed exceeds a critical

threshold and the gas is ventilated (Heinesch et al., 2009; Nomura et al., 2010a; Papakyriakou and Miller, 2011).

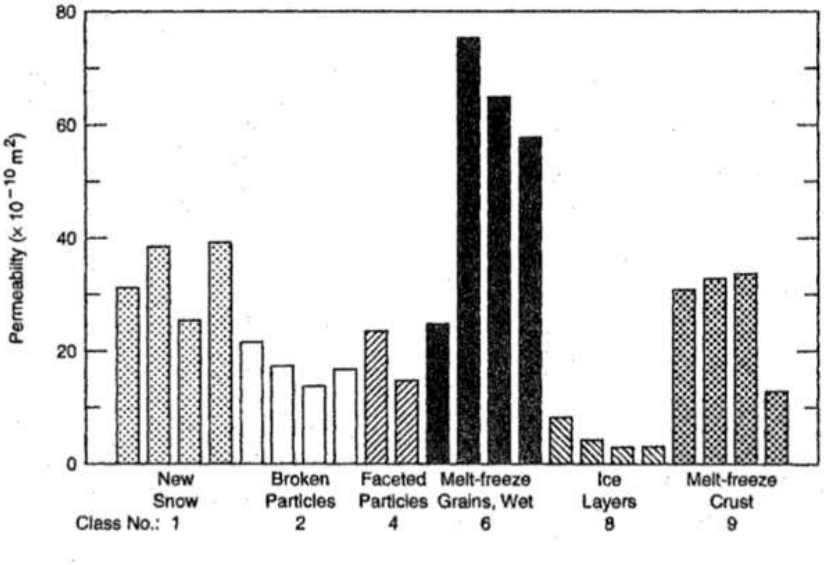

Figure II-23: Measured permeability of snow samples from six different crystal classes (Hardy and Albert, 1993).

II-12 Greenhouse gases: CO_2 and CH_4

II.12.1 The CO_2 and the carbonate system

The bulk ice pCO_2 depends of complex biogeochemical processes governing the carbonate system. While Physical and chemical reactions force carbon species into different phases (gas bubbles, dissolved inorganic carbon and precipitated carbonate), and regulate the exchange of carbon between the atmosphere and the seawater, biological processes transform inorganic into organic forms and vice versa (e.g. Delille et al., 2007, 2014; Dieckmann et al., 2008, 2010; Geilfus et al., 2012 a,b; Nomura et al., 2010, Miller et al., 2015).

Global and regional budgets of air-sea CO_2 exchange have ignored ice-covered regions (Bates and Mathis, 2009) relying instead on the assumption that sea ice cover is impermeable to gases. CO_2 fluxes measurements over sea ice evidenced that sea ice is permeable to gas, and acts as a source or sink for atmospheric CO_2 depending of the season (e.g. Delille et al., 2007; Nomura et al., 2010, 2013) (Table II-7). Two common techniques are widely used to measure sea ice gas fluxes: the chamber-of-accumulation method (Delille et al., 2007) and the eddy covariance technique (Zemmelink et al., 2006). The chamber method monitors the changes of the trace gas concentration against the elapsed time. The chamber registers the flux directly from the surface emitting the flux; ice or snow over short time periods (McMinn et al., 2009; Miller et al., 2015). The eddy covariance (EC) method is based on the quantification of the covariance between measurements of vertical turbulent flux and concentration of the gas of interest (e.g. Burba et al., 2008; Burba, 2013). Unlike chamber techniques, EC monitors fluxes taking place over vast spatial areas (over $100m^2$) over long periods without changing the observed environment (Miller et al., 2015). Since EC and chamber technics monitor fluxes on two different temporal and spatial scales, it makes comparison of the two measured fluxes often ambiguous and complicated (Miller et al., 2015). Although these techniques actually provide different flux magnitudes, they usually agree well on the direction of the flux. Both methods point to sea ice as a source of atmospheric CO_2 during winter and as a sink for atmospheric CO_2 toward spring and summer (Table II-7).

The annual cycle of CO_2 dynamics is more complicated than that of major atmospheric gases (Ar, O_2 and N_2) because it mostly depends on the respective chemical equilibrium of the carbonate species in brine:

$$CO_{2(gas)} \overset{K_H}{\leftrightarrow} CO_{2(aq)} + H_2O \leftrightarrow H_2CO_3 \overset{K_1}{\leftrightarrow} H_2CO_3^- + H^+ \overset{K_2}{\leftrightarrow} CO_3^{2-} + 2H^+$$

(Eq. II-14)

Where K_H is the Henry's law constant for CO_2, K_1 and K_2 are the first and second dissociation constants of the carbonate system respectively, which depend on temperature and salinity (Zeebe and Wolf-Gladrow, 2001).

Table II-7: CO_2 fluxes measurements over sea ice.

Season	References	Technique	CO_2 Flux (mmol m^2 d^{-1}	Location	Sea ice condition
Winter condition Sea ice as a source of atmospheric CO_2	Nomura et al., 2006	Chamber	+0.4 to +0.9	Artificial sea ice	Growth phase
	Geilfus et al., 2013	Chamber	+4.2-to +9.9	Barrow, Alaska	Newly formed sea ice
	Barber et al., 2014	Chamber	+2.49 to +4.21	Young Sound, Greenland	Newly formed sea ice
	Miller et al., 20011	EC-Open path	-60.5 to +74.3	Beaufort Sea, Arctic	Landfast sea ice (winter until spring)
	Sievers et al., 2015	EC-Open Path	-36.1 to +105.9	Young Sound, Greenland	Landfast sea ice (Late winter)
Spring and summer condition Sea ice as a sink of atmospheric CO_2	Delille et al., 2007	Chamber	-5.2 to +1.9	Weddel Sea, Antarctica	Pack ice
	Nomura et al., 2010b	Chamber	-.36 to +1	Hokkaido Bay, Japan	Landfast sea ice
	Geilfus et al., 2014	Chamber	-2.9 to +0.3	Belinghausen Sea, Antarctica	Pack ice
	Geilfus et al., 2015	Chamber	-5.4 to -0.04	Resolute Bay, Nunavut, Canada	Melting landfast sea ice
	Zemmelink et al., 2006	EC-Open path	-6.6to -18.2	Weddel Sea Antarctica	Pack ice
	Papakyriakou and Miller., 2011	EC-Open-Path	-259.2 to +86.4	Centre of the Arctic Archipelago	Landfast sea ice

Temperature exercises a strong control on the inorganic carbon chemistry due to its impact on K_H, K_1 and K_2 and due to its controls on the brine salinity and brine volume fraction (Figure II-24); while sea ice temperature varies vertically and seasonally, bulk ice pCO_2 varies as well. Geilfus et al. (2012a,b) observed pCO_2 values from large supersaturation (of 1843 µatm) in cold ice to a marked undersaturation (down to almost 0 µatm) in warm ice (Figure II-24a).

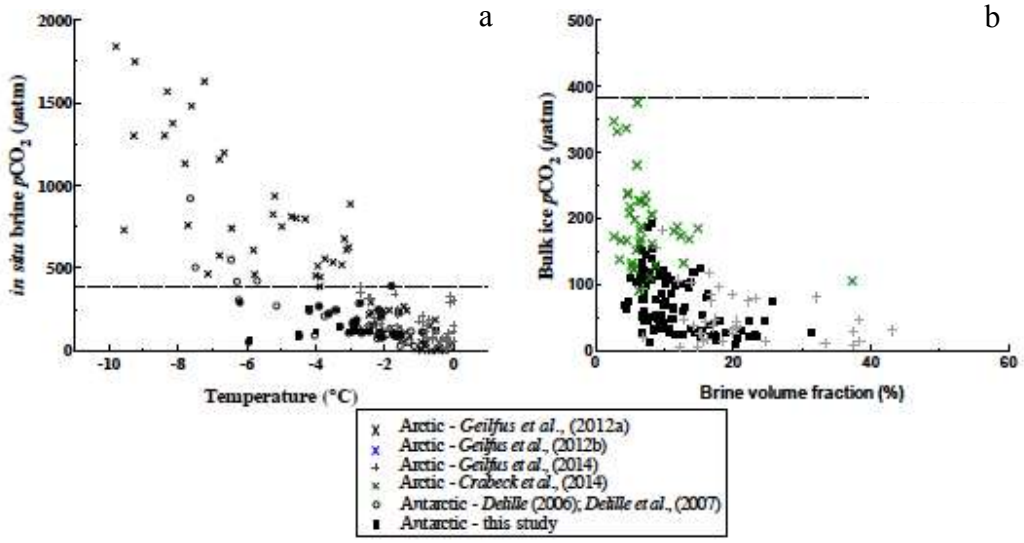

Figure II-24. (a) The relationship between in situ brine pCO_2 in µatm and brine temperature (°C) in the Antarctic (Delille, 2006; Delille et al., 2007; Geilfus et al., 2014) and in the Arctic (Geilfus et al., 2012a), (b) relationship between the bulk ice pCO_2 (in µatm) and the brine volume fraction (V_b %) in Antarctic (Geilfus et al., 2014) and in the Arctic (Geilfus et al., 2012b, 2014; Crabeck et al., 2014); figure from Geilfus et al. (2014).

During winter, the brine concentration effect associated with decreasing temperature promotes high pCO_2 within the brine by two processes (Figure II-24b). First, the increased solute concentration in smaller brine inclusions displaces the carbonate equilibrium to the left in equation II-14, outgassing CO_2. Secondly, it

promotes the precipitation of calcium carbonate crystals as ikaite ($CaCO_3 \cdot 6H_2O$), which produces $CO_{2(g)}$ as well:

$$Ca^{2+} + 2HCO_3^- + 5H_2O \overset{K_{sp}}{\Leftrightarrow} CaCO_3 \cdot 6H_2O + CO_2 \quad \text{(Eq. II-15)}$$

Where $K_{sp,}$ is the ikaite solubility constant.

Ikaite precipitates or dissolves if the ion activity product (IAP) of Ca^{2+} and CO_3^{2-} in brine inclusions is above or below the carbonate saturation (Ω) (Millero and Pierrot, 1998) given by equation II-16:

$$\Omega = \frac{[Ca^{2+}]_{br} \times [CO_3^{2-}]_{br}}{K_{sp}} \quad \text{(Eq. II-16)}$$

Where $[Ca^{2+}]_{br}$ and $[CO_3^{2-}]_{br}$ are the concentration in the brine and K_{sp} is the solubility product at the in situ temperature, salinity and pressure in the brine. The degree of saturation (Ω) is the driving force for the precipitation of the polymorph from supersaturated solutions ($\Omega > 1$) and, conversely, for its dissolution when in contact with undersaturated solutions ($\Omega < 1$).

During the warming season, internal melting decreases the solute concentrations in enlarged brine inclusions, which displaces the carbonate equilibrium toward the right in equation II-14 lowering the brine pCO_2. Similarly, the brine dilution effect promotes ikaite dissolution, which consumes CO_2 as well (Eq.II-15).

Ikaite crystals have recently been observed in both natural (e.g. Dieckmann et al., 2008, 2010) and experimental sea ice (Geilfus et al., 2013; Rysgaard et al., 2014) and are likely a key component of the carbonate system (Rysgaard et al.,

2007; Delille et al., 2014). The specific conditions leading to this precipitation as well as the fate of these precipitates in sea ice are still not fully understood. Rysgaard et al. (2014) commented that a layer of ice could experience several temporal cycles of ikaite precipitation and dissolution as the internal temperature of that ice layer changes.

Besides ikaite precipitation/dissolution, both primary production and respiration within sea ice affect the CO_2 system. However, their contribution to the increase or decrease of pCO_2 in brine is lower than the effect of brine concentration/dilution and ikaite precipitation/dissolution (Dieckmann et al., 2010; Delille et al., 2014; Sogaard et al., 2013; Moreau et al., 2015).

The fate of ikaite crystals and of the CO_2 produced by its precipitation is a major determining factor in whether sea ice is a net source or a net sink for atmospheric CO_2 over an integrated annual cycle. Both ikaite and the CO_2 produced by its precipitation can either be rejected to the underlying seawater or released to the atmosphere, depending on where and when the precipitation and dissolution take place and on sea ice permeability (Geilfus et al., 2013). Delille et al. (2014) reviewed all the possible scenarios (Figure II-25):

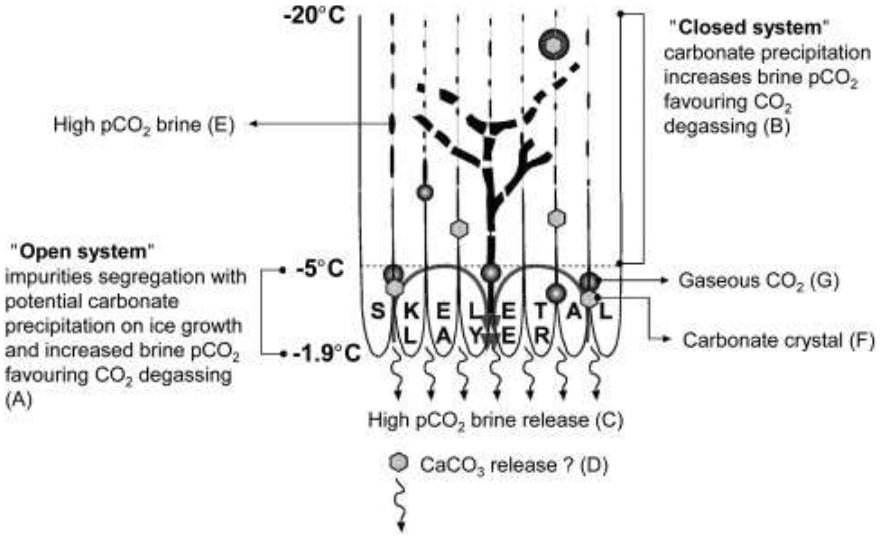

Figure II-25: Fate of carbonate minerals precipitated within sea ice from Delille et al. (2014).

Firstly, if ikaite precipitates in impermeable sea ice, (Figure II-25, (B) "closed system"), brine channels are not connected and both the precipitate and the CO_2 produced by the precipitation (Eq.II.15) stay trapped within the ice. Therefore, as sea ice melts, the dissolution of ikaite will consume CO_2 in the same proportion as the CO_2 produced during the precipitation, making the overall budget of CO_2 nil.

Similarly, if ikaite precipitates in permeable sea ice, and both ikaite and the CO_2 are released and transported out of the ice cover to the underlying seawater (Figure II-25, (C) and (D)), the impact on the CO_2 exchange with the atmosphere is also nil.

Finally, if ikaite precipitates in permeable layer but stays trapped within the ice structure while the CO_2 resulting of the precipitation is expelled into the underlying water (Figure II-25, (C)), and sinks with the brine below the pycnocline,

the ikaite dissolution during sea ice melt would consume CO_2 making sea ice a sink for atmospheric CO_2.

According to Geilfus et al. (2016), most of the precipitated ikaite stays in the ice until the onset of the melt, during which brine rejection and meltwater flushing could carry out more than half of it to the underlying seawater (Geilfus et al., 2016). Recent studies (Sejr et al., 2011; Geilfus et al., 2016) show also that most of the CO_2-rich brine is rejected into the seawater during sea ice growth, but according to the model study of Moreau et al. (2016) less than 2% is exported to depth (below the pycnocline).

In summary, from winter to summer, brine in sea ice changes from being highly supersaturated in CO_2 as a consequence of the increased concentration of solutes, $CaCO_3$ precipitation and microbial respiration, to a marked undersaturation relative to the atmosphere (Nomura et al., 2006; Tison et al., 2008; Geilfus et al., 2013). Decreased pCO_2 from winter to summer in brine is driven by dilution from melting ice, dissolution of carbonate crystals, and net primary production. As the ice warms, its permeability increases, allowing CO_2 transfer across the air-sea ice interface and the sea ice changes from a transient source to a sink for atmospheric CO_2. Recent studies advocate that both the Arctic and Antarctic ice cover acts as sink for CO_2 in polar regions (Rysgaard et al., 2011; Delille et al., 2014). According to Delille et al. (2014), the sea ice cover contributes around 58% of the annual CO_2 uptake by the Southern Ocean.

II.12.2 CH_4 in ice-covered area in the Arctic

CH_4 concentration in the atmosphere is much lower than CO_2, its oxidation product (1.9 vs. 404 μatm (ppmv), 2016 level, http://www.esrl.noaa.gov) but has global warming potential 28 times higher over a 100-year frame (Myhre et al., 2013). Present global atmospheric levels of CH_4 (1840 ppb) have risen by a factor 2.5 since pre-industrial times (<773 ppb) (Spahni et al., 2005). Recent increase of natural CH_4 emission due to Arctic warming and increase precipitation in the tropic has risen the research attention (Dlugokencky et al., 2009). Notably in the Arctic where the decline of sea ice points to unexpected feedbacks for the methane cycle since correlation between enhanced atmospheric methane concentrations and low sea ice concentration have been reported (Parmentier et al., 2013; Damm et al., 2015).

CH_4 supersaturation in Arctic surface seawater is observed on coastal shelves (Damm et al., 2007, 2008; Shakhova et al., 2010a,b; Kitidis et al., 2010) and in the interior basin (Kort et al., 2012; Damm et al., 2015). Parmentier et al. (2013) and Damm et al. (2015) point out that the Arctic Ocean acts potentially as a net source of atmospheric methane. Studies pinpointed that methanogenesis processes occurring in marine sediment are responsible for most of the observed CH_4 flux in Arctic shelf region (Damm et al., 2005). Nonetheless, other sources such as riverine input discharging CH_4-rich water and aerobic CH_4 production associated with the degradation of dimethylsulfoniopropaniate (DMSP) could contribute locally to CH_4 supersaturation in surface water (Damm et al., 2007, 2008, 2010). Under on-going global warming conditions, Arctic shelf seas characterized

by offshore subsea-permafrost have recently received considerable attention since significant CH_4 escape has recently been detected from them, suggesting that changes in polar CH_4 storage are on-going (Shakhova and Semiletov, 2007; Westbrook et al., 2009; Shakhova et al., 2010a,b). Despite the obvious influence of seeps on dissolved CH_4 concentration in the ocean, recent studies (Gentz et al., 2014; Steinle et al., 2015; Myhre et al., 2016) show that CH_4 is rapidly oxidized near the methane source and stored below the pycnocline. Myhre et al. (2016) suggest that dissolved CH_4 captured below the pycnocline may only be released to the atmosphere when physical processes remove this dynamic barrier. Large fluxes may occur particularly during ice break-up or storm events which influence the depth of the pycnocline (Damm et al., 2015; Myhre et al., 2016). The role of the pycnocline in this context should be investigated in more detail.

The detection of CH_4-rich water in marginal ice zones, under sea ice, and in polynyas, as well as the observation of methane emissions around 2 mg m^{-2} d^{-1} in areas of fractional ice cover have raised questions (and speculation) on the role of sea ice in the biochemical cycle of CH_4 in polar regions (Damm et al., 2007, 2010; Kitidis et al., 2010; Kort et al., 2012). To date, CH_4 measurements in sea ice are scarce; Zhou et al. (2014b) and Damm et al. (2015) found CH_4 supersaturation within sea ice cover and indicated that sea ice may act as source of CH_4 for underlying seawater and for the atmosphere. Conversely, He et al. (2013) suggested that methane consuming processes associated with both photo-chemical and biochemical oxidations could take place within sea ice limiting methane emission. Clarifying the processes affecting the CH_4 biochemical cycle and understanding the

current CH_4 budget in ice-covered area, are then important to assess unexpected feedbacks from the methane cycle on the Arctic area.

II-13 Method to measure gas content and characterize air porosity

Atmospheric gases (Ar, O_2 N_2, CO_2 and CH_4) in sea ice are found in easily detectable concentration and it is most likely the precision of the analyses that rise conserns for bulk ice gas measurements (Miller et al., 2015). Generally, gases measurement requires destructive methodology with potential for gas loss to the atmosphere or contamination with ambient air. Moreover, gases in sea ice are present both as solutes (dissolved phase in brine) and as bubbles (gaseous phase in air bubbles); some methods extract both fractions but are unable to differentiate between them, while others measure solely the solutes fractions in the brine (Miller et al., 2015). Reliable methodology to solely extract the gas contained in bubbles is still missing. Once the gas phase is extracted from the ice matrix, the gas mixture is usually analyzed by gas chromatography (GC). O_2 could also be determined by Winkler titration, which is the most precise method (Strickland and Parsons, 1972). In this section, we present the different approaches and common issues associated with gases measurements in sea ice based on the review from Miller et al. (2015).

II.13.1 Bulk ice gas content measurements

The oldest and most common methods for collecting gases from ice are the wet extraction and dry crushing (Miller et al., 2015), as developed for gas measurements in continental ice (e.g. Raynaud et al., 1982). Both methods collect

the air bubbles in the ice and the dissolved phase within the brine (i.e. the total gas content, which cannot be differentiated using these methods).

Dry crushing is a destructive process during which the ice section is put into a vessel together with stainless steel beads. The vessel is evacuated to 10^{-3} torr, and then fixed to an ice crusher as described in Raynaud et al. (1982) and Stefels et al. (2012). The stainless steel beads impact the ice block during the shaking process in a cold room at -25 °C, so that the ice is crushed into a fine powder.

Wet extractions involve melting an ice sample in a vacuum chamber and refreezing of melt-ice samples from the bottom (using a -70 °C cold ethanol bath), so that the whole gas content (dissolved and gaseous fractions) are expelled in the headspace above the refrozen ice (Matsuo and Miyake, 1966).

For each technique, the vacuum stage forces the dissolved gas out of solution; the headspace of each container contains the total gas content (bubbles plus gas dissolved in brine). After the crushing or refreezing sequence, containers are kept at -50°C in a cold ethanol bath and then connected to a gas chromatograph (Trace GC) to analyze the bulk ice gas concentrations (Ar, O_2, N_2, CH_4) or to a Toepler pump for total gas content measurement.

The amount of ice required for the analysis varies in function of the gas species and the sensitivity of the GC detector (Miller et al., 2015). While analyzing major atmospheric gases, we are able to establish vertical profile with a resolution of 5 cm, which roughly corresponds to 60g of ice in 9-cm diameter ice cores cut in a cold room at ‐25°C.

Wet and dry extraction are both destructive methodology; both the cutting process and the evacuation stage of the measurements lead to potential gas loss, the total gas content measured should be considered as the minimum estimate of the true total gas content.

Traditional methods used in continental ice as crushing produce artificially high CO_2 concentrations when used on sea ice sample (e.g. Tison et al., 2002) and are consequently inappropriate for bulk ice pCO_2 measurement. Crushing the ice at -20°C under vacuum disrupts the CO_2-system equilibrium within the brine, releasing CO_2 and potentially precipitating $CaCO_3$ (Tison et al., 2002; Geilfus et al., 2012b). Geilfus et al. (2012b) established a method to analyze bulk ice pCO_2 based on the equilibration of ice sample with a headspace of known CO_2 concentration and volume (dry headspace equilibration) at *in situ* temperatures. To ensure that the $CO_{2(g)}$ signal detected by the gas chromatograph is the ice CO_2 content and not the CO_2 from the headspace, the headspace volume should be minimized and its CO_2 concentration should be near the ice CO_2 concentration (Geilfus et al., 2012b).

Finally, dry extraction by crushing is not suitable for bulk ice CH_4 measurements; the friction and impacts between the stainless steel balls and the metallic walls of the container produces large amount of methane contaminating the sample (Higaki et al., 2006; Miller et al., 2015). The wet extraction method is then an available option while proceeding to CH_4 analysis.

II.13.2 Bulk ice melt measurements

Another common approach for bulk ice gas analysis is melting the ice samples in gas-tight bags, composed of fluoropolymers such as ALTEF or Kynar (Hansen et al., 2000; Rysgaard et al., 2009; Fransson et al., 2013, Miller et al., 2015). This method has been firstly developed to measure bulk ice dissolved inorganic carbon (DIC) and total alkalinity (TA). Once the bag with the sample is sealed, the headspace is removed with a vacuum pump. Then, the ice is melted in the dark below 4°C.

Once melted, gas bubbles previously trapped in ice form a gas phase inside the sealed bag, which is transferred to 12 ml vials for further GC analysis. Sea ice meltwater is usually transferred to 60 ml poisoned vials in order to proceed to headspace analysis followed by GC analysis (Ar, O_2, N_2, CO_2 and CH_4) as described by Abril and Iversen (2002), or into 12 ml for oxygen titration.

The major bias linked to this method is the phase change during melt. Due to new thermodynamic conditions in the bag, the concentration in gaseous and dissolved phases in the bags may not reflect the initial distribution of those phases at *in situ* conditions. Permeability or leaks in the bags could also potentially contaminate the sample.

II.13.3 Dissolved gas concentration measurements in brine

The fraction of dissolved gas is sampled from the brine collected by the sackhole technic. Sackhole sampling consists of drilling an ice core hole without perforating the complete ice cover; the brine from superior depth seeps into the

holes and is collected (Gleitz et al., 1995) (Figure II-26). It is important to not drill beyond the upper limit of the skeletal layer (highly permeable sea ice) because seawater can percolate in the hole due to hydrostatic pressure adjustment and contaminate the brine. Usually the hole is covered with insulator to avoid exposure to ambient atmospheric conditions and exchange with the atmosphere. The sampled brine is transferred to poisoned vial or tube in order to proceed to headspace analysis followed and GC analysis (Ar, O_2, N_2, CO_2 and CH_4).

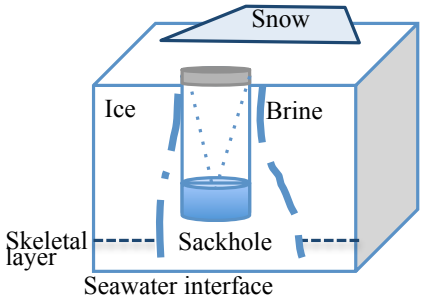

Figure II-26: Representation of sackhole technic for brine sampling .

While this method can produce large quantities of brine over short time periods (depending on ice temperature), it does not lend much insight into the vertical gradients of brine properties; the exact original depth from which the brine seeped is uncertain. In cold winter ice, the low brine volume and the poor connectivity between small brine inclusions make it difficult to collect brine in a reasonable time; prolonged exposure to the atmosphere could produce a rapid release of the brine's gas content. This method is also limited to periods when no melt puddles form on the sea ice surface. During advanced summer melting, the sackhole can be quickly flooded by runoff from the melt ponds and thus no longer represent true brine values (McMinn et al., 2009).

II.13.4 *In situ* gas measurements

The development of *in situ* probes allows the monitoring of gas concentrations at *in situ* condition in sea ice (McMinn et al., 2009). Photochemical probes (i.e. optodes) have been successfully applied to O_2 measurement in sea ice (Mock et al., 2002, 2003; Rysgaard et al., 2007). Gas-permeable silicone chambers (peepers) have been used to measure *in situ* CO_2 concentration in sea ice (Miller et al., 2011; Miller et al., 2015); theoretically, these peepers are suitable to detect other gases species like O_2, CH_4, and N_2O (Holter, 1990; Kammann et al., 2001; Miller et al., 2015).

Although the *in situ* measurement is promising for extended time series of *in situ* gas measurements, high salinities and low temperatures slow down the response times of the immersed probe and make calibration complicated and potentially uncertain (Rysgaard et al., 2007). In situ probes might also locally disturb the sea ice thermodynamic environment due to heat absorption by the probe. In addition, there is uncertainty about the microenvironment sampled; the response of sensor is different if the probe is in contact with a bubble, brine or pure ice matrix (Mock et al., 2002; Miller et al., 2015).

II.13.5 Characterization of sea ice air porosity

II.13.5.1 Derivation of air volume fraction from density measurements

Although sea ice air volume fraction could be deduced from bulk temperature, salinity and density measurements (Cox and Weeks, 1983), dimensional errors in sample preparation can be large enough to occasionally result

in negative gas volume estimates, which is a physical impossibility (Timco and Frederking, 1996). Pustogvar and Kulyakhthtin (2016) reported that the best available method to capture the natural variation of the ice density throughout the ice thickness below the freeboard line is the hydrostatic weighing method. The hydrostatic weighing method is suited for density measurement for ice below the freeboard line because the paraffin can fill open air voids of the snow-ice formed above the water line during the submerging process, which leads to an overestimation of the density (Pustogvar and Kulyakhthtin, 2016). Using this method Pustogvar and Kulyakhthtin (2016) reported air volume fraction <2.7% in columnar first year sea ice using state equations from Cox and Weeks (1983).

II.13.5.2 Thin sections

Perovich and Gow (1996), and Light et al. (2003) employed sea ice sections imaged using transmitted light to describe air inclusions within sea ice. The thickness of the thin sections is selected to be large enough to contain the entire volume of individual inclusions but small enough so that the inclusions did not obscure one another. Perovich and Gow (1996) used thin sections from 1 mm to 3 mm thick and Light et al. (2003) used 3 mm thick thin sections. Perovich and Gow (1996) reached a pixel resolution of 0.03 mm by using a 7x amplifier, while Light et al. (2003) reached a pixel resolution of 0.003 m using a high magnification zoom lens (Leica Monozoom 7 optical system) coupled with a 3x amplifier. Although microstructural analysis of sea ice may produce reliable morphological results for air inclusions, thin sections only represent a small subsample of the ice core. In

addition, the differentiation between air bubbles and liquid brine is sometimes unclear in transmitted images (Loose et al., 2011). Grain boundaries can be as dark as air inclusions and the center of air bubbles can be as light as ice and brine. The thickness of a thin section limits these studies to the interrogation of intact bubbles within a thin section.

References

Abril, G., and Iversen, N.: Methane dynamics in a shallow non-tidal estuary (Randers Fjord, Denmark), Marine ecology progress series, 230, 171-181, 2002.

Andreas, E. L.: A theory for the scalar roughness and the scalar transfer-coefficients over snow and sea ice, Boundary-Layer Meteorology, 38, 159-184, 10.1007/bf00121562, 1987.

Assur, A.: Composition of sea ice and its tensile strength, Arctic sea ice, 598, 106-138, 1958.

Barber, D., Ehn, J. K., Pucko, M., Rysgaard, S., Deming, J. W., Bowman, J. S., Papakyriakou, T., Galley, R. J., and Sogaard, D. H.: Frost flowers on young Artic sea ice: The climatic, chemical and microbial significance of an emerging ice type, Journal of Geophysical Research D: Atmospheres, 119, 11,593-511,612, 10.1002/2014JD021736.Received, 2014.

Bates, N. R., and Mathis, J. T.: The Arctic Ocean marine carbon cycle: evaluation of air-sea CO_2 exchanges, ocean acidification impacts and potential feedbacks, Biogeosciences, 6, 2433-2459, 10.5194/bg-6-2433-2009, 2009.

Bennington, K. O.: Some crystal growth features of sea ice, Journal of Glaciology, 4, 669 - 687, 1963.

Bragg, W. H.: The crystal structure of ice, Proc. Phys. Soc., 34, 98–103, 1922.

Broecker, W. S., and Peng, T. H.: Gas exchange rates between air and sea1, Tellus, 26, 21-35, 1974.

Burba, G. G., McDermitt, D. K., Grelle, A., Anderson, D. J., and Xu, L.: Addressing the influence of instrument surface heat exchange on the measurements of CO_2 flux from open-path gas analysers, Global Change Biology, 14, 1854-1876, 2008.

Burba, G.: Eddy covariance method for scientific, industrial, agricultural and regulatory applications: A field book on measuring ecosystem gas exchange and areal emission rates, LI-Cor Biosciences, 2013.

Burton, J., Prim, R., and Slichter, W.: The distribution of solute in crystals grown from the melt. Part I. Theoretical, The Journal of Chemical Physics, 21, 1987-1991, 1953.

Cheng, B., Vihma, T., and Launiainen, J.: Modelling of superimposed ice formation and sub-surface melting in the Baltic Sea. *Geophysica*, *39*(1-2), 31-50, 2003.

Cole, D. M., Eicken, H., Frey, K., and Shapiro, L. H.: Observations of banding in first-year Arctic sea ice, Journal of Geophysical Research: Oceans, 109, 2004.

Cottier, F., and Wadhams, P.: Linkages between salinity and brine channel distribution in young sea ice, Journal of Geophysical Research: Oceans 104, 15859-15871, 1999.

Cox, G. F. N., and Weeks, W. F.: Salinity variations in sea ice, Journal of Glaciology, 13, 109 - 120, 1974.

Cox, G. F. N., and Weeks, W. F.: Brine drainage and initial salt entrapment in sodium chloride ice, 85, 1975.

Cox, G. F. N., and Weeks, W. F.: Equations for determining the gas and brine volumes in sea-ice samples, Journal of Glaciology, 29, 306 - 316, 1983.

Cox, G., and Weeks, W.: Numerical simulations of the profile properties of undeformed first-year sea ice during the growth season, Journal of Geophysical Research: Oceans, 93, 12449-12460, 1988.

Crabeck, O., Delille, B., Thomas, D., Geilfus, N. X., Rysgaard, S., and Tison, J. L.: CO_2 and CH_4 in sea ice from a subarctic fjord under influence of riverine input, Biogeosciences, 11, 6525-6538, 10.5194/bg-11-6525-2014, 2014.

Curry, J. A., Schramm, J. L., and Ebert, E. E.: Sea ice-albedo climate feedback mechanism, Journal of Climate, 8, 240-247, 1995.

Damm, E., Mackensen, A., Budéus, G., Faber, E., and Hanfland, C.: Pathways of methane in seawater: Plume spreading in an Arctic shelf environment (SW-Spitsbergen), Continental Shelf Research, 25, 1453-1472, 10.1016/j.csr.2005.03.003, 2005.

Damm, E., Schauer, U., Rudels, B., and Haas, C.: Excess of bottom-released methane in an Arctic shelf sea polynya in winter, Continental Shelf Research, 27, 1692-1701, 10.1016/j.csr.2007.02.003, 2007.

Damm, E., Kiene, R. P., Schwarz, J., Falck, E., and Dieckmann, G.: Methane cycling in Arctic shelf water and its relationship with phytoplankton biomass and DMSP, Marine Chemistry, 109, 45-59, 10.1016/j.marchem.2007.12.003, 2008.

Damm, E., Helmke, E., Thoms, S., Schauer, U., Nöthig, E., Bakker, K., and Kiene, R. P.: Methane production in aerobic oligotrophic surface water in the central Arctic Ocean, Biogeosciences, 7, 1099-1108, 10.5194/bg-7-1099-2010, 2010.

Damm, E., Rudels, B., Schauer, U., Mau, S., and Dieckmann, G.: Methane excess in Arctic surface water- triggered by sea ice formation and melting, Scientific Reports, 5, 16179, 10.1038/srep16179, 2015.

Delille, B.: Inorganic carbon dynamics and air-ice-sea CO_2 fluxes in the open and coastal waters of the Southern Ocean, PhD thesis, Department of Astrophysics, Geophysics and Oceanography, Université de Liège, Liège, 296 pp., 2006.

Delille, B., Jourdain, B., Borges, A. V., Tison, J.-L., and Delille, D.: Biogas (CO_2, O_2, dimethylsulfide) dynamics in spring Antarctic fast ice, Limnology and Oceanography, 52, 1367-1379, 10.4319/lo.2007.52.4.1367, 2007.

Delille, B., Vancoppenolle, M., Geilfus, N.-X., Tilbrook, B., Lannuzel, D., Schoemann, V., Becquevort, S., Carnat, G., Delille, D., Lancelot, C., Chou, L., Dieckmann, G. S., and Tison, J.-L.: Southern Ocean CO_2 sink: The contribution of the sea ice, Journal of Geophysical Research: Oceans, 10.1002/2014JC009941, 2014.

Dieckmann, G. S., Nehrke, G., Papadimitriou, S., Göttlicher, J., Steininger, R., Kennedy, H., Wolf-Gladrow, D., and Thomas, D. N.: Calcium carbonate as ikaite crystals in Antarctic sea ice, Geophysical Research Letters, 35, 35-37, 10.1029/2008GL033540, 2008.

Dieckmann, G. S., Nehrke, G., Uhlig, C., Göttlicher, J., Gerland, S., Granskog, M. A., and Thomas, D. N.: Brief communication: Ikaite ($CaCO_3.6H_2O$) discovered in Arctic sea ice, The Cryosphere, 4, 227-230, 2010.

Digby, S. A.: Processes and imagery of first-year fast sea ice during the melt season, Journal of Geophysical Research, 90, 5045-5062, 1985.

Dlugokencky, E., Bruhwiler, L., White, J., Emmons, L., Novelli, P. C., Montzka, S. A., Masarie, K. A., Lang, P. M., Crotwell, A., and Miller, J. B.: Observational constraints on recent increases in the atmospheric CH_4 burden, Geophysical Research Letters, 36, 2009.

Eicken, H.: Salinity Profiles of Antarctic Sea Ice - Field Data and Model Results, Journal of Geophysical Research-Oceans, 97, 15545-15557, 1992.

Eicken, H., Lange, M. A., Hubberten, H. W., and Wadhams, P.: Charateristics and distribution patterns of snow and meteoric ice in the Weddell Sea and their contribution to the mass-balance of sea ice, Annales Geophysicae-Atmospheres Hydrospheres and Space Sciences, 12, 80-93, 10.1007/s00585-994-0080-x, 1994.

Eicken, H., Fischer, H., & Lemke, P. (1995). Effects of the snow cover on Antarctic sea ice and potential modulation of its response to climate change. *Annals of Glaciology*, *21*(1), 369-376.

Eicken, H.: Deriving modes and rates of ice growth in the Weddell Sea from microstructural, salinity and stable-isotope data. In: Jeffries, M.O. (Ed.), Antarctic Sea Ice: Physical Processes, Interactions and Variability: Ant. Res. Ser., 74, pp. 89–122,1998.

Eicken, H., Bock, C., Wittig, R., Miller, H., and Poertner, H. O.: Magnetic resonance imaging of sea-ice pore fluids: methods and thermal evolution of pore microstructure, Cold Regions Science and Technology, 31, 207-225, 2000.

Eicken, H., Krouse, H. R., Kadko, D., and Perovich, D. K.: Tracer studies of pathways and rates of meltwater transport through Arctic summer sea ice, Journal of Geophysical Research-Oceans, 107, 8046, 10.1029/2000JC000583, 2002.

Eicken, H.: From the microscopic to the macroscopic to the regional scale, growth, microstrucutre and properties of sea ice, in: Sea Ice - An introduction to its physics, biology, chemistry and geology, edited by: Science, B., London, pp. 22 - 81, 2003.

Eicken, H., Grenfell, T. C., Perovich, D. K., Richter-Menge, J. A., and Frey, K.: Hydraulic controls of summer Arctic pack ice albedo, Journal of Geophysical Research-Oceans, 109, C08007, 10.1029/2003JC001989, 2004.

Eicken, H., Dmitrenko, I., Tyshko, K., Darovskikh, A., Dierking, W., Blahak, U., Groves, J., and Kassens, H.: Zonation of the Laptev Sea landfast ice cover and its importance in a frozen estuary, Global and Planetary Change, 48, 55-83, 10.1016/j.gloplacha.2004.12.005, 2005.

Eide, L. I., and Martin, S.: The formation of brine drainage features in young sea ice, Journal of Glaciology, 14, 137 - 154, 1975.

Else, B. G. T., Rysgaard, S., Attard, K., Campbell, K., Crabeck, O., Galley, R. J., Geilfus, N. X., Lemes, M., Lueck, R., Papakyriakou, T., and Wang, F.: Under-ice eddy covariance flux measurements of heat, salt, momentum, and dissolved oxygen in an artificial sea ice pool, Cold Regions Science and Technology, 119, 158-169, 10.1016/j.coldregions.2015.06.018, 2015.

Environment Canada, Weather data Almanac, Resolute Station, http://climate.weather.gc.ca/climate_data/almanac_e.htmlStationID=53060).

Feltham, D. L., Untersteiner, N., Wettlaufer, J. S., and Worster, M. G.: Sea ice is a mushy layer, Geophysical Research Letters, 33, 4-7, 10.1029/2006GL026290, 2006.

Fichefet, T., and Maqueda, M. M.: Modelling the influence of snow accumulation and snow-ice formation on the seasonal cycle of the Antarctic sea-ice cover, Climate Dynamics, 15, 251-268, 1999.

Fofonoff, N.: Physical properties of seawater: A new salinity scale and equation of state for seawater, Journal of Geophysical Research, 90, 3332-3342, 1985.

Fransson, A., Chierici, M., Miller, L. A., Carnat, G., Shadwick, E., Thomas, H., Pineault, S., and Papakyriakou, T. N.: Impact of sea-ice processes on the carbonate system and ocean acidification at the ice-water interface of the Amundsen Gulf, Arctic Ocean, Journal of Geophysical Research: Oceans, 118, 7001-7023, 10.1002/2013JC009164, 2013.

Freitag, J.: Untersuchungen zur hydrologie des arktischen meereises: Konsequenzen für den kleinskaligen stofftransport= the hydraulic properties of arctic sea-ice: implications for

the small scale particle transport, Berichte zur Polarforschung (Reports on polar research), 325, 1999.

Garcia, H. E., and Gordon, L. I.: Oxygen solubility in seawater: Better fitting equations, Limnology and oceanography, 37, 1307-1312, 1992.

Galley, R. J., Else, B. G. T., Geilfus, N. X., Hare, A. A., Babb, D., Papakyriakou, T., Barber, D. G., and Rysgaard, S.: Micrometeorological and Thermal Control of Frost Flower Growth and Decay on Young Sea Ice, Arctic, 68, 79-92, 2015.

Garandet, J., Corre, S., Kaddeche, S., and Alboussiere, T.: The influence of convection on the duration of the initial solute transient in alloy crystal growth, Journal of Crystal Growth, 209, 970-982, 2000.

Geilfus, N. X., Carnat, G., Papakyriakou, T., Tison, J. L., Else, B., Thomas, H., Shadwick, E., and Delille, B.: Dynamics of pCO(2) and related air-ice CO2 fluxes in the Arctic coastal zone (Amundsen Gulf, Beaufort Sea), Journal of Geophysical Research-Oceans, 117, 10.1029/2011JC007118, 2012a.

Geilfus, N. X., Delille, B., Verbeke, V., and Tison, J. L.: Towards a method for high vertical resolution measurements of the partial pressure of CO_2 within bulk sea ice, Journal of Glaciology, 58, 287-300, 10.3189/2012JoG11J071, 2012b.

Geilfus, N. X., Carnat, G., Dieckmann, G. S., Halden, N., Nehrke, G., Papakyriakou, T., Tison, J. L., and Delille, B.: First estimates of the contribution of $CaCO_3$ precipitation to the release of CO_2 to the atmosphere during young sea ice growth, Journal of Geophysical Research, 118, 10.1029/2012JC007980, 2013.

Geilfus, N. X., Tison, J. L., Ackley, S. F., Galley, R. J., Rysgaard, S., Miller, L. A., and Delille, B.: Sea ice pCO_2 dynamics and air-ice CO_2 fluxes during the sea ice mass balance in the Antarctic (SIMBA); Bellingshausen sea, Antarctica, Cryosphere, 8, 2395-2407, 10.5194/tc-8-2395-2014, 2014.

Geilfus, N. X., Galley, R. J., Crabeck, O., Papakyriakou, T., Landy, J., Tison, J. L., and Rysgaard, S.: Inorganic carbon dynamics of melt-pond-covered first-year sea ice in the Canadian Arctic, Biogeosciences, 12, 2047-2061, 10.5194/bg-12-2047-2015, 2015.

Geilfus, N.-X., Galley, R. J., Else, B. G., Campbell, K., Papakyriakou, T., Crabeck, O., Lemes, M., Delille, B., and Rysgaard, S.: Estimates of ikaite export from sea ice to the underlying seawater in a sea ice-seawater mesocosm, The Cryosphere, 10, 2173, 10.5194/tc-10-2173-2016, 2016.

Gentz, T., Damm, E., von Deimling, J. S., Mau, S., McGinnis, D. F., and Schlüter, M.: A water column study of methane around gas flares located at the West Spitsbergen continental margin, Continental Shelf Research, 72, 107-118, 2014.

Gleitz, M., Loeff, M. R., Thomas, D. N., Dieckmann, G. S., and Millero, F. J.: Comparison of summer and winter inorganic carbon, oxygen and nutrient concentrations in Antarctic sea ice brine, Marine Chemistry, 51, 81-91, 1995.

Glud, R. N., Rysgaard, S., and Kuhl, M.: A laboratory study on O_2 dynamics and photosynthesis in ice algal communities: quantification by microsensors,O_2 exchange rates, C-14 incubations and a PAM fluorometer, Aquatic Microbial Ecology, 27, 301-311, 2002.

Golden, K. M., Ackley, S. F., and Lytle, V. I.: The percolation phase transition in sea ice, Science, 282, 2238-2241, 1998.

Golden, K. M., Eicken, H., Heaton, A. L., Miner, J., Pringle, D. J., and Zhu, J.: Thermal evolution of permeability and microstructure in sea ice, Geophysical Research Letters, 34, 1-13, 10.1029/2007GL030447, 2007.

Gosink, T. A., Pearson, J. G., and Kelly, J. J.: Gas movement through sea ice, Nature, 263, 41 - 42, 1976.

Granskog, M., Kaartokallio, H., Kuosa, H., Thomas, D. N., and Vainio, J.: Sea ice in the Baltic Sea–a review, Estuarine, Coastal and Shelf Science, 70, 145-160, 2006.

Grenfell, T. C., and Maykut, G. A.: The optical properties of ice and snow in the Arctic Basin, Journal of Glaciology, 18, 445-463, 1977.

Grenfell, T. C.: A theoretical model of the optical properties of sea ice in the visible and near infrared, Journal of Geophysical Research: Oceans, 88, 9723-9735, 1983.

Griewank, P. J., and Notz, D.: Insights into brine dynamics and sea ice desalination from a 1-D model study of gravity drainage, Journal of Geophysical Research: Oceans, 118, 3370-3386, 2013.

Griewank, P. J., and Notz, D.: A 1-D modelling study of Arctic sea-ice salinity, The Cryosphere, 9, 305-329, 10.5194/tc-9-305-2015, 2015.

Haas, C., Thomas, D. N., and Bareiss, J.: Surface properties and processes of perennial Antarctic sea ice in summer, Journal of Glaciology, 47, 613-625, 2001.

Hamme, R. C., and Emerson, S. R.: The solubility of neon, nitrogen and argon in distilled water and seawater, Deep-Sea Research Part I: Oceanographic Research Papers, 51, 1517-1528, 10.1016/j.dsr.2004.06.009, 2004.

Hansen, J. W., Thamdrup, B., and Jørgensen, B. B.: Anoxic incubation of sediment in gas-tight plastic bags: a method for biogeochemical process studies, Marine Ecology Progress Series, 208, 273-282, 2000.

Hardy, J., and Albert, D.: The Permeability of Temperate Snow, Proceedings of the Annual Meeting-Eastern Snow Conference, 1993, 149,

He, X., Sun, L. G., Xie, Z. Q., Huang, W., Long, N. Y., Li, Z., and Xing, G. X.: Sea ice in the Arctic Ocean: Role of shielding and consumption of methane, Atmospheric Environment, 67, 8-13, 10.1016/j.atmosenv.2012.10.029, 2013.

Higaki, S., Oya, Y., and Makide, Y.: Emission of methane from stainless steel surface investigated by using tritium as a radioactive tracer, Chemistry Letters, 35, 292-293, 2006.

Heinesch, B., Yernaux, M., Aubinet, M., Geilfus, N. X., Papakyriakou, T., Carnat, G., Eicken, H., Tison, J. L., and Delille, B.: Measuring air-ice CO_2 fluxes in the Arctic, FluxLetter, The Newsletter of FLUXNET, 2, 9-10, 2009.

Hobbs, P. V., Chang, S., and Locatelli, J. D.: The dimensions and aggregation of ice crystals in natural clouds, Journal of Geophysical Research, 79, 2199-2206, 1974.

Holter, P.: Sampling air from dung pats by silicone rubber diffusion chambers, Soil Biology and Biochemistry, 22, 995-997, 1990.

Hudier, E. J., Ingram, R., and Shirasawa, K.: Upward flushing of sea water through first year ice, Atmosphere-Ocean, 33, 569-580, 1995.

Hunke, E. C., Notz, D., Turner, A. K., and Vancoppenolle, M.: The multiphase physics of sea ice: A review for model developers, Cryosphere, 5, 989-1009, 10.5194/tc-5-989-2011, 2011.

Jardon, F. P., Vivier, F., Vancoppenolle, M., Lourenço, A., Bouruet-Aubertot, P., and Cuypers, Y.: Full-depth desalination of warm sea ice, Journal of Geophysical Research: Oceans, 118, 435-447, 10.1029/2012JC007962, 2013.

Jeffries, M. O., Shaw, R. A., Morris, K., Veazey, A. L., and Krouse, H. R.: Crystal structure, stable isotopes (δ18O), and development of sea ice in the Ross, Amundsen, and Bellingshausen seas, Antarctica, Journal of Geophysical Research: Oceans, 99, 985-995, 1994.

Kammann, C., Grünhage, L., and Jäger, H. J.: A new sampling technique to monitor concentrations of CH_4, N_2O and CO_2 in air at well-defined depths in soils with varied water potential, European Journal of Soil Science, 52, 297-303, 2001.

Kawamura, T., Ohshima, K., Takizawa, T., and Ushio, S.: Physical, structural, and isotopic characteristics and growth processes of fast sea ice in Lützow-Holm Bay, Antarctica, Journal of Geophysical Research: Oceans, 102, 3345-3355, 1997.

Killawee, J. A., Fairchild, I. J., Tison, J. L., Janssens, L., and Lorrain, R.: Segregation of solutes and gases in experimental freezing of dilute solutions: Implications for natural glacial systems, Geochimica Et Cosmochimica Acta, 62, 3637-3655, 1998.

Kitidis, V., Upstill-Goddard, R. C., and Anderson, L. G.: Methane and nitrous oxide in surface water along the North-West Passage, Arctic Ocean, Marine Chemistry, 121, 80-86, 10.1016/j.marchem.2010.03.006, 2010.

Kort, E. A., Wofsy, S. C., Daube, B. C., Diao, M., Elkins, J. W., Gao, R. S., Hintsa, E. J., Hurst, D. F., Jimenez, R., Moore, F. L., Spackman, J. R., and Zondlo, M. A.: Atmospheric observations of Arctic Ocean methane emissions up to 82 degrees north, Nature Geoscience, 5, 318-321, 10.1038/ngeo1452, 2012.

Kotovitch, M., Moreau S., Zhou J., Vancoppenolle M., Gerhard S., Dieckmann, Evers K.-U., Van der Linden F., Thomas D., Tison J.-L., Delille B.: Air-ice carbon pathways inferred

from a sea ice tank experiment, Elementa: Science of the Anthropocene, 75, 7212-7220, 10.1128/AEM.02227-09, 2016.

Krembs, C., Eicken, H., Junge, K., and Deming, J. W.: High concentrations of exopolymeric substances in Arctic winter sea ice: Implications for the polar ocean carbon cycle and cryoprotection of diatoms, Deep-Sea Research Part I: Oceanographic Research Papers, 49, 2163-2181, 10.1016/S0967-0637(02)00122-X, 2002.

Krembs, C., Eicken, H., and Deming, J. W.: Exopolymer alteration of physical properties of sea ice and implications for ice habitability and biogeochemistry in a warmer Arctic, Proceedings of the National Academy of Sciences, 108, 3653-3658, 2011.

Kristensen, M., and Søgaard, D. H.: O_2 dynamics in artificial and natural sea-ice: influence by algae, bacteria and physical processes, 1-127, 2008.

Lake, R., and Lewis, E.: Salt rejection by sea ice during growth, Journal of Geophysical Research, 75, 583-597, 1970.

Landy, J. C., Ehn, J. K., Shields, M., and Barber, D. G.: Surface and melt pond evolution on landfast first-year sea ice in the Canadian Arctic Archipelago, Journal of Geophysical Research: Oceans, 119, 3054-3075, 10.1002/2013JC009617, 2014.

Lange, M. A., Schlosser, P., Ackley, S. F., Wadhams, P., and Dieckmann, G. S.: O_{18} Concentrations in sea ice of the Weddell Sea, Antarctica, Journal of Glaciology, 36, 315-323, 1990.

Langway, C.: Ice fabrics and the universal stage. US Snow, Ice and Permafrost Research Establishment, Technical report 62, 1958.

Ledley, T. S.: Snow on sea ice - competing effects in shaping climate, Journal of Geophysical Research-Atmospheres, 96, 17195-17208, 10.1029/91jd01439, 1991.

Leppäranta, M.: A growth model for black ice, snow ice and snow thickness in subarctic basins, Hydrology Research, 14, 59-70, 1983.

Leppäranta, M., and Manninen, T.: The brine and gas content of sea ice with attention to low salinities and high temperatures, Finnish Institute of Marine Research Internal Report, Helsinki, 2, 6760, 1988.

Light, B., Maykut, G. A., and Grenfell, T. C.: Effects of temperature on the microstructure of first-year Arctic sea ice, Journal of Geophysical Research-Oceans, 108, 3051, 10.1029/2001jc000887, 2003.

Loose, B., McGillis, W. R., Schlosser, P., Perovich, D., and Takahashi, T.: Effects of freezing, growth, and ice cover on gas transport processes in laboratory seawater experiments, Geophysical Research Letters, 36, 1-5, 10.1029/2008GL036318, 2009.

Loose, B., Schlosser, P., Perovich, D., Ringelberg, D., Ho, D. T., Takahashi, T., Richter-Menge, J., Reynolds, C. M., Mcgillis, W. R., and Tison, J. L.: Gas diffusion through columnar laboratory sea ice: Implications for mixed-layer ventilation of CO_2 in the

seasonal ice zone, Tellus, Series B: Chemical and Physical Meteorology, 63, 23-39, 10.1111/j.1600-0889.2010.00506.x, 2011a.

Loose, B., and Schlosser, P.: Sea ice and its effect on CO_2 flux between the atmosphere and the Southern Ocean interior, Journal of Geophysical Research-Oceans, 116, 10.1029/2010jc006509, 2011b.

Maksym, T., and Jeffries, M. O.: A one-dimensional percolation model of flooding and snow ice formation on Antarctic sea ice, Journal of Geophysical Research: Oceans, 105, 26313-26331, 2000.

Martin, S.: Frazil ice in rivers and oceans, Annual Review of Fluid Mechanics, 13, 379-397, 10.1146/annurev.fl.13.010181.002115, 1981.

Matsuo, S., and Miyake, Y.: Gas composition in ice samples from Antarctica, Journal of Geophysical Research, 71, 5235-5241, 1966.

Maykut, G. A., and Untersteiner, N.: Some results from a time-dependent thermodynamic model of sea ice, Journal of Geophysical Research, 76, 1550-+, 10.1029/JC076i006p01550, 1971.

McMinn, A., Gradinger, R., and Nomura, D.: Biogeochemical properties of sea ice, Field Techniques for Sea Ice Research, 259-282, 2009.

Meredith, M., Heywood, K., Dennis, P., Goldson, L., White, R., Fahrbach, E., Schauer, U., and Østerhus, S.: Freshwater fluxes through the western Fram Strait, Geophysical Research letters, 28, 1615-1618, 2001.

Middleton, C. A., Thomas, C., De Wit, A., and Tison, J. L.: Visualizing brine channel development and convective processes during artificial sea-ice growth using Schlieren optical methods. Journal of Glaciology, *62*(231), 1-17, 2016.

Miller, L. A., Papakyriakou, T., Collins, R. E., Deming, J., Ehn, J., Macdonald, R. W., Mucci, A., Owens, O., Raudsepp, M., and Sutherland, N.: Carbon Dynamics in Sea Ice: A Winter Flux Time Series, Journal of Geophysical Research-Oceans, *116*, 10.1029/2009JC006058, 2011.

Miller, L. S., Fripiat, F., Else, B. G. T., Bowman, J. S., Brown, K. A., Collins, R. E., Ewert, M., Fransson, A., Gosselin, M., Lannuzel, D., Meiners, K. M., Michel, C., Nishioka, J., Nomura, D., Papadimitriou, S., Russell, L. M., Sørensen, L. L., Thomas, D. N., Tison, J.-L., van Leeuwe, M. A., Vancoppenolle, M., Wolff, E. W., and Zhou, J.: Methods for biogeochemical studies of sea ice: The state of the art, caveats, and recommendations, Elementa: Science of the Anthropocene, 3, 000038, 10.12952/journal.elementa.000038, 2015.

Millero, F. J., and Pierrot, D.: A chemical equilibrium model for natural waters, Aquatic Geochemistry, 4, 153-199, 1998.

Mock, T., Dieckmann, G. S., Haas, C., Krell, A., Tison, J. L., Belem, A. L., Papadimitriou, S., and Thomas, D. N.: Micro-optodes in sea ice: a new approach to investigate oxygen dynamics during sea ice formation, Aquatic Microbial Ecology, 29, 297-306, 2002.

Mock, T., Kruse, M., and Dieckmann, G. S.: A new microcosm to investigate oxygen dynamics at the sea ice water interface, Aquatic Microbial Ecology, 30, 197-205, 10.3354/ame030197, 2003.

Moreau, S., Vancoppenolle, M., Zhou, J., Tison, J. L., Delille, B., and Goosse, H.: Modelling argon dynamics in first-year sea ice, Ocean Modelling, 73, 1-18, 10.1016/j.ocemod.2013.10.004, 2014.

Moreau, S., Vancoppenolle, M., Delille, B., Tison, J.-L., Zhou, J., Kotovitch, M., Thomas, D. N., Geilfus, N.-X., and Goosse, H.: Drivers of inorganic carbon dynamics in first-year sea ice: A model study, Journal of Geophysical Research: Oceans, 120, 10.1002/2014JC010388, 2015a.

Moreau, S., Kaartokallio, H., Vancoppenolle, M., Zhou, J., Kotovitch, M., Dieckmann, G. S., Thomas, D. N., Tison, J.-L., and Delille, B.: Assessing the O_2 budget under sea ice: An experimental and modelling approach, Elementa: Science of the Anthropocene, 1-11, 10.12952/journal.elementa.000080, 2015b.

Moreau, S., Vancoppenolle, M., Bopp, L., Aumont, O., Madec, G., Delille, B., Tison, J.-L., Barriat, P.-Y., and Goosse, H.: Assessment of the sea-ice carbon pump: Insights from a three-dimensional ocean-sea-ice biogeochemical model (NEMO-LIM-PISCES), Elementa: Science of the Anthropocene, 4, 000122, 10.12952/journal.elementa.000122, 2016.

Myhre, G., Shindell, D., Bréon, F., Collins, W., Fuglestvedt, J., Huang, J., Koch, D., Lamarque, J., Lee, D., and Mendoza, B.: Climate change 2013: the physical science basis. Contribution of Working Group I to the fifth assessment report of the intergovernmental panel on climate change, K., Tignor, M., Allen, SK, Boschung, J., Nauels, A., Xia, Y., Bex, V., and Midgley, PM, Cambridge University Press Cambridge, United Kingdom and New York, NY, USA, 2013.

Myhre, C. L., Ferré, B., Platt, S. M., Silyakova, A., Hermansen, O., Allen, G., Pisso, I., Schmidbauer, N., Stohl, A., Pitt, J., Jansson, P., Greinert, J., Percival, C., Fjaeraa, A. M., O'Shea, S. J., Gallagher, M., Breton, M. L., Bower, K. N., Bauguitte, S. J. B., Dalsøren, S., Vadakkepuliyambatta, S., Fisher, R. E., Nisbet, E. G., Lowry, D., Myhre, G., Pyle, J. A., Cain, M., and Mienert, J.: Extensive release of methane from Arctic seabed west of Svalbard during summer 2014 does not influence the atmosphere, Geophysical Research Letters, 10.1002/2016GL068999, 2016.

Nakawo, M., and Sinha, N. K.: Growth rate and salinity profile of first-year sea ice in the high Arctic, Journal of Glaciology, 27, 315 - 330, 1981.

Neufeld, J. A., and Wettlaufer, J.: Shear-enhanced convection in a mushy layer, Journal of Fluid Mechanics, 612, 339-361, 2008.

Nicolaus, M., Haas, C., and Bareiss, J.: Observations of superimposed ice formation at melt-onset on fast ice on Kongsfjorden, Svalbard, Physics and Chemistry of the Earth, 28, 1241-1248, 10.1016/j.pce.2003.08.048, 2003.

Niedrauer, T. M., and Martin, S.: An experimental study of brine drainage and convection in young sea ice, Journal of Geophysical Research, 84, 1176 - 1186, 1979.

Nomura, D., Yoshikawa-Inoue, H., and Toyota, T.: The effect of sea-ice growth on air-sea CO_2 flux in a tank experiment, Tellus, Series B: Chemical and Physical Meteorology, 58, 418-426, 10.1111/j.1600-0889.2006.00204.x, 2006.

Nomura, D., Yoshikawa-Inoue, H., Toyota, T., and Shirasawa, K.: Effects of snow, snow-melting and re-freezing processes on air-sea ice CO_2 flux, Journal of Glaciology, 56, 262-270, 2010a.

Nomura, D., Eicken, H., Gradinger, R., and Shirasawa, K.: Rapid physically driven inversion of the air-sea ice CO_2 flux in the seasonal landfast ice off Barrow, Alaska after onset surface melt, Continental Shelf Research, 30, 1998-2004, 2010b.

Nomura, D., Granskog, M. A., Assmy, P., Simizu, D., and Hashida, G.: Arctic and Antarctic sea ice acts as a sink for atmospheric CO_2 during periods of snowmelt and surface flooding, Journal of Geophysical Research: Oceans, 6511-6524, 10.1002/2013JC009048, 2013.

Norris, S. J., Brooks, I., de Leeuw, G., Sirevaag, A., Leck, C., Brooks, B., Birch, C., and Tjernstrom, M.: Measurements of bubble size spectra within leads in the Arctic summer pack ice, Ocean Science, 7, 129-139, 2011.

Notz, D.: Thermodynamic and Fluid-Dynamical Processes in Sea Ice, Ph.D. thesis, University of Cambridge, UK, p36, 2005.

Notz, D., Wettlaufer, J. S., and Worster, M. G.: A non-destructive method for measuring the salinity and solid fraction of growing sea ice in situ, Journal of Glaciology, 51, 159-166, 2005.

Notz, D. and Worster, M. G.: A one-dimensional enthalpy model of sea ice, Ann. Glaciol., 44, 123–128, 2006.

Notz, D., and Worster, M. G.: In situ measurements of the evolution of young sea ice, Journal of Geophysical Research: Oceans, 113, 10.1029/2007JC004333, 2008.

Notz, D., and Worster, M. G.: Desalination processes of sea ice revisited, Journal of Geophysical Research: Oceans, 114, 1-10, 10.1029/2008JC004885, 2009.

Oertling, A. B., and Watts, R. G.: Growth of and brine drainage from NaCl-H_2O freezing: A simulation of young sea ice, Journal of Geophysical Research: Oceans, 109, C04013, 10.1029/2001JC001109, 2004.

Onstott, R. G.: SAR and scatterometer signatures of sea ice, Microwave remote sensing of sea ice, 73-104, 10.1029/GM068p0073, 1992.

Owston, P. G.: The structure of ice-I, as determined by x-ray and neutron diffraction analysis, Advances in Physics, 7, 171-188, 10.1080/00018735800101207, 1958.

Papakyriakou, T., and Miller, L.: Springtime CO_2 exchange over seasonal sea ice in the Canadian Arctic Archipelago, Annals of Glaciology, 52, 10.3189/172756411795931534, 2011.

Parmentier, F.-J. W., Christensen, T. R., Sørensen, L. L., Rysgaard, S., McGuire, A. D., Miller, P. A., and Walker, D. A.: The impact of lower sea-ice extent on Arctic greenhouse-gas exchange, Nature Climate Change, 3, 195-202, 10.1038/nclimate1784, 2013.

Pedersen, C. A., Roeckner, E., Lüthje, M., and Winther, J. G.: A new sea ice albedo scheme including melt ponds for ECHAM5 general circulation model, Journal of Geophysical Research: Atmospheres, 114, 2009.

Perey, F. G. J., and Pounder, E. R.: Crystal orientation in ice sheets, Canadian Journal of Physics, 36, 494-&, 1958.

Perovich, D. K., and Gow, A. J.: A quantitative description of sea ice inclusions, Journal of Geophysical Research, 101, 18327, 10.1029/96JC01688, 1996.

Perovich, D. K., Grenfell, T. C., Light, B., and Hobbs, P. V.: Seasonal evolution of the albedo of multiyear Arctic sea ice, Journal of Geophysical Research-Oceans, 107, 2002.

Perovich, D. K., and Richter-Menge, J. A.: Loss of Sea Ice in the Arctic, Annual Review of Marine Science, 1, 417-441, 10.1146/annurev.marine.010908.163805, 2009.

Perovich, D. K., and Polashenski, C.: Albedo evolution of seasonal Arctic sea ice, Geophysical Research Letters, 39, 10.1029/2012GL051432., 2012.

Petrich, C., Langhorne, P. J., and Sun, Z. F.: Modelling the interrelationships between permeability, effective porosity and total porosity in sea ice, Cold Regions Science and Technology, 44, 131-144, 2006.

Petrich, C., and Eicken, H.: Growth, structure and properties of sea ice, Sea Ice, Second Edition (eds D. N. Thomas and G. S. Dieckmann), Wiley-Blackwell, Oxford, UK., 2, 23-77, 2010.

Polashenski, C., Perovich, D., and Courville, Z.: The mechanisms of sea ice melt pond formation and evolution, Journal of Geophysical Research: Oceans, 117, C01001, 10.1029/2011JC007231, 2012.

Pounder, E. R., 1965: The Physics of Ice. Pergamon Press, Oxford, UK.

Pringle, D., Eicken, H., Trodahl, H., and Backstrom, L.: Thermal conductivity of landfast Antarctic and Arctic sea ice, Journal of Geophysical Research: Oceans, 112, 10.1029/2007GL030447, 2007.

Pringle, D. J., Miner, J. E., Eicken, H., and Golden, K. M.: Pore space percolation in sea ice single crystals, Journal of Geophysical Research, 114, 10.1029/2008JC005145, 2009.

Pustogvar, A., and Kulyakhtin, A.: Sea ice density measurements. Methods and uncertainties, Cold Regions Science and Technology, 131, 46-52, 10.1016/j.coldregions.2016.09.001, 2016.

Raynaud, D., Delmas, R., Ascencio, M., and Legrand, M.: Gas extraction from polar ice cores: a critical issue for studying the evolution of atmospheric CO_2 and ice-sheet surface elevation, Annals of Glaciology, 3, 265-268, 1982.

Rysgaard, S., and Glud, R. N.: Anaerobic N_2 production in Arctic sea ice, Limnology and Oceanography, 49, 86-94, 10.4319/lo.2004.49.1.0086, 2004.

Rysgaard, S., Glud, R. N., Sejr, M. K., Bendtsen, J., and Christensen, P. B.: Inorganic carbon transport during sea ice growth and decay: A carbon pump in polar seas, Journal of Geophysical Research: Oceans, 112, 1-8, 10.1029/2006JC003572, 2007.

Rysgaard, S., Glud, R. N., Sejr, M. K., Blicher, M. E., and Stahl, H. J.: Denitrification activity and oxygen dynamics in Arctic sea ice, Polar Biology, 31, 527-537, 2007.

Rysgaard, S., Bendtsen, J., Pedersen, L. T., Ramtøv, H., and Glud, R. N.: Increased CO_2 uptake due to sea ice growth and decay in the Nordic Seas, Journal of Geophysical Research: Oceans, 114, 1-9, 10.1029/2008JC005088, 2009.

Rysgaard, S., Bendtsen, J., Delille, B., Dieckmann, G. S., Glud, R. N., Kennedy, H., Mortensen, J., Papadimitriou, S., Thomas, D. N., and Tison, J. L.: Sea ice contribution to the air-sea CO2 exchange in the Arctic and Southern Oceans, Tellus, Series B: Chemical and Physical Meteorology, 63, 823-830, 10.1111/j.1600-0889.2011.00571.x, 2011.

Rysgaard, S., Wang, F., Galley, R. J., Grimm, R., Notz, D., Lemes, M., Geilfus, N. X., Chaulk, A., Hare, A. A., Crabeck, O., Else, B. G. T., Campbell, K., Sørensen, L. L., Sievers, J., and Papakyriakou, T.: Temporal dynamics of ikaite in experimental sea ice, The Cryosphere, 8, 1469-1478, 10.5194/tc-8-1469-2014, 2014.

Sejr, M. K., Krause-Jensen, D., Rysgaard, S., Sorensen, L. L., Christensen, P. B., and Glud, R. N.: Air-sea flux of CO2 in arctic coastal waters influenced by glacial melt water and sea ice, Tellus Series B Chemical and Physical Meteorology, 63, 815-822, 10.1111/j.1600-0889.2011.00540.x, 2011.

Shakhova, N., Semiletov, I., and Panteleev, G.: The distribution of methane on the Siberian Arctic shelves: Implications for the marine methane cycle, Geophysical Research Letters, 32, 1-4, 10.1029/2005GL022751, 2005.

Shakhova, N., and Semiletov, I.: Methane release and coastal environment in the East Siberian Arctic shelf, Journal of Marine Systems, 66, 227-243, 10.1016/j.jmarsys.2006.06.006, 2007.

Shakhova, N., Semiletov, I., Leifer, I., Salyuk, A., Rekant, P., and Kosmach, D.: Geochemical and geophysical evidence of methane release over the East Siberian Arctic Shelf, Journal of Geophysical Research-Oceans, 115, C08007,10.1029/2009jc005602, 2010a.

Shakhova, N., Semiletov, I., Salyuk, A., Yusupov, V., Kosmach, D., and Gustafsson, O.: Extensive Methane Venting to the Atmosphere from Sediments of the East Siberian Arctic Shelf, Science, 327, 1246-1250, 10.1126/science.1182221, 2010b.

Sievers, J., Sørensen, L. L., Papakyriakou, T., Else, B., Sejr, M., Haubjerg Søgaard, D., Barber, D., and Rysgaard, S.: Winter observations of CO_2 exchange between sea ice and the atmosphere in a coastal fjord environment, The Cryosphere, 9, 1701-1713, 2015.

Skyllingstad, E. D., Shell, K. M., Collins, L., and Polashenski, C.: Simulation of the melt season using a resolved sea ice model with snow cover and melt ponds, Journal of Geophysical Research: Oceans, 120, 5194-5215, 2015.

Souchez, R., Tison, J. L., and Jouzel, J.: Freezing rate determination by the isotopic composition of the ice, Geophysical Research Letters, 14, 599-602, 1987.

Spahni, R., Chappellaz, J., Stocker, T. F., Loulergue, L., Hausammann, G., Kawamura, K., Flückiger, J., Schwander, J., Raynaud, D., and Masson-Delmotte, V.: Atmospheric methane and nitrous oxide of the late Pleistocene from Antarctic ice cores, Science, 310, 1317-1321, 2005.

Stauffer, B., Neftel, A., Oeschger, H., and Schwander J.: CO_2 concentration in air extracted from Greenland ice samples, Geophysical Monograph Washington DC (Eds.), 3, 85-89, 1985.

Steele, M.: Sea ice melting and floe geometry in a simple ice-ocean model, Journal of Geophysical Research Oceans, 97, 17729, 10.1029/92JC01755, 1992.

Stefels, J., Carnat, G., Dacey, J. W., Goossens, T., Elzenga, J. T. M., and Tison, J.-L.: The analysis of dimethylsulfide and dimethylsulfoniopropionate in sea ice: Dry-crushing and melting using stable isotope additions, Marine chemistry, 128, 34-43, 2012.

Steinle, L., Graves, C. a., Treude, T., Ferré, B., Biastoch, A., Bussmann, I., Berndt, C., Krastel, S., James, R. H., Behrens, E., Böning, C. W., Greinert, J., Sapart, C.-J., Scheinert, M., Sommer, S., Lehmann, M. F., and Niemann, H.: Water column methanotrophy controlled by a rapid oceanographic switch, Nature Geoscience, 8, 1-6, 10.1038/ngeo2420, 2015.

Strickland, J. D., and Parsons, T. R.: A practical handbook of seawater analysis, Fisheries Research Board of Canada, Ottawa, Ontario, 1972.

Sturm M, Morris K, Massom R.: The winter snow cover of the West Antarctic pack ice: its spatial and temporal variability., In Antarctic Sea Ice Antarctic Research Series, Jeffries M. O. (ed.); American Geophysical Union: Washington, D.C., 74, 1-18, 1998 .

Taylor, P. D., and Feltham, D. L.: A model of melt pond evolution on sea ice, Journal of Geophysical Research-Oceans, 109, 10.1029/2004jc002361, 2004.

The National Oceanic and Atmospheric Administration (NOAA): available at: http://www.esrl.noaa.gov/gmd/obop/brw/index.html (last acces: september 2016), 2016.

Timco, G. W., and Frederking, R. M. W.: A review of sea ice density, Cold Regions Science and Technology, 24, 1-6, 1996.

Tison, J.-L., Haas, C., Gowing, M. M., Sleewaegen, S., and Bernard, A.: Tank study of physico-chemical controls on gas content and composition during growth of young sea ice, Journal of Glaciology, 48, 177-191, 10.3189/172756502781831377, 2002.

Tison, J. L., Worby, A., Delille, B., Brabant, F., Papadimitriou, S., Thomas, D., de Jong, J., Lannuzel, D., and Haas, C.: Temporal evolution of decaying summer first-year sea ice in the Western Weddell Sea, Antarctica, Deep-Sea Research Part II: Topical Studies in Oceanography, 55, 975-987, 10.1016/j.dsr2.2007.12.021, 2008.

Tsamados, M., Feltham, D., Petty, A., Schroeder, D., and Flocco, D.: Processes controlling surface, bottom and lateral melt of Arctic sea ice in a state of the art sea ice model, Phil. Trans. R. Soc. A, 373, 20140167, 2015.

Tsurikov, V. L.: The formation and composition of the gas content of sea ice, Journal of Glaciology, 22, 67 - 81, 1979.

UNESCO: Eighth report of the joint panel on oceanographic tables and standards, Technical papers in Marine Science, Division of Marine Sciences, Paris, France, 28, 51, 1978.

Untersteiner, N.: Natural desalination and equilibrium salinity profile of perennial sea ice, Journal of Geophysical Research, 73, 1251 - 1257, 1968.

Vancoppenolle, M., Fichefet, T., and Bitz, C. M.: On the sensitivity of undeformed Arctic sea ice to its vertical salinity profile, Geophysical Research Letters, 32, L16502,10.1029/2005GL023427, 2005.

Vancoppenolle, M., Bitz, C. M., and Fichefet, T.: Summer landfast sea ice desalination at Point Barrow, Alaska: Modeling and observations, Journal of Geophysical Research: Oceans, 112, 10.1029/2006JC003493, 2007.

Vancoppenolle, M., Goosse, H., De Montety, A., Fichefet, T., Tremblay, B., and Tison, J. L.: Modeling brine and nutrient dynamics in Antarctic sea ice: The case of dissolved silica, Journal of Geophysical Research: Oceans, 115, 1-18, 10.1029/2009JC005369, 2010.

Vancoppenolle, M., Notz, D., Vivier, F., Tison, J., Delille, B., Carnat, G., Zhou, J., Jardon, F., Griewank, P., and Lourenço, A.: Technical Note: On the use of the mushy-layer Rayleigh number for the interpretation of sea-ice-core data, The Cryosphere Discussions, 7, 3209-3230, 2013.

Wakatsuchi, M., and Kawamura, T.: Formation processes of brine drainage Channels in sea ice, Journal of Geophysical Research-Oceans, 92, 7195-7197, 1987.

Wang, C., Cheng, B., Wang, K., Gerland, S., and Pavlova, O.: Modelling snow ice and superimposed ice on landfast sea ice in Kongsfjorden, Svalbard. *Polar Research*, *34*, 2015.

Wanninkhof, R.: Relationship Between Wind Speed and Gas Exchange, Journal of Geophysical Research, 97, 7373-7382, 10.1029/92JC00188, 1992.

Weeks, W. F., and Gow, A. J.: Preferred crystal orientations in the fast ice along the margins of the Arctic Ocean, Journal of Geophysical Research: Oceans, 83, 5105-5121, 1978.

Weeks, W. F., and Gow, A. J.: Crystal alignments in the fast ice of arctic alaska, Journal of Geophysical Research-Oceans and Atmospheres, 85, 1137-1146, 10.1029/JC085iC02p01137, 1980.

Weeks, W. F., and Ackley, S. F.: The Growth, Structure, and Properties of Sea Ice, in: The Geophysics of Sea Ice, edited by: Untersteiner, N., Springer US, Boston, MA, 9-164, 1986.

Westbrook, G. K., Thatcher, K. E., Rohling, E. J., Piotrowski, A. M., Pälike, H., Osborne, A. H., Nisbet, E. G., Minshull, T. A., Lanoisellé, M., and James, R. H.: Escape of methane gas from the seabed along the West Spitsbergen continental margin, Geophysical Research Letters, 36, 2009.

Wettlaufer, J. S., Worster, M. G., and Huppert, H. E.: Natural convection during solidification of an alloy from above with application to the evolution of sea ice, Journal of Fluid Mechanics, 344, 291-316, 1997.

Whitman, W.: Elimination of salt from sea-water ice, American Journal of Science, 126-132, 1926.

Wise, D. L., and Houghton, G.: The diffusion coefficients of ten slightly soluble gases in water at 10–60 C, Chemical Engineering Science, 21, 999-1010, 1966.

Worster, M. G.: Instabilities of the liquid and mushy regions during solidification of alloys, Journal of Fluid Mechanics, 237, 649-669, 1992.

Worster, M. G., and Wettlaufer, J. S.: Natural convection, solute trapping, and channel formation during solidification of saltwater, Journal of Physical Chemistry B, 101, 6132-6136, 1997.

Worster, M. G., and Jones, D. W. R.: Sea-ice thermodynamics and brine drainage, Philosophical Transactions of the Royal Society of London A: Mathematical, Physical and Engineering Sciences, 373, 20140166, 2015.

Zeebe, R. E., and Wolf-Gladrow, D.: CO_2 in seawater: Equilibrium, Kinetics, Isotopes, No. 65. Gulf Professional Publishing, 2001.

Zemmelink, H. J., Delille, B., Tison, J. L., Hintsa, E. J., Houghton, L., and Dacey, J. W. H.: CO_2 deposition over the multi-year ice of the western Weddell Sea, Geophysical Research Letters, 33, 10.1029/2006GL026320, 2006.

Zhou, J. Y., Delille, B., Eicken, H., Vancoppenolle, M., Brabant, F., Carnat, G., Geilfus, N. X., Papakyriakou, T., Heinesch, B., and Tison, J. L.: Physical and biogeochemical properties in landfast sea ice (Barrow, Alaska): Insights on brine and gas dynamics across

seasons, Journal of Geophysical Research-Oceans, 118, 3172-3189, 10.1002/jgrc.20232, 2013.

Zhou, J., Delille, B., Brabant, F., and Tison, J. L.: Insights into oxygen transport and net community production in sea ice from oxygen, nitrogen and argon concentrations, Biogeosciences, 11, 5007-5020, 10.5194/bg-11-5007-2014, 2014a.

Zhou, J., Tison, J. L., Carnat, G., Geilfus, N. X., and Delille, B.: Physical controls on the storage of methane in landfast sea ice, Cryosphere, 8, 1019-1029, 10.5194/tc-8-1019-2014, 2014b.

Zhou, J.: The physical and biological Controls on the distribution of Gases and solutes in sea ice from Ice growth to ice decay, Universite de Liege, Liege, 2014.

Zhu, J., Jabini, A., Golden, K. M., Eicken, H., and Morris, M.: A network model for fluid transport through sea ice, Annals of Glaciology, 44, 129-133, 2006.

Chapter-III-Optimization of the Gas Chromatograph-GC SRI8610C for the analysis of Ar, O_2, N_2, CO_2, CH_4 and N_2O

Unpublished chapter

Odile Crabeck[1], Marcos Lemes[1] and Katrien Ramagnoli[2]

1. Department of Geological science, CEOS, University of Manitoba, Canada
2. Faculty of Bioscience Engineering, Universiteit Gent, Gent, Belgium

Katrien Romagnoly during her internship as a master student in our facilities, assisted in the development of the method. Marcos Lemes as the lab technician participated to the optimization of the GC, notably by realizing most of the mechanical work.

Abstract

This chapter addresses the optimization of the gas chromatograph GC SRI 8610C for the analysis of major atmospheric gases (Ar, O_2 and N_2) and greenhouse gases (CO_2, CH_4 and N_2O). The default configuration of GC SRI 8610C is suited for the analysis of CO_2, CH_4 and N_2O. After elution in a series of Hayesep columns, CH_4 and CO_2 are detected by a Flame Ionization Detector (FID) coupled with a methanizer and N_2O is detected by Electron Capture Detector (ECD). In order to detect and quantify Ar, O_2 and N_2, we added a molesieve column for the separation of the analytes and a Thermal Conductivity Detector for their quantifications. Our methodological test encountered three issues: (i) the base line of the FID channel was noisy, which resulted in a low signal:noise ratio and a poor detection limit of CH_4 (>3ppmv), (ii) the sensitivity or detector response of the ECD was low, which resulted in a poor detection limit of N_2O (>1ppmv) and (iii) Ar and O_2 eluted together and appeared as a single peak in the chromatogram.

Following an adjustment of the igniter in the FID cell, the system reached the targeted detection limit of 1ppmv for CH_4. After an adjustment of the makeup gas flow rate (N_2) supplying the ECD cell, the detection limit of 0.39 ppmv of N_2O was achieved. Separating the Ar and O_2 signals is challenging because of their similar physical properties, such as kinetic diameters and boiling points. They interact similarly with the stationary phase (column) and consequently elute together. However, we were able to resolve Ar and O_2 signals via the installation of a molesieve column in a cryo-oven unit set at -20°C.

III-1 Introduction

The study of gas dynamics in sea ice requires a reliable gas chromatography technique to identify gas concentration and gas composition of the air trapped in sea ice, in the snow layer above the ice, and the air dissolved in the seawater underneath. Gas chromatography (GC) is an analytical technique by which volatile compounds are analyzed qualitatively and quantitatively. A gas sample is injected into an inert gas stream, known as the mobile phase or the carrier gas (Templeton et al., 2002), after which it is brought onto a column for separation (the stationary phase). The column separates the gas mixture into individual gas species by selective interaction among its stationary phase. For packed column, the stationary phase consists of porous particles packed into a column, while for capillary column, it consists of a thin film of polymer coated on the inside wall of a narrow capillary (Grob and Barry, 2004, p.65). This causes the elution of each gas species at a different times. The retention time indicates the nature of the analyte (parameter of identification), and the peak area or peak height is proportional to its amount or concentration (parameter of quantification) (Lenehan, 2013).

The objective was to set up a GC able to detect both major atmospheric gases (Ar, O_2 and N_2) as well as greenhouse gases (CO_2, CH_4 and N_2O). Since Ar, O_2 and N_2 are the most abundant gases in the atmosphere, they are the most suited gases to describe the parameters controlling physical incorporation and physical transport of gas across the sea ice cover. Since Ar is an inert gas, it can be used as a physical tracer to differentiate physical processes from biogeochemical processes. In order to evaluate the role of sea ice in greenhouse gases emissions and uptake,

measuring CO_2, CH_4 and N_2O is the primary focus. Accurate GC quantification of both greenhouse and major atmospheric gases are important but challenging because it requires the use of multiple detectors and different columns in a single system. This chapter presents the development and validation of a method for Ar, O_2, N_2, CO_2, CH_4 and N_2O analysis by gas chromatography.

III-2 The custom made gas chromatograph

III.2.1 The default configuration of the SRI 8610C GC

By default, the greenhouse gas GC (SRI 8610C) is equipped with two detectors: A Flame Ionization Detector–Methanizer (FID, for CO_2 and CH_4) and an Electron Capture Detector (ECD, for N_2O). A sample is introduced into the GC through syringe injection via electronically-actuated 10-port valve connected to a 1 mL sample loop. The GC oven's front board is also equipped with an on-column injection port that enables variable volume of injection.

The operation of the FID is based on the detection of ions formed during the combustion of organic compounds in a hydrogen/air flame. The generation of these ions is proportional to the concentration of organic species in the sample gas stream (Poole, 2012, p.317). Specifically, the FID is composed of hydrogen-air diffusion flame burning at the end of jet, to which are routed the gas sample (Grob and Barry, 2004, p.277). When the components flow through the flame, the molecules are ionized and formed electrically positive and negative species which produce an increase in current. The resulting current is amplified by an electrometer. The current produced is proportional to the number of carbon atoms

present in the compound (Grob, 1996, p.275, Grob and Garry, 2004, p.300). Since the FID only responds to molecules with a carbon-hydrogen bond, CO_2 is not detectable by the FID unless it is converted into CH_4 by a methanizer. The methanizer converts CO_2 into CH_4 by combustion in the presence of a nickel powder catalyst and hydrogen gas, at a temperature of 350°C (Weiss, 1981).

The ECD is selective to electronegative compounds using a radioactive source (Nickel-63) to emits beta particles (electrons). The produced electrons cloud collides with the molecules of the carrier gas and makeup gas ionizing them and producing a standing current (Grob and Barry, 2004, p.305). When particular species (electronegative compounds) in the gas sample elute from the column into ECD cell, they interact with the ions cloud and capture some electrons, which reduces the standing current (Grob and Barry, 2004, p.305). As a result, the detector electronic has to pulse faster to sustain the standing current (approximately 1 nano ampere) through the electron cloud. Difference in pulse rates produces an analog signal for the data system (Poole, 2012, p.321).

The overall system is operated by helium carrier gas with nitrogen as the makeup gas for the ECD, and hydrogen and air as the combustion gas for the FID. For the hydrogen supply we used the Hydrogen-Generator PGH2-300 (Perkin Elmer®, Ontario, Canada). After injection, the gas sample passes through a 1 mL sample loop, a pre-column (Hayesep-D 3') and two main columns (Hayesep-D 6' in series (Table III-1). The pre-column uses a specific porous polymer that separates water vapor from the analytes of interest (CO_2, CH_4 and N_2O). As the polymer is a mainly inert and non-polar copolymer of polydivinylbenzene (PDVB), the analytes

(CO_2, CH_4 and N_2O) are retained by the pre-column, and water vapor flows freely through (Figure III-1) (SRI Instrument Europe, 2012). Consequently, it is possible to vent out the water vapor molecules without losing the analytes of interest (Figure III-1). Water vapor is viewed as a contaminant as its presence destabilizes the flame of the FID detector.

Table III-1: Column-Hayesep specifications for the separation of CO_2, CH_4 and N_2O.

Column	Type	Stationary phase	Inner dia	Particle size (Mesh)	Length
Hayesep-D 6’	Packed column	Non-polar Porous PDBV	2 mm	80/100	2x1.83 m
Hayesep-D 3’	Packed column	Non-polar Porous PDVB	2 mm	80/100	0.91 m

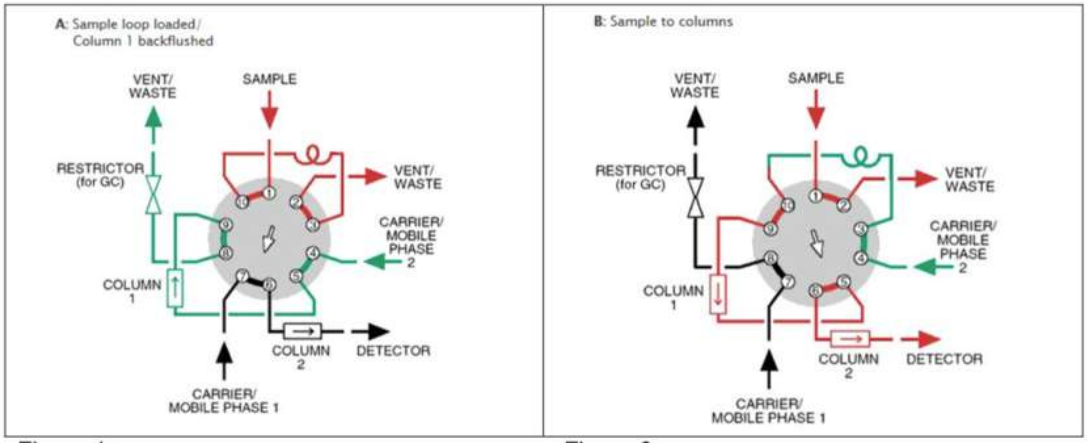

Figure III-1: Schematic diagram of 10-port-valve and theory of operation GC SRI 8610C (SRI Instrument Europe, 2012). Two different positions of the 10-port-valve - "Load-Position" and "Inject-Position." In "Load-Position" in panel A, the sample is flushed in the 1 mL sample loop with one injection by syringe. After you start to run –the valve rotates to the "Inject-Position." "Inject-Position" in panel B the sample loop is switched into the carrier gas stream. The sample passes through the pre-column and main column. The pre-column retains longer CO_2, CH_4 and N_2O than water vapor. Before the water vapor leaves the pre-column, the 10-ports-valve is switched back to the "Load-Position" and a solenoid valve open to backflush the water vapor to vent. Now the flow direction in the pre-column is changed and the analytes are in the main columns on the way to the detectors (SRI Instrument Europe, 2012).

Setup and operation of combustion detectors such as the FID are more complicated because there are combustion gas flows to set and a flame to ignite. Flowrates have direct influence on the maximum achievable sensivity of the detector. Helium is the default carrier used and the flow rate recommended by the manufacturer is 24 mL/min (20 psi). To obtain a stable flame and avoid flame out in the FID cell, it is recommended to use flowrates of combustion gases (hydrogen and air) of 20-25 mL/min (20 psi) for the hydrogen and of 200-250 mL/min (5psi) for the air and to maintain air:hydrogen ratio of 10:1 (Hinshaw, 2005; Poole, 2012, p.318). To achieve high performance with the FID and avoid condensation of the sample compound in the transfer lines and jet, the detector temperature should be

20°C to 50°C higher than the highest column temperature (Grob and Barry, 2004,p.302). The detector temperature has also to be above 150°C to prevent water condensation. The condensation of water vapor in the FID could result in noisy signals and baseline drifts (Hinshaw, 2005). We set the FID cell temperature at 360°C (as recommended by the manufacturer). The ECD requires enough nitrogen makeup flow (>20mL/min) to significantly dilute the carrier gas in order reduce the detector noise (Grob and Barry, 2005, p.307). The default operational settings recommended by the manufacturer SRI are listed in Table III-2.

Table III-2: Default settings for CO_2, CH_4 and N_2O.

Carrier gas He	20 psi -25mL/min
Makeup gas N_2	60 psi -60mL/min
Combustion gas H_2	20 psi -25mL/min
Combustion gas Air	5 psi -250 mL/min
Oven temperature	Isothermal 80°C
FID Temperature	360°C
Flame ignite	-762
ECD Temperature	330°C
ECD current	330 volt

III.2.2 New configuration: addition of a TCD detector and a molesieve column

It is not possible to separate all gases of interest (O_2, N_2, Ar and CO_2, CH_4, N_2O) using a single operating system. Therefore, the SRI 8610C GC was re-configured: the manufacturer added a second 10-ports valve with 1 mL sample loop, and inserted an additional detector; a thermal conductivity detector (TCD) and a molecular sieve column was placed in the oven and connected to the TCD. The TCD is the most common detector to analyze natural gases such as Ar, O_2 and N_2. The TCD is a concentration type detector responding to varaiations of thermal conductivity between (i)-pure carrier gas (helium) and (ii) -carrier gas plus eluted compounds. Since helium has a high thermal conductivity, the sample causes the thermal conductivity to drop. The bigger is the difference between the thermal conductivity of carrier gas and eluted components, the greater is the response of the detector. Specifically, the TCD is composed of four tightly coiled filaments made of a tungsten-rhenium alloy arranged as a Wheatstone bridge circuit (McNair and Miller, 2009, p.116). The electric current present across the filaments, produces heat constantly, this heat is removed at a stable rate by the carrier gas passing through the filaments. The elution of gas compounds of thermal conductivity lower than the carrier gas results in an augmentation of the filaments temperature . The change of temperatures produces a voltage difference, which generates a peak (Poole, 2012, p.312).

A TCD detects Ar, O_2 and N_2 after elution and separation into a packed HP-PLOT molesieve 5Ä column. Molecular sieve columns are strongly polar alumino-

silicates containing various cations in a lattice structure (zeolite; see Table III-3). Separation is based on molecular size and adsorption kinetics. While the molesieve is efficient to separate O_2 and N_2 at room temperature, separating Ar and O_2 is challenging because of their similar physical properties, such as kinetic diameters and boiling points (Hosseinzadeh et al., 2004). Normally, the HP-PLOT molesieve 5Ä column is able to separate Ar and O_2 at room temperature when Ar and O_2 concentrations are close and low (30 ppmv and 50 ppmv, respectively (e.g. Restek Corporation, Restek's PLOT Column Family, 2015, p.8). However, in most environmental samples (air, seawater, sea ice), there are high concentrations of Ar (≈1%) and O_2 (≈21%). As a result, the O_2 peak overlaps Ar and they are indistinguishable. The recommended operational settings for the detection of the major atmospheric gases outlined by the manufacturer SRI are listed in Table III-4.

Table III-3: Column –Molesieve specifications for the separation of Ar, O_2 and N_2.

Column	HP-Molecular sieve zeolite 5 Ä
Type	Packed
Length	1x30 m
Inner diameter	0.53 mm
Film thickness	50 µm

Table III-4: Default settings for Ar, O_2 and N_2 detection.

Carrier gas	Helium
Carrier gas flow pressure	16 psi (20 mL/min)
TCD Temperature*	120°C
Oven temperature	Isothermal 29°C (min oven temperature)

*To prevent damage to the detector, the temperature should be <150°C and 30°C to 50°C greater than highest oven ramp temperature.

III.2.3 Summary of the re-configured SRI 8610C GC

With the new configuration, the greenhouse gas GC (SRI 8610C) has been equipped with three detectors (FID, ECD, TCD), two 10-ports sample valve, as well as two on-column injectors (Figure III-2). The three detectors are separated into two circuits. The first channel links an injector to a 10-ports valve that is equipped with a 1 mL sample loop connected to a HP-PLOT molesieve 5Ä column that elutes the gas compound before being detected by the TCD. The second channel links a second injector to another 10-ports valve equipped with a 1 mL sample loop, connected to a series of Haysep columns that elute the gas compound before being detected by the FID and ECD. The two channels are fully independent, and the complete analysis requires the injection of two samples. Since the optimal settings for the separation of greenhouse gases (T=80 °C; Table III-2) and natural gases (room temperature; Table III-4) are too different, no attempt was made to connect both channels for a single injection method. All samples were manually injected with gastight syringes.

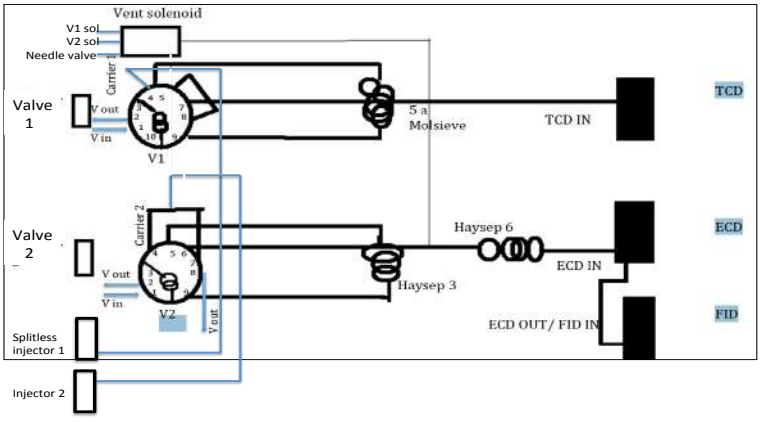

Figure III-2: Re-configured greenhouse gases GC SRI 8610C.

III-3 Criteria for system performance and method validation

III.3.1 Method approach

We developed an approach for problem assessment and method validation for a custom-made multi-detectors gas chromatograph (Figure III-3). The performance of the equipment is based on several gas chromatography parameters such as peak resolution (R), peak asymmetry (A_s), detector response or sensitivity (R_s) and the detection limit (Minimum Detectable Concentration – MDC) (Dolan, 2002; Heftmann, 2004, p.348). The validation of the method is based on the calibration of the instrument, and trueness and precision of the measurement, which according to ISO (1994) define together the accuracy of the measurement.

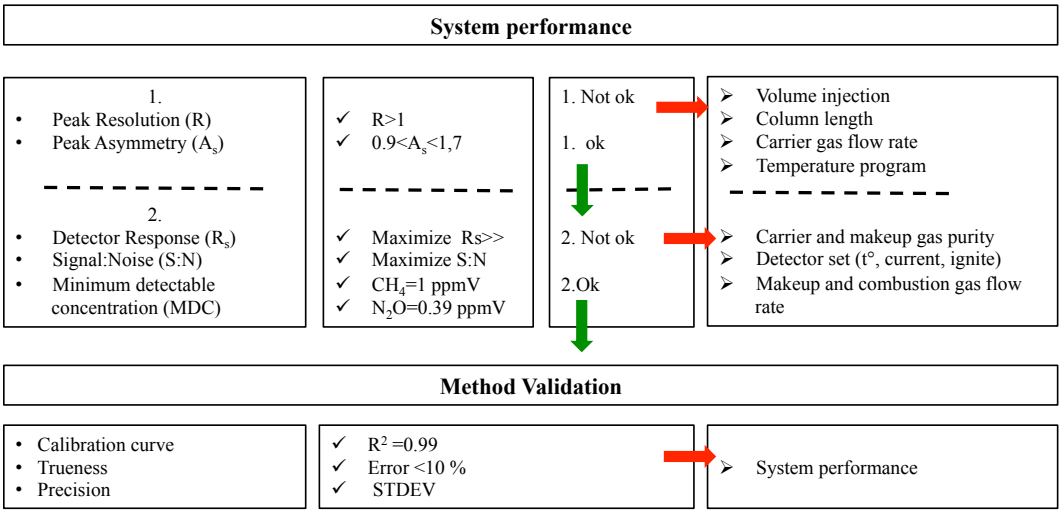

Figure III-3: Schematic representation of the approach for problem assessment and method validation for multi-detectors custom-made gas chromatograph.

In gas chromatography, the resolution (R) defines the ability to separate 2 peaks, given by:

$$R= \frac{(t_{r2}-t_{r1})}{1/2(w_1+w_2)} = \frac{(t_{r2}-t_{r1})}{4\sigma} \quad \text{(Eq.- III-1)}$$

Where t_{r2}, t_{r1} are the retention times and W_1, W_2 are the peak widths at half height of two immediately adjacent peaks. A resolution of at least 1 or 1.5 (Dolan, 2002; Lenehan, 2013) is needed for quantitative analyses; when R = 1, 2.5% of one area still overlaps 2.5% of the second area.

To achieve good resolution, compounds should elute as sharp symmetric peaks at different times, yet in practical chromatography, perfectly Gaussian peaks are uncommon. Often peaks appear with a front steeper than the rear. This asymmetry also called tailing is defined by the peak asymmetry factor (A_s):

$$A_s=\frac{b}{a} \quad \text{(Eq.- III-2)}$$

Where a and b are the widths of the front and back half of the peak at 10% of the peak height. Usually peak asymmetry factor between 0.9 and 1.7 are considered valid for most analysis (Dolan, 2002). While using the correct column, the resolution can be increased by adjusting the column length (L), the temperature, and the flow rate of the carrier gas. Longer columns provide more resolving power than shorter columns of the same inner diameter, but they also increase analysis time and should be used only for applications demanding the utmost in separation power. Carrier gas choice and linear velocity (flow rate) significantly affect column separation efficiency (Lenehan, 2013; Poole, 2012 p.57). The flow rate of the carrier gas through the system determines the retention time and peak sharpness. A

higher flow rate lowers the retention time and sharpens the peak, while a lower flow rate increases the retention time and broadens the peak. However, past the optimal flow rate, a higher flow rate could broaden the peak as well. A higher temperature program will decrease analysis time, but may result in a loss of resolution if it is increased too high (base line drift).

The detector response or sensitivity (R_s) is the ratio between the signal produced by an analyte, and the quantity of analyte producing the signal. Ideally, and for easy computation, this ratio is unity (one) (Heftmann, 2004, p.348). The detector response is defined by:

$$R_s = \frac{A_{pi}}{C_i} \quad \text{(Eq.- III-3)}$$

Where $A_{pi}$is the area of the peak from the compound i and C_i is the concentration injected of the compound i. Improving the detector response resulted in an improved detection limit, where the minimal mass or concentration of the compound could be detected.

The detection limit or minimum detectable concentration (MDC) is defined as the concentration that will produce a signal equivalent to at least three times the noise signal. Therefore, the MDC is greatly tied to the background noise level of the system that includes high frequency (e.g. electronic) and lower frequency (usually chemical) noise. Increasing the detection limit is achieved by increasing the signal, decreasing the noise, or a combination of both (Heftmann, 2004, p.349). Our targeted minimum concentration was 0.39 ppmv for N_2O, and approximately

1 ppmv for CH_4. Since the other analytes are present in large amounts in the studied environment, they do not challenge the minimum detection limit.

A calibration curve is a plot that compares an instrumental response to a change of concentration of a analyte in a specific sample matrix (the chemical background of the sample). It is obtained by measuring the instrument response of analytes of known concentrations (standards), and establishing an equation, which fits the calibration data. With the exception of the ECD , which displays a nonlinear response function to N_2O concentrations, our detectors show a linear instrumental response in the analytical range; a correlation coefficient (R^2) of 0.99 is a standard requirement. The ECD gives a non-linear detection of N_2O as ECD sensitivity decreases with increasing concentrations of N_2O (about 3-4 orders of magnitude) (Klemedtsson et al., 1986).

Trueness is how closely the result of an experiment agrees with the "true" or expected result, and can be expressed as an absolute error, (E) or as a percentage of relative error (E_r %):

$$E_r = \frac{(C_m - C_t)}{C_t} \times 100 \qquad \text{(Eq.III-4)}$$

Where C_m is the value measured and C_t is the true value of sample. Trueness is tested through a recovery test, consisting of 10 injections of a reference gas (gas standard).

When a sample is analyzed several times, the individual results are rarely the same. Instead, the results are randomly scattered; precision is a measure of this variability (ISO,1994). A closer agreement between individual analyses lead to

more precise results. However, it is important to understand that precision does not imply trueness. The precision of an analytical method is most often defined by the variance, standard deviation, or coefficient of variation of a set of measurements. Daily injection of ambient air is used for precision control.

III.3.2 Gas purity as a pre-requirement for system performance

Water vapor and O_2 can interact with the stationary phase and cause significant problems such as high baseline noise and column bleed in the output gas chromatogram, which both reduces the dectectors sensitivity (FID, TCD and ECD) and decreases column lifetime (Hayesep and moleseive), the carrier gas should be free of impurities (Grob and Barry, 2004, p.279). Particularly, the presence of O_2 and water vapor cause oxidation of the detector wires in the TCD cell. The FID is also extremely sensitive to hydrocarbon impurities present in the combustion gas (hydrogen and air). Hydrocarbon impurities can increase baseline noise and reduce the detector sensitivity. Grade 6.0 is required for carrier gas (helium), makeup gas (nitrogen) and combustion gas (hydrogen and air; see Table III-5). For cost effectiveness, we used compressed helium and nitrogen, both with a grade of 5.0, connected to a triple gas filter that filtered O_2, moisture, and hydrocarbons, which guarantees us to obtain a purity of grade 6.0 (Super-Clean Gas Filter Kit, Thermo Fisher Scientific®, USA) A hydrogen generator is also connected to gas filter to ensure the purity of grade 6.0.

Table III-5: Carrier, makeup and combustion gas purity.

Carrier gas	Compressed helium	Purity 6
Makeup gas (ECD)	Compressed nitrogen	Purity 6
Combustion gas (FID)	Hydrogen (generator)	Purity 6
	Compressed air	Purity 6

III.3.3 Standard gases for calibration

We used three certified standard mix gases by Praxair for routine calibration of the instrument and to test the trueness of the measurements (Table III-6). It is important that the lower and higher standard gas cover the range of analytes targeted in the study. Under high pressure, potential absorption surfaces in the disposable valve may cause local phase separation. Thus, we recommend purging the valve for a few seconds before taking the standard gas to ensure that the gas species are well mixed.

Table III-6: Standard gas composition.

	Std 1		**Std 2**		**Std 3**	
	Requested	**Certified**	**Requested**	**Certified**	**Requested**	**Certified**
CO_2 (ppmv)	100	106 ±2%	400	390 ±2%	1000	996 ±2%
CH_4 (ppmv)	1	0.95 ±5%	10	10 ±5%	100	101 ±2%
N_2O (ppmv)	1	0.95 ±5%	2	2 ±5%	5	4.9 ±5%
Ar (%)	0.5	0.507 ±2%	1	0.99 ±2%	2	1.99 ±2%
O_2 (%)	9.5	9.51 ±2%	18	18.1 ±2%	38	38.1 ±2%
N_2 (%)	90	Balance	81	Balance	60	Balance

III-4 System performance and method validation

III.4.1 The detection of CO_2, CH_4 and N_2O on the FID and ECD channels

We carried out a series of tests to determine the optimal injection and detection parameters in order to improve the performance of the system. There were two options for the injection – directly injecting the sample into the column, or using the 10-ports valve with 1mL sample loop. We recommend injecting at least 1.5 mL of gas using the 10-ports valve with 1mL sample loop, as we obtained larger peaks with this method than with direct column injection. While using the settings recommended by the manufacturer (Table III-2), the following issues were encountered: (i) the baseline for the FID channel was too noisy to accurately detect concentrations less than 5 ppmv of CH_4, and (ii) the sensitivity (detector response) of the ECD was too low to accurately detect concentrations less than 2 ppmv of N_2O. However, the default settings suited CO_2 detection in the range of the standard gas appropriately ($R>1$, $0.9<A_s<1.7$).

III.4.1.1 Improving the detection limit of CH_4 and N_2O

While the recommended settings seemed adequate to resolve 5 ppmv of CH_4 (Figure III-4a), we were unable to accurately detect 1 ppmv of CH_4 due to a noisy baseline (Figure III-4b). The signal:noise ratio for a 5 ppmv of CH_4 sample was 11.5:1.07, as the MDC is at least three times greater than the noise signal, the minimum detectable concentration was 3.22 ppmv (Figure III-4b).

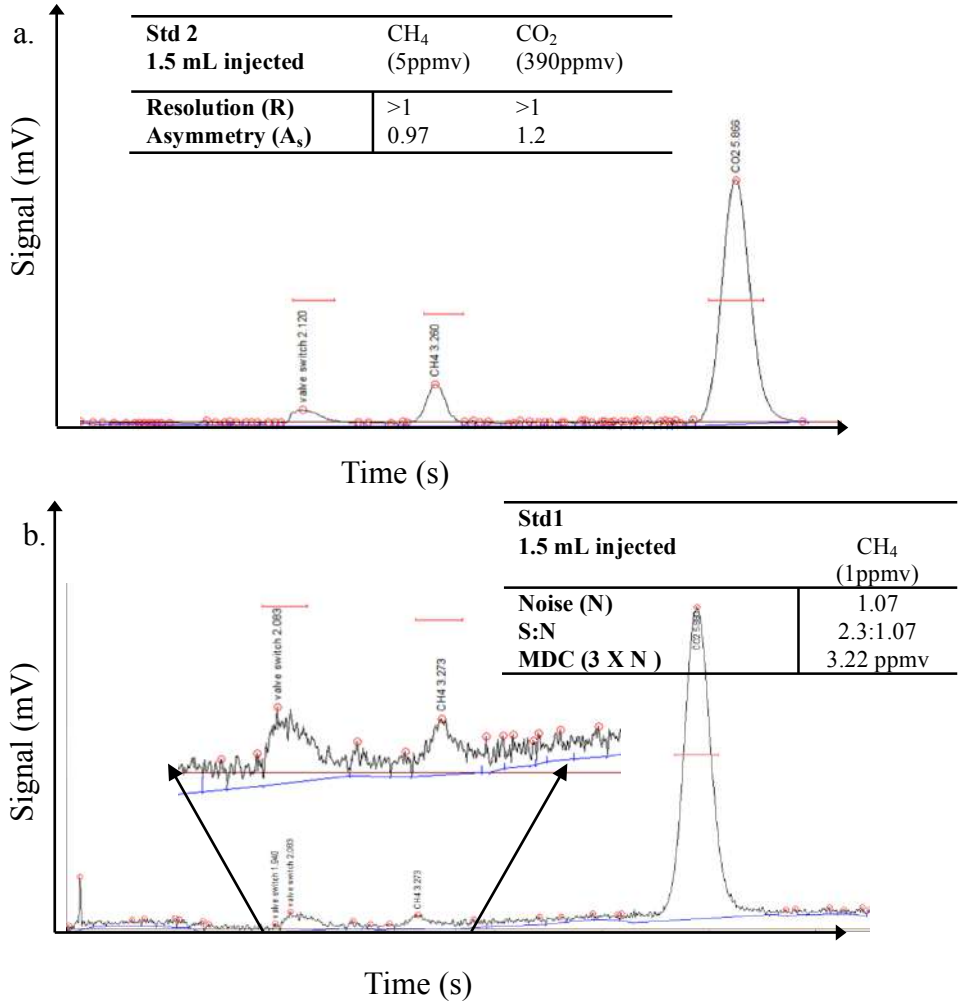

Std 2 **1.5 mL injected**	CH_4 (5ppmv)	CO_2 (390ppmv)
Resolution (R)	>1	>1
Asymmetry (A_s)	0.97	1.2

Std1 **1.5 mL injected**	CH_4 (1ppmv)
Noise (N)	1.07
S:N	2.3:1.07
MDC (3 X N)	3.22 ppmv

Figure III-4: Chromatogram after injection 1.5 mL of (a) 5ppmv -CH_4 and 390 ppmv -CO_2 (STD 2) and (b) of 1 ppmv -CH_4 and 100 ppmv -CO_2 (STD 1), using the recommended settings listed in Table III-2. In (b) the CH_4 is not quantifiable due to the noisy baseline.

In order to reduce the noise and improve the methane detection limit, we set the flame igniter at -400 (initially -762) and lowered the ceramic foot of the igniter by1-2 mm. When the voltage of the igniter is reduced, the flame itself burns more smoothly and the signal offset decreases, which results in a higher signal:noise ratio. By adjusting the igniter, the noise was reduced by a factor of 16. This enabled

us to obtain the targeted minimum detectable concentration of 1 ppmv (Figure III-5) and reach a new detection limit of 0.2 ppmv –CH_4.

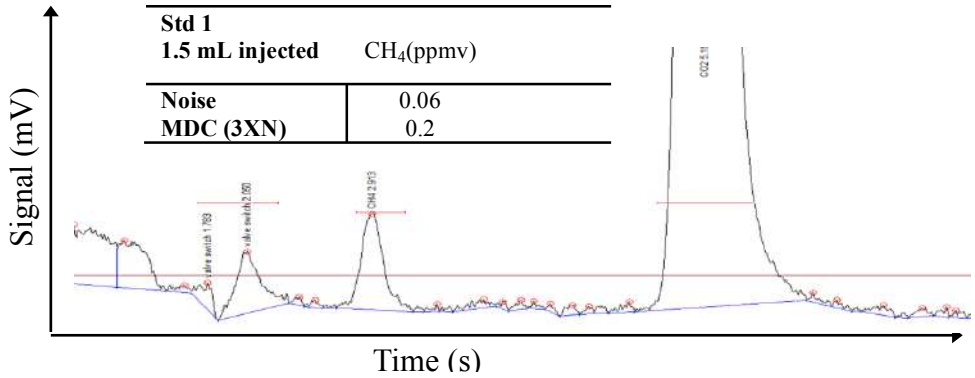

Figure III-5: Chromatogram after injection of 1.5mL of 1 ppmv -CH_4 (STD1), after modification of the igniter of the FID cell. The CH_4 is now quantifiable.

To improve the sensitivity of ECD, we tested the ECD current in the range of 280 – 380 Volts by 10-Volt intervals with a fixed detector temperature of 330°C as recommended by the manufacturer (default settings, Table III-2). We found larger peaks and better sensitivity while the current was 330 Volts. However, atmospheric N_2O concentrations (0.39 ppmv), as well as standard gas 1 (1 ppmv), were not quantifiable using this set up (Figure III-6a). The baseline was very stable with low noise, therefore increasing the signal was the only option to both improve the detector sensitivity and reach detection limits of 0.39 ppmv. The sensitivity of the ECD detector depends on the makeup gas flow (Grob and Barry, 2004, p.307). Makeup flow acts as a doping agent. If the makeup flow is too fast, the dilution of the sample in the makeup gas flow is too strong and the time to catch secondary electrons is too short; this results in decreased detector sensitivity (Grob and Barry,

2004, p.307). We tested the effect of the flow rate of the makeup gas (N_2) on the sensitivity (detector response) by decreasing the flow rate from 60 psi to 20 psi; at 20 psi we reached a response factor of 500 (peak area of 500 for 1 ppmv injected; Figure III-6b). This is close to the detector performance according to the manufacturer's specifications, which state that the injection of 1ppmv of N_2O corresponds to a peak area of 600. The new configuration enables the detection of atmospheric concentrations of N_2O; injection of 1.5 mL of 0.39 ppmv-N_2O resulted in peak area of 220. By changing the makeup gas flow rate, we multiplied the response factor by 13 and we detected concentration 6 times lower than our initial tests.

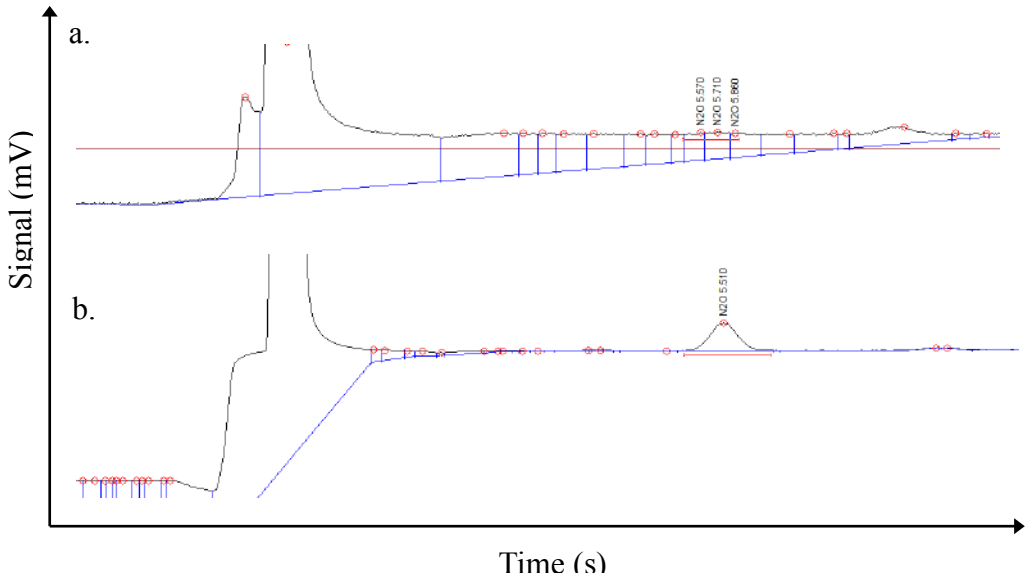

Figure III-6: Chromatogram after injection of 1.5mL of 1 ppmv -N_2O (a) using the default settings listed in Table III-2 (makeup gas flow rate of 60 psi) and (b) after adjustment of the makeup gas flow rate (20 psi), the N_2O peak is quantifiable.

III.4.1.2 Optimal oven temperature and carrier gas flow rate

Since, the targeted MDC for CH_4 and N_2O was reached, we looked at minimizing the run time. In order to minimize the run time without losing peak resolution, we looked for the optimal oven temperature and flow rate for the carrier gas. We tested the oven temperature in the range of 60°C to 120°C by 10°C increments (Figure III-7a (CO_2, CH_4) and -c (N_2O)), and the carrier gas flow rate in the range of 15 psi to 30 psi by 5 psi increments (Figure III-7b (CO_2, CH_4) and-d (N_2O)). Temperature and flow rate affected column efficiency. When the oven temperature is higher, the gas travels through the column at a faster rate, resulting in sharper peaks. Temperatures higher than 110°C degraded the resolution of CO_2 and CH_4 due to the presence of a baseline drift (i.e. long term noise; Figure III-7a). A flow rate under 25 psi degraded the resolution of CH_4, which elutes just before the air when the valves are switched; the reduced flow rate caused a broadening of the air peak (Figure III-7b). Changes in temperature and flow rate did not affect the resolution of N_2O (Figure III-7c-d); increasing the temperature and flow rate contributed to reduced retention time. We found that an isothermal run at 100°C with a carrier gas flow at 25 psi was the best compromise to obtain both an accurate peak and short analysis time. By implementing the new settings stated in Table III-7, it is possible to detect the three gases in less than five minutes at concentrations as low as 1 ppmv and 0.39 ppmv for CH_4 and N_2O respectively.

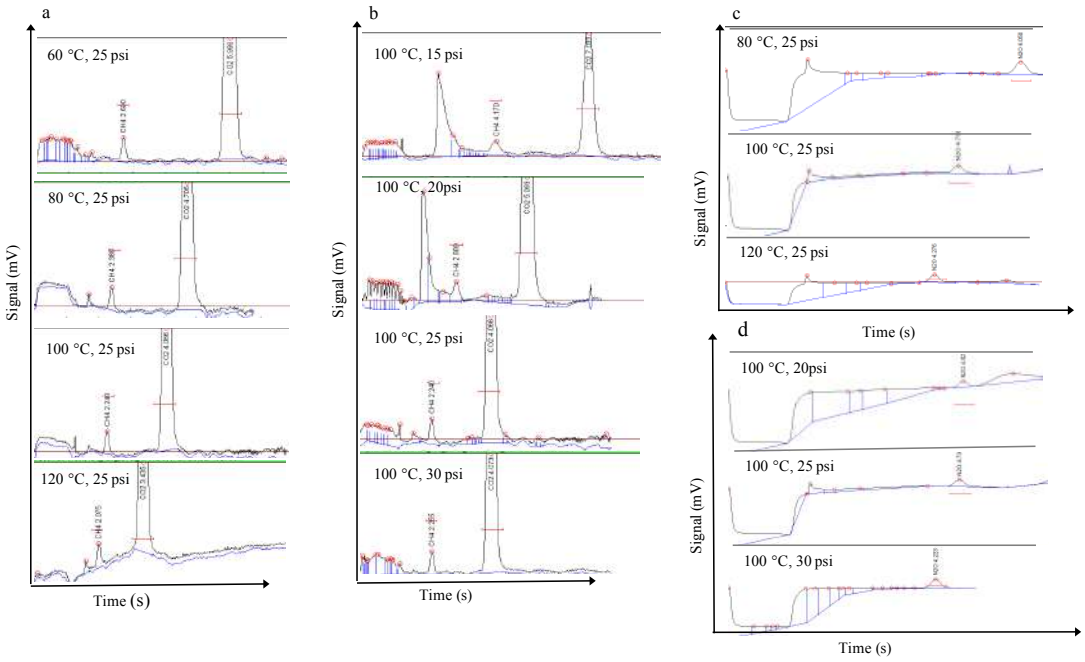

Figure III-7: Chromatogram after injection 1.5 mL of 100 ppmv –CO_2, 1 ppmv –CH_4 and 1ppmv –N_2O (STD 1). (a) Effect of oven temperature and (b) flow rate on CO_2 and CH_4 detection and retention time. (c) Effect of oven temperature and (d) flow rate on N_2O detection and retention time.

Table III-7: New GC settings for CO_2, CH_4, and N_2O detection.

Carrier gas He	25 psi -30mL/min
Makeup gas N_2	20 psi -20mL/min
Combustion gas H_2	20 psi -25mL/min
Combustion gas Air	5 psi -250mL/min
Oven temperature	Isothermal 100°C
FID Temperature	360°C
Flame ignite	-400
ECD Temperature	330°C
ECD current	330 volt

III.4.1.3 Method validation for CO_2, CH_4 and N_2O detection

An excellent linear (R^2=0.99) GC response was demonstrated within the range of the standard gas for both CO_2 and CH_4 (Figure III-8). The calibration of N_2O signal from the ECD may be nonlinear over the extended analysis range (0.39 ppmv to 5.00 ppmv). The ECD gives a non-linear detection of N_2O as ECD sensitivity decreases with increasing concentrations of N_2O (Klemedtsson et al., 1986). Therefore, the standard curve is fitted using a second order polynomial.

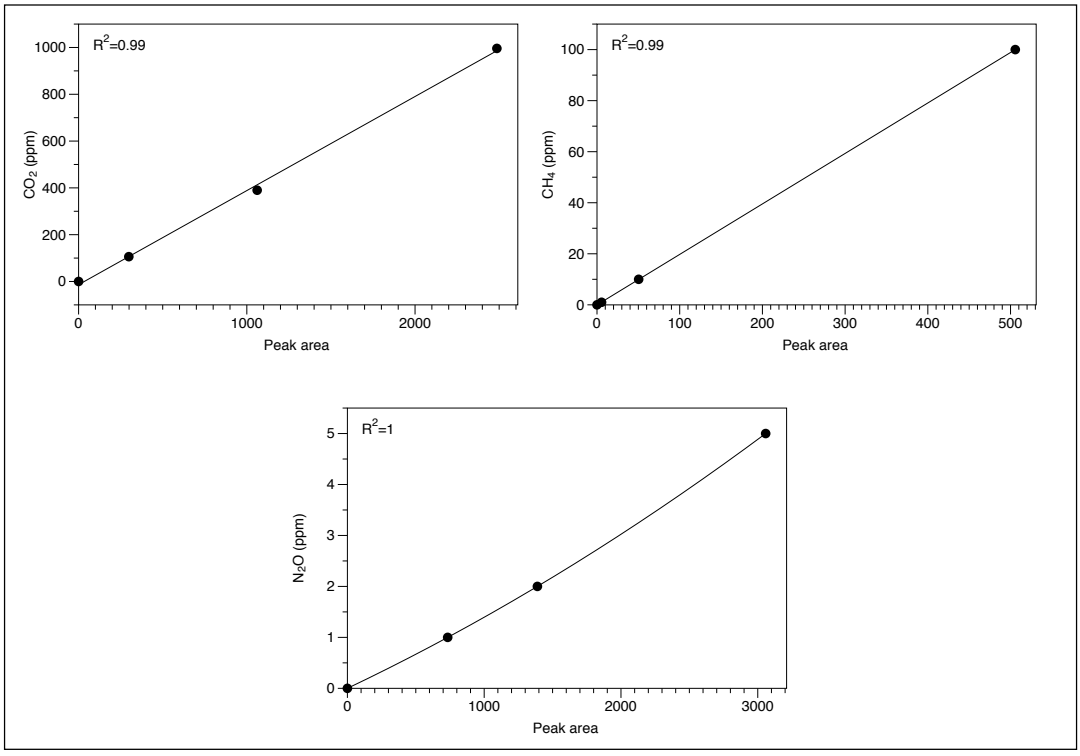

Figure III-8: Calibration curve for CO_2, CH_4 and N_2O.

The trueness of a series of measurements is expressed as the difference between the returned values by the instrument and the true value of the measured analytes (Eq.III-4). The recovery test consisted of 10 injections in a row of the

standard gas 2, and showed that the method returned the true value within 2% error for each gas species (Table III-8). The returned value deviated from the true value by 0.18%, 1.51 % and -1.93% for CO_2, CH_4 and N_2O, respectively. Positive error means that the method returned values slightly higher than the reference value, while negative error, means that the method returned slightly lower values than the reference value.

Table III-8: Recovery test for CO_2, CH_4, and N_2O detection; 10 injections of the standard 2.

Number of injection	**CO2 390 ppmv**	**CH4 10 ppmv**	**N2O 1.95 ppmv**
1	403.41	10.30	1.84
2	399.07	9.60	1.84
3	375.70	10.21	1.88
4	397.74	10.35	1.90
5	387.33	9.86	1.97
6	398.60	10.40	1.95
7	357.48	9.10	1.98
8	384.85	10.42	1.88
9	395.39	10.83	1.94
10	393.18	10.44	1.94
Ref Value (%)	390.00	10.00	2.00
STDEV	13.85	0.49	0.05
Mean	389.28	10.15	1.91
RSTDEV (%)	3.56	0.05	2.62
Error (%)	0.18	1.51	-1.93

Precision describes a level of measurement that yields consistent results when repeated. An inter-laboratory comparison was performed to verify the precision of analyses. Forty exetainer vials were filled with ambient air, ten of

which were sent to the department of Soil Sciences at the University of Manitoba to be analyzed by gas chromatograph (GC Agilent), while the remaining 30 vials were injected daily for 30 days (i.e. one injection per day) using the modified SRI 8610C GC. The precision as described by STDEV is 462.87 ± 27.3 ppmv, 2.41 ± 0.26 ppmv and 0.38± 0.05 ppmv for CO_2, CH_4 and N_2O, respectively (Table III-9).

Table III-9: Precision test for CO_2, CH_4 and N_2O detection; daily injection of ambient air.

Number of injection	**CO_2**	**CH_4**	**N_2O**
1	500.34	2.50	0.41
2	431.33	2.15	0.39
3	479.52	2.29	0.39
4	451.34	2.04	0.39
5	474.38	2.09	0.39
6	455.43	2.22	0.40
7	507.61	2.31	0.39
8	486.04	2.85	0.41
9	471.28	2.69	0.40
10	500.34	2.50	0.41
11	431.33	2.25	0.39
12	479.52	2.29	0.39
13	474.38	2.09	0.39
14	455.43	2.22	0.40
15	438.55	2.38	0.44
16	427.78	2.30	0.42
17	427.09	2.60	0.43
18	446.86	2.10	0.46
19	432.47	2.31	0.44
20	450.93	2.29	0.41
21	500.34	2.50	0.32
22	431.33	2.85	0.30
23	479.52	2.29	0.30
24	407.16	2.44	0.26
25	474.38	2.09	0.30
26	455.43	2.22	0.31
27	507.61	2.31	0.39
28	486.04	2.85	0.41
29	471.28	2.69	0.40
30	450.98	2.35	0.40
STDEV	27.30	0.26	0.05
Mean	462.87	2.41	0.38
RSTDEV (%)	5.90	9.90	12.61
Confidence interval (ppmv)	9.61	0.09	0.02
Precision error % (with a 99% confidence interval)	2.08	5.04	4.44

III.4.2 The detection of Ar, O_2 and N_2 on the TCD Channel

To facilitate the separation of Ar and O_2 at room temperature, we directly injected a small sample volume (50 µL) in the column. While using the default set up from Table III-4 and in-column injection, we obtained a stable baseline and a clear detection of N_2; however, Ar and O_2 were eluting together (Figure III-9).

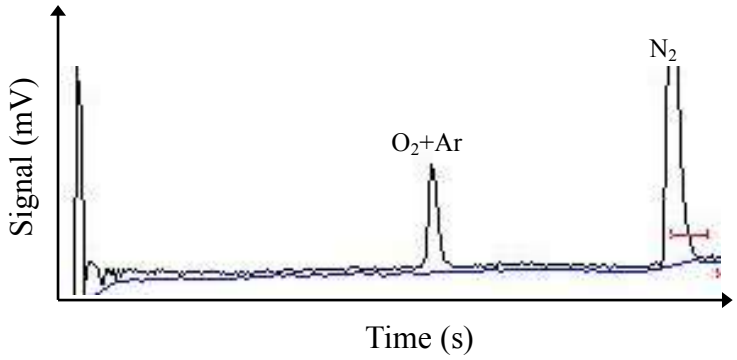

Figure III-9: Chromatogram after injection of 50µL of standard gas 1 (0.5%-Ar, 9.5%-O_2, 90%-N_2) using the default settings listed in Table III-4.

III.4.2.1 Improving the resolution of Ar and O_2

To improve the separation of Ar and O_2, their time spent in the column should be maximized. Three possible ways to increase the retention time are: (1) increasing the length of the column, (2) decreasing the flow rate of the carrier gas, and (3) decreasing the oven temperature. Suppressing O_2 in the gas mixture would facilitate a better resolution of Ar; however, this is not the best option. Since O_2 is a biogenic gas, the system should be designed to measure rather than suppress its concentration, due to its usefulness in many environmental cases. To obtain the best separation, the oven temperature was lowered as much as possible; the lowest feasible temperature of the GC oven is 29°C. Although we could not separate Ar-

O_2 at this temperature, we set up the molesieve 5Ä column outside of the GC oven and lowered the ambient lab temperature to 18°C. Under these conditions, two identical molesieve 5Ä columns were placed behind each other to maximize the separation time in the columns. Regardless, the resolution was still less than 1.

The flow rate of the carrier gas through the system determines the retention time and peak sharpness. A higher flow rate lowers the retention time and sharpens the peak, while a lower flow rate increases the retention time and broadens the peak. However, past the optimal flow rate, a higher flow rate could broaden the peak as well. Flow rate is dependent upon the ratio between pressure drop and column length, thus a longer column requires a higher pressure to obtain the same linear velocity. We tested the flow rate over a pressure range of 10 psi – 30 psi by 2 psi increments at a constant temperature of 18°C, and used two column length scenarios (one column and two columns in series). In all cases, fluctuations in flow rate did not contribute significantly to improve the resolution.

Since it was not possible to separate Ar from O_2 at the ambient lab temperature under different flow rates and column lengths, we installed an O_2 trap in the system. Previous studies (e.g. Raj et al. 1996) used a palladium alumina catalyst to eliminate O_2 and obtain accurate Ar readings. Cu-wires were used as catalysts to react with O_2 and form the oxidized CuO. This reaction required a temperature of 250°C (Chang et al., 2005). Therefore, the catalyst was placed inside the GC oven, which was set at 250°C, and the molesieve column remained outside the GC unit at room temperature (18°C). Due to the addition of more materials to the system (catalyst unit and tubing), a larger injection volume was required.

Sample volumes of 1.5 mL were injected through the 1mL sample loop and subjected to a carrier gas pressure of 14 psi (default settings, Table III-4). This allowed us to resolve Ar but only when the O_2 concentration of the standard gas was less than 30%. High O_2 concentrations (e.g. 38% in standard gas 3) compared to its contact time with the Cu-wires resulted in O_2 breakthrough and no adequate calibration curve could be established. No further attempts to trap the O_2 before detection was made.

The only remaining parameter to manipulate was temperature. In the 1960's temperatures as low as -72°C were used to obtain a good separation (Lard and Horn, 1960). In a first attempt to separate Ar from O_2, the columns were cooled by ice packs outside of the GC unit, which enabled them to reach a temperature of -10°C. This temperature was low enough to begin separating Ar from O_2 for a sample volume of 100 µL with 2% Ar and 38% O_2 (Figure III-10a). However, it is difficult to maintain a stable temperature while using ice packs. As time passes, the temperature increases and the separation between Ar and O_2 decreases as well. To stabilize the temperature, we installed a portable freezer (cryo-oven) set at -20°C (internal temperature -18°C) in which we placed the molesieve column; this arrangement resulted in satisfactory peak separation (Figure III-10a-b-c). We then adjusted both the optimal flow rate (Figure III-10b) and injection volume on the new configuration (Figure III-10C). We tested several injection volumes ranging from 50 µL – 500 µL. For volumes greater than 100 µL, the peak resolution begins to degrade (Figure III-10c). We obtained best resolution only with injection volumes of 50 µL and 100 µL. A flow rate below 14 psi caused peak broadening

and degraded the peak resolution (Figure III-10b). Further method optimizing was achieved with a flow rate of 16 psi and an injection volume of 100 µL, resulting in superior peak resolution and sufficient peak symmetry. While the moleseive column retains large molecules like H_2O and CO_2, we recommend turning off the cryo-oven and setting the GC oven temperature at 250°C to clean the moleseive column overnight.

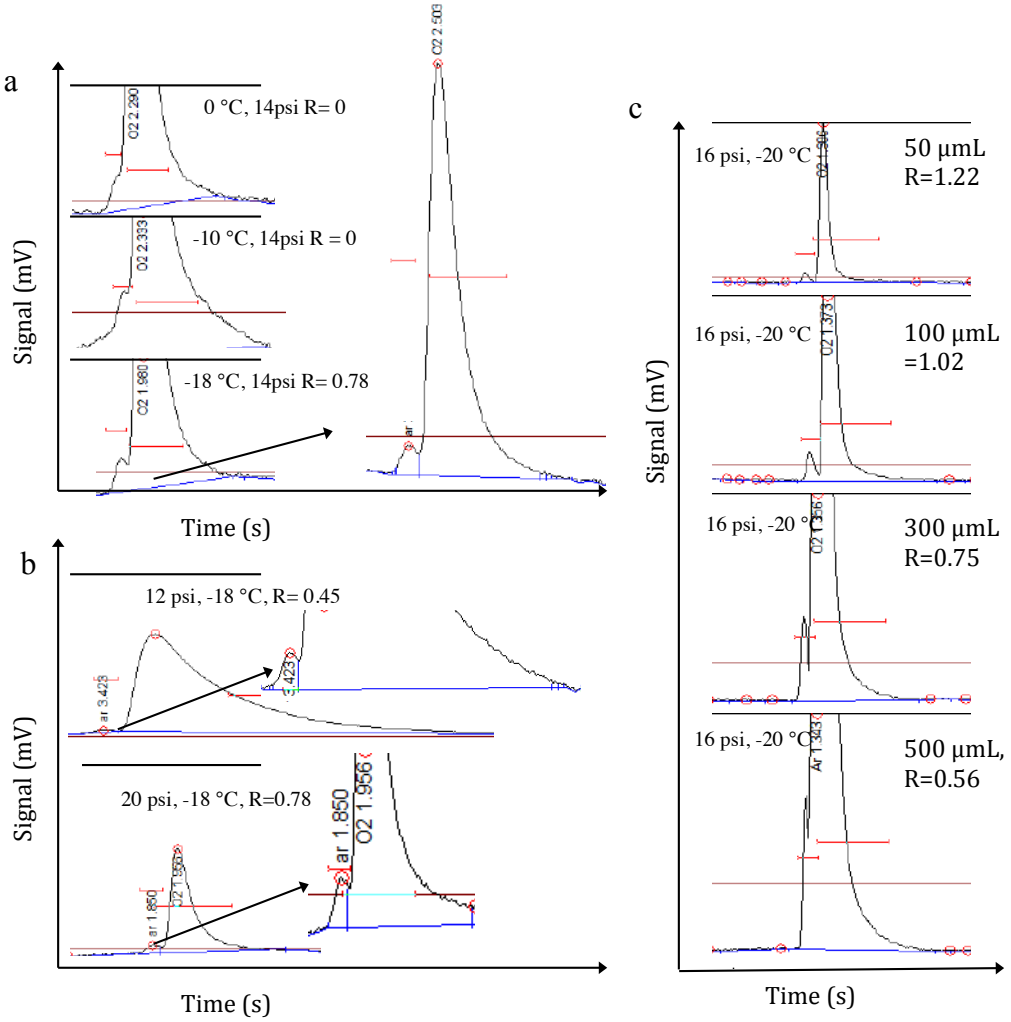

Figure III-10: Chromatogram of injection of standard 3; 2%-Ar and 38%-O_2 showing the effect of (a) the temperature, (b) the flow rate (c) volume of injection for the peak resolution between Ar and O_2.

III.4.2.2 Method validation for the detection of Ar, O_2 and N_2

To validate the method, we established a calibration curve, and tested the trueness and precision of the measurements. An excellent linear (R^2=0.99) GC response was demonstrated within the range of the standard gas for O_2 (R^2 = 0.99), Ar (R^2 = 0.99) and N_2 (R^2 = 0.99; Figure III-11).

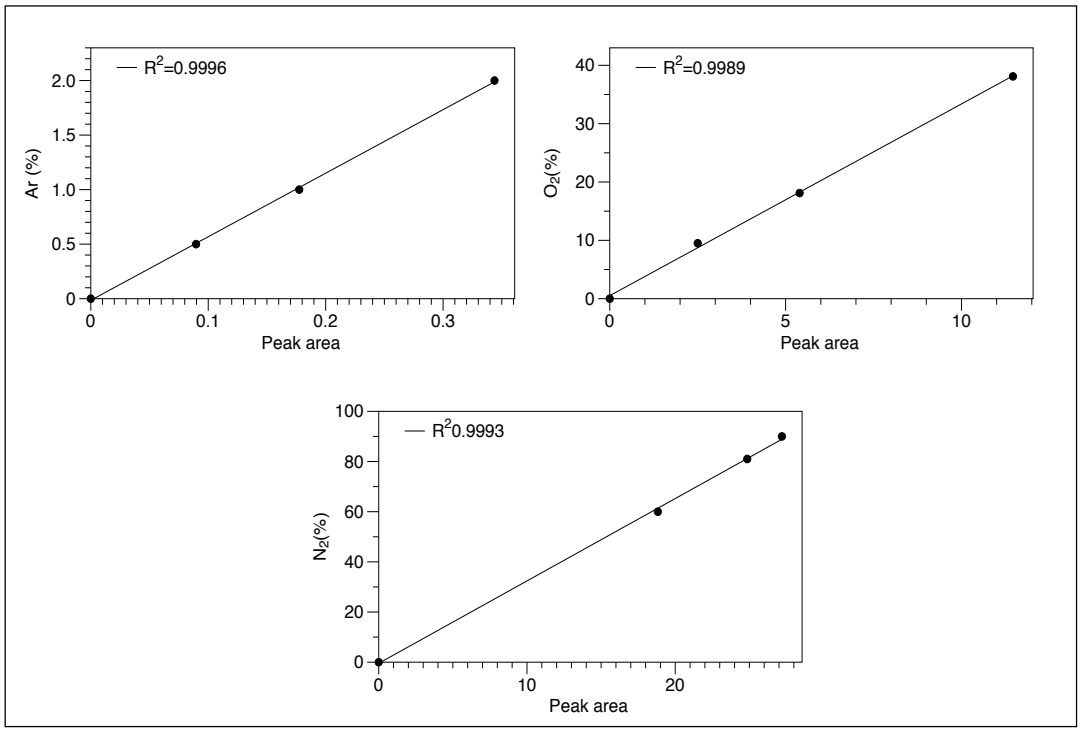

Figure III-11: Calibration curve for Ar, O_2 and N_2.

Trueness is a measure of the system's ability to return the true value (Eq.III-4). The recovery test consisted of 10 injections in a row of the standard gas 1. The method returned the expected value within 5% error (Table III-10). The returned value deviated from the true value by 4%, 0.21%, and -2.8 % for Ar, O_2 and N_2, respectively.

Table III-10: Recovery test for Ar, O_2 and N_2 detection, 10 injections of the standard gas 1.

Number of injection	**Ar 0.5 %**	**O_2 9.5 %**	**N_2 90 %**
1	0.50	9.13	84.40
2	0.46	10.01	93.41
3	0.45	9.75	107.06
4	0.48	9.25	90.83
5	0.42	9.74	89.40
6	0.51	8.83	73.34
7	0.46	10.71	97.81
8	0.46	8.85	89.13
9	0.49	9.27	86.64
10	0.48	9.18	91.30
Ref Value (%)	0.5	9.5	90
STDEV	0.027	0.54	10.00
Mean	0.5	9.48	92.61
RSTDEV%	5.29	5.65	10.80
Error (%)	4%	0.21%	-2.8%

The method's precision was tested with daily injections of ambient air (Table III-11). The precision test was conducted under the same operating conditions (same equipment, same laboratory) over a long interval of time (one month). The precision given by the STDEV for Ar, O_2 and N_2 was 0.9± 0.11%, 20.89 ± 0.66% and 79.53± 4.88% respectively.

Table III-11: Precision test for Ar, O_2 and N_2 detection; daily injection of ambient air.

Number of injection	Ar	O_2	N_2
	0.93 (%)	**20.95 (%)**	**78.08 (%)**
1	1.05	19.79	75.39
2	0.98	19.75	75.15
3	0.93	22.03	80.25
4	0.95	21.58	80.54
5	0.91	20.92	79.12
6	1.01	21.09	76.42
7	0.98	22.26	76.14
8	0.96	21.54	76.54
9	0.97	21.60	75.32
10	0.66	21.07	74.82
11	0.96	21.28	76.23
12	0.91	21.03	77.76
13	0.79	21.11	86.78
14	0.78	20.94	87.22
15	0.75	21.08	86.72
16	0.76	19.98	82.78
17	0.73	21.56	86.18
18	0.83	21.61	87.72
19	0.78	21.11	89.15
20	0.77	20.16	83.35
21	0.76	19.71	82.98
22	0.83	21.38	72.97
23	1.01	20.78	85.30
24	1.00	20.68	74.36
25	0.83	20.17	76.25
26	0.93	20.09	73.67
27	1.04	21.13	74.41
28	1.08	20.66	77.17
29	0.93	20.43	78.86
30	1.02	20.57	77.10
31	0.99	20.60	78.65
STDEV	0.11	0.66	4.88
Mean	0.90	20.89	79.53
RSDTEV %	12.51	3.17	6.13
Confidence interval (%)	0.04	0.23	1.72
Precision Error % (with a 99% confidence interval)	4.40	1.11	2.16

III-5 Conclusions

After the implementation of a third detector (TCD) and molesieve column in a cryo-oven set at -20°C, the greenhouse gas GC (SRI 8610C) is able to detect a suite of atmospheric gases. By adjusting the igniter set-up on the FID, we significantly decreased the noise and were able to detect CH_4 concentrations as low as 0.2 ppmv. While reducing the makeup gas flow rate on the ECD channel, we increased the response detector and improved the detection of N_2O; we detected concentrations of N_2O as low as 0.39 ppmv. An excellent linear GC response was demonstrated within the range of the standards gas for Ar, O_2, N_2, CO_2, CH_4 and N_2O. For both major atmospheric gases and greenhouse gases, we reached satisfactory accuracy required for the measurements.

Table III-12: Summary.

Analyte	**Calibration Range (%)**	**R^2**	**Error (%)**	**Precision (rstdv,%)**	**Resolution (R)**	**MDC (%)**
Ar	9.5-38	0.998	4	12.51	<1	
O_2	27-90	0.999	0.21	3.17	<1	n/a
N_2	0.5-2	0.999	-2.8	6.13	>1	
Analyte	**Calibration Range (ppmv)**	**R^2**	**Error (%)**	**Precision (rstdev,%)**	**Resolution (R)**	**MDC (ppmv)**
CO_2	100-100	1.00	0.18	5.90	>1	n/A
CH_4	1-100	0.999	1.51	9.90	>1	0.2
N_2O	1-5	0.996	-1.93	12.61	>1	<0.39

References

Chang, Y., Lye, M. L., and Zeng, H. C.: Large-scale synthesis of high-quality ultra long copper nanowires, Langmuir, 21, 3746-3748, 2005.

Dolan, J.W.: Peak tailing and Resolution, LC resources Inc, Walnut Creek, California, USA, 20.5, 430-437, 2002.

Grob, R. L., and Barry, E. F.: Modern practice of gas chromatography. John Wiley & Sons, New-York, USA, 2004.

Heftmann, Erich, ed. Chromatography: Fundamentals and applications of chromatography and related differential migration methods-Part A: Theory. Vol. 69. Elsevier, 2004.

Hinshaw, J.: The flame ionization detector, GC connection, LCGC North America, 13, 1262-1272, 2005.

Holm T.: Aspects of the mechanism of the flame ionization detector, Journal of Chromatography A, 842, 221–227, 1999.

Hosseinzadeh Hejazi, S. A., Rajendran, A., Sawada, J. A., and Kuznicki, S. M.: Dynamic Column breakthrough and process studies of high-purity oxygen production using silver exchanged titanosilicates (Ag-ETS-10), Industrial & Engineering Chemistry Research, 2016.

ISO.: Accuracy (trueness and precision) of measurement methods and results – Part 3: Intermediate measures of the precision of a standard measurement method in statistical methods for quality control. International Organization for Standardization (ISO), Geneva, 5725-3, 75–104, 1994.

Klemedtsson, L., Simkins, S., and Svensson, B.: Tandem thermal-conductivity and electron-capture detectors and non-linear calibration curves in quantitative nitrous oxide analysis, Journal of Chromatography A, 361, 107-116, 1986.

Lard, E., and Horn, R.: Separation and determination of argon, oxygen, and nitrogen by gas chromatography, Analytical Chemistry, 32, 878-879, 1960.

Lenehan, C. E.: Chromatography: Basic Principles, In Siegel J.A. and Sauko P.J. (eds) Forensic Chemistry, Flinders University, Adelaide, SA, Australia, 573-578, doi.10.1016/B978-0-12-382165-2.00244-0, 573-578, 2013.

McNair, H. M., & Miller, J. M.: Detectors. Basic Gas Chromatography, Second Edition, . John Wiley & Sons, Inc., Hoboken, NJ, USA. doi: 10.1002/9780470480106.ch7, 2009.

Poole, C. F., and Poole S. K.: Chromatography today, Elsevier, New York, 2012.

Raj, S., Sumangala, R., Lal, K., and Panicker, P.: Gas chromatographic analysis of oxygen and argon at room temperature, Journal of chromatographic science, 34, 465-467, 1996.

Restek Corporation, Restek's PLOT Column Family, http://www.restek.com/pdfs/PCSS1163F-UNV, USA, 2015.

SRI Instruments Europe, European Greenhouse gas Chromatograph, http://www.sriinstrumentseurope.com/en/pdf/european_greenhouse_gas_chromatograph.pdf, 2012.

Weiss, R. F.: Determinations of carbon dioxide and methane by dual catalyst flame ionization chromatography and nitrous oxide by electron capture chromatography, Journal of Chromatographic Science, 19, 611-616, 1981.

Chapter-IV-First '*in situ*' determination of gas transport coefficients (D_{Ar}, D_{O_2} and D_{N_2}) from bulk gas concentration measurements (Ar, O_2, N_2) in natural sea ice.

A peer-reviewed scientific research paper published in October 2014 in Journal of Geophysical Research Oceans, 119, 6655-6668, doi:10.1002/2014JC009849.

Odile Crabeck[1*], Bruno Delille.B[2], Soren Rysgaard.S[1,3,4], David N. Thomas[6,7], Nicolas-Xavier Geilfus [1,3], Brent Else[8], Jean-Louis Tison J-L[5].

1. Department of Geological science, CEOS, University of Manitoba, Canada
2. Unité d'océanographie chimique, MARE, Université de Liège, Belgium
3. Arctic Research Centre, Aarhus University, C.F. Denmark
4. Greenland Climate Research Centre, Greenland Institute of Natural Resources, Nuuk, Greenland
5. Laboratoire de glaciologie, DSTE, Université Libre de Bruxelles, Belgium
6. School of Ocean Sciences, Bangor University, Menai Bridge, Anglesey, U.K.
7. Marine Research Centre, Finnish Environment Institute, Helsinki, Finland.
8. Department of Geography, University of Calgary, Calgary, Alberta, Canada

To achieve consistency trough this document, terminology and symbolic might differ from the published version.

I did all the analysis and leaded the manuscript (writing, discussion and figures). My co-authors reviewed and helped thoroughly with the edition. Jean-Louis, Bruno, Thomas and Soren provided comments and several detailed reviews of the discussion. Brent helped with the final edition of the paper.

Abstract

We report bulk gas concentrations of Ar, O_2 and N_2, as well as their transport coefficients, in natural landfast subarctic sea ice in southwest Greenland. The observed bulk ice gas composition was 1.09% Ar, 27.5% O_2 and 71.4% N_2. Most previous studies suggest that convective transport is the main driver of gas displacement in sea ice and have neglected diffusion processes. According to our data, brine was stratified within the ice, so that no convective transport could occur within the brine system. Therefore, diffusive transport was the main driver of gas migration. By analysing the temporal evolution of an internal gas peak within the ice, we deduced the bulk gas transport coefficients for argon (D_{Ar}), oxygen (D_{O_2}) and nitrogen (D_{N_2}). The values fit to the few existing estimates from experimental work, and are close to the diffusivity values in water (10^{-5} cm^2 s^{-1}). We suggest that air bubbles escaping from the brine to the atmosphere as the ice gets more permeable during melt could be responsible for the previously reported high transport coefficients. These results underline that when there is no convective transport within the sea ice, the transport of gas by diffusion through the brine, either in the liquid or gaseous phases, is a major factor in controlling the ocean–atmosphere exchange.

IV-1 Introduction

To date, only a limited number of studies describing the natural gas composition of sea ice are available (e.g. Matsuo and Miyake, 1966; Rysgaard and Glud, 2004; Tison et al., 2002; Zhou et al., 2013). These studies typically found a total gas content lower than 23.75 ml STP kg^{-1} ice; a value expected if seawater is instantly frozen, and reported bulk ice gas compositions on the order of ≈⅓ O_2 and ≈⅔ N_2, similar to atmospheric and seawater compositions. The formation of these air inclusions has been described in detail by Tsurikov, (1979) who identified nine key processes that trap gases in sea ice. Most importantly, during the freezing process the expelled dissolved gases are trapped in the brine, or in bubbles that are released at the ice-seawater interface (Figure IV-1: initial gas entrapment). Increased concentrations of solutes in brine by freezing results in further formation of air bubbles by nucleation processes (Figure IV-1: post genetic process). More air inclusions can be created during sea ice melt, as water vapor forms inside the brine pockets above the freeboard line. Finally, drained bine pockets and channels may be replaced by atmospheric gases.

The presence of a gas phase in sea ice creates the potential for gas exchange with the atmosphere, although unfortunately gas transfer at the sea ice-atmosphere interface is not well constrained (Zemmelink et al., 2006; Heinesch et al., 2009; Else et al., 2011; Loose et al., 2011; Miller et al., 2011; Papakyriakou and Miller, 2011; Sørensen et al., 2013). For example, studies have shown that sea ice can act as a source (e.g. Nomura et al., 2006; Miller et al., 2011; Geilfus et al., 2012, 2013) or a sink for atmospheric CO_2 (e.g. Zemmelink et al., 2006; Rysgaard et al., 2007;

Nomura et al., 2010; Papadimitriou et al., 2012), with the reported fluxes spanning several orders of magnitude.

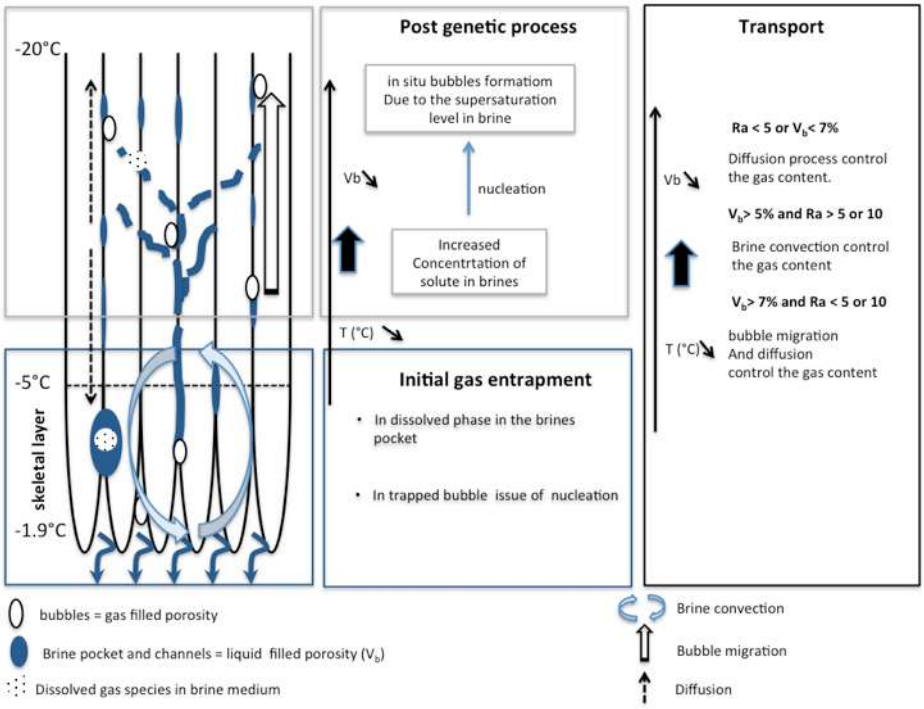

Figure IV-1: Schematic view of gas entrapment and evolution in sea ice. During the freezing process the expelled dissolved gases are trapped in the brine solution, or in bubbles that are released at the ice-seawater interface. Increased concentration of the brine by freezing results in further formation of air bubbles by nucleation processes. The main transport processes of gas within the sea ice depend on the permeability and convection threshold given by the brine volume and the Rayleigh number. If V_b is under 5%, no convection occurs in sea ice and gas transport is controlled by diffusion process. During diffusion, the gas can be released both into the underlying water and to the atmosphere as a function of the gradient concentration. While V_b is above 5% and Ra >5 or 10, brine convection occur and brine can exchange with the seawater underneath. If the V_b exceeds 7.5%, bubbles are able migrate upward and gas maybe released to the atmosphere.

Three main processes should be considered for gas transport within sea ice (Figure IV-1: transport): a) convection with the brine medium, b) diffusion along the concentration gradient (in the dissolved state within the brine medium) and c) upward gas movement under buoyancy (in the gaseous state within the brine

medium). All three require that there is a certain level of permeability in the sea ice, which may differ depending on the process considered. According to Golden et al. (1998, 2007), the permeability of sea ice rapidly increases when the brine volume fraction exceeds 5%. At brine volume fractions below 5% no brine convection is expected to occur, and the ice cover is often considered impermeable to gas exchange. A recent study by Zhou et al. (2013) suggests that a brine volume of ≈ 7% is required for upward bubble migration (through bubble buoyancy). These observations are consistent with Loose et al. (2011) who suggest that the permeability threshold for gas transport could be different from the permeability threshold for brine convection (i.e. gravity drainage) or bubble migration. Past studies (Gosink et al., 1976; Loose et al., 2009, 2011; Shaw et al., 2011) have actually suggested that diffusive transport is the major control on gas fluxes through sea ice, and it appears to be active even at low brine volumes. Diffusion across the sea ice cover should therefore be considered as an alternative transport process for the exchange of gas between the ocean, the sea ice and the atmosphere in the absence of convection processes (i.e. brine drainage under brine density instability).

The aim of the present study was to examine the physical processes that affect mass transport of atmospheric gases across and within sea ice. Unlike previous studies, which have used artificial gas tracers (e.g. Gosink et al., 1976), or artificial sea ice (e.g. Loose et al., 2011), we used measurements of natural gas concentrations in natural sea ice samples. By studying the temporal evolution of the vertical profile of Ar, O_2 and N_2, we were able to compute diffusivities of these gases in a natural environment. Since only one study (Gosink et al., 1976) reports

such measurements in natural environment, our findings significantly enhance scientific understanding of gas transport in sea ice. Furthermore, our observations can be used to validate previous studies made in the laboratory and other experimental settings.

IV-2 Study site

The sampling was conducted from 10 to 16 March 2010 on first-year landfast sea ice in Kapisillit in the vicinity of Nuuk, SW Greenland (64°26´N 50°13´W, Figure IV-2). To follow the temporal evolution of the sea ice, we sampled sea ice and the underlying water column at the same site on three occasions: 11 March, 13 March and 15 March. Sampling was performed within an area of about 25 m^2 in order to minimize bias from spatial heterogeneity. The water depth at the location ranged from 40 to 45 m, and the mean salinity of seawater in the Kapisillit fjord was 32.9. The air temperatures during the study period ranged from -8.8 °C to +2.9 °C (average -3.2 °C). The survey took place before the onset of the spring algal bloom: Concentrations of chlorophyll-a were 2.8 ± 0.4 µg L^{-1} (SE, n = 3) in the bottom 12 cm of ice, while the average concentration across the entire ice thickness was 1.0 ± 1.2 µg L^{-1} (SE, n=3) (Long et al., 2012; Søgaard et al., 2013).

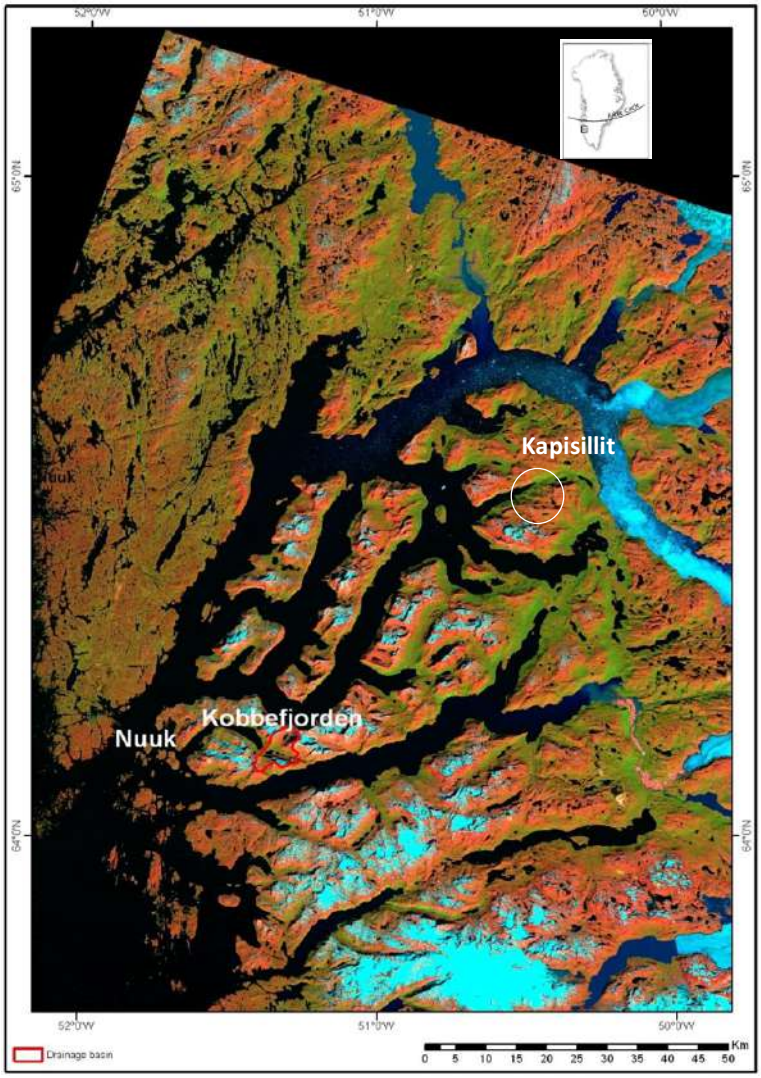

Figure IV-2: Study site –Landfast sea ice in Godthåbsfjord, SW Greenland. Circle includes the Bay with the study site and the settlement Kapisillit.

IV-3 Methods

IV.3.1 Sea ice temperature, salinity and texture

Ice cores were extracted using a stainless-steel corer with an internal diameter of 9 cm (Kovacs Ent., Lebanon, USA). Cores were immediately wrapped in polyethylene bags and stored at the sampling site in insulated containers filled with individual cooling bags pre-cooled at -20°C. In the laboratory, ice cores were

kept at -20°C in the dark to ensure brine/gas immobilization and to inhibit biological processes (Eicken et al., 1991). On a replicate core extracted from the same location, *in situ* ice temperature was measured with a depth resolution of 5 cm, using a calibrated probe (Testo 720) inserted into pre-drilled holes (with the same diameter as the probe), perpendicular to the ice core axis. The precision of the probe was ± 0.1 °C. This "temperature" ice core was immediately cut into 5 cm slices, stored in polyethylene buckets, and left to melt. Back in the laboratory, bulk ice salinity was measured with a portable conductivity meter (Orion Star Series Meter WP-84TP) with a precision of ±0.1. To describe the texture of the ice, horizontal thin sections were produced in 10 cm sections from a third ice core, using the standard microtone (Leica SM2400) following the procedure described by Langway (1958) and Tison et al. (2008). The images from horizontal thin sections were collected with a digital camera (Nikon Coolpix S200, 7.1 megapixels) between crossed polarizers.

IV.3.2 Total gas content

The total volume of gas within sea ice (content in mL STP of gas per kg of ice) was measured with a resolution of 5 cm using the wet extraction method (Raynaud et al., 1982). In short, ice samples from the retained core were placed in an evacuated glass container. The ice was then melted and refrozen from the bottom using a -70°C cold ethanol bath. This technique of melting-refreezing releases both the dissolved gas in the brine and the gas content from the bubbles (Tison et al., 2002). After the refreezing, the container was connected to a Toepler pump

extraction system, and the entire gas volume was directed through a pre-vacuumed line to a mercury-graduated burette. Knowing the exact weight of the sample analyzed, the ice temperature, and atmospheric pressure, we calculated the STP gas content of the sample with a precision of ±5%.

IV.3.3 Gas composition

Argon (Ar), oxygen (O_2) and nitrogen (N_2) were analyzed by gas chromatography. Extraction of the gas phase from the ice used the dry-crushing technique as developed for gas measurements in continental ice (Raynaud et al., 1982). Each ice core was cut in successive 5 cm sections, and 60 g of each section was put into a vessel together with stainless steel beads. The vessel was evacuated to 10^{-3} torr, and then fixed to an ice crusher as described in Raynaud et al. (1982) and Stefels et al. (2012). The stainless steel beads impact the ice block during the shaking process, so that the ice is crushed into a fine powder. The cutting and shaking processing took place in a cold room at -25 °C. After crushing, the vessel was kept at -50°C in a cold ethanol bath, and connected to a gas chromatograph equipped with a thermal conductivity detector for concentration analyses (Skoog et al., 1997). We used AlphagazTM2 He (Air Liquid –P0252) as the carrier gas, and a 22 ml packed column (Mole Sieve 5A 80/100; 5m x 1/8"). The gas collected included both the air bubbles in the ice, and the dissolved phase within liquid brine.

We compared the evolution of Ar, O_2, and N_2 concentration in bulk ice to the inventory constrained by the solubility in brine at atmospheric saturation. The latter represents the maximum concentration of Ar, O_2 and N_2 in the dissolved

phase, if no supersaturation existed in the brine (Carte, 1961; Lubtkin, 2003; Zou et al., 2013). It is obtained by calculating the temperature and salinity dependent solubility of Ar, O_2 and N_2 in the brine (Garcia and Gorden, 1992; Hamme and Emerson, 2004) and multiplying it by the relative brine volume (brine volume fraction b/V, see below) to express it as micromoles per litre of bulk ice ($C_{saturation}$). Zhou et al. (2013) showed than these relationships remain valid for the range of temperature and salinity found in sea ice. The difference between observed concentration in bulk ice ($C_{bulk\ ice}$) and the theoretical saturation concentration in brine ($C_{saturation}$) provides a maximum estimate of the gas concentration in the ice that resides in the gas phase, C_B (i.e. the gas content of bubbles, assuming no supersaturation in the brine):

$$C_B = C_{bulk\ ice} - C_{saturation} \qquad \text{(Eq.- IV-1)}$$

We also calculated the supersaturation factor, (SAT_f):

$$SAT_f = {}^{C_{bulk\ ice}}/_{C_{saturation}} \qquad \text{(Eq.- IV-2)}$$

and the percent gas content in the bubbles, (f_B):

$$f_B = \left({}^{C_B}/_{C_{bulk\ ice}}\right) \times 100 \qquad \text{(Eq.- IV-3)}$$

IV.3.4 Liquid/air porosity and Rayleigh number

The brine volume, (b), was computed using the state equations of Cox and Weeks (1983) and of Leppäranta and Manninen (1988) for bulk ice temperature < -2 °C and ≥ -2 °C, respectively, neglecting the air volume fraction (air porosity). Brine salinity, (S_{br}), was derived from the observed sea ice temperatures and

freezing point of seawater (UNESCO, 1978). The brine volume fraction or liquid porosity, (V_b), was calculated as brine volume/bulk sea ice volume (b/V, expressed in %).

The air volume (i.e. L gas phase per L of ice, bubble volume, air porosity), (a), was determined by multiplying C_B by the gas molar volume using gas law normalised at the average ice temperature (-3.2 °C) (Vm = 22.14 x 10^{-6} L mol^{-1}), and summing the contribution of all gas species:

$$a = C_B \times Vm \qquad \text{(Eq.-IV-4)}$$

The air porosity or air volume fraction was calculated as a percentage of the volume total of ice, V_a:

$$V_a = \left({}^{a}/_{\text{Bulk ice volume}} \right) x100 \quad \text{(Eq.- IV-5)}$$

This calculated value is a maximum percentage, supposing that no supersaturation existed in the brine, and only considering Ar, O_2 and N_2 concentrations in the ice. Note also that this value is slightly underestimated since C_B is calculated from $C_{saturation}$ (Eq.IV-1), itself overestimated since we neglected the air porosity in the use of Cox and Weeks (1983) formulation to estimate the brine volume fraction. Cox and Weeks (1983) estimated the air porosity to be between 1% to 5%.

The Rayleigh number is a parameter that primarily determines the onset of convection (e.g. gravity drainage) and provides information about the vertical stability in the brine system. The Rayleigh number (Ra) was estimated using the definition of Notz and Worster (2009).

IV-4 Results

IV.4.1 Physical ice properties

Detailed physical properties of the sea ice cores are presented elsewhere (Kaartokalllio et al., 2013; Søgaard et al., 2013; Crabeck et al., 2014). In short, the ice consisted of columnar crystals, and was relatively warm throughout, with a slight temperature gradient (Figure IV-3a) from top (-2.8 to -3.8 °C) to bottom (-0.8 to -1.2°C). The ice was covered by a thin layer of frozen snow, less than 3 cm thick during all the sampling period. The average bulk ice salinity was 3.2, and the ice salinity profiles deviated from the classical C-shape due to a variable localised riverine input (Figure IV-3b). During the survey, the brine volume fraction fell below the permeability threshold of 5% at various depths (Figure IV-3c), indicating that the atmosphere was not effectively connected to the seawater through the ice. Furthermore, the Rayleigh number ranged from 0 to 0.3 (Figure IV-3d), and remained well below the theoretical convection threshold of 5 (Vancoppenolle et al., 2010) or 10 (Notz and Worster, 2008) throughout the ice. Thus, we do not expect that convective transport of brine occurred at any time, or at any level of the sea ice. However, the V_b exceeds 30% in the bottom of the ice (Figure IV-3c), and there was no brine convection because the driving buoyancy given by the brine density gradient was not large enough to overcome dissipation.

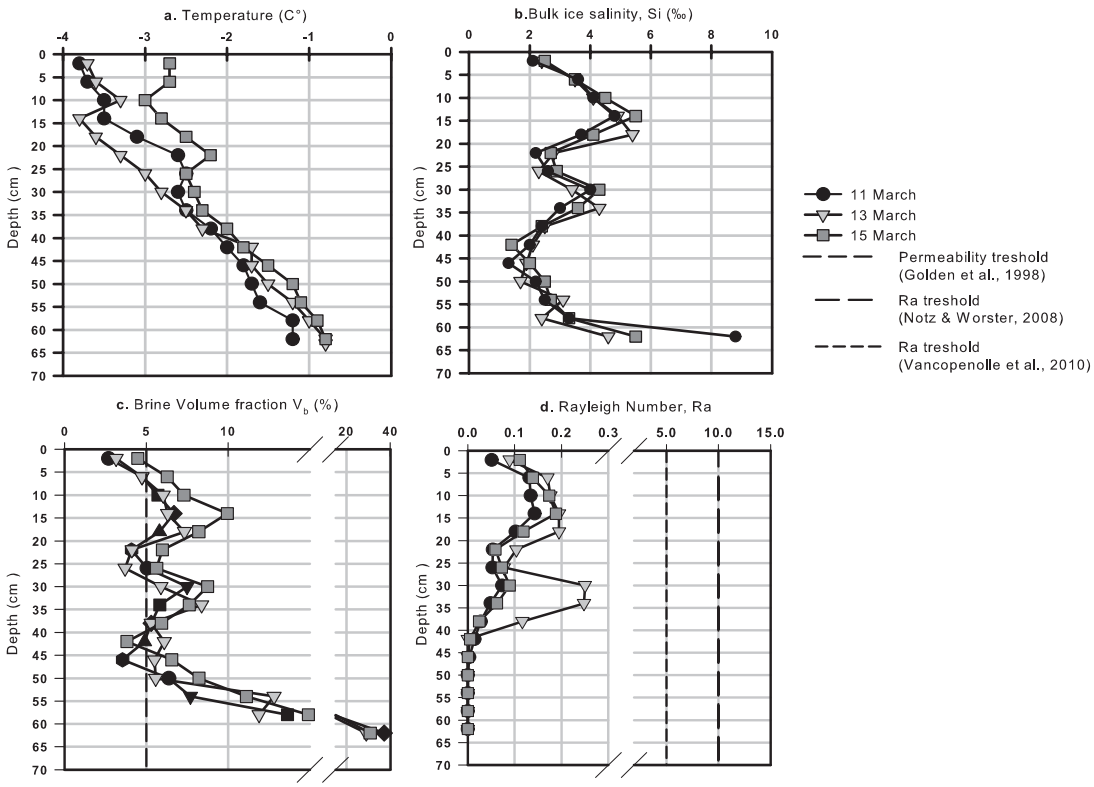

Figure IV-3: (a) Bulk ice salinity, S_i (b) Temperature, (c) Brine volume fraction or liquid porosity, V_b. The vertical dashed line is a reference value for the permeability threshold according to Golden et al. (1998, 2007), (d) Rayleigh number, Ra, the dotted lines are a reference value for the convection threshold according to Notz and Worster (2008) and Vancoppenolle et al. (2010) respectively.

IV.4.2 Gas composition

At all dates, the total gas content in sea ice ranged from 4 to 23.2 ml STP kg^{-1} ice, consistently lower than the 23.75 ml STP kg^{-1} ice expected for instantly frozen seawater (Cox and Weeks, 1983). This is consistent with past findings (e.g. Tison et al., 2002), and is a result of the rejection of gases during ice formation. Furthermore, a peak in gas content in the ice was observed between 25 cm and 35 cm below the surface at all sampling dates (Figure IV-4a).

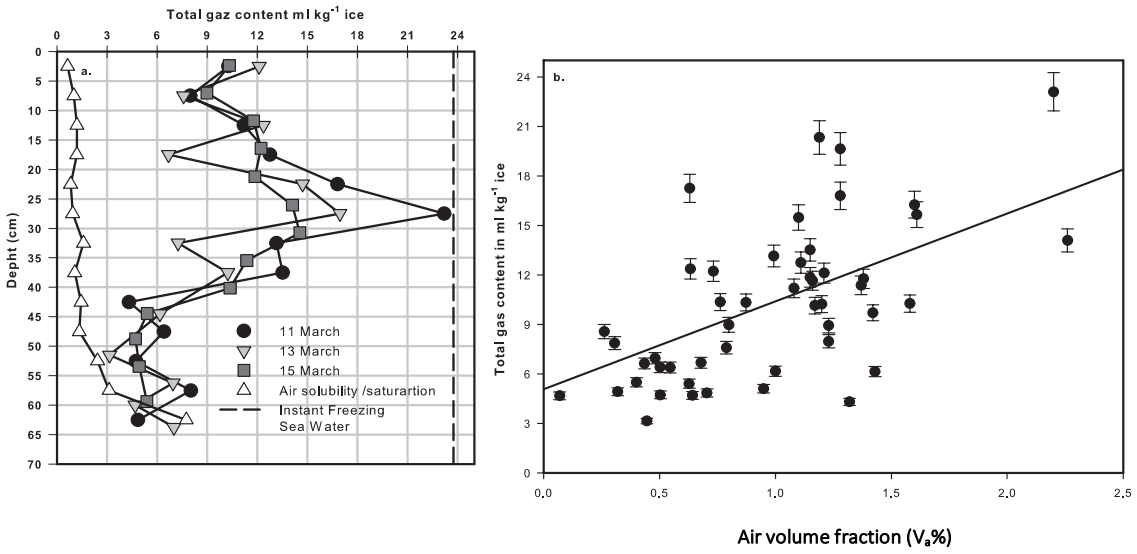

Figure IV-4: Evolution of the total gas content in bulk sea ice as compared to solubility at atmospheric saturation (white triangle; air solubility). The latter was obtained by multiplying the calculated solubility in brine, by the relative brine volume. (b) Relationship between the total gas content measured with the toepler pump and the computed air porosity (V_a). A regression line is shown (r^2=0,37, P<0,001) and its intersection with the y axis represent the maximum volume of dissolved gas in the brine.

Mixing ratios in sea ice ranged from 0.94% to 1.29% for Ar, 22.7% to 32.7% for O_2, and 68.2 to 76.3% for N_2 (Table IV-1). These correspond to a bulk ice Ar concentration of 1.3 - 11.7 µmol L^{-1} ice (average 5.4 µmol L^{-1} ice), a bulk ice O_2 concentration of 40 - 275 µmol L^{-1} ice (average 132 µmol L^{-1} ice) and a bulk ice N_2 concentration of 57 - 830 µmol L^{-1} ice (average 354 µmol L^{-1} ice). Each gas profile (for each sampling date) had minimum concentrations in the bottom of the sea ice and a peak around 27 cm below the ice surface (Figure IV-5). Over time the Ar, O_2 and N_2 gas peaks decreased. Between 11 and 13 March, O_2 and Ar concentrations decreased by 13.9 and 13.6%, respectively, while N_2 concentrations decreased 3 times faster (32.1%).

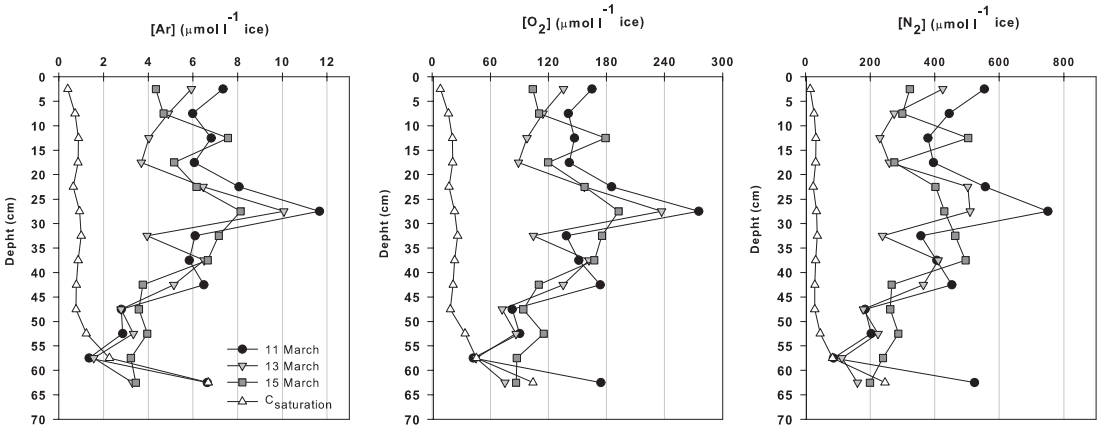

Figure IV-5: Evolution of Ar, O_2 and N_2 concentrations in bulk sea ice as compared to solubility at atmospheric saturation (white triangle). The latter was obtained by multiplying the calculated solubility in brine by the relative brine volume.

Table IV-1: Relative proportion of Ar, O_2 and N_2 in landfast sea ice at Kapisillit.

Gas composition (%)	Ar		O_2		N_2	
	Min	Max	Min	Max	Min	Max
11 March	0.94	1.28	22.7	32.7	68.2	76.3
13 March	0.970	1.25	23.9	31.4	67.2	75.1
15 March	0.973	1.29	24.1	30.5	68.2	74.9
Sea ice Tsurikov (1979)	0.9	1.1	20.6	29.0	54.2	76.8
Sea ice Tison et al. (2002)	n/a	n/a	24.36	30.46	69.54	78.08
Sea water (t= 0 °C, S=33)	1.69		34.84		61.14	
Atmospheric composition	0.93				20.95	78.08

Each gas species exceeded the concentrations calculated at atmospheric saturation (Table IV-2). The saturation factor (SAT_f) (Eq.IV-2) varied from 0.82 to 39 for N_2, from 0.64 to 20.2 for O_2 and from 0.52 to 18.5 for Ar. Maximum supersaturation factors were systematically observed in the middle of the ice, 27.5 cm below the ice surface, while minimum saturation were observed in the

permeable bottom 5 cm of the ice (Table IV-3). N_2 was the most supersaturated gas species, with an average saturation factor of 9.16, compared to 6.88 for O_2 and 5.05 for Ar. According to equation IV-3, more than 70% of the gas species were in the gas phase while less than 30% was dissolved in the brine (Table IV-3).

Overall, the brine porosity (i.e. V_b, brine volume) represented 3 to 8% of the ice volume, except in the bottom 5 cm where V_b exceeded 30%. The calculated air porosity (V_a) was at most 2.2% of the ice volume, and it was equal, or close to, 0 in the bottom 5 cm. This means that all gas species were dissolved in the brine in the bottom horizons of the sea ice. The total porosity varied from 4 to 12%, except in the bottom 5 cm where it exceeded 30%.

Table IV-2: Saturation factor,(SAT_f), computed following the equation IV-2.

Gas species	**Saturation factor ($C_{bulk\ ice}/C_{saturation}$)**	
	MIN	**Max**
Ar	0.52	18.5
O_2	0.64	20.2
N_2	0.82	39

Table IV-3: Temporal evolution of sea ice properties at the gas maximum[a].

	a. March 11			b. March 13			c. March 15		
	Mean depth gas (cm)			Mean depth gas (cm)			Mean depth (cm)		
	22.5	27.5	32.5	22.5	27.5	32.5	22.5	27.5	32.5
T(°C)	-2.59	-2.54	-2.54	-3.26	-2.92	-2.61	-2.24	-2.46	-2.34
Bulk Salinity	2.25	3.12	3.37	2.74	2.67	3.96	2.72	3.42	3.95
V_b (%)	4.2	5.97	6.45	4.00	4.48	7.36	5.93	6.75	8.05
$C_{bulk\ ice}$, Ar (µmol L^{-1} ice)	8.06	11.66	6.10	6.461	10.07	3.95	6.16	8.14	7.16
$C_{bulk\ ice}$, O_2 (µmol L^{-1} ice)	185.34	275.30	138.46	156.98	236.99	104.47	157.39	192.53	175.34
$C_{bulk\ ice}$, N_2 (µmol L^{-1} ice)	556.15	750.16	356.72	502.57	509.60	238.42	402.63	429.87	463.61
$C_{saturation}$, Ar (µmol L^{-1} ice)	0.65	0.92	1.00	0.58	0.66	1.13	0.95	1.05	1.27
$C_{saturation}$, O_2 (µmol L^{-1} ice)	13.29	18.97	20.50	11.94	13.66	23.21	19.45	21.64	26.13
$C_{saturation}$, N_2 (µmol L^{-1} ice)	23.43	33.48	36.18	20.89	24.00	40.92	34.44	38.21	46.22
C_B, Ar (µmol L^{-1} ice)	7.42	10.74	5.10	5.88	9.40	2.82	5.22	7.08	5.88
C_B, O_2 (µmol L^{-1} ice)	172.05	256.32	117.96	145.04	223.26	81.27	137.95	170.89	149.21
C_B, N_2 (µmol L^{-1} ice)	532.72	716.68	320.54	481.69	485.60	197.51	368.19	391.66	417.39
f_B, Ar (%)	91.97	92.07	83.61	90.99	93.38	71.33	84.61	87.04	82.20
f_B, O_2 (%)	92.83	93.11	85.19	92.39	94.23	77.78	87.64	88.76	85.10
f_B, N_2 (%)	95.79	95.54	89.86	95.84	95.28	82.83	91.45	91.11	90.03
B, Ar (L gas L^{-1} ice)	0.0002	0.0002	0.0001	0.0001	0.0002	0.0001	0.0001	0.0002	0.0001
B, O_2 (L gas L^{-1} ice)	0.0038	0.0057	0.0026	0.0032	0.0049	0.0018	0.0031	0.0038	0.0033
B, N_2 (L gas L^{-1} ice)	0.0118	0.0159	0.0071	0.0107	0.0108	0.0044	0.0082	0.0087	0.0092
V_a (%)	1.6	2.22	0.98	1.40	1.59	0.62	1.13	1.26	1.27
Total Porosity (air+brine) (%)	5.78	8.15	7.43	5.45	6.07	7.98	7.06	8.01	9.32

[a]The reported values are sea ice temperature (T), relative brine volume (V_b), bulk ice gas concentration ($C_{bulk\ ice}$), saturation concentration in brine multiplied by the relative brine volume ($C_{saturation}$), gas concentration in bubbles (C_B), the fraction of gas content in bubble (f_B), the bubble volume (B), and relative air volume or air porosity (V_a).

IV-5 Discussion

IV.5.1 Gas profiles

All sampling dates showed a peak of gas content between 25 and 35 cm depth, which decreased over time. As the fjord is periodically influenced by riverine input (Mortensen et al., 2011) this layer could be formed during periods with freshwater flowing under the growing ice. This would create fresher less permeable ice layers and at the same time increase the total gas content due to the higher gas content in freshwater relative to seawater (Figure IV-3a and Figure IV-5).

Gas profiles in sea ice result from both physical and/or biological processes. Ar is an inert gas and therefore is not involved in biogeochemical processes, and so it can be used as a tracer of physical processes involved in gas concentration and transport within sea ice (Zhou et al., 2013). In contrast, O_2 and N_2 are biogenic gases and their dynamics involve both physical and biogeochemical processes. In seawater, the Ar:O_2 ratio is commonly used to infer the physical processes contributing to oxygen supersaturation, and to quantify the net biological oxygen production (e.g; Cassar et al., 2009; Castro-Morales et al., 2013). However, the strong correlation (r^2>0.89, P≤0.01) between Ar and both O_2 and N_2 in this study (Figure IV-6), suggests that physical transport processes mainly controlled the gas compositions within the sea ice, biological processes only having a minor effect. These observations are in agreement with the abiotic laboratory sea ice experiment described by Tison et al. (2002). In addition, Søgaard et al. (2013) have shown that the total dissolved inorganic carbon within the ice cover in the same area resulted

mainly of physical exports via brine convection and of the precipitation/dissolution of calcium carbonate rather than of biological processes.

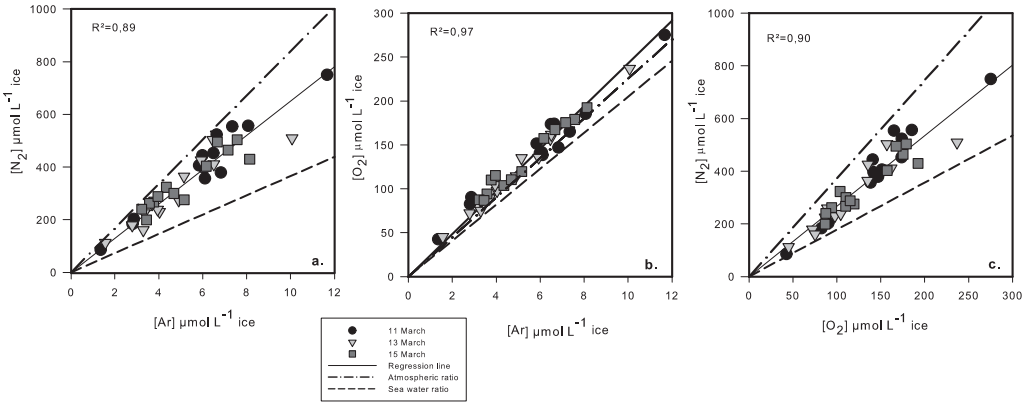

Figure IV-6: Relationship between Ar, O_2 and N_2 in the sea ice samples. The solid line is the regression line. The solid line represents the seawater ratios (N_2:Ar, O_2:Ar, N_2: O_2) while the dashed line represents the atmospheric ratios (N_2:Ar, O_2:Ar, N_2: O_2).

The relative proportion of Ar, O_2 and N_2 in bulk sea ice in this study are intermediate between the relative gas composition in dissolved seawater and the atmospheric gas composition (Table IV-1 and Figure IV-6). These results are in agreement with the past studies of Matsuo and Miyake (1966) and Tison et al. (2002) and reflect the mixed contribution of the dissolved and gaseous fractions of each gas, with the dominance of the gaseous (bubble) fraction (as also shown by the regression line in Figure IV-6 being closer to the atmospheric ratio and the f_B values in Table IV-3). Each gas species in the bottom ice layers was close to, or below, atmospheric saturation (Figure IV-5), confirming the results of Zhou et al. (2013) that the gas incorporation at the ice-seawater interface occurs close to the atmospheric solubility value.

The ice was enriched in N_2 (i.e. highest saturation factor) compared to O_2 and Ar (Table IV-2). The gas composition is a function of a chemical separation of gases diffusing across the boundary layer at the ice-seawater interface during the ice growth (Carte, 1961; Killawee et al., 1998; Loose et al., 2009, 2011). Because the N_2 diffusion coefficient is lower than the O_2 and Ar diffusion coefficients, the flux of N_2 from sea ice to the water is slower and, hence, the incorporation rate of N_2 is larger than O_2 and Ar, leading to N_2 enrichment within sea ice.

Moreover, solubility of N_2 is only half the solubility of O_2 if nucleation process occurs at the ice-seawater interface. This results in relatively more N_2 in the gas phase as compared with the other gases. The growing ice will therefore be enriched in nitrogen bubbles that would otherwise have diffused as a solute towards the water reservoir.

IV.5.2 Air porosity, and bubble formation from brine supersaturation

The estimated air porosity (V_a) was 1 to 2.2% of the ice volume (Table IV-3). These estimates are in the lower end of the estimates (1 to 5%) based on Cox and Weeks (1983), but are close to the range (1.3 to 1.9%) reported by Loose et al. (2011). Figure IV-4b shows that the total gas content in sea ice is linearly related to bubble volume (R^2=0.37; P≤0.01, Figure IV-4b). We used this relationship to infer that at V_a=0 (i.e. no bubbles are present), the total gas content (which must be contained exclusively in the brine) would be approximately 5.6 ml kg^{-1}. This implies that gas comes out of solution to form bubbles when the gas concentration in the brine exceeded this value. The average air solubility of the brine medium was

2.06 ml kg^{-1}±0.91 so nucleation within the sea ice system appeared at saturation factor between 1.9 and 4.9. These results are comparable to the findings of Killawee et al. (1998) in fresh water, who observed bubble nucleation when saturation was between 2.2 and 2.5 times atmospheric saturation at the ice-seawater interface. Note that the relatively low R^2 of the relationship between gas porosity and total gas content (Figure IV-4b) is not surprising given the potential bias affecting both methods: First, total gas content and C_B (which is used to reconstruct the air porosity (V_a) were measured on two different cores; and secondly the C_B estimate is calculated from equation IV-1, in which $C_{saturation}$ is derived from a brine volume fraction estimate that does not take into account the air content (i.e. it is a simplification of the Cox and Weeks (1983) formulation).

IV.5.3 A first assessment of gas transport coefficients in sea ice at constant brine volume

For each gas, we observed a decreasing peak with time at 27.5 cm below the ice surface (Figure IV-5). This gradual decrease of the gas concentration suggests that there was a gas movement within the sea ice. The gases species displaced symmetrically from the highest concentration situated at 27.5 cm below the ice surface to lower concentration. Given the fact that the ice was not affected by brine convection mechanisms (see section IV- 4.1 Physical ice properties, Figure IV-3d.), the mode of transportation was either through molecular diffusion in the brine (aqueous diffusion), or bubble buoyancy. A particular characteristic of the diffusive process is that it implies a mass transport, without involving bulk motion. Following Fick's laws, the diffusion transport is proportional to the anti-gradient of

the local concentrations as the fluxes go from a region of higher concentration to a region of lower concentration. The Fick's second law of diffusion describes the change of concentration with time as:

$$\frac{\partial C_{bulk\ ice}}{\partial t} = D\left(\frac{\partial^2 C_{bulk\ ice}}{\partial z^2} + \frac{1}{A}\frac{\partial A}{\partial z}\frac{\partial C_{bulk\ ice}}{\partial z}\right) \text{(Eq.- IV-6)}$$

Where $C_{bulk\ ice}$ is the bulk ice concentration in μmol L^{-1} (= nmol cm^{-3}), t is the time in s, D is the diffusion coefficient expressed in $cm^2\ s^{-1}$, z is the length in cm, and A is the cross-sectional area over which diffusion is occurring in cm².

The diffusion of gas within sea ice is thought to occur through the network of brine. Assuming the brine network can be described as a tube perpendicular to the ice cover (i.e z direction) of section area, A., the geometry of the problem is similar to decay of a pulse (Cussler, 2009, p34). In the decay of pulse model, the diffusion occurs away from a sharp pulse of solute (i.e the gas peak at 27.5 cm below the ice surface). The initially steep concentration gradient weakens gradually by diffusion in the z direction (i.e the brine channel perpendicular to the ice cover) into the smooth curves (Figure IV-7).

For this first estimate of D-values, we assumed that diffusion occurs in a one-dimensional medium of infinite length where the cross-sectional area is considered as constant. This cross sectional area is the brine network and since the V_b only varied between 2 and 3% during the sampling period we can assume, it was constant. Hence, the third term of the second Fick's law, $\left(\frac{1}{A}\frac{\partial A}{\partial z}\frac{\partial C_{bulk\ ice}}{\partial z}\right)$ (Eq. IV-6) is zero.

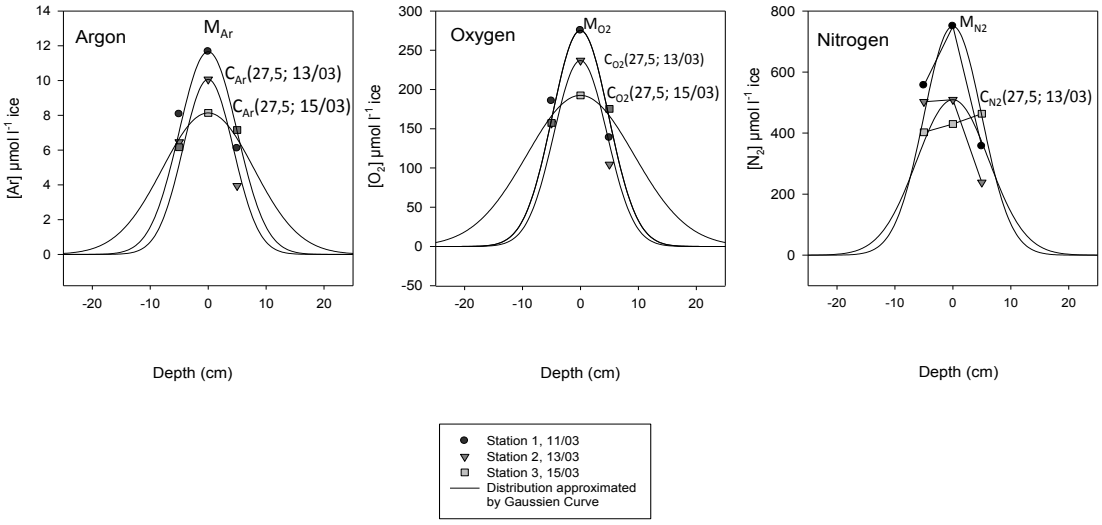

Figure IV-7: Best-fit curves of the gas peak situated at 27.5 cm below the ice surface. For each species the concentration distribution is approximated by a Gaussian curve fit with 3 parameters.

We approximated the vertical gas concentrations around the peak as a normal distribution (Figure IV-7) by applying a curve fit procedure that assumes that the concentrated solute was originally located at z = 0 (i.e. 27.5 cm below the ice surface), and diffused as per the Gaussian profile where the mathematical solution for the decay of pulse is given by:

$$\overline{C} = \frac{M/A}{\sqrt{4\pi Dt}} e^{-z^2/4Dt} \qquad \text{(Eq.- IV-7)}$$

where M is the total solute introduced in the system, A is the cross sectional area in cm, Z is the length of the system over which the solute diffuses in cm, D is the diffusion coefficient expressed in $cm^2\ s^{-1}$ and t is the time expressed in s. The boundary conditions for this equation are as follows: (1) far from the pulse, the solute concentration is zero: $t > 0$; $z = \infty$; $C = 0$; (2) because diffusion occurs at the same speed in both directions (constant section), the pulse is symmetric; (3) all of

the solute is initially located at z = 0. At position z=0, the evolution of the peak concentration over time is given by:

$$C(0,t)= \frac{M}{\sqrt{4\pi Dt}}\times dz \qquad \text{(Eq.- IV-8)}$$

Where dz is the length of the section on which the gas concentration is measured, 5 cm. C(0,t) is the gas concentration successively measured on March 13 and on March 15, 27.5 cm below the ice surface (Z=0), (27.5, 13/03), C (27.5, 15/03), respectively). M is the total quantity introduced in the system, calculated from the maximum concentration observed on March 11, 27.5 cm below the ice surface (Table IV-4). From equation IV-8, we can then compute values of D for each gas species as:

$$D = \frac{\left(\frac{M}{C(0,t)}\times dz\right)^2}{4\pi t} \qquad \text{(Eq.- IV-9)}$$

In this first approach, computed D_{Ar} ranged from 1.54 to 1.76 × 10^{-5} cm^2 s^{-1} (±17%), D_{O2} from 1.54 to 1.77 × 10^{-5} cm^2 s^{-1} (±11%), and D_{N2} equal to 2.49 × 10^{-5} cm^2 s^{-1} (±8%) (Table IV-4). We computed D_{N2} only for the first period because, the peak decreased faster and asymmetrically, suggesting that other processes are involved.

Table IV-4: Diffusivity coefficients deduced from equations IV-8 and IV-9 and comparison reference values in the literature.

	Data		
Gas peak 27.5 (cm) Z=0	11 March M	13 March C (0, 13/03)	15 March C (0,15/03)
[Ar] µmol L^{-1} ice	11.66	10.7	8.13
[O_2] µmol L^{-1} ice	275.3	236.9	192.5
[N_2] µmol L^{-1} ice	750.1	509.6	429.8
	Results		
Diffusion in sea ice	D_{Ar} $10^{-5}cm^2s^{-1}$	$D_{O2}10^{-5}cm^2s^{-1}$	D_{N2} $10^{-5}cm^2s^{-1}$
Kapisillit (-3.5 >T (°C)<-2; 5,4%<V_b<8.05%)	1.54-1,76 (± 17%)	1.55-1.74 (± 9%)	2.49 (± 11%)
	References		
Diffusion in water	D_{Ar} $10^{-5}cm^2s^{-1}$	$D_{O2}10^{-5}cm^2s^{-1}$	D_{N2} $10^{-5}cm^2s^{-1}$
Broecker and Peng (1974) (T=0 °C)	0.88	1.17	0.95
Stauffer et al. (1985) (T=0 °C)	n/a	2.08	1.61
Wise and Houghton (1966) (T=10 °C)	1.7	1.7	1.8
Diffusion in sea ice	D_{SF6} $10^{-5}cm^2s^{-1-}$	D_{O2} $10^{-5}cm^2s^{-1}$	D_{CO2} $10^{-5}cm^2s^{-1}$
Gosink et al. (1976) (-15>T (°C)< -7)	0.9	n/a	40
Loose et al. (2011) (-4 <T (°C)< -12, 6%<V_b <8%)	13 (±40%)	3.9 (±41%)	n/a
Diffusion in gas phase (Cusller, 3 ed , 2009)		10^{-1} cm^2s^{-1}	

IV.5.4 Gas diffusion pathways and bubble buoyancy

As described above, there are two mechanisms for gas transport in sea ice in the absence of brine convection: (1) the dissolved gas can diffuse in the brine solution following the concentration gradient, or (2) the bubbles can move upward

along the grain boundaries and in the brine network under buoyancy (Loose et al., 2011; Zhou et al., 2013). If bubbles are mobile, we expect (1) a faster net gas transport (i.e. higher calculated diffusivities) and (2) a preferential apparent diffusion in the positive (upward) direction. Our computed transport coefficients are of the same magnitude as the aqueous molecular diffusion values (1 to 2×10^{-5} $cm^2\ s^{-1}$) at similar temperatures (Table IV-4). This suggests that the gas species primarily diffused through the brine channels in the dissolved phase. However, according to equations IV-1 and IV-3 more than 70% of the gas species were residing in bubbles (as a maximum estimate). The observed symmetrical distribution of the gas around the peak through time also suggests that the bubbles remained immobile. An explanation for this observation is that the permeability of the bulk ice was too low to allow for differential bubble movement under buoyancy. Zhou et al. (2013) have recently demonstrated that brine volumes higher than 7% are necessary for bubble differential movement in the brine network, as a result of tortuosity. Figure IV-3c shows that this condition was not fulfilled above 50 cm depth (the area of interest), at least for the 11 and 13 March measurements. The observed increase in brine volume fraction between 13 and 15 March is consistent with higher calculated diffusivities (some bubbles might actually have escaped and accumulated within the less permeable top 5 cm (Figure IV-3c and Figure IV-5).

Overall, our estimates of the gas retained in bubbles as a proportion of bulk ice gas concentrations, and the estimated air porosities are probably overestimates. According to Light et al. (2003), bubble nucleation is not only a function of the saturation level of the solution but also of the size of the brine channel. Thus, a

minimum brine channel size may be required to form a stable bubble (Light et al., 2003). The achieve a stable bubble, the bubble radii should be large enough so that the surface tension stay inferiror at the internal tension of the brine (Light et al., 2003). On the other hand, the majority of bubbles observed by Light et al. (2003) were found enclosed in brine inclusions, and none were observed isolated in the ice matrix. Although the gases we measured, were primarily in the bubble phase, this does not exclude aqueous diffusion through the brine medium. If the bubbles are contained within the brine inclusions, the gas trapped in the bubbles may be exchanged with the surrounding brine and diffuse into the aqueous phase through the brine network. A possible connection, and exchange, between air and liquid porosities has also been suggested by Loose et al. (2011).

The diffusivity of Ar and O_2 showed similar transport coefficients, and the same trend over time. The values are also similar to those of Wise and Houghton (1966) in water at 10 ℃ (salinity not specified), 1.7×10^{-5} cm^2 s^{-1}. However, the calculated D_{O2} values are about 2 times lower than those reported (3.9×10^{-5} cm^2 s^{-1} ±41%) by Loose et al. (2011) for sea ice with similar porosities. Sea ice is a particularly heterogeneous environment, and the geometry and tortuosity of the channels would be expected to have a substantial influence on gas migration, especially in the form of bubble buoyancy. This is supported by the slight increase of D over time, which may be related to the increasing brine volume allowing easier diffusion and/or easier bubbles buoyancy. Therefore, it is not surprising that our values differ from those of Loose et al. (2011). It also suggests that it may be

desirable to establish a relationship between porosity and molecular diffusion, but the available data do not cover a wide enough range of values to make this feasible.

As mentioned previously, the calculated value of D_{N2} was higher than D_{O2} and D_{Ar}. However, according to Broecker and Peng (1974) and Stauffer et al. (1985), D_{N2} would be expected to be lower than D_{O2}. Moreover, the peak decreased less symmetrically. Loose et al. (2011), suggest a multiphase-diffusion where transport of a part of the gas occur by liquid diffusion and another part by gas diffusion, or by bubble buoyancy. This may accelerate the depletion of the gas fraction because the bubble buoyancy is much faster than aqueous diffusion. Based on the solubility coefficient (i.e. Bunsen, β), the gas species with the lowest solubility will be enriched in the gas phase; which is referred to as "solubility partitioning" (Loose et al., 2011). O_2 is twice as soluble in water compared with N_2, and so the ability of N_2 to partition more easily into the gas phase may imply a faster transport pathway and hence higher "apparent" diffusivities with an asymmetric evolution of the gas peak. Note that this solubility partitioning could also be involved in the chemical separation in the boundary layer during the ice growth. Thus, the supersaturation level to initiate the nucleation process would be reached earlier for N_2. The growing ice would be enriched in nitrogen bubbles that would otherwise have diffused as a solute towards the water reservoir. It is, however, not clear yet how such boundary layer processes are compatible with the mushy layer approach for sea ice growth.

IV-6 Conclusions

Our study investigated the transport of gas in natural sea ice in the absence of brine convection. The low average bulk ice salinity (3.2) induced a stratified brine network, which prevented convective exchanges trough brine transport between the ice, water, and atmosphere. Hence, the transport of gas species was mainly diffusive or buoyant. We used the temporal evolution of gas distribution in sea ice to compute the bulk ice transport coefficients for Ar, N_2 and O_2 as conservative dissolved gas tracers of mass transport.

Based on the total gas content (i.e. included dissolved and gaseous gas species), the bulk ice concentration of Ar, O_2 and N_2, and the air porosity, we conclude that gas species are preferentially located in bubbles. The gas incorporation at the ice-seawater occurred close to the atmospheric solubility value, and the air porosity was close to zero in the bottom of the ice, hence, the nucleation process occurred mainly in the brine. Bubble nucleation requires supersaturation of dissolved gas in the brine, and in this study the nucleation process was observed once the concentration exceeded 2.7 times the atmospheric saturation. This level of supersaturation is in agreement with previous work on bubble nucleation in sea ice (e.g. Killawee et al., 1998).

In this study, the effective gas diffusion rates across sea ice ranged from 1.54 to 1.76 $\times 10^{-5}$ cm^2 s^{-1} (±17%) for Ar, from 1.54 to 1.77 $\times 10^{-5}$ cm^2 s^{-1} (±11%) for O_2, and was 2.49 $\times 10^{-5}$ cm^2 s^{-1} (±8%) for N_2. We computed this transport rate over a narrow range of total porosity, 4 to 8%. It was therefore not possible to ascertain a relationship between porosity and the diffusion coefficient, however,

these data provides some estimation of the magnitude of diffusive processes for ice layers close to the permeability limit of 5%.

Although most gases were located in bubbles, the effective diffusivities for Ar, O_2, and N_2 were similar to the solute diffusion rate in water ($\approx 10^{-5}$ cm^2 s^{-1}). The preference for gases to exist in bubbles does not exclude an aqueous diffusion through the brine medium. The majority of bubbles observed by Light et al. (2003) were trapped inside brine inclusions and none were found isolated in the ice matrix. We hypothesize that the nucleation process occurs in the brine network and that the gas contained in bubbles can be exchanged with the brine and diffuse into the aqueous phase. This work therefore extends to natural sea ice, the hypothesis that there is a connection and exchange between air porosity and liquid porosity as previously suggested by Loose et al. (2011). Finally, the preferential partitioning of N_2 into gas phase could result in a greater apparent diffusion rate in comparison to O_2 and Ar, as well as a larger rate of incorporation at the ice-seawater interface during the initial freezing process.

References

Broecker, W. S., and Peng, T. H.: Gas exchange rates between air and sea1, Tellus, 26, 21-35, 1974.

Carte, A. E.: Air bubbles in ice, Proceedings of the Physical Society, 77, 757-768, 1961.

Cassar, N., Barnett, B. A., Bender, M. L., Kaiser, J., Hamme, R. C., and Tilbrook, B.: Continuous High-Frequency Dissolved O_2/Ar Measurements by Equilibrator Inlet Mass Spectrometry, Analytical Chemistry, 81, 1855-1864, 10.1021/ac802300u, 2009.

Castro-Morales, K., Cassar, N., Shoosmith, D. R., and Kaiser, J.: Biological production in the Bellingshausen Sea from oxygen-to-argon ratios and oxygen triple isotopes, Biogeosciences, 10, 2273-2291, 2013.

Crabeck, O., Delille, B., Thomas, D., Geilfus, N. X., Rysgaard, S., and Tison, J. L.: CO_2 and CH_4 in sea ice from a subarctic fjord under influence of riverine input, Biogeosciences, 11, 6525-6538, 10.5194/bg-11-6525-2014, 2014.

Cussler, E. L.: Diffusion: mass transfer in fluid systems, Cambridge university press, 2009.

Eicken, H., Lange, M. A., and Dieckmann, G. S.: Spatial variability of sea ice properties in the Northwestern Weddell Sea, Journal of Geophysical Research-Oceans, 96, 10603-10615, 1991.

Else, B. G. T., Papakyriakou, T., Galley, R., Drennan, W. M., Miller, L. A., and Thomas, H.: Wintertime CO_2 fluxes in an Arctic polynya using eddy covariance: Evidence for enhanced air-gas transfer during ice formation, Journal of Geophysical Research, 116, 2011.

Garcia, H. E., and Gordon, L. I.: Oxygen solubility in seawater: Better fitting equations, Limnology and oceanography, 37, 1307-1312, 1992.

Geilfus, N. X., Carnat, G., Papakyriakou, T., Tison, J. L., Else, B., Thomas, H., Shadwick, E., and Delille, B.: Dynamics of $pCO(_2)$ and related air-ice CO_2 fluxes in the Arctic coastal zone (Amundsen Gulf, Beaufort Sea), Journal of Geophysical Research-Oceans, 117, 10.1029/2011JC007118, 2012.

Geilfus, N. X., Carnat, G., Dieckmann, G. S., Halden, N., Nehrke, G., Papakyriakou, T., Tison, J. L., and Delille, B.: First estimates of the contribution of $CaCO_3$ precipitation to the release of CO_2 to the atmosphere during young sea ice growth, Journal of Geophysical Research, 118, 10.1029/2012JC007980, 2013.

Golden, K. M., Ackley, S. F., and Lytle, V. I.: The percolation phase transition in sea ice, Science, 282, 2238-2241, 1998.

Golden, K. M., Eicken, H., Heaton, A. L., Miner, J., Pringle, D. J., and Zhu, J.: Thermal evolution of permeability and microstructure in sea ice, Geophysical Research Letters, 34, 2007.

Gosink, T. A., Pearson, J. G., and Kelly, J. J.: Gas movement through sea ice, Nature, 263, 41 - 42, 1976.

Hamme, R. C., and Emerson, S. R.: The solubility of neon, nitrogen and argon in distilled water and seawater, Deep-Sea Research Part I: Oceanographic Research Papers, 51, 1517-1528, 10.1016/j.dsr.2004.06.009, 2004.

Heinesch, B., Yernaux, M., Aubinet, M., Geilfus, N. X., Papakyriakou, T., Carnat, G., Eicken, H., Tison, J. L., and Delille, B.: Measuring air-ice CO_2 fluxes in the Arctic, FluxLetter, The Newsletter of FLUXNET, 2, 9-10, 2009.

Kaartokallio, H., Søgaard, D., Norman, L., Rysgaard, S., Tison, J.-L., Delille, B., and Thomas, D.: Short-term variability in bacterial abundance, cell properties, and incorporation of leucine and thymidine in subarctic sea ice, Aquatic microbial ecology, 71, 57-73, 2013.

Killawee, J. A., Fairchild, I. J., Tison, J. L., Janssens, L., and Lorrain, R.: Segregation of solutes and gases in experimental freezing of dilute solutions: Implications for natural glacial systems, Geochimica Et Cosmochimica Acta, 62, 3637-3655, 1998.

Langway, C.: Ice fabrics and the universal stage. US Snow, Ice and Permafrost Research Establishment, Technical report 62, 1958.

Leppäranta, M., and Manninen, T.: The brine and gas content of sea ice with attention to low salinities and high temperatures, Helsinki, 1988.

Light, B.: Effects of temperature on the microstructure of first-year Arctic sea ice, Journal of Geophysical Research, 108, 1-16, 10.1029/2001JC000887, 2003.

Long, M. H., Koopmans, D., Berg, P., Rysgaard, S., Glud, R. N., and Sogaard, D. H.: Oxygen exchange and ice melt measured at the ice-water interface by eddy correlation, Biogeosciences, 9, 1-11, 10.5194/bg-9-1-2012, 2012.

Loose, B., McGillis, W. R., Schlosser, P., Perovich, D., and Takahashi, T.: Effects of freezing, growth, and ice cover on gas transport processes in laboratory seawater experiments, Geophysical Research Letters, 36, L05603, L0560310.1029/2008gl036318, 2009.

Loose, B., Schlosser, P., Perovich, D., Ringelberg, D., Ho, D. T., Takahashi, T., Richter-Menge, J., Reynolds, C. M., McGillis, W. R., and Tison, J. L.: Gas diffusion through columnar laboratory sea ice: implications for mixed-layer ventilation of CO_2 in the seasonal ice zone, Tellus Series B-Chemical and Physical Meteorology, 63, 23-39, 10.1111/j.1600-0889.2010.00506.x, 2011.

Lubetkin, S.: Why is it much easier to nucleate gas bubbles than theory predicts?, Langmuir, 19, 2575-2587, 2003.

Matsuo, S., and Miyake, Y.: Gas composition in ice samples from Antarctica, Journal of Geophysical Research, 71, 5235-5241, 1966.

Miller, L. A., Papakyriakou, T., Collins, R. E., Deming, J., Ehn, J., Macdonald, R. W., Mucci, A., Owens, O., Raudsepp, M., and Sutherland, N.: Carbon Dynamics in Sea Ice: A Winter Flux Time Series, Journal of Geophysical Research-Oceans, 116, 10.1029/2009JC006058, 2011.

Nomura, D., Yoshikawa-Inoue, H., and Toyota, T.: The effect of sea-ice growth on air-sea CO2 flux in a tank experiment, Tellus, Series B: Chemical and Physical Meteorology, 58, 418-426, 10.1111/j.1600-0889.2006.00204.x, 2006.

Nomura, D., Yoshikawa-Inoue, H., Toyota, T., and Shirasawa, K.: Effects of snow, snow-melting and re-freezing processes on air-sea ice CO_2 flux, Journal of Glaciology, 56, 262-270, 2010.

Notz, D., and Grae Worster, M.: In situ measurements of the evolution of young sea ice, Journal of Geophysical Research: Oceans, 113, 10.1029/2007JC004333, 2008.

Papadimitriou, S., Kennedy, H., Norman, L., Kennedy, D. P., Dieckmann, G. S., and Thomas, D. N.: The effect of biological activity, $CaCO_3$ mineral dynamics, and CO_2 degassing in the inorganic carbon cycle in sea ice and late winter-early spring in the Weddell Sea, Antarctica, Journal of Geophysical Research, 117, 10.1029/2012JC008058, 2012.

Papakyriakou, T., and Miller, L.: Springtime CO_2 exchange over seasonal sea ice in the Canadian Arctic Archipelago, Annals of Glaciology, 52, 10.3189/172756411795931534, 2011.

Raynaud, D., Delmas, R., Ascencio, M., and Legrand, M.: Gas extraction from polar ice cores: a critical issue for studying the evolution of atmospheric CO_2 and ice-sheet surface elevation, Annals of Glaciology, 3, 265-268, 1982.

Rysgaard, S., and Glud, R. N.: Anaerobic N_2 production in Arctic sea ice, Limnology and Oceanography, 49, 86-94, 2004.

Rysgaard, S., Glud, R. N., Sejr, M. K., Bendtsen, J., and Christensen, P. B.: Inorganic carbon transport during sea ice growth and decay: A carbon pump in polar seas, Journal of Geophysical Research-Oceans, 112, 10.1029/2006JC003572, 2007.

Shaw, M. D., Carpenter, L. J., Baeza-Romero, M. T., and Jackson, A. V.: Thermal evolution of diffusive transport of atmospheric halocarbons through artificial sea-ice, Atmospheric Environment, 45, 6393-6402, 10.1016/j.atmosenv.2011.08.023, 2011.

Skoog, D. A., West, D. M., Holler, F. J.: Chimie analytique, De Boeck Univ., Paris,2015.

Søgaard, D. H., Thomas, D. N., Rysgaard, S., Norman, L., Kaartokallio, H., Juul-Pedersen, T., Glud, R. N., and Geilfus, N. X.: The relative contributions of biological and abiotic processes to the carbon dynamics in subarctic sea ice, Polar Biology, DOI 10.1007/s00300-013-1396-3, 2013.

Sørensen, L. L., Jensen, B., Glud, R. N., McGinnis, D. F., Sejr, M. K., Sievers, J., Søgaard, D. H., Tison, J. L., and Rysgaard, S.: Parameterization of atmosphere–surface exchange of CO2 over sea ice, The Cryosphere, 8, 853-866, 10.5194/tc-8-853-2014, 2014.

Stefels, J., Carnat, G., Dacey, J. W., Goossens, T., Elzenga, J. T. M., and Tison, J.-L.: The analysis of dimethylsulfide and dimethylsulfoniopropionate in sea ice: Dry-crushing and melting using stable isotope additions, Marine chemistry, 128, 34-43, 2012.

Tison, J.-L., Haas, C., Gowing, M. M., Sleewaegen, S., and Bernard, A.: Tank study of physico-chemical controls on gas content and composition during growth of young sea ice, Journal of Glaciology, 48, 177-191, 10.3189/172756502781831377, 2002.

Tison, J. L., Worby, A., Delille, B., Brabant, F., Papadimitriou, S., Thomas, D., de Jong, J., Lannuzel, D., and Haas, C.: Temporal evolution of decaying summer first-year sea ice in the Western Weddell Sea, Antarctica, Deep-Sea Research Part Ii-Topical Studies in Oceanography, 55, 975-987, 10.1016/j.dsr2.2007.12.021, 2008.

Tsurikov, V. L.: The formation and composition of the gas content of sea ice, Journal of Glaciology, 22, 67 - 81, 1979.

UNESCO: Eight report of the joint panel on oceanographic tables and standards, Technical papers in Marine Science, 28, 1978.

Vancoppenolle, M., Goosse, H., De Montety, A., Fichefet, T., Tremblay, B., and Tison, J. L.: Modeling brine and nutrient dynamics in Antarctic sea ice: The case of dissolved silica, Journal of Geophysical Research: Oceans, 115, 2010.

Wise, D. L., and Houghton, G.: The diffusion coefficients of ten slightly soluble gases in water at 10–60 C, Chemical Engineering Science, 21, 999-1010, 1966.

Zemmelink, H. J., Delille, B., Tison, J. L., Hintsa, E. J., Houghton, L., and Dacey, J. W. H.: CO2 deposition over the multi-year ice of the western Weddell Sea, Geophysical Research Letters, 33, 2006.

Zhou, J. Y., Delille, B., Eicken, H., Vancoppenolle, M., Brabant, F., Carnat, G., Geilfus, N. X., Papakyriakou, T., Heinesch, B., and Tison, J. L.: Physical and biogeochemical properties in landfast sea ice (Barrow, Alaska): Insights on brine and gas dynamics across seasons, Journal of Geophysical Research-Oceans, 118, 3172-3189, 10.1002/jgrc.20232, 2013.

Chapter-V-CO_2 and CH_4 in sea ice from a subarctic fjord under influence of riverine input.

A peer-reviewed scientific research paper published in October 2014 in Journal of Biogeosciences, 11, 6525-6538, doi:10.5194/bg-11-6525-2014.

Odile Crabeck[1], Bruno Delille[2], David Thomas[3,4], Nicolas-Xavier Geilfus[6], Soren Rysgaard[1, 5,6], Jean-Louis Tison[7].

1. Center for Earth Observation Science, Department of Geological Science, University of Manitoba, Winnipeg, Canada
2. Unité d'Océanographie Chimique, Université de Liège, Liège, Belgium
3. School of Ocean Sciences, Bangor University, Menai Bridge, Anglesey, U.K.
4. Marine Research Centre, Finnish Environment Institute, Helsinki, Finland.
5. Greenland Climate Research Centre, c/o Greenland Institute of Natural Resources, Nuuk, Greenland
6. Arctic Research Centre, Aarhus University, Aarhus, Denmark
7. Laboratoire de Glaciologie, D.S.T.E., Université Libre de Bruxelles, Bruxelles, Belgium

To achieve consistency trough this document, terminology and symbolic might differ from the published version.

I did all the analysis and leaded the manuscript (writing, discussion and figures). My co-authors reviewed and helped thoroughly with the edition. Jean-Louis, Bruno, Thomas and Soren provided comments and several detailed reviews of the discussion.

Abstract

We present the CH_4 concentration [CH_4], the partial pressure of CO_2 (pCO_2) and total gas content in bulk sea ice from subarctic, landfast sea ice in the Kapisillit fjord, Greenland. Fjord systems are characterized by freshwater runoff and riverine input and based on $\delta^{18}O$ data, we show that >30 % of the surface water originated from periodic river input during ice growth. This resulted in fresher sea ice layers with higher gas content than is typical from marine sea ice. The bulk ice [CH_4] ranged from 1.8 to 12.1 nmol L^{-1}, which corresponds to a partial pressure ranging from 3 to 28 ppmv. This is markedly higher than the average atmospheric methane content of 1.9 ppmv. Evidently most of the trapped methane within the ice was contained inside bubbles, and only a minor portion was dissolved in the brine. The bulk ice pCO_2 ranged from 60 to 330 ppmv indicating that sea ice at temperatures above -4°C is undersaturated compared to the atmosphere (390 ppmv). This study adds to the few existing studies of CH_4 and CO_2 in sea ice, and we conclude that subarctic sea ice can be a sink for atmospheric CO_2, while being a net source of CH_4.

V-1 Introduction

The main driver of climate warming is the accumulation of greenhouse gases such as CO_2, CH_4 and N_2O within the atmosphere. Among these, CO_2 is the most important in terms of radiative forcing followed by methane (Ramaswamy et al., 2001). The concentrations of these gases in the atmosphere are 390 ppmv and 1.9 ppmv, respectively (2013 levels - http://www.esrl.noaa.gov/gmd/aggi/). Sea ice was for long considered as an inert barrier for gas exchange between the atmosphere and the ocean (Tison et al., 2002), but there is growing evidence to suggest that in fact sea ice might significantly contribute to the fluxes of climatically active biogases (CO_2, CH_4) between the ocean and the atmosphere (Semiletov et al., 2004; Zemmelink et al., 2006; Delille et al., 2007; Geilfus et al., 2012a, 2013a; Nomura et al., 2013). However, the regional and global-scale impacts of sea ice on such gas exchanges are still unknown (Parmentier et al., 2013).

While the Arctic Ocean acts as pump for the atmospheric CO_2 (Bates and Mathis, 2009; Takahashi et al., 2009), recent studies show that the Arctic Ocean is a net source of atmospheric methane (Parmentier et al., 2013). Indeed, recent airborne measurements in the central Arctic basin have shown substantial methane emissions around 2 mg m^{-2} d^{-1} in areas of open leads and fractional ice cover (Parmentier et al., 2013). Moreover, Damm et al. (2005, 2007, 2010) and Kort et al. (2012) reported methane supersaturation in Arctic surface water and point to sediments as being the main source. Several studies have suggested that methane accumulates in Arctic water underlying sea ice, where it can be subsequently

oxidized (Kvenvolden et al., 1993; Savvivech et al., 2004; Kitidis et al., 2010; Shakhova et al., 2010). While methane oxidation is one of the known sinks for methane, the future retreat of the Arctic sea ice cover could limit the residence time of methane in the water column and the subsequent rates of methane oxidation. Parmentier et al. (2013) report a positive correlation between sea ice cover extent and methane emissions confirming a relationship between reduced sea ice extent and a potential impact on gas exchange around the Arctic Ocean. However, to our knowledge, few studies have focused directly on CH_4 within sea ice itself (Zhou et al., 2014). Sea ice is an effective barrier to turbulent diffusion and ebullition flux across the sea-air interface, but since it is one of the largest biomes in the Arctic, it is a massive system for CH_4 storage and its transformation through biogeochemical processes.

Climatological reconstructions of air-sea CO_2 fluxes show that the polar oceans act as significant atmospheric CO_2 sinks, although the complexity and coverage of sea ice are still poorly represented (Takahashi et al., 2009). Studies by Delille et al. (2007) and Geilfus et al. (2012a) provide evidence that during spring and summer, CO_2 concentrations in sea ice brine reach minimum levels due to the combined effects of brine dilution, calcium carbonate dissolution and algal photosynthesis. Hence, sea ice acts as a carbon pump during spring and summer. In contrast, during ice formation there are indications that sea ice acts as a CO_2 source as a consequence of the concentration of solutes in brine, $CaCO_3$ precipitation and microbial respiration (Nomura et al., 2006; Tison et al., 2008; Geilfus et al., 2013b).

In this study we had three main objectives: (1) To document and discuss the interaction between landfast sea ice, riverine input and gas dynamics; (2) To quantify CH_4 concentrations in bulk sea ice and to gain key information on the effect of sea ice cover on methane emissions in ice-covered seas; (3) To increase our understanding of the pCO_2 dynamics in sea ice, by taking measurements of the spatial and temporal distributions of pCO_2 in the surface ice. Combined these are all highly pertinent for evaluating the role of coastal Arctic sea ice in the carbon cycle (Parmentier et al., 2013).

V-2 Field work

V.2.1 Study site

The sampling was conducted from 10 March to 16 March 2010 on first-year landfast sea ice in Kapisillit, in the vicinity of Nuuk, SW Greenland (64°26´N 50°13´W) (Figure V-1). The water depth at the location was between 40 and 45 m, and the average salinity of the seawater in the fjord during this period was 32.9. The air temperatures ranged from -8.8 °C to +2.9 °C, with an average temperature of -3.2 °C. The survey took place before the onset of the algae bloom and the concentration of chlorophyll-a in the bottom 12 cm of ice was 2.8 ± 0.4 μg L^{-1} (SE, n = 3), and the average concentration across the entire ice thickness was 1.0 ± 1.2 μg L^{-1} (SE, n=3) (Long et al., 2012; Søgaard et al., 2013).

V.2.2 Field sampling

To follow the temporal evolution of the sea ice, we sampled the sea ice and water column at the same station on 4 separate occasions: 11 March, 13 March, 15

March and 16 March. Sampling was conducted within an area of about 25 m^2 in order to minimize bias from spatial heterogeneity. For each station, 5 ice cores were extracted using a Kovacs drill corer with internal diameter of 9 cm (Kovacs Ent., Lebanon, USA). Cores were immediately wrapped in polyethylene bags and stored on the sampling site in a well-insulated box with cooling bags (pre-cooled to -20 °C) which ensured brine and gas immobilization and inhibited biological processes (Eicken et al., 1991). Back in the laboratory, the ice cores were stored in a cold room at -25 °C before further gas extraction and analyses.

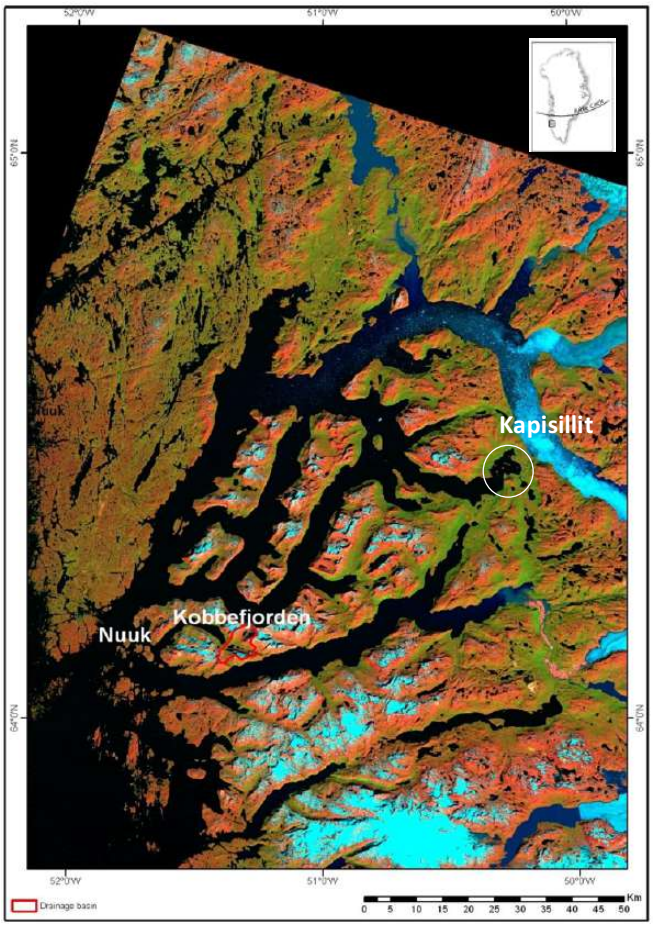

Figure V-1: Study site –Landfast sea ice in Godthåbsfjord, SW Greenland. Circle includes the Bay with the study site and the settlement Kapisillit.

Bulk ice temperature profiles were measured *in situ*, directly after the ice core extraction, at a depth resolution of 5 cm using a calibrated probe (Testo 720, Hampshire, UK) inserted into pre-drilled holes perpendicular to the ice core depth axis. These holes had the same diameter as the probe. The precision of the probe was ± 0.1 °C. This 'temperature' ice core was immediately cut into 5 cm ssections. Each section is then kept in individual polyethylene pots and left to melt at 4°C. Bulk ice salinity (S_i) was measured on each section with a conductivity meter (Orion Star Series Meter WP-84TP, Beverly, USA) which had a precision of ±0.1 for salinity.

Brine was sampled using the sackhole sampling technique at 20 cm and 40 cm below the ice surface (Gleitz et al., 1995). All sackholes were overlaid by a plastic lid to avoid snow and ice shavings falling into the pit (Thomas et al., 2010). Under-ice seawater samples were collected through the ice core hole, at 0, 1 and 9 m depth. Both brine and seawater were collected with a peristaltic pump (Cole Palmer, Masterflex® - Environmental Sampler). Samples for dissolved methane were stored in 60 ml vials poisoned with 60 µl of saturated mercury chloride ($HgCl_2$).

V-3 Methods

V.3.1 Ice texture

To describe the texture of the ice, horizontal thin sections were produced for each 10 cm section of the entire ice column, using the standard microtone (Leica SM2400) procedure described by Langway (1958) and Tison et al. (2008). The

images from horizontal thin sections were recorded with a camera (Nikon Coolpix S200) between crossed polarizers.

V.3.2 Water stable isotope ($\delta^{18}O$)

The stable oxygen isotope ratios ($\delta^{18}O$) were measured in melted ice core sections, and in discrete under-ice water and brine samples. Samples for oxygen isotope composition were transferred into glass vials, filled completely and tightly capped with poly-seal closures. Analysis was performed on a Picarro Isotopic Water Analyzer, L2120-*I* (Picarro, Sunnyvale, USA) equipped with a PAL auto sampler (Leap Technologies, Carrboro, USA). Details of the method can be found in Versteegh et al. (2012). Results are expressed in standard $\delta^{18}O$ notation using the V-SMOW standard as a reference. Agreement between triple consecutive injections of the same sample was usually within ±0.1‰.

V.3.3 Brine volume fraction and Rayleigh number

The brine volume, (b), was computed using the state equations of Cox and Weeks (1983) and of Leppäranta and Manninen (1988) for bulk ice temperature < -2 °C and ≥ -2 °C, respectively, neglecting the air volume fraction (air porosity). Brine salinity (S_{br}) was drivated from bulk ice temperature measurments and the freezing point of seawater (Unesco, 1978). The brine volume fraction (V_b) was calculated as b/bulk sea ice volume (%).

The Rayleigh number is a parameter that determines the onset of convection (i.e. gravity drainage) and it provides information about the vertical stability within the brine inclusions. The Rayleigh number, Ra, following the definition of Notz and Worster (2008), for a given ice depth z, was estimated using:

$$Ra_L = \frac{g \Delta h_{br,z\text{-}sw} \rho_w \beta_w \ \Delta S_{br,z\text{-}sw} \ \Pi(\phi_v)}{K_i \eta} \quad \text{(Eq. V-1)}$$

Where g is the gravitational acceleration g=9.81 m s^{-2}, h is the ice thickness (m); ΔS_{br-sw} represents the salinity difference between the brine salinity determined by surface temperature and the seawater salinity at the ice-seawater interface; ρ_w and β_w are the density of pure water and the haline expansion coefficient of seawater, both taken at 0 °C from Fofonoff (1985). $\Pi(\overline{\phi_v})$ is the effective ice permeability (m^2) computed using the formula of Freitag (1999) as a function of the average solid volume in the ice cover. μ = 1.79x 10^{-3} (kg m^{-1} s^{-1}) is the dynamic viscosity of seawater at 0°C. Ki is the thermal diffusivity ($m^2 s^{-1}$) (Notz and Worster, 2008).

V.3.4 Total gas content

The total volume of gas within sea ice (content in mL STP of gas per kg of ice) was measured - at a resolution of 5 cm - using the wet extraction method (Raynaud et al., 1988): Ice samples were placed in a glass container and then subjected to vacuum at a pressure of 10^{-2} torr. The ice was melted and then slowly refrozen at the bottom of the container using a -70°C cold ethanol bath. This technique of melting and refreezing releases both the dissolved gas in the brine and the gas content from the bubbles in the headspace. After the refreezing, the container was connected to a Toepler pump for extraction (Raynaud et al., 1988).

V.3.5 CH_4 content

The methane from bulk sea ice ($[CH_4]_{bulk\ ice}$) was extracted (at 5 cm resolution) using the wet extraction method (Raynaud et al., 1988). After refreezing, the headspace of the container contained both gas from the bubbles and the dissolved gas from the brine. The container was then connected to a gas chromatograph (Trace GC), which had a flame ionisation detector (FID) and was equipped with a micro packed Shincarbon ST column (Skoog et al., 1997).

Concentrations of CH_4 from the seawater, $[CH_4]_{sw}$, and brine, $[CH_4]_{br}$, were determined by the technique described by Abril and Iversen (2002): A headspace of 30 ml of N_2 was created in the samples that was vigorously shaken and left overnight to ensure equilibration between meltwater sample and the headspace before injecting into a gas chromatograph, SRI 8610C, equipped with a FID. CH_4:N_2 mixtures (Air Liquide) of 1, 10 and 30 ppmv CH_4 were used as standards. The dissolved CH_4 concentrations were calculated using the solubility coefficient given by Yamamoto et al. (1976).

V.3.6 Bulk ice pCO_2 determination

The bulk ice pCO_2 was analyzed using a modification of the technique described by Geilfus et al. (2012b). The method is based on the equilibration of a sea ice samples with a mixture of N_2 and CO_2 of known concentration (standard gas) at the *in situ* temperature and subsequently rapidly extract the gases into a GC under vacuum. The ice sample is cut to fit tightly into the container, minimizing the headspace volume whilst ensuring a constant headspace volume. The headspace of

the pre-vacuumed container holding the ice sample is filled with the standard gas is injected at atmospheric pressure (1013 μatm). The container containing the ice and the standard gas is placed in a thermostatic bath to bring the ice sample back to the *in situ* temperature. After 24 h, the sample is assumed to have retrieved the *in situ* physical (brine volume fraction) and chemical conditions and have equilibrated with the standard gas. The air phase is then injected into an evacuated line linked to a gas chromatograph (Varian 3300, Palo Alto, California, USA). The pressure difference between the vacuum line and the container forces all of the remaining CO_2 (i.e. CO_2 not yet in equilibrium with the standard gas) to be rapidly extracted from the brine into the GC line. According to Geilfus et al. (2012b), this protocol is only valid for ice samples that were permeable at the *in situ* temperature. We used a 550 ppmv CO_2 standard for the equilibration process.

V.3.7 Seawater pCO_2

The *in situ* pCO_2 of brine and of seawater from underneath the ice was measured with a custom-build equilibration equipment (Delille et al., 2007). The instrument includes a membrane contractor equilibrator (Membrana, Liqui-cell), which connects to a non-dispersive infrared gas analyzer (IRGA, Li-Cor 6262, Nebraska, USA) via a closed air loop (Geilfus et al., 2012a, Geilfus et al., 2014). Brine and air flow through the equilibrator and IRGA at rate of 2 L min^{-1} and 3 L min^{-1}, respectively. The *in situ* temperature as well as the temperature at the outlet of the equilibrator were continuously recorded by a Li-Cor temperature sensor (Geilfus et al., 2012a). A temperature correction for pCO_2 was applied assuming

that the relation of Copin-Montégut (1988) is valid at low temperature and high salinity. Each device was locked in an insulated container with a 12 V power source to maintain the internal temperature above 0°C (Geilfus et al., 2012a).

V-4 Results

V.4.1 Water column

Although the average fjord water salinity was 32.9, it dropped to below 20 at the ice-seawater interface (Figure V-2b, lower part). The $\delta^{18}O$ dropped from –0.957 ‰ at 1.09 m depth to -7.32 ‰ at the ice-seawater interface (Figure V-2c, lower part).

V.4.2 Sea Ice

The sea ice thickness ranged from 62 cm to 66 cm. Except for a thin layer of granular ice at the top of the ice, the ice exclusively consisted of columnar ice indicating that ice growth occurred through quiet congelation of seawater at the ice–seawater interface (Eicken, 2003). We repeatedly observed tilted columnar ice crystal between 24 cm and 32 cm suggesting that there had been a current at the ice-seawater interface during ice growth (Figure V-3).

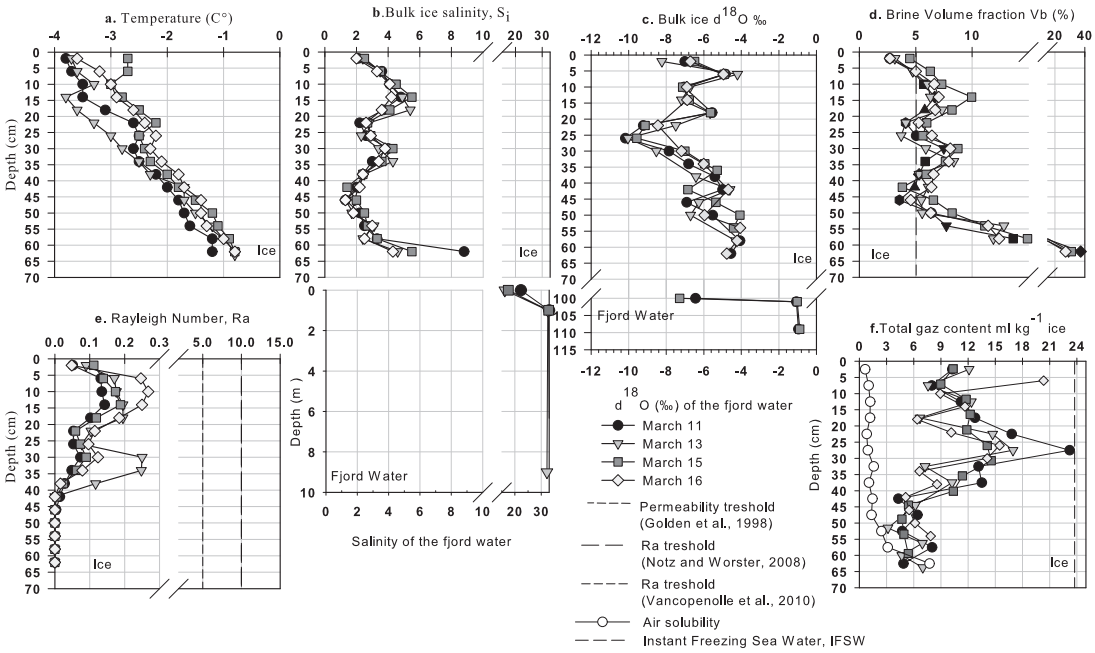

Figure V-2: Panel (a) shows bulk ice temperature,(b) bulk ice salinity, (S_i) and underneath water salinity,(c) bulk ice $\delta^{18}O$ content and $\delta^{18}O$ of the underneath water, (d) brine volume fraction (V_b), the dashed line is a reference value for the permeability threshold following Golden et al. (1998), (e) Rayleigh number, Ra, the solid and dotted lines are a reference value for the convection threshold according to Notz and Worster (2008) and Vancoppenolle et al. (2010), respectively, (f) the total gas content in the ice cover; the white circle represent the air solubility at atmospheric saturation within the ice, the latter was obtained by multiplying the calculated solubility in brine by the relative brine volume. The dotted line is a reference value for the total gas content for instant freezing seawater (Cox and Weeks, 1983).

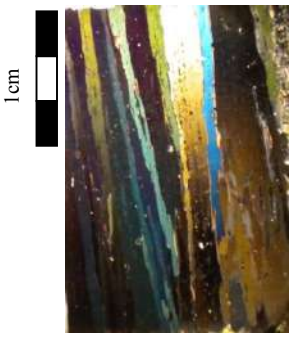

Figure V-3: Tilted columnar ice crystal from March 15 (right) between 24 cm and 32 cm below the sea ice surface.

The bulk ice temperature ranged from -3.7 °C to -0.8 °C with the lowest values in the upper layers (Figure V-2a). The temperatures on 15 and 16 March were slightly higher than on the 11 and 13 March. The averaged bulk ice salinity was 3.2 (Figure V-2b). Each profile exhibited a salinity profile that shifted from the typical C-shaped profile to a reversed S-shaped due to a drop of the salinity around 25 cm and 15 cm below the surface. The ice porosity profiles (i.e. brine volume fraction) were similar to those for the bulk ice salinity. For each, the brine volume fraction dropped under the permeability threshold of 5 % (Golden et al., 1998, 2007) at 25 cm and at 45 cm (Figure V-2d). During the survey, the brine network was therefore not fully connected preventing the internal fluid transport. The Rayleigh number (Ra), describing the probability that fluid transport occurs by convection within the brine network at a given depth in the sea ice, never exceeded 0.3 and therefore the expected critical convection threshold of 10 following Notz and Worster (2008) or 5 from Vancoppenolle et al. (2010) – (Figure V-2e) was not obtained during our study. During the four days, S_i and V_b did not evolve and no temporal evolution trend was observed.

The $\delta^{18}O$ ice isotopic composition ranged from -4 ‰ to -10 ‰ (Figure V-2c). The observed isotopic distributions displayed (1) depletion in heavy isotope at the same depth as the drop of the bulk ice salinity was observed (≈ 25 cm) and, (2) variation along the ice column greater than the maximum allowed by the fractionation coefficients. According to the literature (e.g. Souchez et al., 1987, 1988; Eicken et al., 1998) the fractionation rate depends on the freezing rate and on the thickness of the boundary layer. The isotopic fractionation coefficients for most

sea ice growth rates vary from 1.5 ‰ and 2.5 ‰, and reach an equilibrium value of 2.7 ‰ for a zero growth rate (Eicken et al., 1998; Eicken et al., 2005). On 11 March, the isotopic composition (18 to 22 cm) dropped from -5.5 ‰ to -9.2 ‰ (Δ=3.7 ‰). On 15 March, the isotopic composition (22 to 26 cm) changed from -5.6‰ to -9.1‰ (Δ=3.6 ‰). The fractionation process within sea ice itself cannot explain these shifts.

V.4.3 Gas content

V.4.3.1 Gas total

All values are below the expected content of Instant Freezing Seawater (IFSW) (Cox and Weeks, 1983) and ranged between 4 and 23.2 mL STP kg^{-1} ice (Figure V-2f). A peak in gas content was observed between 25 cm and 35 cm, where both the bulk ice salinity, and the brine volume fraction were at their lowest and where the ice was depleted in $\delta^{18}O$.

V.4.3.2 CH_4 content

The concentration of dissolved CH_4 in the seawater ranged from 5.7 to 18.4 nmol L^{-1} and the maximum concentrations were measured at the ice-seawater interface (Figure V-4). The bulk ice methane concentration, $[CH_4]_{bulk\ ice}$, ranged from 1.8 to 12.1 nmol L^{-1} (Figure V-4). The methane, as part of total gas volume (i.e. mixing ratio: $[CH_4]_{bulk\ ice}$ divided by the total gas content of the ice), ranged from 3.2 ppmv to 28.7 ppmv during the study, with an average value of 11.8 ppmv.

The dissolved methane measured in the brine liquids, $[CH_4]_{br}$, ranged from 12.0 to 17.0 nmol L^{-1}.

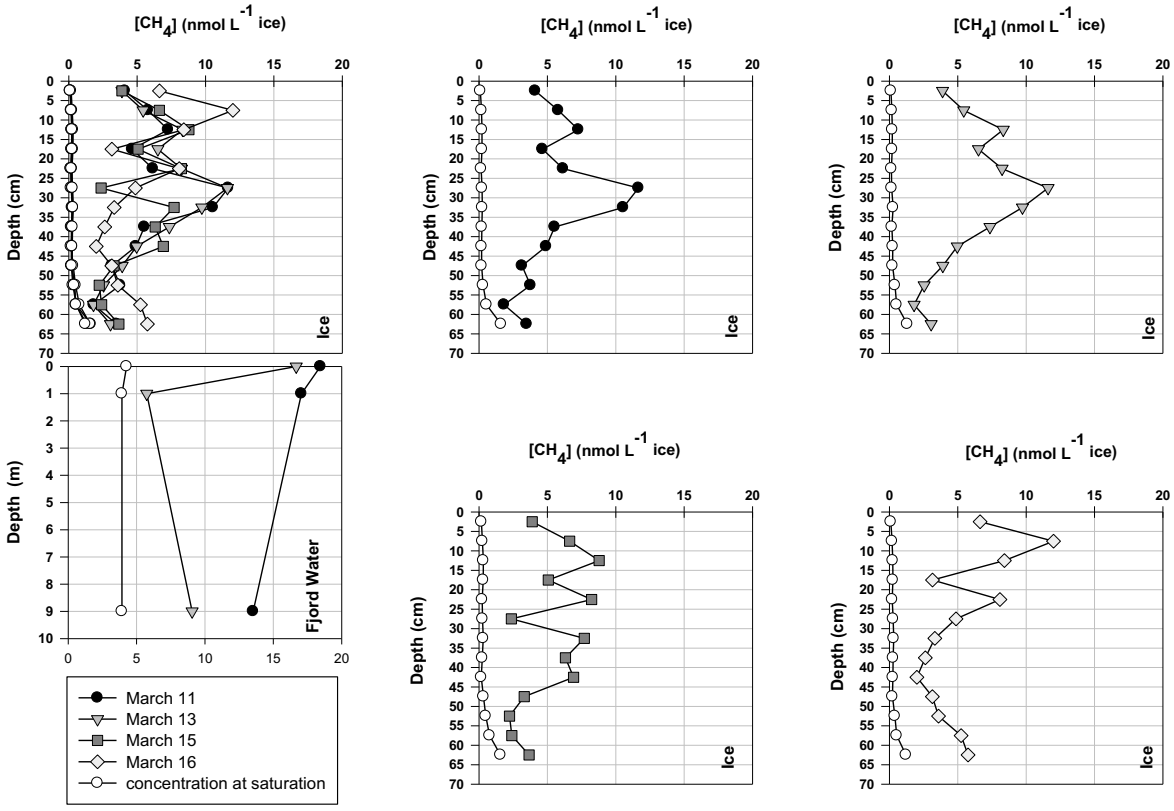

Figure V-4: Evolution of CH_4 concentration ($[CH_4]_{bulk\ ice}$) in bulk sea ice as compared to the solubility concentration at atmospheric saturation (white circle). The latter was obtained by multiplying the calculated solubility in brine by the relative brine volume.

V.4.3.3 Bulk ice pCO_2

The pCO_2 of the underlying seawater (below 0.5 m) was slightly undersaturated compared to the atmosphere (390 ppmv) and very undersaturated (77-130 ppmv) compared to the atmosphere at the ice-seawater interface. For the ice column, the average bulk ice pCO_2 was 194 ppmv. Except on 16 March the bulk

ice pCO_2 increased from a minimum, lower than 185 ppmv, at the bottom of the ice to a maximum, exceeding 330 ppmv, in the top layers of the ice (Figure V-5).

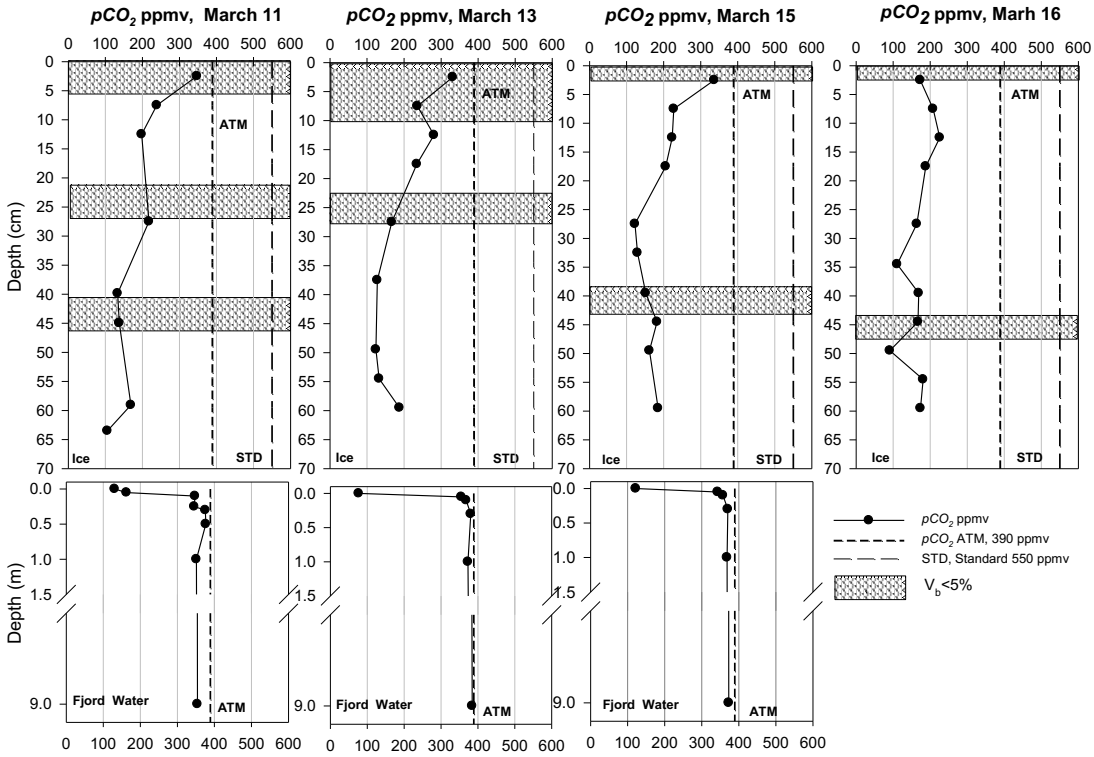

Figure V-5: In the upper part of the figure: high-resolution pCO_2 profiles for each station. The long dashed lines show standard gas concentration used for equilibration (STD, 550 ppmv). The hatched areas show impermeable layer within the ice cover. Ice layers are assumed to be permeable when their brine volume fraction exceeds 5% (Golden et al., 1998). The lower part of the graph shows the pCO_2 of the fjord water. In each graph the short dotted line shows the atmospheric CO_2 concentration.

V-5 Discussion

V.5.1 Riverine input and sea ice fjord system

V.5.1.1 Fresh water input at the ice-seawater interface

A thin surface layer with low salinities (S_{surf} < 20) and strong isotope depletion ($\delta^{18}O_{surf}$ < -8 ‰) characterized the upper part of the water column. The

low salinities and heavy isotope depletion could result from a dilution process, which implies a mixing of the fjord water with a water mass either from melting ice or from the Kapisillit River, or both. Assuming a conservative mixing between the three end members, the fraction of river water and the melting ice in the fjord water surface can be deduced from the following equations:

$$1 = f_{riv} + f_{ice} + f_{fjord} \qquad \text{(Eq.- V-1)}$$

$$S_{surf}=S_{riv}\times f_{riv}+S_i\times f_{ice}+f_{fjord}\times S_{fjord} \qquad \text{(Eq.- V-2)}$$

$$\delta^{18}O_{surf}=f_{riv}\times\delta^{18}O_{riv}+f_{ice}\times\delta^{18}O_{ice}+f_{fjord}\times\delta^{18}O_{fjord} \qquad \text{(Eq.- V-3)}$$

Where f_{riv}, f_{ice} and f_{fjord} are the fraction of river water, melting ice and fjord water present at the surface of the fjord. S_{surf}, S_{fjord}, S_{riv} and S_i are the salinity of the surface water ($S_{surf} < 20$), the fjord water at 9 m depth ($S_{fjord} = 32.9$), the river water (which is assumed to equal 0) and the bottom bulk ice salinity ($4.6<S_i<8.8$). Where $\delta^{18}O_{surf}$, $\delta^{18}O_{riv}$, $\delta^{18}O_{ice}$ and $\delta^{18}O_{fjord}$ are the $\delta^{18}O$ content of the fjord surface layer (-6.44 ‰$< \delta^{18}O_{surf} <$ -7.82 ‰), the river water ($\delta^{18}O_{riv}$ =-14.84 ‰), the bottom of the ice ($\delta^{18}O_{ice}$ = -4,55‰) and the fjord water at 1,09 m depth ($\delta^{18}O_{fjord}$ = -0.957 ‰). Based on the results from these equations the fraction of freshwater during the sampling period varied from 33 % to 50 % and water from the melting ice was less 2%. This is in agreement with the study of Long et al. (2012) from the same area at the same period revealed low rates of ice melt at a maximum of 0.80 mm d^{-1}. As the river was unfrozen below its surface, we suggest that the stratification results of an input of fresh water from the Kapisillit River.

V.5.1.2 Freshwater for earlier ice growth

In the previous section we have shown that freshwater from the Kapisillit River contributed to the low salinities close to the ice-seawater interface. During earlier ice growth, a freshwater input may have produced similar changes of salinity, gas content, and isotope content into the water from which the sea ice had formed. If no change had occurred in the parent water, we would expect that the isotopic composition of sea ice from the under-ice water would monotonically shift towards higher $\delta^{18}O$ values due to isotopic fractionation favouring the incorporation of heavy isotopes into the solid phase (ice) as compared to the liquid phase (Souchez et al., 1988; Eicken et al., 1998). Similarly, due to salt rejection during the freezing process, the salinity of sea ice would be shifted towards lower salinities than the parent seawater. The salt rejection rate as well as the isotopic fractionation depends mostly on the sea ice growth rate (Eicken, 2003). Once sea ice is formed, desalination occurs. The combined effects of salt segregation, brine convection and brine expulsion account for the characteristic "C-shape" of the salinity profile, which evolves into the " I -shape" during the melting period (Eicken, 2003). The $\delta^{18}O$ profiles should, however, still monotonically increase towards the bottom of the ice, since most of the isotopic signal is recorded into the ice crystals themselves.

According to our data, the average bulk ice salinities (S_i) of 3.2, was two times lower than typical values observed in first-year ice (Cox and Weeks, 1988; Eicken, 2003) and close to the bulk ice salinity ($2 < S_i < 4.7$) of sea ice grown under influence of brackish water in the Laptev region of the Arctic Ocean (Eicken et al.,

2005). The low S_i induced a low brine volume fraction (V_b) that exceeded 10 % only in the bottom horizons of the ice and fell below the permeability threshold of 5 % (Golden et al., 1998, 2007) in the first 5 cm, between 20-30 cm, and at 45 cm depth (Figure V-5; dotted area). Thus, the brine network was stratified and not fully interconnected during the sampling period. Our measurements suggest that no fluid transport, by convective processes, could have taken place during the sampling period, since the Rayleigh numbers (Ra) were well below the threshold of 10 (Notz and Worster, 2008), or 5 (Vancoppenolle et al., 2010).

There was a positive correlation between the bulk ice salinity and the isotope content between the 20-30 cm interval (Figure V-6).

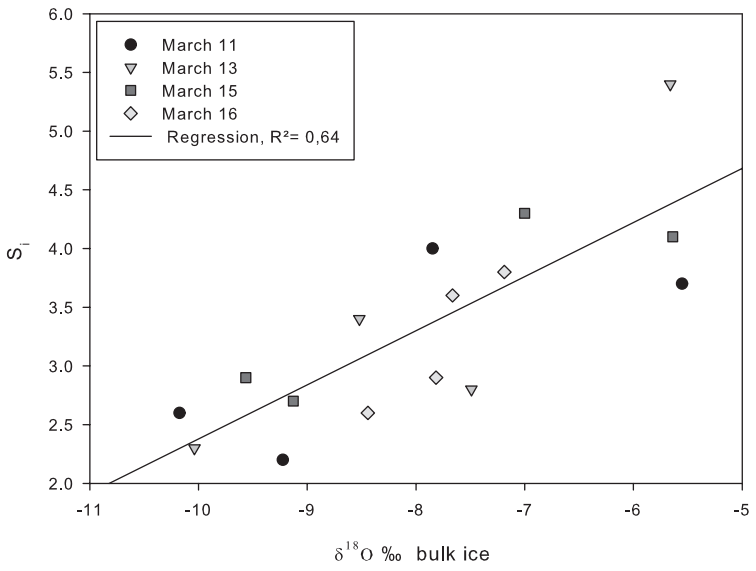

Figure V-6: Relationship between the bulk ice $\delta^{18}O$ content and bulk ice salinity (S_i) from 20 cm to 30 cm below the ice surface.

The isotopic composition measured on bulk sea ice results from a contribution of both brine and pure ice. Since the brine accounts for less than 10%

of the ice volume, the ice isotopic composition measured originates mainly from the pure ice. As no fractionation occurs in the solid phase during melting (Jouzel and Souchez, 1982), the $\delta^{18}O$ content in pure ice should not change over time and should depend only on processes occurring during freezing and on the composition of the underlying seawater (Eicken et al., 1998). On the other hand, the bulk ice salinity originates from the brine medium. Like the ice isotopic content, the bulk ice salinity depends on the ice growth velocities and on the composition of the underlying seawater. But once the ice is formed, desalination occurs. Sea ice loses salt primarily through brine drainage, convective transport, or flushing (Untersteiner, 1968). Since the bulk ice salinity is still correlated with the ice isotopic signal (Figure V-6; $R^2=0.64$, $p<0.001$), it appears that no major desalination process has been active within the ice cover. Therefore, this ice should hold the original characteristics inherited from the parent water during the freezing process.

S-shaped profiles in the ice isotopic distribution and bulk ice salinity are uncommon and cannot be explained by the freezing or by desalination processes. Since the ice was sampled before the beginning of surface melt, and as there are no indications of either convective processes, meltwater penetration or superimposed-layers in the sampled ice volume, it suggests that both the anomalies in the ice salinity profiles, and the heavy isotopic depletion in the ice, are mainly due to changes of water mass. We also note that the repeatedly oriented columnar ice crystal observed between 24 cm and 32 cm (Figure V-3) suggest the presence of a current at the ice-seawater interface.

The bulk ice salinity and the ice isotope distribution can be used as proxy to track the salinity and the isotopic composition of the parent water, and deduce indirectly the proportion of river water. Thus, we may infer the ratio of river water contained in the sea ice volume from isotope mass balance using the equation developed by Eicken et al. (2005):

$$f_{riv}=\frac{\left[\delta^{18}O_{ice}-\varepsilon-\delta^{18}O_{fjord}\right]}{\left[\delta^{18}O_{riv}-\delta^{18}O_{fjord}\right]} \qquad \text{(Eq.- V-4)}$$

Where $\delta^{18}O_{ice}$, $\delta^{18}O_{fjord}$, $\delta^{18}O_{riv}$ are the isotopic composition of the ice, fjord water at 1.09 m depth, and river water, respectively. ε is the sea ice fractionation coefficient ranging between 1.5 ‰ and 2.7 ‰ (Eicken et al., 1998, Eicken et al., 2005). Since $\delta^{18}O_{fjord}$ and $\delta^{18}O_{riv}$ are constant over winter (November to April) (Fitzner et al., 2013), we can derive the temporal changes in surface water composition, namely the fraction of river water f_{riv} and the salinity of the surface parent water mass S_p (Eicken et al., 2005). According to Eicken et al. (2005), S_p is given as:

$$S_p = (1-f_{riv})\times S_{fjord} \qquad \text{(Eq.- V-5)}$$

The maximum f_{riv} deduced from the ice isotopic mass balance occurs when the sea ice reached a thickness of between 20 and 30 cm. The computed salinity shows that at this time S_p had to drop by a factor of 1.7 and could not exceed 18. This shift probably induced the drop in bulk ice salinity in the horizon at 25 cm below the surface.

V.5.1.3 Gas content and freshwater input

The total gas content was always lower than the 23.75 mL STP kg^{-1} value expected in IFSW (Cox and Weeks, 1983). This is in agreement with previous reports that gases in seawater are preferentially expelled from the growing ice, as for other impurities (Cox and Weeks, 1983, 1988; Killawee et al., 1998; Tison et al., 2002; Loose et al., 2009, 2011). The range of total gas content values for all the samples was 4 to 23.2 mL STP kg^{-1}, which is comparable to the range obtained by Matsuo and Miyake (1966) for natural sea ice (2.2 to 21.2 mL STP kg^{-1}) and the range of 3 to18 mL STP kg^{-1} obtained by Tison et al. (2002) for artificial sea ice. In this study there was a peak of gas content between 25 cm and 35 cm associated with the lowest salinities. As demonstrated above, the change of salinity was caused by a change in the parent water due to an input of freshwater. By computing f_{riv} and S_p during the ice growing period, we can further assess the freezing temperature of the parent ice water, following the equation of UNESCO (1978). Based on the salinities and temperatures of the surface water, we can compute the gas content of the surface parent water at each stage of ice growth using the solubility law given by Garcia and Gordon (1992) for O_2, and Hamme and Emerson (2004) for N_2 and Ar. When the ice reached a thickness of 25 cm, the salinity of the parent water decreased by a factor of 1.7, increasing the gas solubility by a factor 1.05, although the sea ice gas content had been increased by a factor of 2.1. The increasing gas content in the parent water, dictated by the increasing solubility could not fully explain the gas peak in the middle horizons of the ice. Tison et al. (2002) showed

that the initial gas content of sea ice is affected by a current at the ice-seawater interface that was 3 times higher than the gas content of sea ice grown with a stagnant ice-seawater interface. According to Tison et al. (2002), the current zone is characterized by a thinner boundary layer in which both salts and gases are controlled by diffusion. Due to this thin boundary layer, the current zone reaches the critical value necessary for early bubble nucleation. Once started, bubble nucleation ensures that that the gasses that would otherwise have diffused as a solute towards the water will be entrapped as bubbles in the sea ice. Moreover, the total gas content depends on the ice growth velocity; while ice from freshwater grows faster than ice from salty water, more gases were trapped in the sea ice cover. Thus, we propose that the peak in sea ice gas content is a result of the increasing gas content in the parent water and the presence of a current under the sea ice-seawater interface; both caused by a flux of fresh water.

V.5.2 Greenhouse gases in sea ice

V.5.2.1 CH_4

The methane concentration was measured in the water column $[CH_4]_{sw}$, in the ice cover $[CH_4]_{bulk\ ice}$ and in the brine medium $[CH_4]_{br}$. First, we compare $[CH_4]_{sw}$ and $[CH_4]_{bulk\ ice}$ with the methane concentration at saturation; $[CH_4]_{sat\ sw}$ and $[CH_4]_{sat\ bulk\ ice}$. The concentration at saturation is the concentration of methane dissolved in a liquid (i.e. brine or seawater) in equilibrium with the atmospheric partial pressure of methane. The saturation is determined by the solubility, which depends on the temperature and salinity. CH_4 saturation with respect to the

atmosphere at the sea surface was calculated assuming a 2010 atmospheric mixing ratio of 1.9 ppmv, using the CH_4 solubility equation of Wiesenburg and Guinasso (1979) corrected for the *in situ* temperature and salinity. We assumed that the relationships from the reference are valid for the range of temperature and salinity found in the ice (Zhou et al., 2014). The bulk ice saturation $[CH_4]_{sat\ bulk\ ice}$ was obtained by multiplying the calculated solubility in brine (nmol L^{-1} brine) by the relative brine volume (L brine L^{-1} bulk ice). The ratio between the observed $[CH_4]_{bulk\ ice}$ to the $[CH_4]_{sat\ bulk\ ice}$ determines the supersaturation level expressed in

$$\% \left(\frac{[CH_4]_{bulk\ ice}}{[CH_4]_{sat\ ice}} \times 100\right).$$

According to Weisenburg and Guinasso (1979), the methane concentration in equilibrium with the atmospheric pressure for seawater salinities <32.9 and at -1.9°C is 3 to 4 nmol L^{-1}. Thus, the dissolved methane in the surface water was 4.5 times the concentration at saturation (i.e 450 % supersaturated). Such high concentrations, up to 15 nmol L^{-1}, suggest that the top layer of the water column was somehow affected by near-sources (i.e. sediment degassing, riverine input). These measurements are similar to the values (5-55 nmol L^{-1} water) reported by Damm et al. (2007) in Storfjorden (Svalbard Archipelago) and in the fjords of Spitsbergen (Damm et al., 2005). The observed concentrations are, however, lower than the concentration in East Siberian Arctic Shelf (ESAS) measured by Shakhova et al. (2010). Due to the thawing subsea-permafrost, CH_4 – rich bubbles released from the sea floor rise up through the water column. As far as we aware no subsea-thawing permafrost has been reported in Gothabsfjord. Damm et al. (2008) suggest

that methane plumes in the water originate from sediments during winter and from *in situ* production during phytoplankton bloom during the summer. As our studies took place before the algal bloom, one of the main methane sources should be the sediment. The methane released from sediments rises trough the water column by convective processes and accumulates under the ice. However, we have to consider the Kapissillit River that runs through a fen (Jensen and Racsh, 2011) as potential source of dissolved methane at the surface of the water column. The fen in the fjord area is a source of CH_4 due to the permanently wet conditions that promote anaerobic decomposition, by which CH_4 is an end product (Jensen and Racsh, 2011). Like CH_4 maxima in the overlying sea ice also coincide with salinity minima, the Kapisillit River is most likely the major sources of CH_4 into the fjord system.

The range of CH_4 concentrations in the bulk ice (1.8 - 12.1 nmol L^{-1} ice) is in agreement with measurements (15 to 25 nmol L ice) reported by Lorenson and Kvenolden (1993) and Zhou et al. (2014). The deduced mixing ratio ranged between 3 ppmv and 28 ppmv indicating that the methane concentration within the sea ice was consistently higher than that in the atmosphere (1.9 ppmv). The sea ice CH_4 concentrations exceeded atmospheric saturation with saturation state ranging from 1200 % to 70000 % with an average saturation level of 2400 %. Thus, sea ice could plausibly act as a methane source for the atmosphere.

First, we compare $[CH_4]_{\text{bulk ice}}$ with $[Ar]_{\text{bulk ice}}$ (bulk ice Ar, O_2, N_2 were measured by gas chromatography and the profiles are discussed in Crabeck et al. (2014). As the diffusion process controls the gas motion within the sea ice (Crabeck

et al., 2014), Ar can be used as a tracer of physical processes. In marine biology, the O_2:Ar ratio is commonly used to infer the physical processes contributing to oxygen supersaturation, and to quantify the net biological oxygen production (Cassar et al., 2009). Our CH_4 samples were randomly distributed related to the Ar ($R^2 \leq 0.21$, $p<0.01$; Figure V-7).

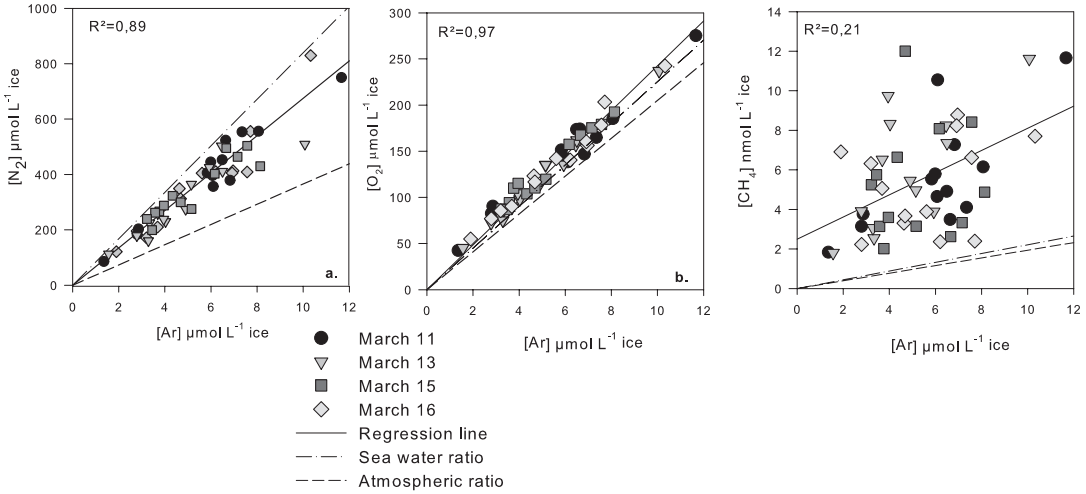

Figure V-7: Relationship between Ar, O_2, N_2 and CH_4 concentration within the sea ice cover. The solid line is the regression line. The slope of the dashed equals to the seawater ratio (N_2:Ar, O_2:Ar, CH_4:Ar) while the slope of dotted-dashed line equals to the atmospheric ratio (N_2:Ar, O_2:Ar, CH_4:Ar).

The CH_4: Ar ratio was systematically higher than the atmospheric and seawater ratios. Hence, CH_4 was preferentially accumulated within the sea ice cover relative to Ar. This could be related to *in situ* biological production, since methane is produced by methanogen bacteria in anoxic conditions. DNA (deoxyribonucleic acid) from methanogen archaea as well as anaerobic pathways have been observed in Arctic sea ice (Rysgaard and Glud, 2004; Collins et al., 2010). However, high-resolution O_2 measurements in the Kapisillit sea ice showed there were no anoxic conditions during the sampling period (Crabeck et al., 2014). Denitrification, which

is an anaerobic process producing more energy per organic carbon unit than methanogenesis was not active within the sea ice due to presence of oxygen. In addition, the ratio $Ar:N_2$, showed no significant deviations to the seawater ratio (Figure V-7). Therefore, we conclude that the methane accumulation was not related to biological *in situ* production. We suggest that the accumulation of methane was due to (1) the initial CH_4 concentration in the seawater and (2) the bubble formation that can act as a methane trap. Assuming a steady rate of incorporation for each gas, the accumulation and supersaturation (up to 450 %) of CH_4 in the surface water leads to a larger incorporation of CH_4 in the ice, and consequently greater CH_4 accumulation relative to Ar. The bulk ice methane concentration ($[CH_4]_{bulk\ ice}$) represents the total methane content within the sea ice as the sum of the dissolved methane in the brine medium ($[CH_4]_{br}$) and the methane trapped in bubbles ($[CH_4]_{bubbles}$) We can deduce the fraction of the methane trapped in bubbles, $f_{[CH4]bubbles}$ using the following relationships:

$$[CH_4]_{bulk\ ice} = [CH_4]_{bubbles} + [CH_4]_{br} \quad \text{(Eq.- V-6)}$$

$$f_{[CH_4]_{bubbles}} = \left(\frac{([CH_4]_{bulk\ ice} - [CH_4]_{br})}{[CH_4]_{bulk\ ice}} \right) \times 100 \quad \text{(Eq.- V-7)}$$

Based on these relationships, the trapped methane bubbles contributed up to 70 % of the sea ice methane content. According to our estimates, methane bubbles were preferentially accumulated in the upper layers of the sea ice. We pinpoint two sources of methane bubbles; (1) the methane bubbles trapped during the freezing process and (2) the *in situ* formation of methane bubbles within the brine medium. During the freezing process, dissolved impurities (ions and gases)

are rejected from the growing ice matrix (Understeiner, 1968; Cox and Weeks, 1983; Killawee et al., 1998) and are accumulated in thin layer at the advancing freezing front. As the partial pressures of gases increases at ice-seawater interface, bubbles can form and be trapped along ice crystal boundaries (Tsurikove,1979; Killawee et al., 1998; Tison et al., 2002, Loose et al., 2010). Taking into account, that the surface water was initially supersaturated with CH_4, the value to trigger the nucleation process, will be reached earlier than for the other gases. Thus, the growing ice was enriched in methane by bubble formation that would otherwise have diffused as a solute towards the water reservoir (Tison et al., 2002).

As the sea ice temperature decreases, brine become further concentrated and supersaturated and gases can nucleate from the solution (Killawee et al., 1998; Tison et al., 2002). As CH_4 has the lowest solubility (Weisemburg and Guinasso, 1979), bubble formation had to be triggered. Once formed, bubbles can physically only move upward due to the buoyancy effect and be released to the atmosphere unless they are blocked by impermeable ice layerst (Zhou et al., 2013, 2014). In contrast the dissolved component in the brine can diffuse to the underlying seawater. Hence, bubble formation leads to an accumulation of CH_4 inside the ice cover. The upward migration of the bubbles could partially explain the preferential bubble accumulation in the top 20 cm of the ice column, a process recently discussed for the Ar in Zhou et al. (2013) and modelled by Moreau et al. (2014).

V.5.2.2 pCO_2

The pCO_2 of the water column was slightly undersaturated (354-384 ppmv) compared to the atmosphere (390 ppmv), whereas at the ice-seawater interface the pCO_2 was largely under saturated (77-130 ppmv). As noted above, the thin surface layer was under the influence of mixing processes, which could produce a reduction of the water pCO_2 at ice-seawater interface. Moreover, the annual monitoring measurements provided by the Nuuk Ecological Research Operations observed year-round pCO_2 undersaturated surface water in the Gothabsfjord system (Rysgaard et al., 2012).

The range of 77-330 ppmv and average of 194 ppmv for the bulk ice pCO_2 is in the same range as the profiles of bulk sea ice pCO_2 measured on natural and experimental sea ice (Geilfus et al., 2012a). According to Geilfus et al., (2012a,b) and Delille et al., (2007) the bulk ice pCO_2 is undersaturated once ice temperature is above -4°C. One of the main factors controlling the inorganic carbon dynamics within sea ice appears to be the temperature. As temperature increases, the subsequent decrease of the salinity promotes the brine dilution and a decrease of the brine pCO_2. According to our data, the bulk ice pCO_2 was inversely correlated to the ice temperature. Indeed, the high values of bulk ice pCO_2 (up 330 ppmv) were associated with the coldest temperature (-3 to - 4 °C) and as the temperature increased with the ice thickness, the bulk ice pCO_2 decreased to ≈ 100 ppmv -190 ppmv and reached the same range of pCO_2 concentration as the underlying seawater, ≈ 76 ppmv-130 ppmv.

Other processes affect the pCO_2 concentrations within sea ice such as the precipitation and dissolution of calcium carbonate (Dieckmann et al., 2008; Geilfus et al., 2012b, 2013a,b; Papadimitriou et al., 2007, 2012; Rysgaard et al., 2007, 2011, 2013). During the sea ice melt the carbonate dissolution promotes lower pCO_2 conditions (Rysgaard et al., 2011). Søgaard et al. (2013) suggested that the main factor controlling the total alkalinity and the dissolved inorganic carbon of the sea ice of Kapisillit was the dissolution of calcium carbonate crystals. Hence, dissolution of calcium carbonates, associated with the high temperature and the subsequent decrease of salinity was likely the reason for the observed low bulk ice pCO_2 during our study also.

Finally, primary production as well bacterial respiration can affect the inorganic carbon dynamics within sea ice (Delille et al., 2007; Rysgaard et al., 2007; Papadimitriou et al., 2012; Kaartokalio et al., 2013; Søgaard et al., 2013). Ice melting through spring and summer will produce both a continuous reduction of the bulk ice pCO_2 and an increase of the ice permeable features leading to pCO_2 undersaturated sea ice relative to the atmosphere and hereby enhance the air-sea flux of CO_2,

V-6 Conclusions

The freshwater runoff from the surrounding land influenced the sea ice during formation, and was evident as a thin freshwater layer at the sea ice-water column interface. This caused deviation from the traditional C-shaped ice salinity profile and depletion in heavy isotope of the sea ice cover. Moreover, the low bulk ice

salinity induced a stratified brine network, which prevented the convective exchange between the ice, the water and the atmosphere. The freshwater, also potentially triggered by higher temperatures and/or storms, caused increased buoyancy and currents velocities at the sea ice-seawater interface, which would have accelerated the nucleation processes in the boundary layer and consequently increased the total gas content of the ice.

The partial pressure of CH_4 exceeded the atmospheric CH_4 content and sea ice could potentially be a source of CH_4 for the atmosphere. During periods of sea ice cover, CH_4 can accumulate within or below the sea ice, and when the ice breaks up and melts during spring and summer, large CH_4 fluxes to the atmosphere could be expected. During sea ice break-up, Gosink and Kelley (1979) and Shakhova et al. (2010) observed an increase CH_4 concentration in the atmosphere above sea ice as well as in surface seawater.

While the CH_4 from the seawater is accumulated within the sea ice cover, the sea ice provides an interface in which the methane could be stored and transformed over time by biogeochemical processes. Further studies based on longer times series and carbon isotope signatures $\delta^{13}CH_4$ will provide us the opportunity to study the potential methane oxidation rate within the sea ice cover. i.e. the sea ice could provide a layer at the ocean surface where CH_4 is degraded and, hence, acts as sink for oceanic CH_4.

We measured an average pCO_2 value of 194 ppmv in bulk sea ice, and so the upper layer of the sea ice cover was greatly undersaturated compared to the atmosphere. It would be expected that the resulting air to sea flux of CO_2 would

increase when sea ice starts to melt. This study adds to the few existing studies of CH_4 and CO_2 in sea ice and we conclude that subarctic sea ice could possibly be a significant sink for atmospheric CO_2, while at the same time being a net source of CH_4.

References

Abril, G. and Iversen, N.: Methane dynamics in a shallow non-tidal estuary (Randers Fjord, Denmark), Marine Ecology Progress Se- ries, 230, 171–181, 10.3354/meps230171, 2002.

Bari, S. A. and Hallet, J.: Nucleation and growth of bubbles at an ice-water interface, J. Glaciol., 13, 489–520, 1974.

Bates, N. R. and Mathis, J. T.: The Arctic Ocean marine carbon cycle: evaluation of air-sea CO2 exchanges, ocean acidification impacts and potential feedbacks, Biogeosciences, 6, 2433–2459, 10.5194/bg-6-2433-2009, 2009.

Collins, R. E., Rocap, G., and Deming, J. W.: Persistence of bac- terial and archaeal communities in sea ice through an Arctic winter, Environ. Microbiol., 12, 1828–1841, 10.1111/j.1462- 2920.2010.02179.x, 2010.

Copin Montégut, C.: A new formula for the effect of temperature on the partial pressure of carbon dioxide in seawater, Mar. Chem., 25, 29–37, 1988.

Cox, G. F. N. and Weeks, W. F.: Equations for determining the gas and brine volumes in sea-ice samples, J. Glaciol., 29, 306–316, 1983.

Cox, G. F. N. and Weeks, W. F.: Numerical simulations of the profile properties of undeformed 1st-year sea ice during the growth season, J. Geophys. Res.-Oceans, 93, 12449–12460, 10.1029/JC093iC10p12449, 1988.

Crabeck, O., Delille, B., Rysgaard, S., Thomas, D. N., Geilfus, N. X., Else, B., and Tison, J. L.: First "in situ" determination of gas transport coefficients (DO_2, DAr, and DN_2) from bulk gas concentration measurements (O_2, N_2, Ar) in natural sea ice, Journal of Geophysical Research: Oceans, 119, 6655-6668, 10.1002/2014JC009849, 2014.

Damm, E., Mackensen, A., Budeus, G., Faber, E., and Hanfland, C.: Pathways of methane in seawater: Plume spreading in an Arctic shelf environment (SW-Spitsbergen), Cont. Shelf Res., 25, 1453–1472, 10.1016/j.csr.2005.03.003, 2005.

Damm, E., Schauer, U., Rudels, B., and Haas, C.: Excess of bottom- released methane in an Arctic shelf sea polynya in winter, Cont. Shelf Res., 27, 1692–1701, 10.1016/j.csr.2007.02.003, 2007.

Damm, E., Kiene, R. P., Schwarz, J., Falck, E., and Dieckmann, G.: Methane cycling in Arctic shelf water and its relationship with phytoplankton biomass and DMSP, Mar. Chem., 109, 45- 59, 10.1016/j.marchem.2007.12.003, 2008.

Damm, E., Helmke, E., Thoms, S., Schauer, U., Nöthig, E., Bakker, K., and Kiene, R. P.: Methane production in aerobic oligotrophic surface water in the central Arctic Ocean, Biogeosciences, 7, 1099–1108, 10.5194/bg-7-1099-2010, 2010.

Delille, B., Jourdain, B., Borges, A. V., Tison, J. L., and Delille, D.: Biogas (CO_2, O_2, dimethylsulfide) dynamics in spring Antarctic fast ice, Limnol. Oceanogr., 52, 1367–1379, 2007.

Dieckmann, G. S., Nehrke, G., Papadimitriou, S., Gottlicher, J., Steininger, R., Kennedy, H., Wolf-Gladrow, D., and Thomas, D. N.: Calcium carbonate as ikaite crystals in Antarctic sea ice, Geo- phys. Res. Lett., 35, L08501, 10.1029/2008GL033540, 2008.

Eicken, H.: From the microscopic to the macroscopic to the regional scale, growth, microstrucutre and properties of sea ice, in: Sea ice – An introduction to its physics, biology, chemistry and geology, edited by: Science, B., London, 22–81, 2003.

Eicken, H., Lange, M. A., and Dieckmann, G. S.: Spatial variability of sea ice properties in the Northwestern Weddell Sea, J. Geo- phys. Res.-Oceans, 96, 10603–10615, 1991.

Eicken, H., Weissenberger, J., Bussmann, I., Freitag, J., Schuster, W., Delgado, F. V., Evers, K. U., Jochmann, P., Krembs, C., Gradinger, R., Lindemann, F., Cottier, F., Hall, R., Wadhams, P., Reisemann, M., Kousa, H., Ikavalko, J., Leonard, G. H., Shen, H., Ackley, S. F., and Smedsrud, L. H.: Ice-tank studies of physical and biological sea-ice processes, in: Ice in Surface Waters, edited by: Shen, H. T., 1, 363–370, 1998.

Eicken, H., Dmitrenko, I., Tyshko, K., Darovskikh, A., Dierk- ing, W., Blahak, U., Groves, J., and Kassens, H.: Zonation of the Laptev Sea landfast ice cover and its importance in a frozen estuary, Global Planet. Change, 48, 55–83, 10.1016/j.gloplacha.2004.12.005, 2005.

Fitzner, A., van As D., Bendtsen, J., Dahl-Jensen, D., Fettweis, X., Mortensen, J., and Rysgaard, S.: Estimating the glacial meltwater contribution to the freshwater budget from salinity and $\delta^{18}O$ measurements in Godthåbsfjord, submitted to JGR, 2014.

Fofonoff, N. P.: Physical-properties of seawater – a new salinity scale and equation of state for seawater, J. Geophys. Res.- Oceans, 90, 3332–3342, 10.1029/JC090iC02p03332, 1985.

Freitag, J.: Untersuchungen zur Hydrologie des arktischen Meereises-Konsequenzen für den kleinskaligen Stofftransport, Ber. Polarforsch./Rep. Pol. Res., 325, 1999.

Garcia, H. E. and Gordon, L. I.: Oxygen solubility in seawater – better fitting equations, Limnol. Oceanogr., 37, 1307–1312, 1992.

Geilfus, N. X., Carnat, G., Papakyriakou, T., Tison, J. L., Else, B., Thomas, H., Shadwick, E., and Delille, B.: Dynamics of pCO_2 and related air-ice CO_2 fluxes in the Arctic coastal zone (Amundsen Gulf, Beaufort Sea), J. Geophys. Res.-Oceans, 117, C00G10, 10.1029/2011jc007118, 2012a.

Geilfus, N. X., Delille, B., Verbeke, V., and Tison, J. L.: Towards a method for high vertical resolution measurements of the partial pressure of CO_2 within bulk sea ice, J. Glaciol., 58, 287–300, 10.3189/2012JoG11J071, 2012b.

Geilfus, N. X., Carnat, G., Dieckmann, G. S., Halden, N., Nehrke, G., Papakyriakou, T., Tison, J. L., and Delille, B.: First estimates of the contribution of $CaCO_3$ precipitation to the release of CO_2 to the atmosphere during young sea ice growth, J. Geophys. Res., 118, 10.1029/2012JC007980, 2013a.

Geilfus, N. X., Galley, R. J., Cooper, M., Halden, N., Hare, A., Wang, F., Søgaard, D. H., and Rysgaard, S.: Gypsum crystals observed in experimental and natural sea ice, Geophys. Res. Lett., 40, 6362–6367, 10.1002/2013GL058479, 2013b.

Gleitz, M., Vonderloeff, M. R., Thomas, D. N., Dieckmann, G. S., and Millero, F. J.: Comparison of summer and winter in- organic carbon, oxygen and nutrient concentrations in Antarctic sea-ice brine, Mar. Chem., 51, 81–91, 10.1016/0304- 4203(95)00053-t, 1995.

Golden, K. M., Ackley, S. F., and Lytle, V. I.: The percolation phase transition in sea ice, Science, 282, 2238–2241, 1998.

Golden, K. M., Eicken, H., Heaton, A. L., Miner, J., Pringle, D. J., and Zhu, J.: Thermal evolution of permeability and microstructure in sea ice, Geophys. Res. Lett., 34, L16501, 10.1029/2007GL030447, 2007.

Gosink, T. A. and Kelley, J. J.: Carbon-monoxide evolution from arctic surfaces during spring thaw, J. Geophys. Res.-Oc. Atm., 84, 7041–7041, 10.1029/JC084iC11p07041, 1979.

Hamme, R. C. and Emerson, S. R.: Measurement of dissolved neon by isotope dilution using a quadrupole mass spectrometer, Mar. Chem., 91, 53–64, 10.1016/j.marchem.2004.05.001, 2004.

Jensen, L. M. and Rasch, M. (Eds.): NERO – Nuuk Ecological Research Operations, 3rd Annual Report 2010, Roskilde, National Environmental Research Institute, Aarhus University, Aarhus, 84 pp., 2011.

Jouzel, J. and Souchez, R. A.: Melting refreezing at the glacier sole and the isotopic composition of the ice, J. Glaciol., 28, 35–42, 1982.

Kaartokallio, H., Sogaard, D. H., Norman, L., Rysgaard, S., Tison, J. L., Delille, B., and Thomas, D. N.: Short-term variability in bacterial abundance, cell properties, and incorporation of leucine and thymidine in subarctic sea ice, Aquat. Microb. Ecol., 71, 57–73, 10.3354/ame01667, 2013.

Killawee, J. A., Fairchild, I. J., Tison, J. L., Janssens, L., and Lorrain, R.: Segregation of solutes and gases in experimental freezing of dilute solutions: Implications for natural glacial systems, Geochim. Cosmochim. Ac., 62, 3637–3655, 1998.

Kitidis, V., Upstill-Goddard, R. C., and Anderson, L. G.: Methane and nitrous oxide in surface water along the North-West Passage, Arctic Ocean, Mar. Chem., 121, 80–86, 10.1016/j.marchem.2010.03.006, 2010.

Kort, E. A., Wofsy, S. C., Daube, B. C., Diao, M., Elkins, J. W., Gao, R. S., Hintsa, E. J., Hurst, D. F., Jimenez, R., Moore, F. L., Spackman, J. R., and Zondlo, M. A.: Atmospheric observations of Arctic Ocean methane emissions up to 82 degrees north, Nat. Geosci., 5, 318–321, 10.1038/ngeo1452, 2012.

Kvenvolden, K. A., Lilley, M. D., Lorenson, T. D., Barnes, P. W., and McLaughlin, E.: The Beaufort Sea continental-shelf as a seasonal source of atmospheric methane, Geophys. Res. Lett., 20, 2459–2462, 10.1029/93gl02727, 1993.

Langway, C. C.: Ice fabrics and the universal stage Rep. 62, U.S. Snow, Ice and 496 Permafrost Research Establishment, Wilmette, Illinois, 1958.

Leppäranta, M. and Manninen, T.: The brine and gas content of sea ice with attention to low salinities and high temperatures, Helsinki,1988.

Long, M. H., Koopmans, D., Berg, P., Rysgaard, S., Glud, R. N., and Søgaard, D. H.: Oxygen exchange and ice melt measured at the ice-water interface by eddy correlation, Biogeosciences, 9, 1957–1967, 10.5194/bg-9-1957-2012, 2012.

Loose, B., McGillis, W. R., Schlosser, P., Perovich, D., and Taka- hashi, T.: Effects of freezing, growth, and ice cover on gas transport processes in laboratory seawater experiments, Geophys. Res. Lett., 36, L05603, 10.1029/2008gl036318, 2009.

Loose, B., Schlosser, P., Perovich, D., Ringelberg, D., Ho, D. T., Takahashi, T., Richter-Menge, J., Reynolds, C. M., McGillis, W. R., and Tison, J. L.: Gas diffusion through columnar laboratory sea ice: implications for mixed-layer ventilation of CO_2 in the seasonal ice zone, Tellus B, 63, 23–39, 10.1111/j.1600- 0889.2010.00506.x, 2011.

Matsuo, S. and Miyake, Y.: Gas composition in ice samples from Antarctica, J. Geophys. Res., 71, 5235–5241, 1966.

Moreau, S., Vancoppenolle, M., Zhou, J. Y., Tison, J. L., Delille, B., and Goosse, H.: Modelling argon dynamics in first-year sea ice, Ocean Modelling, 73, 1–18, 10.1016/j.ocemod.2013.10.004, 2014.

Nomura, D., Yoshikawa-Inoue, H., and Toyota, T.: The effect of sea-ice growth on air-sea CO2 flux in a tank experiment, Tellus B, 58, 418–426, 2006.

Nomura, D., Eicken, H., Gradinger, R., and Shirasawa, K.: Rapid physically driven inversion of the air-sea ice CO2 flux in the seasonal landfast ice off Barrow, Alaska after onset surface melt, Cont. Shelf Res., 30, 1998–2004, 2010.

Nomura, D., Granskog, M. A., Assmy, P., Simizu, D., and Hashida, G.: Arctic and Antarctic sea ice acts as a sink for atmospheric CO_2 during periods of snowmelt and surface flooding, J. Geophys. Res.-Oceans, 118, 6511–6524, 10.1002/2013JC009048, 2013.

Notz, D., and Grae Worster, M.: In situ measurements of the evolution of young sea ice, Journal of Geophysical Research: Oceans, 113, 10.1029/2007JC004333, 2008.

Papadimitriou, S., Thomas, D. N., Kennedy, H., Haas, C., Kuosa, H., Krell, H., and Dieckmann, G. S.: Biogeochemical composition of natural sea ice brines from the Weddell Sea during early austral summer, Limnol. Oceanogr., 52, 1809–1823, 2007.

Papadimitriou, S., Kennedy, H., Norman, L., Kennedy, D. P., Dieck- mann, G. S., and Thomas, D. N.:The effect of biological activity, $CaCO_3$ mineral dynamics, and CO_2 degassing on the inorganic carbon cycle in sea ice during the late winter-early spring in the Weddell Sea, Antarctica, J. Geophys. Res.-Oceans, 117, C08011, 10.1029/2012JC008058, 2012.

Parmentier, F.-J. W., Christensen, T. R., Sørensen, L. L., Rysgaard, S., McGuire, A. D., Miller, P. A., and Walker, D. A.: The impact of lower sea-ice extent on Arctic greenhouse-gas exchange, Nature climate change, 195–202, 10.1038/NCLIMATE1784, 2013.

Ramaswamy, V., Chanin, M. L., Angell, J., Barnett, J., Gaffen, D., Gelman, M., Keckhut, P., Koshelkov, Y., Labitzke, K., Lin, J. J. R., O'Neill, A., Nash, J., Randel, W., Rood, R., Shine, K., Shiotani, M., and Swinbank, R.: Stratospheric temperature trends: Observations and model simulations, Rev. Geophys., 39, 71–122, 10.1029/1999rg000065, 2001.

Raynaud, D., Chappellaz, J., Barnola, J. M., Korotkevich, Y. S., and Lorius, C.: Climatic and CH_4 cycle implications of glacial inter- glacial CH4 change in the vostok ice core, Nature, 333, 655–657, 10.1038/333655a0, 1988.

Rysgaard, S. and Glud, R. N.: Anaerobic N2 production in Arctic sea ice, Limnol. Oceanogr., 49, 86–94, 2004.

Rysgaard, S., Glud, R. N., Sejr, M. K., Bendtsen, J., and Christensen, P. B.: Inorganic carbon transport during sea ice growth and decay: A carbon pump in polar seas, J. Geophys. Res.- Oceans, 112, C03016, 10.1029/2006JC003572, 2007.

Rysgaard, S., Bendtsen, J., Delille, B., Dieckmann, G. S., Glud, R. N., Kennedy, H., Mortensen, J., Papadimitriou, S., Thomas, D. N., and Tison, J. L.: Sea ice contribution to the air-sea CO_2 exchange in the Arctic and Southern Oceans, Tellus B, 63, 823–830, 10.1111/j.1600-0889.2011.00571.x, 2011.

Rysgaard, S., Mortensen, J., Juul-Pedersen, T., Sørensen, L. L., Lennert, K., Søgaard, D. H., Arendt, K. E., Blicher, M. E., Sejr, M. K., and Bendtsen, J.: High air-sea CO_2 uptake rates in nearshore and shelf areas of Southern Greenland: Temporal and spatial variability, Mar. Chem., 128–129, 26–33, 10.1016/j.marchem.2011.11.002, 2012.

Rysgaard, S., Søgaard, D. H., Cooper, M., Puc´ko, M., Lennert, K., Papakyriakou, T. N., Wang, F., Geilfus, N. X., Glud, R. N., Ehn, J., McGinnis, D. F., Attard, K., Sievers, J., Deming, J. W., and Barber, D.: Ikaite crystal distribution in winter sea ice and implications for CO_2 system dynamics, The Cryosphere, 7, 707–718, 10.5194/tc-7-707-2013, 2013.

Savvichev, A. S., Rusanov, I. I., Yusupov, S. K., Pimenov, N. V., Lein, A. Y., and Ivanov, M. V.: The biogeochemical cycle of methane in the coastal zone and littoral of the Kandalaksha Bay of the White Sea, Microbiology, 73, 457–468, 10.1023/B:MICI.0000036992.80509.2a, 2004.

Semiletov, I. P., Makshtas, A., Akasofu, S. I., and Andreas, E. L.: Atmospheric CO2 balance: The role of Arctic sea ice, Geophys. Res. Lett., 31, L05121, 10.1029/2003GL017996, 2004.

Shakhova, N., Semiletov, I., Leifer, I., Salyuk, A., Rekant, P., and Kosmach, D.: Geochemical and geophysical evidence of methane release over the East Siberian Arctic Shelf, J. Geophys. Res.-Oceans, 115, C08007, doi:10.1029/2009jc005602, 2010.

Skoog, D. A., West, D. M., and Holler, F. J.: Chimie Analytique, De Boeck Université, 552 Paris, Bruxelles, 1997.

Sogaard, D. H., Thomas, D. N., Rysgaard, S., Glud, R. N., Norman, L., Kaartokallio, H., Juul-Pedersen, T., and Geilfus, N. X.: The relative contributions of biological and abiotic processes to car- bon dynamics in subarctic sea ice, Polar Biol., 36, 1761–1777, 10.1007/s00300-013-1396-3, 2013.

Souchez, R., Tison, J. L., and Jouzel, J.: Freezing rate determination by the isotopic composition of the ice, Geophys. Res. Lett., 14, 599–602, 10.1029/GL014i006p00599, 1987.

Souchez, R., Tison, J. L., and Jouzel, J.: Deuterium concentration and growth-rate of antarctic 1st-year sea ice, Geophys. Res. Lett., 15, 1385–1388, 10.1029/GL015i012p01385, 1988.

Takahashi, T., Sutherland, S. C., Wanninkhof, R., Sweeney, C., Feely, R. A., Chipman, D. W., Hales, B., Friederich, G., Chavez, F., Sabine, C., Watson, A., Bakker, D. C. E., Schuster, U., Metzl, N., Yoshikawa-Inoue, H., Ishii, M., Midorikawa, T., Nojiri, Y., Kortzinger, A., Steinhoff, T., Hoppema, M., Olafsson, J., Arnarson, T. S., Tilbrook, B., Johannessen, T., Olsen, A., Bellerby, R., Wong, C. S., Delille, B., Bates, N. R., and de Baar, H. J. W.: Climatological mean and decadal change in surface ocean pCO_2, and net sea-air CO_2 flux over the global oceans, Deep-Sea Res. Pt. I, 56, 554–577, 10.1016/j.dsr2.2008.12.009, 2009.

The National Oceanic and Atmospheric Administration (NOAA): available at: http://www.esrl.noaa.gov/gmd/obop/brw/index.html (last acces: July 2013), 2013.

Thomas, D. N., Papadimitriou, S., and Michel, C.: Biogeochemistry of sea ice, in: Sea Ice – second edition, edited by: Thomas, D. N. and Dieckmann, G. S., Wiley-Blackwell, Oxford, 2, 621 pp., 2010.

Tison, J. L., Haas, C., Gowing, M. M., Sleewaegen, S., and Bernard, A.: Tank study of physico-chemical controls on gas content and composition during growth of young sea ice, J. Glaciol., 48, 177–191, 2002.

Tison, J. L., Worby, A., Delille, B., Brabant, F., Papadimitriou, S., Thomas, D., de Jong, J., Lannuzel, D., and Haas, C.: Temporal evolution of decaying summer first-year sea ice in the Western Weddell Sea, Antarctica, Deep-Sea Research Part Ii-Topical Studies in Oceanography, 55, 975–987, 10.1016/j.dsr2.2007.12.021, 2008.

UNESCO: Eight report of the joint panel on oceanographic tables and standards, Technical papers in Marine Science, 28, 1978.

Untersteiner, N.: Natural desalination and equilibrium salinity profile of perennial sea ice, J. Geophys. Res., 73, 1251–1257, 1968.

Vancoppenolle, M., Goosse, H., de Montety, A., Fichefet, T., Tremblay, B., and Tison, J. L.: Modeling brine and nutrient dynamics in Antarctic sea ice: The case of dissolved silica, J. Geophys. Res.-Oceans, 115, C02005, 10.1029/2009jc005369, 2010.

Versteegh, E. A. A., Blicher, M. E., Mortensen, J., Rysgaard, S., Als, T. D., and A. D. Wanamaker Jr.: Oxygen isotope ratios in the shell of *Mytilus edulis*: archives of glacier meltwater in Greenland?, Biogeosciences, 9, 5231–5241, 10.5194/bg-9-5231- 2012, 2012.

Wiesenburg, D. A., and Guinasso Jr., N. L.: Equilibrium solubility of methane, carbon monoxide and hydrogen in water and seawater, J. Chem. Eng. Data, 24, 356–360, 1979.

Yamamoto, S., Alcauskas, J. B., and Crozier, T. E.: Solubility of methane in distilled water and seawater, J. Chem. Eng. Data, 21, 78–80, 10.1021/je60068a029, 1976.

Zemmelink, H. J., Delille, B., Tison, J. L., Hintsa, E. J., Houghton, L., and Dacey, J. W. H.: CO_2 deposition over the multi-year ice of the western Weddell Sea, Geophys. Res. Lett., 33, L13606, 10.1029/2006GL026320, 2006.

Zhou, J. Y., Delille, B., Eicken, H., Vancoppenolle, M., Brabant, F., Carnat, G., Geilfus, N. X., Papakyriakou, T., Heinesch, B., and Tison, J. L.: Physical and biogeochemical properties in land- fast sea ice (Barrow, Alaska): Insights on brine and gas dynam- ics across seasons, J. Geophys. Res.-Oceans, 118, 3172–3189, 10.1002/jgrc.20232, 2013.

Zhou, J., Delille, B., Brabant, F., and Tison, J. L.: Insights into oxygen transport and net community production in sea ice from oxygen, nitrogen and argon concentrations, Biogeosciences, 11, 5007-5020, 10.5194/bg-11-5007-2014, 2014a.

Zhou, J., Tison, J.-L., Carnat, G., Geilfus, N.-X., and Delille, B.: Physical controls on the storage of methane in landfast sea ice, The Cryosphere, 8, 1019–1029, 10.5194/tc-8-1019-2014, 2014b.

Chapter-VI-Imaging air volume fraction in sea ice using non-destructive X-ray tomography

A peer-reviewed scientific research paper published in May 2016 in Cryosphere, 10, 1125–1145, doi:10.5194/tc-10-1125-2016.

Odile Crabeck[1], Ryan Galley[1], Bruno Delille[2], Brent Else[3], Nicolas-Xavier Geilfus[1], Marcos Lemes[1], Mathieu Des Roches[5], Pierre Francus[5], Jean-Louis Tison[6] and Soren Rysgaard[1,4,7]

1. Department of Geological Sciences, Centre for Earth Observation, University of Manitoba, Winnipeg, Manitoba, Canada
2. Unité d'Océanographie Chimique, MARE, Université de Liège, Liège, Belgium
3. Department of Geography, University of Calgary, Calgary, Alberta, Canada
4. Arctic Research Centre, Aarhus University, Aarhus, Denmark
5. Centre Eau terre et Environement, INRS-Été-Quebec, Quebec, Canada
6. Laboratoire de Glaciologie, DSTE, Université Libre de Bruxelles, Bruxelles, Belgium
7. Greenland Climate Research Centre, Greenland Institute of Natural Resources, Nuuk, Greenland

To achieve consistency trough this document, terminology and symbolic might differ from the published version.

I did all the analysis and leaded the manuscript (writing, discussion and figures). Ryan Galley helped thoroughly with the edition and provided advice and recommendation for the figures. Jean-Louis, Bruno and Soren provided comments and several detailed reviews of the discussion.

Abstract

Although the presence of a gas phase in sea ice creates the potential for gas exchange with the atmosphere, the distribution of air bubbles and transport of gases within the sea ice are still poorly understood. Currently no straightforward technique exists to measure the vertical distribution of air volume fraction in sea ice. Here, we present a new fast and non-destructive X-ray computed tomography technique to quantify the air volume fraction and produce separate images of air inclusions in sea ice. The technique was performed on relatively thin (4 – 22 cm) sea ice collected from an experimental ice tank. While most of the internal layers showed air-volume fractions <2%, the ice-atmosphere interface (top 2 cm) systematically showed values up to 5%. We suggest that the air volume fraction is a function of both the bulk ice gas saturation factor and the brine volume. We differentiate micro bubbles ($\emptyset < 1$ mm), large bubbles ($1 < \emptyset < 5$ mm) and macro bubbles ($\emptyset > 5$mm). While micro bubbles were the most abundant type of air bubbles, most of the air porosity observed resulted from the presence of large and macro bubbles. The ice texture (granular and columnar) as well as the permeability state of ice are important factors controlling the air volume fraction. The technique developed is suited for studies related to gas transport and bubble migration.

VI-1 Introduction

Sea ice is a multi-phase system consisting of ice crystals, salt precipitates, brine, and air bubbles (i.e. air inclusions). The abundance and morphology of brine and air inclusions are strongly dependent on the temperature and salinity of the sea ice (Cox and Weeks, 1983; Weeks and Ackley, 1986). Microscale studies of sea ice inclusions have in large part focused on the formation and morphology of brine inclusions (as pockets and/ or channels) (e.g. Bennington, 1967; Cox and Weeks, 1975; Eide and Martin, 1975; Cole and Shapiro, 1998; Eicken et al., 2000; Bock and Eicken, 2005; Notz and Worster, 2008; Hunter et al., 2009; Galley et al., 2015). Inclusions in large part control the transfer of heat, salt, gases, and radiation between the ocean and atmosphere (Light et al., 2003). Brine and air inclusions in sea ice also affect the optical and electromagnetic properties of sea ice, and are often sites of biological activity (Fritsen et al., 1994; Krembs et al., 2000; Vancoppenolle et al., 2013).

Studies on the formation and morphology of air inclusions and gas transport within sea ice are sparse. The air porosity quantitatively defined by the air volume fraction (V_a %) has generally been neglected in past work; it has long been assumed that gas species in sea ice were dissolved in brine and subject to the same processes as brine inclusions, and that the air volume fraction is minor compared to the brine volume fraction. Mushy layer theory, whose equations are now used as the physical basis for liquid exchange processes within sea ice neglect the presence of air inclusions (Worster, 1992; Worster, 1997; Feltham et al., 2006; Rees Jones and Worster, 2013). Omission of air inclusions in sea ice research propagates a lack of

understanding of gas transport within sea ice, though studies in the last decade have revealed substantial CO_2 fluxes at the sea ice-atmosphere interface (Semiletov et al., 2004; Zemmelink et al., 2006; Delille et al., 20014; Nomura et al., 2014; Geilfus et al., 2014, 2015). It was also recently argued that a major part of the natural gases (oxygen, nitrogen and argon) as well as methane (CH_4) reside in the gas phase inside bubbles in sea ice rather than dissolved in the brine (Zhou et al., 2013; Crabeck et al., 2014a,b; Moreau et al., 2014). Therefore, the physical properties and processes of air inclusions in sea ice can potentially control the sea ice–atmosphere exchange of gases. The most important process leading to the formation of air inclusions from entrapped brine is brine volume reduction by freezing (Zhou et al., 2013; Crabeck et al., 2014a; Moreau et al., 2014). Increasing brine salinity during winter due to sea ice temperature reduction results in reduced gas solubility causing supersaturation (the brine concentration effect), which leads to bubble formation if the sum of the partial pressures of all the dissolved gases is higher than the local hydrostatic pressure.

Previous studies of air inclusions morphology in sea ice were based on horizontal thin sections (e.g. Grenfell, 1983; Perovich and Gow, 1991, 1996; Light et al., 2003; Cole et al., 2004). Grenfell (1983), Perovich and Gow (1996) and Cole et al. (2004) highlighted that the columnar ice is usually depleted in air inclusions while top granular ice is described as bubbly with larger air inclusions. Grenfell (1983) observed bubble number distribution in small subsamples cut from first year sea ice and reported diameters ranging from 0.2 to 4 mm. Perovich and Gow (1996) measured mean bubble diameters ranging from 0.036 mm to 0.56 mm for 30 cm

thick pancake ice and mean diameter of 2.6 mm on a multi-year hummock. Light et al. (2003) recorded 100 images from thin sections in transmitted light and reported bubble diameters between 0.008 mm to 0.14 mm in columnar ice that was 175 cm thick (Light et al., 2003).

Limitations of current methods have resulted in a lack of details on determination of air volume fraction. Those methods provide inadequate profiles of the vertical distribution of air inclusions in sea ice, especially in the context of ocean-sea ice-atmosphere exchange of gas. The sea ice air-volume fraction is most often determined empirically from bulk temperature, salinity and density measurements (after Cox and Weeks, 1983). However, small errors associated with sea ice density measurements result in large errors in the calculated air volume fraction. Perovich and Gow (1996), and Light et al. (2003) used sea ice sections imaged using transmitted light to describe air inclusions within sea ice, given the caveats that undisturbed microstructure required careful thermal control, size may be limited, and the differentiation between air bubbles and brine is often complicated in transmitted images (Loose et al., 2010). While thin section studies are relevant to detail morphometric analysis of inclusions, profile of air volume fraction cannot be deduced from thin section analysis. Another approach is high resolution measurements of the total gas content along a vertical profile using techniques initially developed for continental ice cores (melting-refreezing and toepler pump extraction or summing individual gases concentrations measured using gas chromatography (GC) (Tison et al., 2002). These techniques however operate under vacuum, and therefore collect both the dissolved and gaseous phases.

Also, this technique does not provide information on the morphology of the bubble content. A third approach used previously is to melt the ice sample in a gas tight container and quantify total gas volume (Rysgaard and Glud, 2004). A problem with this approach, however, is that gases equilibrate to a new bulk gas concentration depending on the salinity and temperature of the melting ice and hence do not represent the actual gas volume at *in situ* conditions.

We propose a methodological advancement employing computed tomography; CT X-ray imaging, for measurement of air inclusions within sea ice. For many years CT X-ray has been widely used as a medical diagnostic tool. This non-invasive technique has largely contributed to the study of rock fractures and rock porosity, and has recently been applied to the sea ice field, advancing percolation theory for the brine system (Golden et al., 2007; Obbard et al., 2009; Pringle et al., 2009). Here we present high-resolution profiles of the distribution of air inclusions in sea ice, which are derived from CT X-ray images of whole ice cores at the sub-millimeter scale. A detailed statistical analysis of the air volume fraction in experimental sea ice is presented, as well as comparisons to the air volume equations of Cox and Weeks (1983) and measurement of total gas content. Throughout this work, we highlight the parameters and processes influencing the air porosity (air volume fraction, V_a).

VI-2 Methods

VI.2.1 Sea ice Environmental Research Facility (SERF)

The Sea ice Environmental Research Facility (SERF) at the University of Manitoba (Winnipeg, Canada) is an in-ground concrete pool with dimensions of 23.3 m (length) x 9.2 m (width) x 2.75 m (depth). It is filled each year with seawater formulated on site to closely replicate the chemistry of Arctic surface seawater (e.g. Geilfus et al., 2013; Hare et al., 2013; Rysgaard et al., 2014). In January 2013 an experiment was initiated from open water conditions, where sea ice was allowed to grow to 22 cm thick between 13 and 26 January. Ice cores were collected on 14, 16 and 25 January to measure bulk ice gas composition, temperature, salinity, and density, and for computed tomography (CT) X-ray imaging.

VI.2.2 Sea ice core: temperature, salinity and texture

At least four ice cores were extracted on each sampling occasion using a Mark II core barrel with an internal diameter of 9 cm (Kovacs Ent., Lebanon NH, USA). One of the cores was destructively interrogated to measure an *in situ* ice temperature profile at a depth resolution of 2 cm using a calibrated probe (Testo 720, precision ± 0.1°C) inserted into pre-drilled holes perpendicular to the ice core depth axis. The second ice core extracted was immediately cut into 2-cm slices which were stored in polyethylene buckets and left to melt close to 0°C. Bulk ice salinity of the melt of these 2-cm sections was derived from sample conductivity and temperature measured with an Orion Star Series WP-84TP conductivity meter (precision ± 0.1) using the equations of Grasshoff et al. (1983). For sea ice gas

content and CT X-ray imaging, the third and fourth cores were immediately wrapped in polyethylene bags and stored at -20°C in the dark to ensure brine/gas immobilization and to inhibit biological processes (Eicken, 1991).

VI.2.3 Gas composition

The bulk ice concentration of argon (Ar), oxygen (O_2) and nitrogen (N_2) expressed in μmol L^{-1} ice were analyzed using gas chromatography (trace GC). The dry-crushing technique as developed for gas measurements in continental ice (e.g. Raynaud et al., 1982) was used to extract the gas phase from the sea ice samples in a cold laboratory at -25°C. Each ice core sample for gas composition was cut in 5-cm sections, and 60 g of each section were put into a vessel together with stainless steel beads which was evacuated to 10^{-3} torr, and then fixed to an ice crusher (after Raynaud et al., 1982; Stefels et al., 2012). The stainless steel beads impact the ice block during the shaking process, crushing it into a fine powder. After crushing, the vessel was kept in a cold ethanol bath (-50°C) and connected to a gas chromatograph (Trace GC) equipped with a thermal conductivity detector for concentration analyses (Skoog et al., 1997). We used AlphagazTM2 He (Air Liquid –P0252) as the carrier gas and a 22 ml packed column (Mole Sieve 5A 80/100; 5 m x 1/8”). Gas collected included both gaseous fraction in air bubbles and the dissolved fraction within the brine, which cannot be differentiated using this method. The total gas content (ml L^{-1} ice) was derived from the sum of the Ar, O_2 and N_2 concentrations initially expressed in μmol L^{-1} ice and applying the ideal gas law. Since both the cutting process and evacuation stage during the measurement

process lead to potential gas lost, the total gas content measured is a minimum estimate of the true total gas content.

The saturation level of a gas affects bubble nucleation in brine inclusions and is therefore a crucial parameter determining gas flux at the ice-atmosphere interface. Theoretically, nucleation occurs when the sum of the partial pressures of dissolved gases is higher than the local hydrostatic pressure. We therefore compared (i) the gas concentrations profile measured in bulk ice; $C_{bulk\ ice}$ to (ii) the theoretical inventory predicted by the solubility in brine at atmospheric saturation; $C_{Saturation}$ (i.e. the maximum concentration of Ar, O_2 and N_2 in the dissolved phase when the brine is not supersaturated (Carte, 1961; Lubetkin, 2003; Zhou et al., 2013). $C_{Saturation}$ is obtained by calculating the temperature and salinity-dependent solubility of Ar O_2 and N_2 in the brine (Garcia and Gordon, 1992; Hamme and Emerson, 2004) and multiplying it by the relative brine volume (i.e. the brine volume fraction (V_b), see below) and expressed in ml L^{-1} of bulk ice. These relationships are valid for the range of temperature and salinity found in sea ice (Zhou et al., 2013). It is important to note that as $C_{bulk\ ice}$ is measured on 5-cm ice sections while $C_{saturation}$ is computed using 2-cm sections, we can compute more than one $C_{saturation}$ value for each $C_{bulk\ ice.}$ The ratio between the gas concentration measured ($C_{bulk\ ice}$) and the air concentration at equilibrium ($C_{saturation}$) gives the saturation factor SAT_f: As a result, we present the mean SAT_f and its standard deviation for each $C_{bulk\ ice}$ (5-cm section). When a strong gradient of temperature, salinity, and therefore brine volume occurs in a $C_{bulk\ ice}$ 5-cm section, the standard deviation of SAT_f increases.

VI.2.4 Bulk ice density and air volume fraction

To compute the brine volume fraction and the air volume fraction, the bulk ice density of 5-cm core sections was measured with the Mass-Volume technique in a cold lab (-20°C) and the Cox and Weeks (1983) equations were then employed. Ice core sections were cut into cubes of 5 cm^3 and weighed precisely to determine their mass (M). The dimensions of the sample were measured giving their volume (V). The density of the ice (ρ_i) calculated by:

$$\rho_i = \frac{M}{V} \qquad \text{(Eq.- VI-1)}$$

This common technique is easily applied, but there are several possible sources of errors: obtaining a dimensionally perfect ice sample is difficult, and inaccuracies in the measurement of the sample dimensions lead to volume error (Timco and Frederking, 1996).

To limit error induced by imperfect sample dimensions, we used a precision diamond wire saw. The length of each edge (the number of edges per cube = 12) was found to deviate from 5 cm by ± 0.07 cm on average (total number of edges measured = 96; 8 ice cubes) yielding an average precision for ice density of ±4.4%, as a result of the cutting process. While deviation of 0.7 mm on the dimension of the ice cube has little effect on the precision of the density and of the calculated brine volume fraction (relative standard error <5%), it produces relative standard errors as high as 163% on the air volume fraction computed using the equations of Cox and Weeks (1983) (Table VI-1).

Table VI-1: Effect of dimensional error on brine volume and air volume fraction computed by mass–volume density measurement using state equation from Cox and Weeks (1983).

Temperature (°C)	Salinity	Length (cm)	Ice cube volume (cm^{-3})	Masse (g)	Density ($g\ cm^{-3}$)	V_b (%)	V_a (%)
-5.00	5.00	4.93	119.82	113.75	0.95	5.1	-1.3
-5.00	5.00	5.00	125	113.75	0.91	4.9	2
-5.00	5.00	5.07	130.32	113.75	0.87	4.7	6.3
Relative standard error		**±1.4%**	**±4.2%**		**±4.4%**	**±4.1 %**	**±163 %**

VI.2.5 Liquid porosity: brine volume fraction

The brine volume was calculated according to Cox and Weeks (1983) using *in situ* temperature, bulk ice salinity, and bulk ice density measurements from the cores. Brine salinity (S_b) was calculated using *in situ* sea ice temperatures and the freezing point of seawater (UNESCO, 1978). The brine volume fraction, (V_b, expressed in %), was calculated from the ratio of brine volume and bulk sea ice volume (b/V). In previous works, sea ice air volume fraction is ubiquitously neglected, so historically, sea ice porosity refers solely to the brine volume fraction. In the context of this paper, the terms brine inclusions and brine volume fraction refers to liquid porosity. The permeability threshold of $V_b = 5\%$ following Golden et al. (1998, 2007) defines permeable and impermeable columnar sea ice.

VI.2.6 Ice texture

To describe the ice crystal texture, horizontal thin sections of maximum 10 cm length were produced in a cold lab at -20°C using the standard microtome (Leica

SM2400) procedure described by Langway (1958) and Tison et al. (2008). Images of these backlit horizontal thin sections were taken in the cold lab between crossed polarizing sheets with a camera (Nikon Coolpix S200).

VI.2.7 Air porosity: air volume fraction by CT X-ray imaging:

VI.2.7.1 General principle

CT-scanning is a non-destructive radiographic approach to examine materials by creating a three-dimensional image of density contrasts. Ice cores were imaged using a third generation Siemens Somatom Volume Access sliding gantry medical CT-Scanner (Siemens SOMATOM Definition AS+ 128) at the Institut National de la Recherche Scientifique (INRS-ETE, Quebec). The ice cores were stored at -20°C and scanned at room temperature. The scan duration was less than 15 seconds. Including transport of the ice samples from the storage freezer to the CT instrument was less than 75 seconds. We therefore assume that no temperature changes in the core occurred. Data was acquired in spiral mode with a pitch factor of 0.6; the X-ray source was set at 120kV and 150 mAs. These configurations produced 1152 projections for each reconstructed axial slice. The image size is limited by the manufacturer to 512 x 512 pixels, so the pixel resolution is defined by the chosen field of view (FOV). The smallest selectable FOV is 50 x 50mm providing a pixel resolution of 0.0977 mm in the transverse plane. This FOV is too small to contain the whole core in one image; so four reconstructions of each core were produced and concatenated together using Matlab. The Siemens SAFIRE (Sinogram Affirmed Iterative Reconstruction) reconstruction algorithm was used

(three iterations). The convolution kernel is J70h, a medium-sharp filter. The result of the concatenation is an image size of 1024 x 1024 pixels with a FOV of 100 mm x100 mm and a pixel resolution of 0.097 mm (x-y) and a slice thickness (z) of 0.6 mm. By scanning a core from top to bottom, a three-dimensional "stack" of images was produced by compiling individual transverse slices and longitudinal slices (Figure VI-1a) yielding 0.097 × 0.097 × 0.6 mm (0.0056 mm^3) voxel volumes within square (1024 x 1024 voxel) images.

Hounsfield (1973) and Knoll (1989) describe the X-ray technique in detail. The Hounsfield Unit (HU) value for each voxel corresponds to linear X-ray attenuation, where denser materials and higher atomic numbers result in greater X-ray attenuation (Duliu, 1999). Ice core density was calculated in terms of tomographical intensity (TI) (in Hounsfield Units for each voxel):

$$TI=\left(\frac{\mu}{\mu_w}-1\right)\times 1000 \qquad \text{(Eq.- VI-2)}$$

Where μ is the linear absorption coefficient of the bulk core, and μ_w is the linear absorption coefficient of water. μ is a function of the radiation energy and the atomic number of the core component crossed by the beam and varies in relation to the density of the material. Resulting images are represented in grey scale where darker tones indicate lower density material (e.g. air) (Figure VI-1a-c). Density measurements were made relative to freshwater and expressed in TI where water = 0 HU and air = -1000 HU. We observed Hu unit from -1024 to +616, +499 and +766 on 14, 16 and 25 January, respectively. Positive values are related to brine and to a minor extend precipitated salt (e.g. 60 HU < TI < 766 HU) and slightly

negative values are related to ice (e.g. TI = -84 HU, Kawamura 1988). We estimate the tomographic intensity of pure ice crystals using the mode of the histogram (Figure VI-1d, TI = -74 HU).

VI.2.7.2 Processing X-ray Images and analysis

The process of pixel selection to create binary images of air inclusions, thereby defining the air volume fraction (air porosity, V_a) in the CT-imagery, was performed by means of thresholding following the determination of a region-of-interest (ROI) created by the removal of all pixels not belonging to the core sample (i.e. the sample container, disturbance of the core edges by coring and/or storage, the supporting bench, and surrounding air from each slice). The images were individually examined and ambiguous pixels around the sea ice core sample were also removed. The bottom slices of each imaged ice core were removed due to observed brine drainage resulting from the coring method. A three-dimensional orthoslice view as well as two transversal slices of the ice core sample extracted on 16 January are shown in Figure VI-1. The bottom of the ice core from which brine drainage occurred during core extraction can be clearly differentiated from the rest of the core sample unaffected by brine loss on both the orthoslice and transversal slice views (Figure VI-1a-c). CTan and ImageJ software were used to quantitatively measure morphometric characteristics of binary (black and white) images.

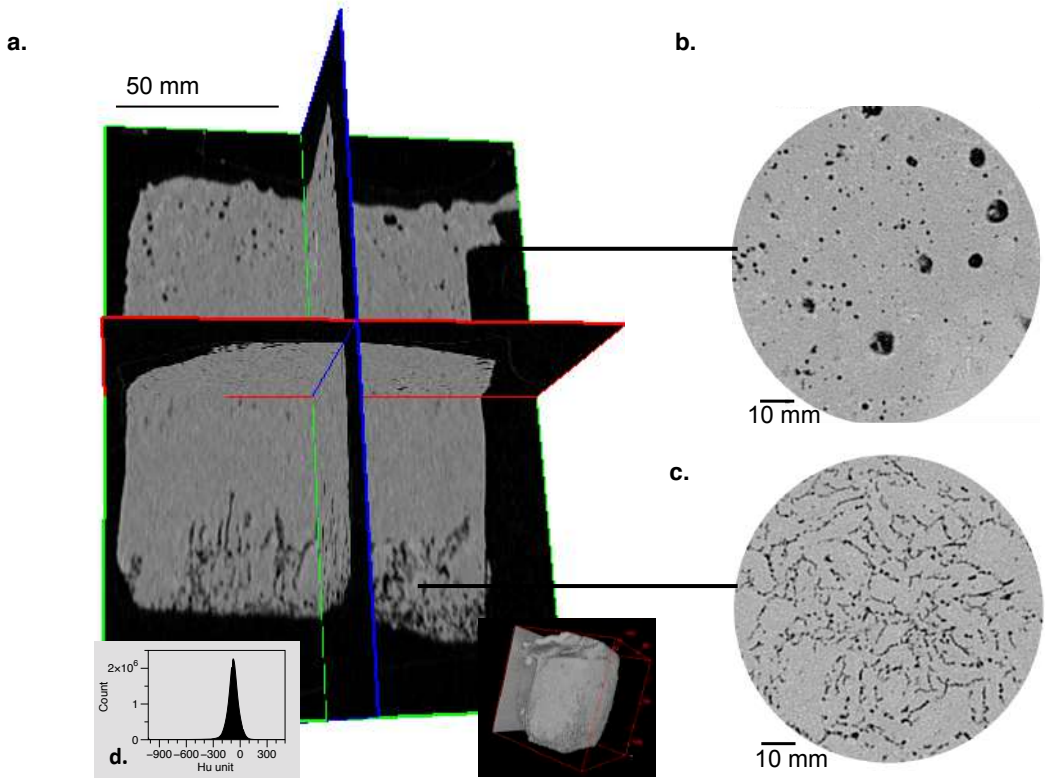

Figure VI-1: (a) 3-D orthoslice view from raw images of 16 January, consisting of two longitudinal slices and one transversal slice, lighter grey area represents the ice matrix and black area represents the air inclusions (i.e. bubbles); (b) top transversal slice at 0.65 mm depth, every black dot represents an air inclusion (i.e. bubbles); (c) bottom transversal slice at 8 cm depth, all the black dots show drained brine; (d) histogram of HU-unit (CT-value) recorded for 186 transversal slices of 0.6mm thick for 16 January.

Determination of the most applicable threshold is therefore of the utmost importance here, as in all image classifications in the multitude of fields that employ the technique. Three approaches are typical for determining an optimal threshold; manual threshold selection based on the human visual system, automated threshold selection based on image data, usually employing the image histogram, and a threshold based on a mixture model approach.

There are many automated segmentation techniques described in the literature. In this study segmentation algorithms representing a selection of

established thresholding techniques chosen on the basis that they (i) suited a unimodal histogram (Figure VI-1d), and they (ii) showed potential for automated characterization of pore space in geomaterials. Global thresholding specifically was selected on the basis of comparative reviews by Sezgin and Sankur (2004) and Iassonov et al. (2009). Global thresholding may be divided into several subcategories depending on the applied approach. These subcategories include those based on signal entropy considerations (Shannon and Weaver, 1948; Pal and Pal, 1989; Pal, 1996) to separate background and foreground voxels, including EN-Kapur and EN-Yen (Kapur et al., 1985; Yen et al., 1995). There exist global thresholding methods that analyze histogram shape (HS), including HS-Zack and HS-Tsai (Tsai, 1995; Zack et al., 1997). Finally, segmentation may be accomplished by clustering (CL) methods, which separate background (i.e. ice) and foreground voxels (i.e. air) by approximating the histogram with a combination of two or more statistical distributions, including CL-Otsu and CL-Ridler (Ridler and Calvard, 1978; Otsu, 1979).

Each segmentation method was tested on the three core image sets (633 total image slices), as well as on selected parts of each image set to insure that the algorithm response was stable. The results of each segmentation method were visually evaluated by comparing the raw and segmented images (Figure VI-2) and by computing linear profiles of Hu-value (Figure VI-3) through cross-sectional images and examining them visually to determine the efficacy of various thresholds in identifying air inclusions.

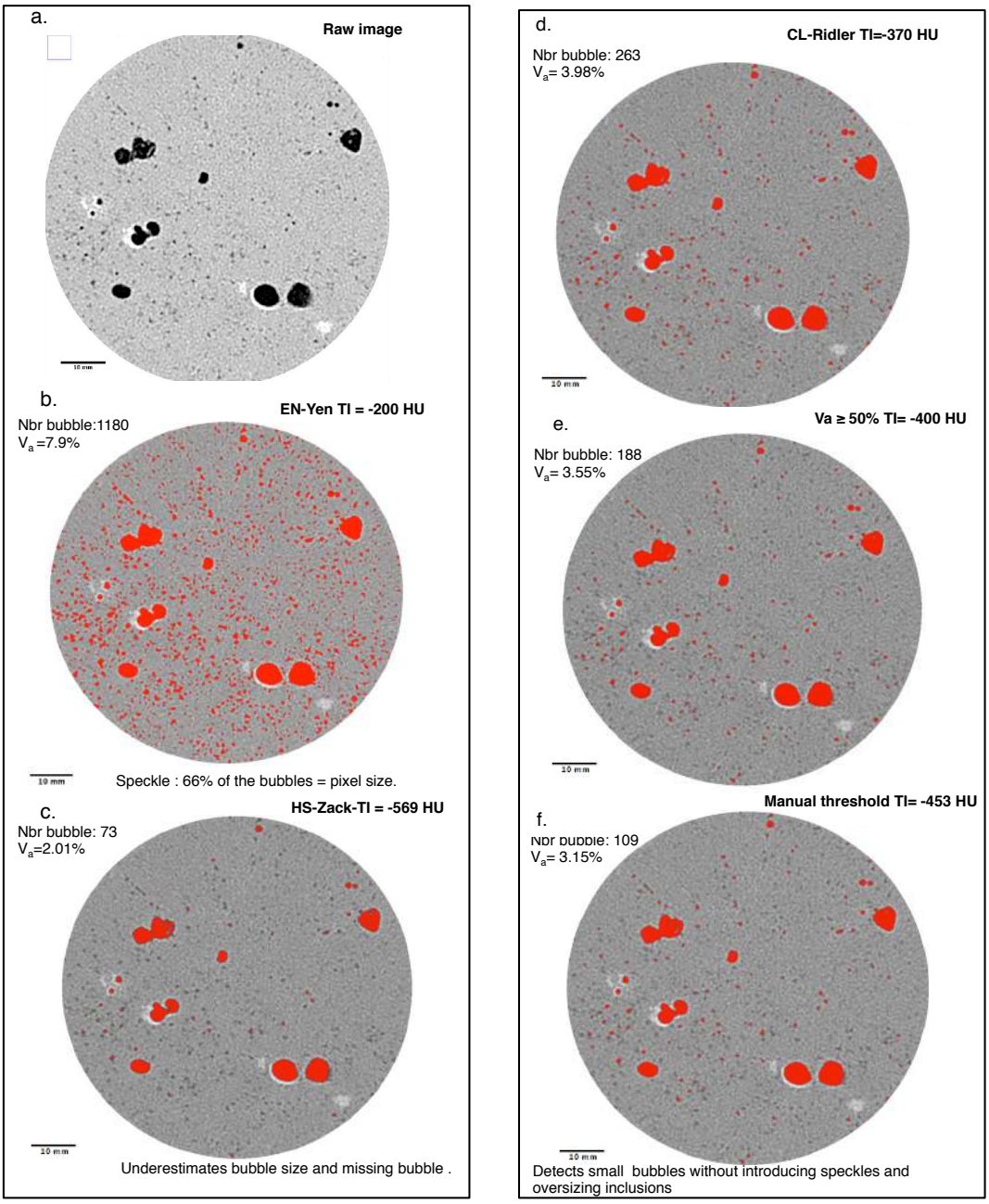

Figure VI-2: (a) Raw transversal slice where grey pixels represent ice, black pixels represent air, and darker grey pixels are mixed pixel-containing air and background (ice). (b) and (c) transversal slices showing the air selected pixels in red using a HU value of −200 and of −569 as threshold selected by the EN-Yen (b) and the HS-Zack algorithm (c), respectively. (d), (e) and (f) transversal slices showing the air selected pixels in red using a HU-value of −370, of −400 and of −453 as threshold selected by (d) CL-Ridler algorithm, (e) by pixels containing a minimum of 50% of air and (f) by manual thresholding.

Analysis of variance (ANOVA) demonstrated significant ($p < 0.005$) differences between thresholds produced by the interrogated segmentation methods. The EN-Yen (max-entropy) algorithm produced a relatively high threshold (TI = -200 HU), which introduced noise and speckle in the image; 66% of 1180 total inclusions detected by the EN-Yen threshold were the size of a single pixel (Figure VI-2b, EN-Yen). The HS-Zack (Zack et al., 1997; Rosin, 2001) method produced a low threshold (TI= -569 HU) that (i) did not detect small bubbles, and (ii) underestimated the size of bubbles detected (Figure VI-2c, HS-Zack). The segmentation threshold produced by the CL-Ridler (TI = -370 HU), method, accurately identified bubbles in all images, including detecting very small bubbles, without introducing speckle in the segmented image (Figure VI-2d, CL-Ridler).

Manual segmentation thresholds were defined by inspecting a variety of different bubbles in different slices, (e.g. Figure VI-3). Figure VI-3 indicates that visual thresholds were subjective; the pixel scale actually makes visual bubble delineation more ambiguous. Bubble number 2 (Figure VI-3) is best delineated by TI = -453 HU, while bubble number 3 (Figure VI-3) is best visually delineated by TI = -373 HU. In the context of the variety of bubble morphology and the differences in columnar and granular sea ice in the 633 transverse image slices, the visual segmentation threshold was set at TI = -453 HU.

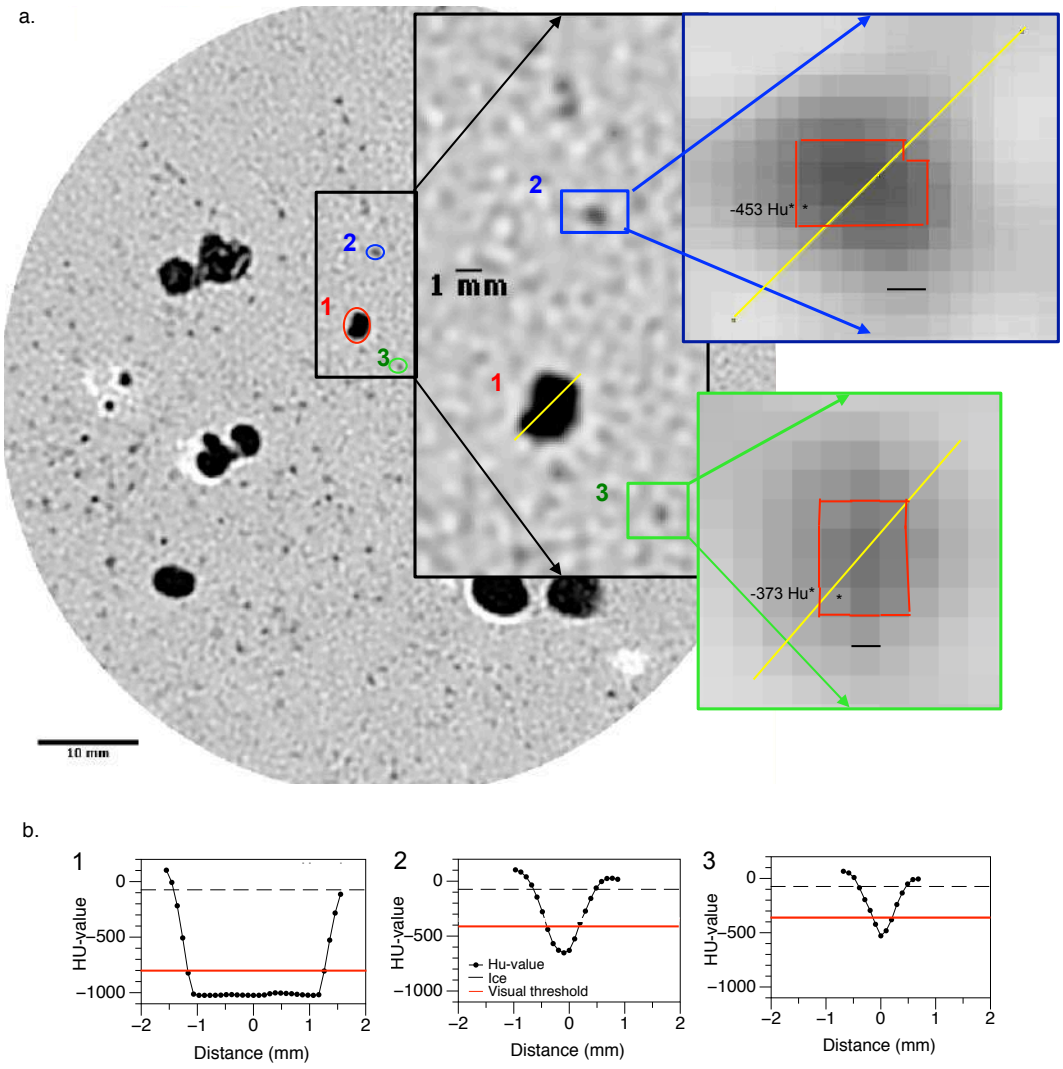

Figure VI-3: (a) Raw transversal slice where grey pixels represent ice and black pixels represent air; darker grey pixels are mixed pixels containing air and background (ice) and white pixels contain brine. We highlighted three air inclusions: an air inclusion (1) larger than the spatial resolution and two inclusions (2 and 3) which are smaller than the spatial resolution, their HU value never reached the HU value of air; instead they appeared as mixed pixels and their HU value reflects the proportion of air, ice and brine in the pixel. The red line shows the visual boundary of the bubble where the lowest HU value observed for pixel (*) is the visual threshold. (b) The distribution of HU value along the transects (yellow lines in a).

Finally, the tomographic intensity of "mixed pixels" which appear as varying shades of grey is dependent of the proportion of air (V_{air}), ice (V_{ice}) an brine (V_{brine}) in the pixel and the proportions of the tomographic intensities of those constituents (air (Hu_{air}), ice (Hu_{ice}) and brine (Hu_{brine})) in the following mixture model:

$$Hu=(V_{air} \times Hu_{air})+(V_{ice} \times Hu_{ice})+(V_{brine} \times Hu_{brine}) \quad \text{(Eq.- VI-3)}$$

$$1=V_{air}+V_{ice}+V_{brine} \quad \text{(Eq.- VI-4)}$$

The TI of pure ice crystals is determined using the mode of the histogram containing all the data from each core ($TI_{pure\ ice}$ = -74 HU). Brine TI values ranged from 60 to 500 depending on brine salinity; we selected the middle point of that range (TI_{brine} = 200 HU). Finally, TI_{air} = -1000 HU. According to the mixture model (equation V-3), any pixel TI ≤ -400 HU contains at least 50% air and is therefore selected as part of an air inclusion (Table VI-2 and Figure VI-2e).

Table VI-2: Estimation of the HU value of a pixel containing at least 50% of air. Assuming the HU value of air, of ice and brine are −1000, −74 and 200, respectively.

V_{air} =50%	V_{air} x Hu_{air}	0%<V_{ice}<50%	V_{ice} x Hu_{ice}	0%<V_{brine}<50%	V_{brine} x Hu_{brine}	Hu value*
0.5	-500	0	0	0.5	100	-400
0.5	-500	0.1	-7.4	0.4	80	-427.4
0.5	-500	0.2	-14.8	0.3	60	-454.8
0.5	-500	0.3	-22.2	0.2	40	-482.2
0.5	-500	0.4	-29.6	0.1	20	-509.6
0.5	-500	0.5	-37	0	0	-577

*$Hu=(V_{air}\times Hu_{air})+(V_{ice} \times Hu_{ice})+(V_{brine}\times Hu_{brine})$

The CL-Ridler (TI = -370 HU) threshold, as well as the manual threshold (TI = -453 HU) and the mixture model threshold, which selects pixel containing 50% air (TI = -400 HU) were used to compute the air volume fraction for each of the transverse slices in each of the three ice cores imaged. Analysis of variance (ANOVA) demonstrated no significant difference ($p < 0.005$) between the air volume fraction computed using the mixture model threshold and the air volume fraction computed using the visually defined threshold (TI = -453 HU) or the most applicable automated threshold (CL-Ridler, TI = -370 HU). The CL-Ridler and the visual threshold produced mean V_a values that were statistically different ($p < 0.005$).

Hereafter, the air volume fraction is presented as the mean of the air volume fraction results computed using the three selected thresholds. The potential range of the V_a from each of the three methods is represented by the standard deviation of this mean.

Our method endeavors to meet the challenge of CT X-ray image threshold selection in porous materials while lacking knowledge of the optimal segmentation result. Selecting the most applicable threshold is imperfect because the resolution of the CT-image used will almost always be insufficient to resolve every object of interest (in this case air inclusions in sea ice). When the object of interest is smaller than the spatial resolution of the imager, it appears as a mixed pixel, where the voxel TI is a function of the amount of air, of ice and/or brine in the voxel, resulting in voxel TI different than that of pure ice (or pure air) by some amount. In this way delineation of an object using TI thresholds is complicated by the TI's of adjacent

pixels/materials. If an air bubble (TI = -1000 HU) is adjacent to both ice (TI = -74 HU, Figure VI-1d) and brine (TI = 200 HU) the pixel(s) those respective boundaries will be roughly -537 on the ice-side and -400 on the brine-side. In granular sea ice (where bubbles are sufficiently large to be resolved by CT-scan), mixed pixel concerns mainly the edges of the large and macro bubbles, while in columnar sea ice where bubble are small compared to the pixel size, most of the bubbles appeared as mixed pixels as they include both air and background (ice/brine). We are able to compute the V_a in granular layer with a relative error of ±16% and in columnar sea ice with a relative error of ±43%. The morphology of air inclusions is characterized quantitatively using their diameters (Ø, mm) in the transverse (x-y) plane. While it is ambiguous to report exact diameter from mixed pixel, we classified bubble diameters into three categories at a millimeter scale: micro bubbles ($\emptyset < 1$ mm), large bubbles ($1\text{mm} < \emptyset < 5\text{mm}$), and macro bubbles ($\emptyset > 5\text{mm}$).

V_a must be clearly differentiated from the GC-derived bulk ice total gas content (in ml L^{-1} ice), which refers to the amount of Ar, O_2 and N_2, both (i) in dissolved phase in brine and (ii) in the gas phase in bubbles measured in 5-cm depth increments. In this work, we use the terms “bubbles” and “air inclusions” interchangeably to denote gas phase inclusions in sea ice.

VI-3 Results

VI.3.1 Environmental conditions

At the Sea Ice Environmental Research Facility (SERF), the ambient air temperature varied between -5°C and -32°C through the experiment from 13 to 26

January. The average air temperature for the period was -22°C. Three main snowfall events occurred during the experiment. Snowfall on 14 to 15 January covered the sea ice surface with 1 cm of snow. Snowfall from 19 to 23 January deposited 6-9 cm of snow over the entire pool. On the morning of 23 January, the snow was manually cleared off the ice surface to investigate the insulating effect of snow on the ice temperature and ikaite precipitation (see Rysgaard et al., 2014). Finally, from 24 January to the end of the experiment on 26 January, 8 cm of snow covered the entire pool. Surface elevation from Lidar data (not shown), indicates that the ice surface did not move appreciably in the vertical for the duration of the experiment even as a result of snow removal. Periodically the sea ice froze to the side of the pool resulting in a hydrostatic pressure head in the seawater below, causing episodic percolation of seawater at the freezing point upwards through the sea ice volume resulting in wet snow-ice and slush at the sea ice surface on 16 January. A slush layer (up to 3 cm thick) was also observed at the snow base on 20 January. This episodic hydrostatic pressure head and resultant upward percolation of seawater through the sea ice caused the granular layer of the sea ice volume to thicken over time, likely by the formation of snow-ice layers as the slush layer froze. On 14 January, the 0.7 cm thick granular layer consisted of frazil ice, on 16 January, the granular layer thickened to 1.7 cm (consisting of the initial 0.7 cm of frazil and 1 cm of snow-ice). On 25 January, the granular layer had thickened again to 4 cm consisting of the initial granular sea ice layer of 14 January, the snow-ice layer of 16 January and an additional 2.3 cm thick snow-ice layer (Figure VI-4).

Below the granular ice layer, the sea ice crystal texture transitioned nearly immediately to columnar ice on all three dates (Figure VI-4).

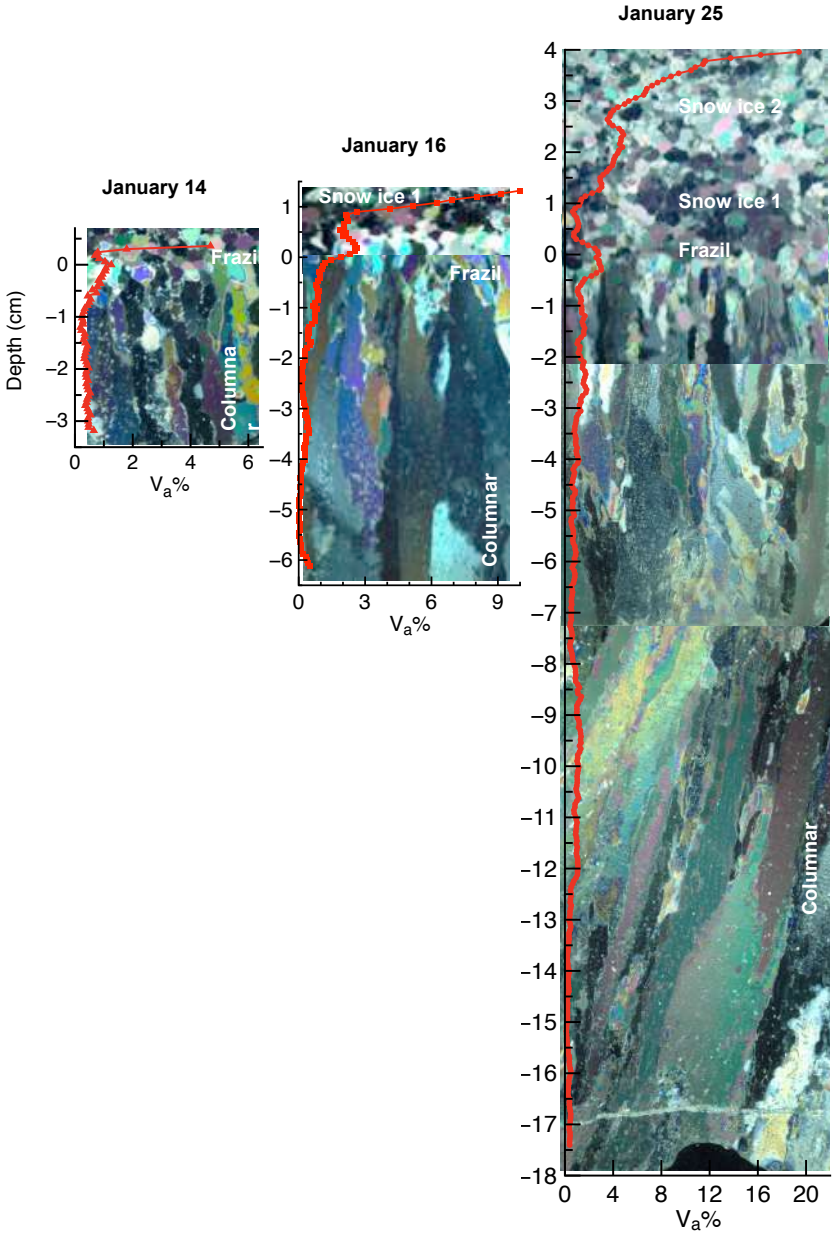

Figure VI-4: Sea ice microstructural images overlain by the air volume fraction (red curve) for 14, 16 and 25 January. The x scale differs for each date in order to visualize vertical change. The zero depth is fixed at the boundary between granular and columnar ice. Through the studied period ice grew from the bottom increasing the columnar layer, as well as by the top due to additional formation of snow-ice.

VI.3.2 Temperatures, salinity, brine volume fraction and bulk ice density

Sea ice temperature, bulk salinity, brine volume and bulk ice density profiles for cores sampled on 14 January (4 cm thick), 16 January, (8 cm thick) and 25 January (22 cm thick) are shown in Figure VI-5 and Table VI-3.

On 14 January, the bulk salinity profile was approximately linear, and evolved to a more C-shaped profile on 16 and 25 January as the granular top layer remained saline and the top of the columnar layer desalinated through the experiment (Figure VI-5). Calculated brine volume (V_b) profiles were similar in shape to the salinity profiles with minimum V_b occurring in the middle of the columnar ice layer on 16 and 25 January (Figure VI-5). According to Golden et al. (1998, 2007) the permeability threshold for columnar sea ice of 5% V_b indicates that the whole ice volume on 14 January and near the bottom parts of the columnar ice layer on 16 and 25 January were permeable to liquid.

Bulk ice densities ranged from 0.84 g cm^{-3} ± 0.020 g cm^{-3} to 0.92 g cm^{-3} ± 0.023 g cm^{-3}. The lowest densities were systematically found at the surface of the ice cover (Figure VI-5).

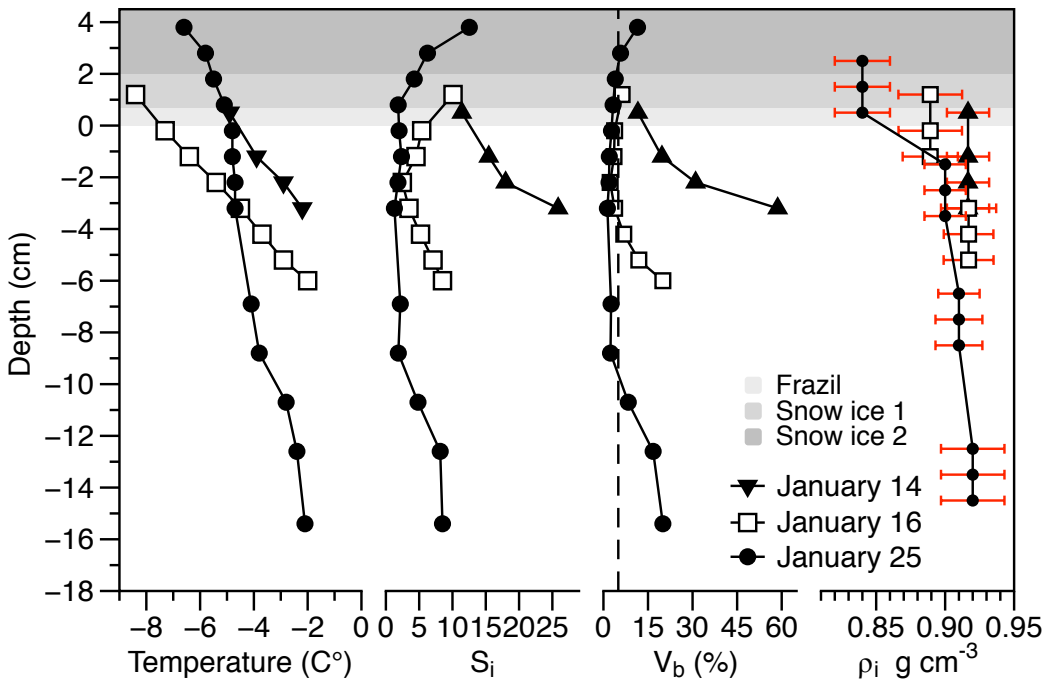

Figure VI-5: Ice *in situ* temperature (°C), bulk ice salinity, and brine volume fraction (V_b) and bulk ice density profiles (g cm^{-3}) on 14, 16 and 25 January. The dotted line at 5% on the V_b panel refers to the theoretical liquid permeability threshold for columnar sea ice (Golden et al., 1998). Red bars on the density profiles indicate the standard deviation of the mean of density measurements derived from the mass–volume technique.

VI.3.3 Bulk ice total gas content

The total gas content in the sea ice volume increased from its minimum in the bottom permeable columnar layer to its maximum in the top granular layer on 14, 16 and 25 January. The total gas content in the sea ice volume also increased over time (Figure VI-6). The total gas content of the permeable columnar bottom of each of the ice cores (and the entire core on 14 January) were close to the concentration at saturation with respect to calculated theoretical atmospheric gas concentrations, leading to saturation factor ranging from 0.8 to 1.2. This will be referred to as "subsaturated" ($SAT_f \leq 1.2$). On the contrary, the total gas content of

the impermeable columnar layers and the granular surface layers of the sea ice were largely greater than the concentration at saturation leading to saturation factor ranging from 9.5 to 16. These will be referred to as supersaturated ($SAT_f > 1.2$).

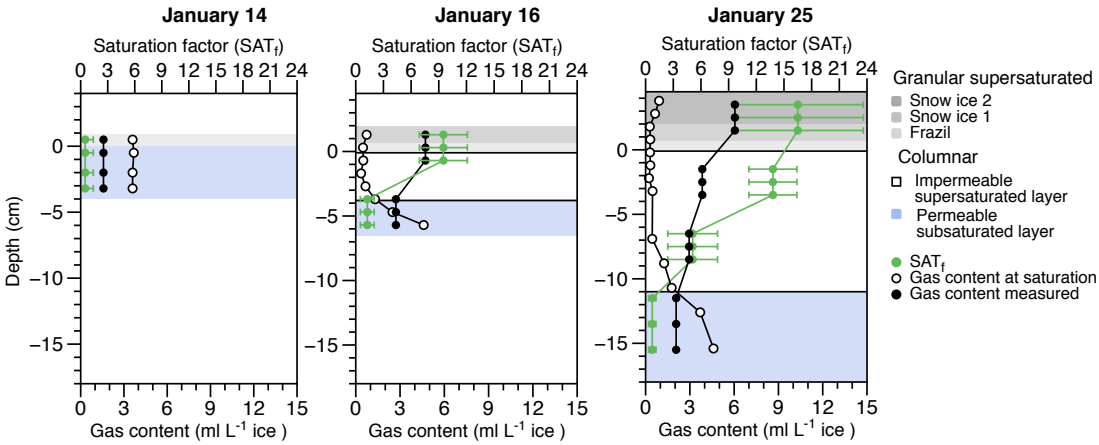

Figure VI-6: Profiles of the total gas content in bulk sea ice measured by gas chromatography as the sum of Ar, O_2 and N_2 (black symbols) compared (i) to the theoretical bulk ice gas content at atmospheric saturation (white symbols) and (ii) the saturation factor (green symbols). The blue area highlights subsaturated columnar sea ice ($SAT_f \leq 1.2$), the white area highlights the supersaturated columnar sea ice ($SAT_f > 1.2$) and the grey area represents successively the supersaturated granular layers (frazil and snow-ice layers).

VI.3.4 Air Porosity

VI.3.4.1 Air volume fraction (V_a) derived from CT X-ray Image Analysis

For each of the three dates sampled, the air volume fraction increased from the bottom columnar ice layer to the granular surface ice layer and increased overall from 14 to 25 January (Figure VI-4 and Figure VI-7a-c) in the same way as was shown by the total gas content analysis (Figure VI-6).

In columnar ice, we distinguish permeable ($V_b > 5\%$) and subsaturated ($SAT_f \leq 1.2$) ice near the bottom (Figure VI-7a and b, shaded blue) from the

impermeable ($V_b < 5\%$) and supersaturated ($SAT_f > 1.2$) ice in the middle sea ice layers (Figure VI-7a and b, white area). In the permeable subsaturated bottom sea ice, the air volume fraction was less than 1%, for each sampling date (Table VI-3). In the intermediate supersaturated impermeable columnar layer, the air volume fraction was typically under 2% and increased from 14 to 25 January. At the transition between the impermeable and permeable columnar ice on 16 and 25 January (Figure VI-7c, shaded pink), we observed a slight increase in V_a.

On all three dates, the maximum air volume fraction occurred in the granular layers nearest the atmosphere interface increasing from the base of the granular layer (Figure VI-7c and d). As the granular ice layer thickened by snow-ice formation from 0.7 cm to 4 cm, V_a in these layers increased (Figure VI-7c and d). In the granular layers, the brine volume exceeded 5% (Figure VI-5) and the saturation factor was above 9 on 16 and 25 January (Figure VI-6).

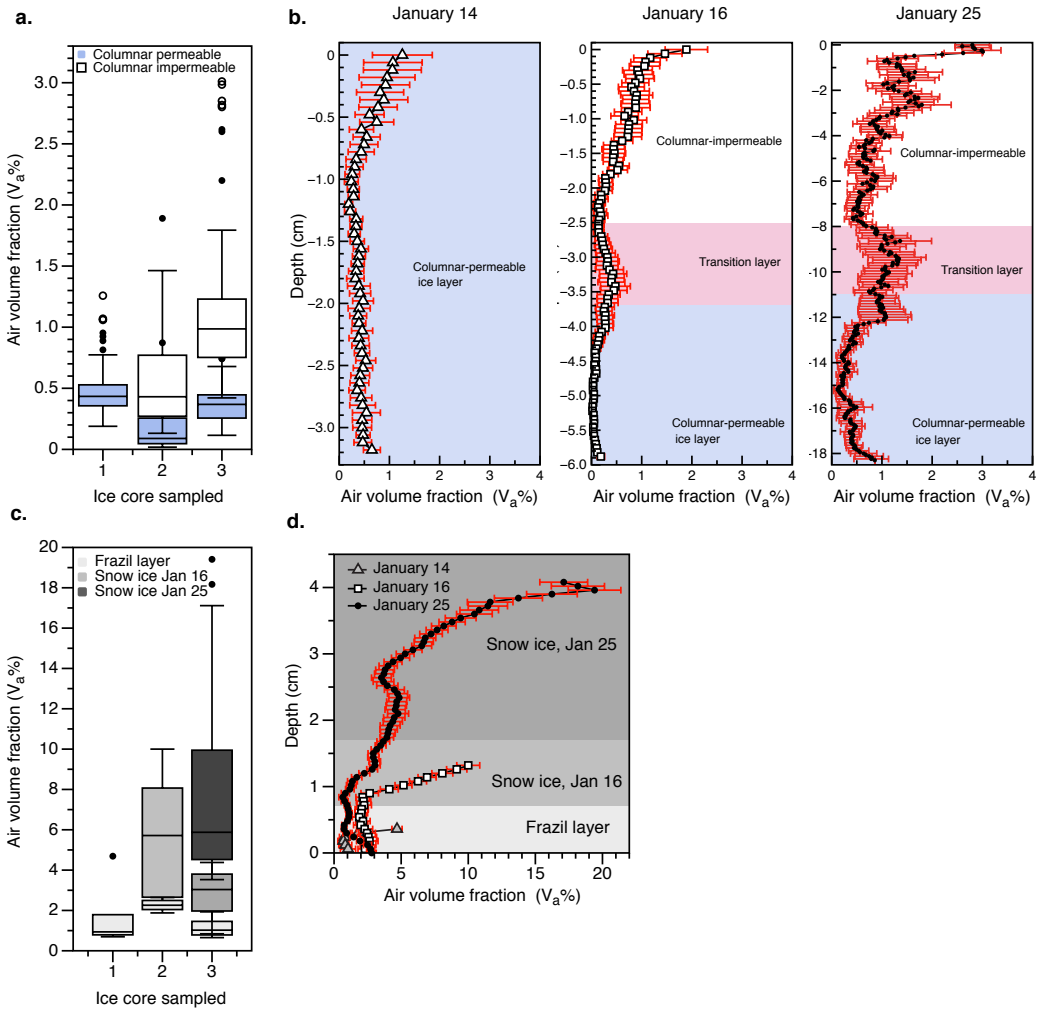

Figure VI-7: (a) IQR box plot showing the distribution of CT-derived V_a computed for every 0.6mm thick slice of each ice core in the columnar impermeable (white) and bottom columnar permeable layers (blue) on 14 January (1), 16 January (2) and 25 January (3), respectively. The box is defined by the first and third quartiles of the distribution, the line in the box is the median, the circles represent the outliers (an outlier is any data that is more than 1.5 times the length of the IQR box from either end of the IQR, T bars). (b) V_a profile in the columnar layers for 14, 16 and 25 January, respectively. The y scale differs for each date to obtain better visualization of the V_a profile. The errors bars show the potential range of CT-derived V_a in each transverse slice. (c) IQR box plot showing the distribution of CT-derived V_a computed for every 0.6mm thick slice of each ice core in granular layers and (d) V_a profile in granular ice for each sampling date.

VI.3.4.2 Air inclusion morphology

The morphology of air inclusions is characterized quantitatively using their diameters (Ø, mm) in the transverse (x-y) plane (Figure VI-8). We classified CT-derived bubble diameters into three categories: micro bubbles (Ø < 1 mm), large bubbles (1 mm < Ø < 5mm), and macro bubbles (Ø > 5 mm) (Figure VI-8). Bubbles smaller than the pixel size (0.097 mm in the transverse plane) represented less than 10% of the bubble population in any type of ice except for the impermeable supersaturated columnar layer on 16 January (Figure VI-9a). Most of the bubbles had diameters ≤1 mm; bubbles of this size were common at every depth in every ice type interrogated by the CT imager (Figure VI-9a and b). Due to the non-destructive nature of the CT X-ray method we were able to observe larger bubbles with diameters as large as 18.2 mm in granular sea ice (Figure VI-9b).

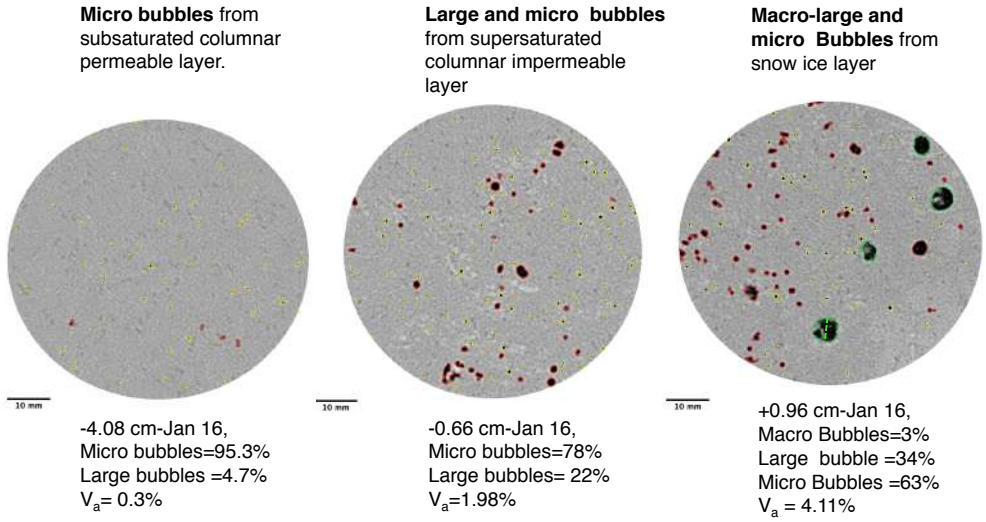

Figure VI-8: Transversal slice at different depth highlighting the proportion of micro (yellow), large (red) and macro (green) bubbles in each slice (e.g. [Nbr micro/(Nbr micro+NbrLarge+Nbr Macro)]×100).

For each ice core, the bubble size increased from the bottom columnar layer, to the top granular layer and increased over time in the same way as observed by the total gas content measured using the GC method (Figure VI-9b). The bottom permeable subsaturated columnar ice contained almost exclusively micro bubbles on all three dates (Figure VI-9a and b). Large bubbles occurred more frequently in the intermediate impermeable supersaturated columnar layer than in the bottom permeable subsaturated columnar layer. Macro bubbles were exclusively found close to the ice-atmosphere interface in the snow-ice layer (Figure VI-9b).

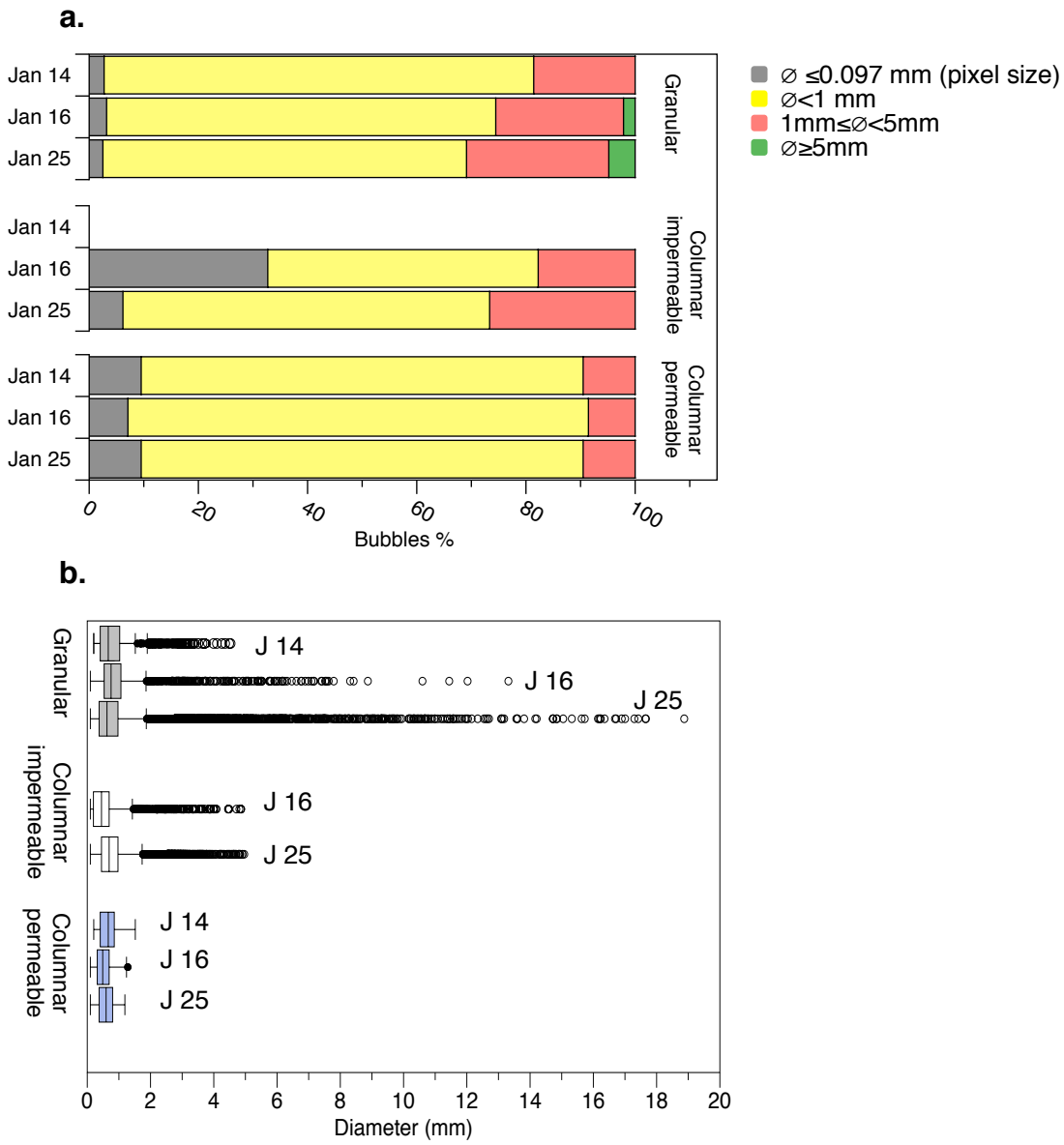

Figure VI-9: (a) The proportion of micro, large, and macro bubbles for each ice type and sampling date. (b) IQR box plot showing the distribution of the bubble diameters, per ice type and sampling dates. The box is defined by the first and third quartiles of the distribution, the line in the box is the median, the circles represent the outliers (an outlier is any data that is more than 1.5 times the length of the IQR box from either end of the IQR, T bars).

Table VI-3: Summarizes the main sea ice characteristics and sea ice properties.

Data		January 14	January 16	January 25
Ice thickness (cm)		4	8	22
Temperature (C°)		-4.1- -1.7	-8.4- -1.6	-5.2- -2.1
Salinity		11.4-25.8	2.26-10.3	1.3-12.5
Brine volume fraction (%) (V_b, liquid porosity)		11.8-58.6	2.26-20.4	1.3-20.6
Bulk ice Density (g cm^3)		0.91	0.89-0.92	0.84-0.92
Air volume fraction (%)(V_a, CT-derived air porosity)	**Granular**	0.69-5.09	1.8-10	0.69-19.41
	Columnar impermeable	n/a	0.13-1.89	0.42-3.01
	Columnar permeable	0.18-1.25*	0.02-0.87	0.11-0.85
Air inclusions diameter (mm)	**Granular**	0.097-4.53	0.097-13.31	0.97-18.2
	Columnar impermeable	n/a	0.097-4.86	0.097-4.96
	Columnar permeable	0.097-1.12	0.097-1.08	0.097-1.18
Gas composition (average mixing ratio)	**O_2 %**	23.7	29.4	27.24
	Ar %	1.4	2.2	1.96
	N_2 %	74.9	68.4	70.8
Buk ice total gas content (ml L^{-1} ice, O_2+Ar+N_2)		1.58	2.5-4.7	2-6.5
Gas Saturation factor (SAT_f)		0.82	9.5 (top) -1.2 (bottom)	16 (top)-0.9 (bottom)

* 98% of the air volume fraction recorded was under 1 %.

VI-4 Discussion

VI.4.1 Computed tomography X-ray imaging as a non-destructive method to compute the sea ice air volume fraction

By using computed tomography X-ray imaging with a voxel size of 0.0056 mm^3 we provide high-resolution profiles of the vertical distribution of air inclusions in sea ice, from which the sea ice air volume fraction are computed every 0.6 mm. Taking into account the relative errors of V_a ± 16% in granular layer and V_a ± 43%

in columnar ice, results of image analysis indicated that the air volume was < 2% in most of the columnar ice, but systematically reached 5% in the granular/snow-ice top layer where an air volume fraction as high as 19% was observed.

CT X-ray images (of porous materials in particular) are of such high resolution (in this case voxel = 0.0056 mm^3), use such large sample volumes and are so quick that traditional methodology can hardly be used to validate the imaged data at the same resolution. Nevertheless, we compared our CT-derived V_a results to air volume fraction computed based on density measurements (Cox and Weeks, 1983) Figure VI-10a). The density (M/V) derived air volume profiles were always larger (Figure VI-10a) but both methods derive large difference between granular and columnar air porosity and showed similar trends (Figure VI-10b). The precision in density-derived V_a is very low (±163%), compared with the relative standard deviation from CT- derived ai volume fraction of V_a ± 16% in granular layer and V_a ± 43% in columnar sea ice. The CT-derived air volume fraction also compared to the bulk ice total gas content (ml L^{-1} ice) data derived from the GC analysis (using 60 g samples from 5-cm thick sections) (Figure VI-10c). The vertical gradients in the two datasets increased similarly from the ice bottom to the sea ice surface and both the total gas content (ml L^{-1} ice) and the CT-derived air volume fraction increased as the ice thickened over time.

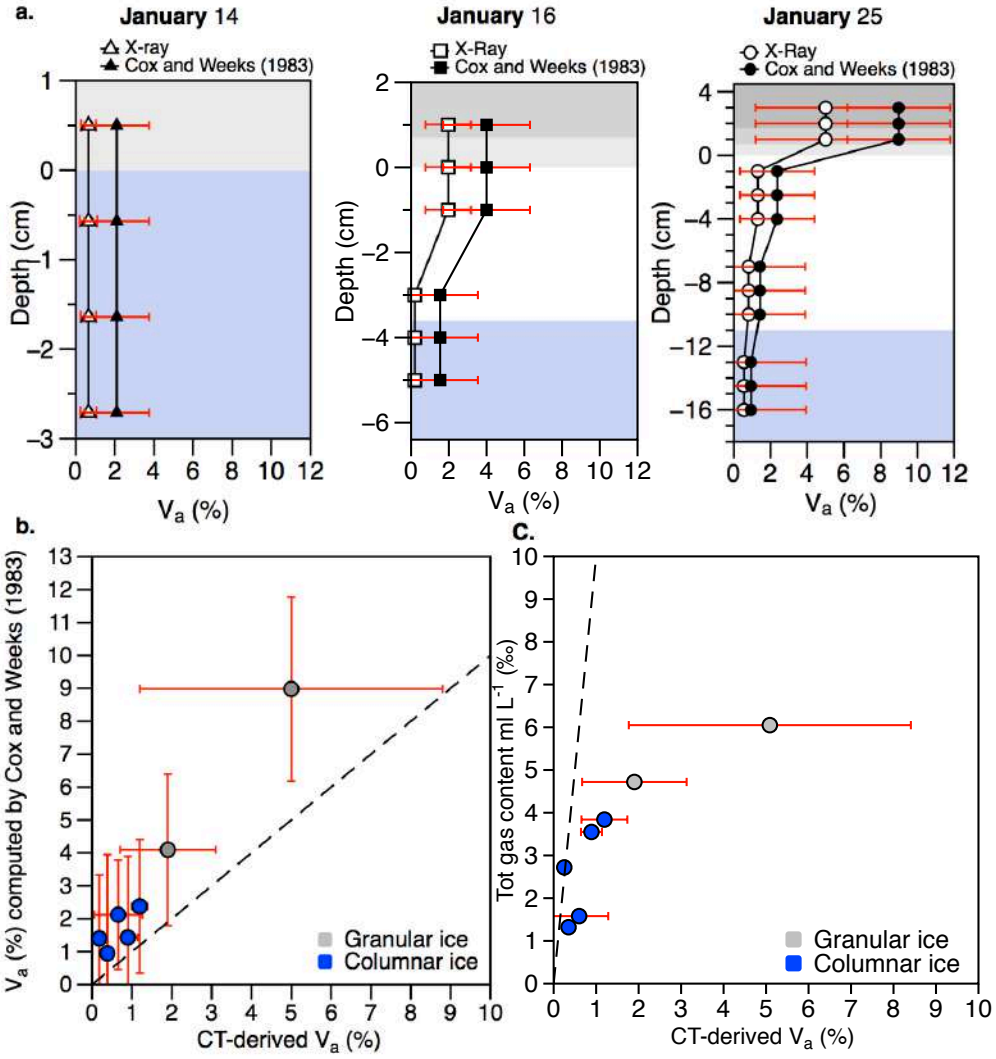

Figure VI-10: (a) Air volume fraction profiles derived from the Cox and Weeks (1983) equations (filled black symbols) using density measurements, with error bars showing the standard deviation from the mean of the results (black symbols). These are compared to the CT-derived air volume fraction averaged for 5-cm section (white symbols) which error bars show the standard deviation of the mean along the 5-cm section. (b) The relationship between CT-derived air volume fraction and the Cox and Weeks (1983) air volume fraction where the dotted line signifies the 1:1 relationship. (c) The relationship between CT-derived air volume and the GC-derived bulk ice total gas content measured where the dotted line signifies the 1:1 relationship. In (b) and (c) the CT-derived air volume fractions are averaged for 5-cm section and error bars show the standard deviation of the mean along the 5-cm section. Where CT-derived air volume fraction spans a large range of values along the section (e.g. granular ice), the standard deviation of CT-derived air volume fraction increases.

Correlation between CT-derived air volume fraction and the bulk ice gas content (ml L^{-1} ice; Figure VI-10c) is not straightforward due in part to methodological constraints. The data compared well in columnar sea ice while in granular layer, we observed large deviations (Figure VI-10c). In granular ice, the total gas content was much lower than the CT-derived air volume fraction. CT-image voxels are 0.0056 mm^3, whereas the bulk ice total gas content was measured on 5-cm sections. Those 5-cm thick sections did not always resolve the changes in ice type. Within the 5-cm sections, gas might span a large range of concentration as does the air volume fraction in granular sea ice (Figure VI-10c, error bar); therefore, if thinner sections had been analyzed for the total gas content (ml L^{-1} ice) the values obtained might have been higher in the top part of the ice core, similar to the CT image data. Moreover, the measurement of the total gas content is a destructive sampling process, involving multiple steps in which the gas could potentially leave the ice. During the cutting process, some bubbles are inevitably cut in half, so part of the gas is lost. This is further complicated by the fact that the probability of cutting a large bubble (with high gas content) is greater than for a small bubble with low gas content. Potential gas loss could also happen during the evacuation phase of the measurement of the total gas content (see section VI-2.3 Gas composition). For all these reasons, the total gas content (ml L^{-1} ice) is likely to be particularly underestimated in the granular surface ice due the analytical procedure. The data however agree well in columnar sea ice. The bulk ice total gas content measured by gas chromatography includes both gas dissolved in brine and gas trapped in bubbles, while CT-derived air volume fraction only account for gas

trapped in bubbles. Then, we expect the total gas content values to be slightly higher than the CT-derived air volume fraction due to the dissolved contribution. In reality, the total gas content appears to be slightly lower (Figure VI-10c). It suggests that either the CT-derived air volume fraction is slightly overestimated in columnar sea ice due to the thresholding process or that the total bulk gas content is slightly underestimated due to gas loss during the cutting and evacuation phase of the measurement. Finally, the bulk ice total gas content was measured on different ice cores from those used for the CT-measurements, which may have introduced some spatial variability.

The temperature during storage finally potentially influences our computation. Storing sea ice at -20°C alters the sea ice microstructure and its inclusions (e.g. Cox and Weeks, 1986). Light et al. (2003) proceeded to a cooling sequence (-2°C to -25°C) and a warming sequence (-25°C to -2°C) on ice thin sections. According to their results cooling sea ice caused inclusions to shrink in size including the disappearance of the smallest air inclusions, while warming increased the size of existing air inclusions without forming new bubbles. Considering that the smallest bubbles could have disappeared and some have shrunk in size, our computed air volume fraction should be considered as a minimum estimate of the true air volume fraction. In the absence of a method that preserves the natural temperature gradient within sea ice immediately and without change upon extraction, *ex situ* analysis of sea ice samples after storage at low temperatures is an established protocol.

Although microstructural analysis of sea ice may produce reliable morphological results for air inclusions, thin sections only represent a small subsample of the ice core, are time consuming, can be operator-dependent, and the area and thickness of a thin section limit these studies to the measurement of intact bubbles within a thin section. Density-derived air volume fraction results from the Mass-Volume technique generally have large errors and very low vertical resolution because they require large core subsample volumes (e.g. 5 cm^3). On the contrary, CT X-ray imaging clearly distinguishes between air inclusions and the ice matrix providing high-resolution sub-millimeter profiles of the air volume vertical distribution with a better precision linked almost entirely to the segmentation process and the resolution of the scanner. X-ray tomography allows: (1) fast visualization of the air inclusions, especially when compared to transmitted images; (2) the ability to increase the size of the dataset compared to thin section microstructural analysis by imaging the whole core. Future work should involve micro CT X-ray with a voxel resolution of an order of magnitude higher than the present one in order to detect the small bubbles in columnar sea ice as well as research on the effect of temperature changes on sea ice air inclusions.

VI.4.2 Size of the air inclusions (i.e. bubbles): Micro, large and macro air porosity

While large and macro bubbles account for less than 14%, 22% and 27% of the bubble population observed for January 14, 16 and 25 respectively (Figure VI-11a), the large and macro bubbles contribute systematically to more than 50% of the total air volume fraction produced (Figure VI-11a). Even in bottom columnar

ice where large bubbles represent less than 10% of the bubble population (Figure VI-11d), they contributed to 40 % and 22 % of the air porosity of bottom columnar ice on 14 and 25 January, respectively (Figure VI-11d). For each ice type (Figure VI-11), granular (b.), columnar impermeable (c.) and columnar permeable (d.)), it is clear that the largest bubbles contribute most to the air porosity (Table VI-4, Figure VI-11), which is not surprising as the latter depends on air bubble size cubed. However, air porosity in the permeable columnar layer where the proportion of large bubbles decreased (Figure VI-12), seems largely to be controlled by the amount of bubbles (i.e. bubble density number). Increasing the number of bubbles produces also a linear increase in the air volume fraction (Figure VI-12) in columnar ice.

Table VI-4: Classification and properties of the air inclusions.

Air inclusion Classification	**Abundance*** **(% of the total Nbr of air inclusions observed)**	**Contribution** (% of V_a produced by the air inclusion)**	**Location**
Micro	78%	29%	Columnar and Granular
Large	20.7%	47%	Columnar and Granular (depends most likely of V_b)
Macro	1.3%	24%	Granular/snow-ice

*The "abundance" is the proportion of micro, large, and macro bubbles on the total number of air inclusions observed (100% is the total number of inclusions in the three data sets (14 Jan+16 Jan+25 Jan)). **The "contribution" is the percentile of the porosity produced by the micro, large and macro inclusions (100% is the total of air volume fraction observed in the three data sets (14 Jan+16 Jan+25 Jan)).

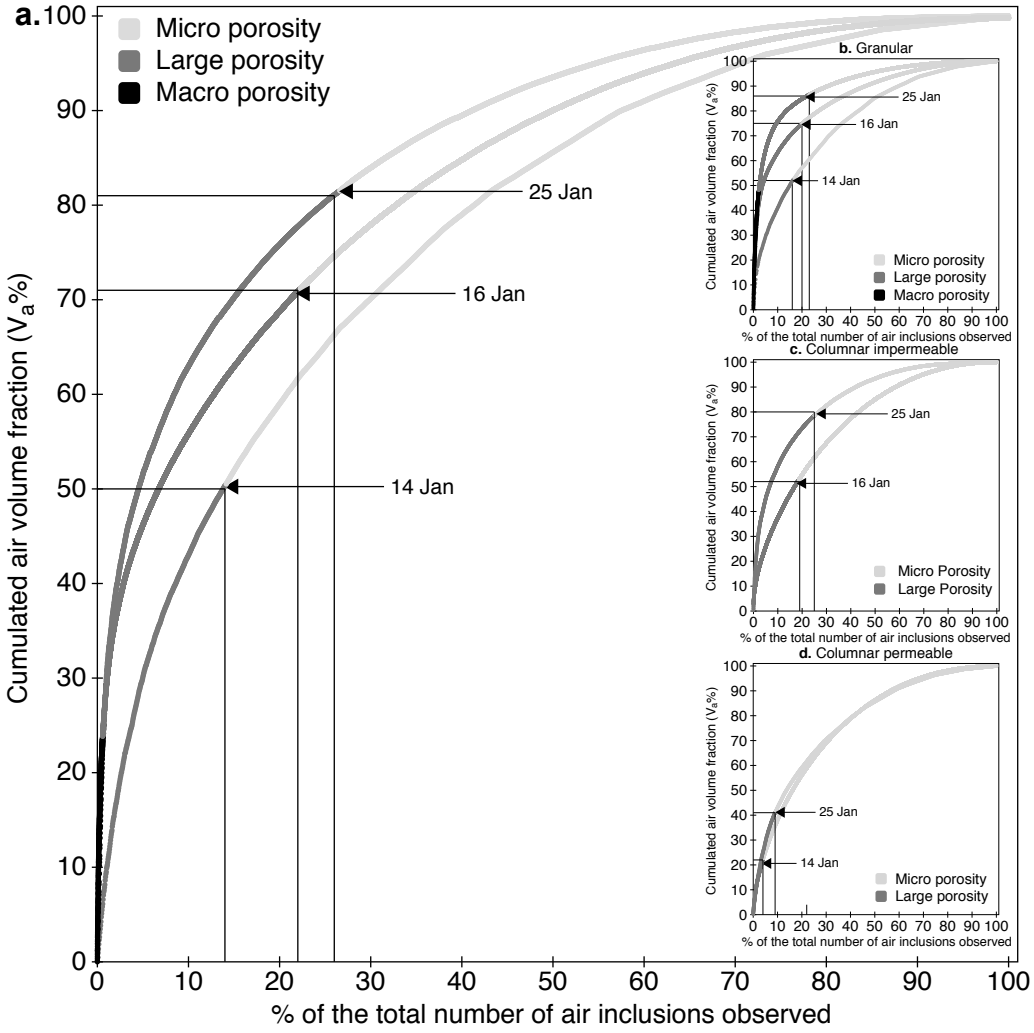

Figure VI-11: The cumulated contribution of the macro, large and micro bubbles to the cumulated relative air volume fraction for the whole ice core (a), and in granular (b), columnar impermeable (c) and columnar permeable ice (d). It shows that, a smaller number of large bubbles (e.g. Large on 25 January) produced most of the air volume fraction (i.e. porosity), and this is true for both the whole ice core (a) and for each type of ice (b, c, d).

For the air volume fraction to increase above 3% (e.g. Figure VI-12 in the granular layer), the presence of large and macro bubbles is required (Figure VI-12).

Large bubbles were more prevalent when brine volume increased (Figure VI-13a, red and grey circles). Light et al. (2003) observed that bubbles were

contained within brine and concluded that bubble size was limited by the size of the brine inclusion in which they resided. In several slices, we observed lighter pixels around air inclusions indicating these bubbles likely formed in a brine pocket. The CT-scanner used here cannot unambiguously identify these pixels as brine inclusions. To visualize both air and brine inclusions in the same images, finer resolution with respect to sample density and finer spatial resolution are required. For example, Obbard et al. (2009) showed that micro X-ray computed tomography with a higher voxel resolution of one order of magnitude is suitable for visualization of brine and air inclusions.

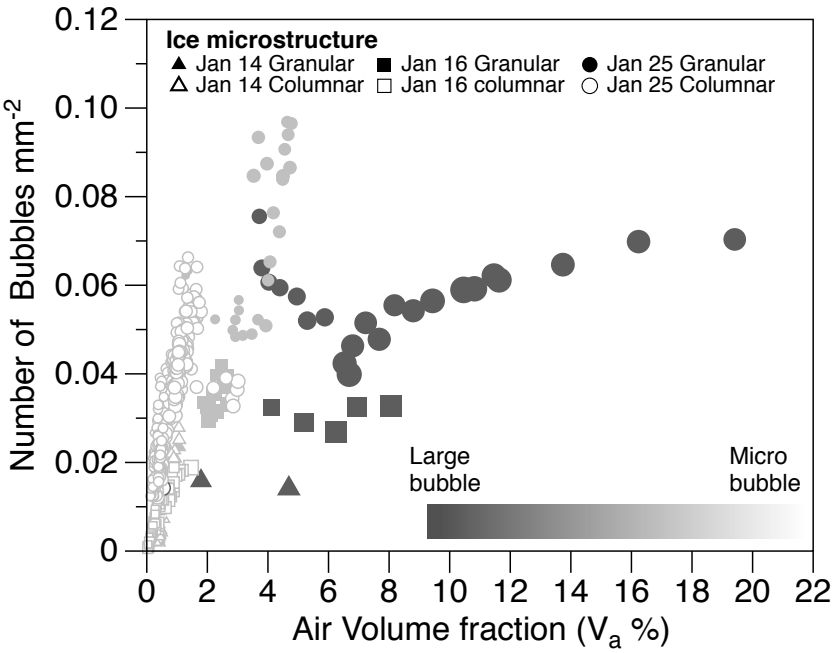

Figure VI-12: The relationship between bubble density: number of bubbles per mm^{-2} (slice area) and air volume fraction per slice as a function of both bubble size class and ice type (granular and columnar crystal texture).

VI.4.3 Mechanism for gas incorporation and bubbles development

In our sea ice samples, the top granular layers are supersaturated, have large air volume fractions (V_a > 5%) and contain macro bubbles. The impermeable columnar layers are supersaturated as well but contain lower air volume fractions (Va < 2%) and contain micro to large bubbles. The bottom permeable columnar layers are subsaturated, contain air volume fractions <1%, and contain almost exclusively micro bubbles (see summary Table IV-5).

Table VI-5: Physical characteristics of the various ice types. Where the brine volume exceeds the permeability threshold for columnar ice of 5% V_b (Golden et al., 1998, 2007), the ice layer is referred to as permeable.

Data		January 14	January 16	January 25
Granular	**Permeability**	Permeable V_b=11%	Permeable V_b=6.2%	Permeable 3.9%<V_b<12%
	Saturation	n/a	Supersaturated SAT_f=9.5	Supersaturated SAT_f=16
	Air volume fraction	0.74%-5.09%	1.8%-10%	0.69%-19.41%
	Bubble class	Micro and large	Micro, large and macro	Micro, large and macro
Intermediate columnar	**Permeability**	n/a	Impermeable	Impermeable
	Saturation	n/a	Supersaturated	Supersaturated
	Air volume fraction	n/a	V_a<2%	V_a<2%
	Bubble class	n/a	Micro and large	Micro and large
Bottom columnar	**Permeability**	Permeable	Permeable	Permeable
	Saturation	Subsaturated SAT_f≤1.2	Subsaturated SAT_f≤1.2	Subsaturated SAT_f≤1.2
	Air volume fraction	Va<1%	Va<1%	Va<1%
	Bubble class	90 % Micro	90 % Micro	90% Micro

In the multiphase sea ice system, the ratio between dissolved gas and bubbles should depend on the bulk ice gas saturation state. In a closed system, when bubble nucleation is exclusively solubility driven, we expect the air volume fraction to be a function of the saturation factor, which would lead to subsaturated sea ice being bubble-free, and high air volume fractions in supersaturated sea ice. However, the observed relationship between air volume fraction and saturation factor is not straightforward (Figure VI-13b) and highlights difference between the type of ice (i) bottom permeable columnar ice, (ii) intermediate impermeable columnar ice and (iii) top granular ice.

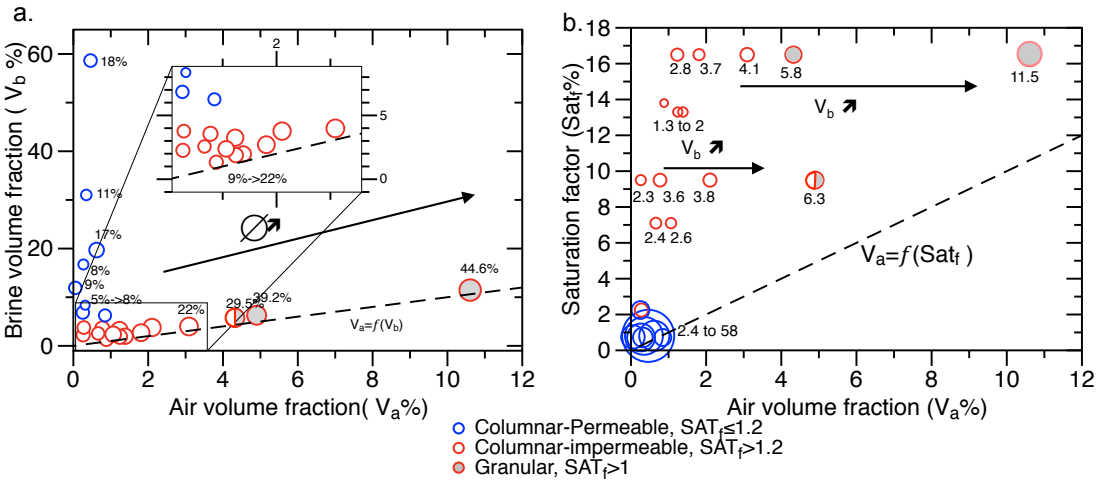

Figure VI-13: (a) Relationship between brine volume fraction and air volume fraction as a function of the bubble size (where the size of each marker circle is proportional to the percentage of bubbles with diameters >1mm, written as %value next to some of circles). (b) Relationship between the air volume fraction and the saturation factor as a function of the brine volume fraction. The size of each circle denotes the brine volume fraction (%, written next to some of the circles). In each panel, the bottom columnar permeable subsaturated ice ($SAT_f \leq 1.2$, blue circles) is differentiated from the columnar impermeable supersaturated ice ($SAT_f > 1.2$, red circles), and from the top granular supersaturated ice ($SAT_f > 1.2$, grey circles). In each panel, the dotted line signifies the 1:1 relationship.

VI.4.3.1 Bottom permeable columnar ice

Within the permeable subsaturated columnar layer near the sea ice bottom, the air volume fraction is lower than 1 % due to the subsaturated state of the ice, and independent of the brine volume fraction (Figure VI-13a and b, blue circles). As long as the brine is able to exchange with the underlying seawater (i.e. when the V_b is > 5% after Golden et al., 1998), the saturation factor remains low and gas species remain dissolved in the brine and can be rejected to the underlying water by convection from the permeable columnar layer. This limits bubble formation, and hence the air volume fraction was < 1% (Figure VI-13a and b, blue circles). Although the air volume fraction is low in these layers, it is somewhat surprising that the air volume fraction is > 0; in theory, bubble nucleation occurs when SAT_f > 1, so these subsaturated layers should be bubble-free, though bubble nucleation from saturated gas solutions has been observed at much lower saturations than theoretically expected (Lubetkin, 2003). On 14 January, 75% of the bubbles observed were located in subsaturated permeable bottom layer of columnar sea ice. On 16 and 25 January, 11% and 13% (respectively) of the air inclusions observed were situated in subsaturated permeable sea ice. Bubble nucleation processes are favoured where (i) there are geometrical imperfections (Wilt 1986); (ii) at "active sites" on a heterogeneous surface that can be chemically, structurally, or geometrically inhomogeneous (Deutscher and Fletcher, 1990; Kozisek et al., 2000); and (iii) by heterogeneous supersaturation away from thermodynamic equilibrium (Li and Yortsos 1994), conditions which are all met in sea ice. The contact of the

three phases (solid ice, liquid brine, air bubble and precipitated salt) in brine inclusions produced a highly heterogeneous surface, which is both chemically and structurally inhomogeneous. Moreover, full-depth convection on 14 January and convection confined to the permeable subsaturated bottom columnar layer of sea ice ($V_b \approx 20\%$) on 16 and 25 January likely produced local fluctuations in the amount of gas-saturated liquid, creating the possibility of local or episodic supersaturation that may have produced bubbles as has been observed by Zhou et al. (2013). Convection driven nucleation processes likely produced micro bubbles in columnar permeable sea ice, which contributed to 9% of the total air volume fraction observed (Table VI-6). Therefore, brine drainage is only effective for the transport of dissolved gas to the underlying seawater. The rejection of dissolved gas contributes to maintain gas concentrations close to the equilibrium. Nucleation processes driven by the convective exchange in the bottom layer however limited by the saturation state increase the total gas content (ml L^{-1} ice) of sea ice by ensuring that gas trapped in bubbles remains within the sea ice and is not rejected to the underlying water (Tison et al., 2002).

On 16 and 25 January, we observed a slight increase of air volume fraction at the transition between the subsaturated permeable columnar sea ice and the supersaturated impermeable columnar sea ice at two-thirds of the total sea ice thickness (isotherm -4.1°C and -3.8°C, respectively) (Figure VI-7b, shaded pink area). This imparts that bubbles created by convection-driven nucleation in the permeable bottom layer, naturally accumulate at the brine permeability transition as result of their buoyancy. Our work indicates that brine will start to supersaturate

(SAT_f = 2.7 to 5) under cooling (isotherm -4.1°C and -3.8°C, respectively) when the sea ice begins to become vertically impermeable to liquid, leading to solubility-driven nucleation. During ice growth period, we could expect an increase of air volume fraction above the permeable bottom layer forming a layer of entrapped bubbles. As long as the intermediate columnar ice stays impermeable (i.e. absence of warming), this bubbly transition layer will grow thicker as the ice thickens.

VI.4.3.2 Intermediate impermeable columnar sea ice

Within the supersaturated impermeable columnar layer, bubble nucleation is solubility driven and we expect the air volume fraction to be a function of the saturation factor. Within the supersaturated impermeable columnar layer, the air volume fraction becomes increasingly a function of the saturation factor as the brine volume increases (Figure VI-13b, red circles). At low brine volumes, the air volume fraction is low regardless of the saturation factor, as indicated by the accumulation of red circles in the top left corner of Figure VI-13b. As brine volume increases in the impermeable supersaturated intermediate columnar layer, both air volume fraction and bubble size increase (Figure VI-13a and b). At a given SAT_f, there are more gas molecules available to go into the gas phase when brine volume increases, thereby increasing the air volume fraction and the size of existing bubbles. We therefore suggest that bubble nucleation is a function of the saturation factor as well as the brine volume. Solubility-driven nucleation produced micro bubbles and large bubbles depending on the brine volume in this layer, contributed to 44% of the total observed air volume fraction (Table VI-6).

VI.4.3.3 Granular sea ice

We observed an increase of air volume fraction nearest the ice-atmosphere interface and generally within the ice surface granular ice layer (Figure VI-7c and d). This granular surface layer had the highest gas content, the highest saturation factor, the highest air volume fraction ($5\% < V_a < 19.4\%$) and contained bubbles with diameters as large as 4.5, 13, and 18 mm on 14, 16 and 25 January, respectively Table IV-5 and Figure VI-9b). The increase of air volume fraction and the total gas content (largely underestimated) in the surface granular layer can be explained by a combination of several processes.

The formation of frazil ice is known to contain more gas than columnar ice because it traps gas directly from the atmosphere (Tsurikov, 1979; Cole et al., 2004; Zhou et al., 2013); this explains the increase of air volume fraction in the frazil ice formed on 14 January. Snow-ice formation observed thereafter on 16 and 25 January trapped gas initially contained within the snow. Moreover, rapid freezing of slush forces gasses out of solution, building up the air volume fraction nearest the ice–atmosphere interface.

Macro bubbles are exclusively found in granular layer. They seem resulting of aggregation of discrete bubble like an aggregation of soap bubbles. A succession of 0.6 mm thick transversal slices at +2.28 cm depth from 25 January is shown in Figure VI-14. In the first slice at +2.28 cm depth (Figure VI-14, far left panel) four individual bubble bases are identifiable from which a single top bubble is formed at +2.46 cm depth (Figure VI-14 far right panel). The rapid freezing of slush in

porous snow could potentially produce bubble aggregation. Granular sea ice and snow-ice accounted for 26% of the bubble population observed, and snow-ice formation accounted for 47% of the total porosity recorded indicating that physical processes associated with snow on new and young sea ice play an important role in the gas dynamics of new and young sea ice.

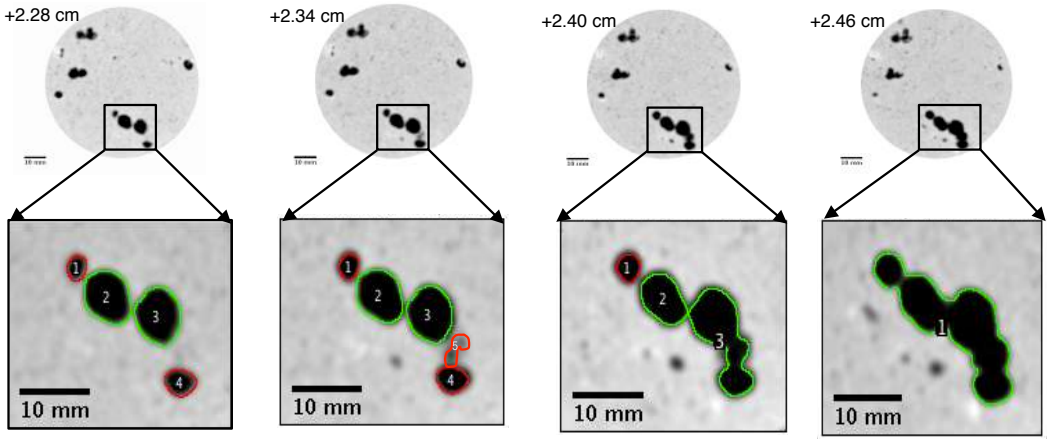

Figure VI-14: Four successive slices in the snow-ice layer on 25 January from+2.28 to+2.46cm below the surface. At 2.28 cm, four individual bottom end of bubbles exist where at 2.46 cm, the top end of each bubbles are joined and formed a single bubble.

VI.4.4 The fate of gas versus the fate of salt

Bulk salinity and bulk ice total gas content (ml L^{-1} ice) of sea ice is lower than in the seawater from which it formed, because gases in seawater are preferentially expelled from growing ice, along with salts (Cox and Weeks, 1983, 1988; Killawee et al., 1998; Tison et al., 2002; Loose et al., 2009, 2011). The range of total gas content values for our samples was 1.6 to 6.5 mL L^{-1}, which is in the lower end of ranges reported by Matsuo and Miyake (1966), Tison et al. (2002) and Crabeck et al. (2014b). Zhou et al. (2013) suggested that gas transport through sea

ice occurs via processes diverging from those controlling the transport of salt. Since we do not observe similar profiles of these two parameters over time, this also suggests that the same processes do not regulate bulk ice salinity and bulk ice gas content. Rapid desalination occurred between 14 and 16 January, and the bulk salinity profile evolved towards a C-shaped profile over time (Figure VI-5). In contrast, we observed a linear increase of gas content (ml L^{-1}) (Figure VI-6) and air volume fraction (Figure VI-7) from the base to the sea ice surface and within sea ice as it thickened over time. The transport of gases through sea ice is different from that of the solutes because gases may be present in the form of bubbles, on top of being dissolved in the brine. Our results indicate that a great deal of the gas content of sea ice exists in bubbles and not in the dissolved phase in brine, suggesting that desalination processes have a limited effect on sea ice gas content. Salts dissolved in brine can diffuse and/or be rejected in the underlying seawater during brine convection events, while bubbles are trapped in the ice matrix and can only migrate upward by buoyancy.

The presence of large bubbles and air volume fraction > 5% in the top of the ice cover should potentially mediate gas fluxes over sea ice. Partitioning between gaseous phase and dissolved phase is of paramount importance for gas transport in sea ice, as it controls the direction of transport – upward versus downward as well as the magnitude. If the gases are in the dissolved phase, they will be mainly transported downwards with the brine, like the other solutes. Few exceptions are the gas diffusion within the brine network that transport gases both ways in function of the concentration gradient (Crabeck et al., 2014a), and upward

brine expulsion at the ice-atmosphere interface. If the gases are in the gas phase (i.e. bubbles), they are only transported upward due to bubbles buoyancy. Kotovich et al. (2016) observed that air-ice gas transfer coefficients for CO_2 in young permeable artificial sea ice is 5 times larger during ice growth compared to ice decay. They suggest that this difference is due to the formation and transport of bubbles during ice growth. This process appears to provide a very efficient pathway to transport gases within and out of the ice. Indeed, 1D modelling suggests that bubbles migrating upward out of the ice contribute to 80% of the CO_2 fluxes from sea ice to the atmosphere during ice growth (Kotovitch et al., 2016).

Table VI-6: Main parameters influencing the air volume fraction.

Nucleation Processes	**Limitation factor**	***Abundance (% of the total Nbr of air inclusions observed)**	***Contribution (% of V_a produced by the inclusions)**	**Type of air inclusions produced**	**Location**
Convection driven	Saturation level	14%	9%	Most likely micro	subsaturated columnar
Solubility Driven	Brine volume fraction	60%	44%	Micro to large	Supersaturated Columnar
Snow-ice formation		26%	47%	Micro Large Macro	Granular/ snow--ice

*****The "abundance" is the proportion of the inclusions concerned by the processes on the total of inclusion observed (100% is the total of inclusions observed in the three data sets (14 Jan+16 Jan+25 Jan)). ******The "contribution" is the percentile of the porosity produced by the inclusions formed by convection driven, solubility driven and snow-ice formation processes, respectively (100% is the total of air volume fraction observed in the three data sets (14 Jan+16 Jan+25 Jan)).

VI-5 Conclusions and perspectives

We used computed tomography X-ray imaging to quantify air inclusion distribution in sea ice, from which we derive the air volume fraction. Air inclusions are quickly and easily identified by X-ray tomography and quantitatively analyzed using segmentation techniques. The threshold selection is a crucial step requiring careful examination to provide successful results. The results from the CT X-ray analysis showed similar trends to conventional density and bulk ice total gas content (ml L^{-1} ice) measurement methods. X-ray imaging is non-destructive and allows for a direct determination of air inclusions in sea ice at high resolution with low errors and creates large datasets very quickly. However, the medical CT-scan show some limitation to resolve air inclusions in columnar sea ice, since accurate definition of air inclusion in columnar sea ice would require higher resolution. Further studies should involve Micro-CT scan with pixel size of an order of magnitude smaller.

We differentiate between micro bubbles, large bubbles and macro bubbles based on their diameters. Micro bubbles are found both in the bottom columnar permeable layers ($V_b > 5\%$) and in the intermediate columnar impermeable layers ($V_b < 5\%$) as well as in granular layers. Large bubbles are found more frequently where brine volume exceeded 5% and macro bubbles occur exclusively in the granular snow-ice layer (i.e. ice formed by the infiltration of snow) nearest the ice-atmosphere interface. Although micro bubbles are the most abundant type of bubbles observed, they only accounted for 14% of the total air volume fraction produced. In contrast, macro bubbles linked to granular snow-ice layer accounted

for 1% of the total number of bubbles but they produced 29% of the air volume fraction observed. While the air volume fraction results from a mix of micro, large and, macro bubbles, the factor controlling the air volume fraction is most likely the size of the air inclusions (i.e. bubbles) (Table VI-4).

We suggest that bubbles observed in the bottom subsaturated permeable layers are formed by convection-driven nucleation. Here the amount and size of the bubbles are limited by the low saturation state of the brine. Bubbles observed in impermeable columnar supersaturated sea ice are formed by solubility-driven nucleation, where the amount and bubble size is limited by the amount of brine. In growing sea ice, a maximum exists at a given depth just above the permeability transition, confirming the important role of this transition zone in shaping the vertical air volume fraction distribution. Macro bubbles located in the near-surface sea ice are linked to the presence of granular ice and the formation of snow-ice (Table VI-6).

We conclude that processes regulating the vertical distribution of salts do not control the vertical distribution of gases, because most of the total gas content (ml L^{-1} ice) exists as bubbles rather than being dissolved in the brine as previously argued (Tison et al., 2002; Zhou et al., 2013; Crabeck et al., 2014a,b; Moreau et al., 2014). Once micro and/or macro bubbles form they are segregated from the transport pathway of dissolved salts, because bubbles will not drain out of the ice by convection due to their low density, so nucleation leads to an accumulation of gas in sea ice. Our work provides the first detailed visual demonstration and quantification of these processes.

As a result of the presence of large bubbles and higher air volume fraction measurements in sea ice we introduce new perspectives on processes regulating gas exchange at the ice-atmosphere interface, and note that further work should investigate, the effect of air volume fraction on sea ice permeability parameterizations. CT X-ray imaging may allow for visualizations of transport pathways, for example the upward migration of bubbles. CT X-ray imaging could be used to investigate the effect of different thermal and crystal texture regimes on bubble formation, dimensions, and their vertical and horizontal distribution in a large number of replicate cores from the same ice cover. This information is vital to the improvement of models involving transport of biochemical compounds and gas transfer between the ocean and the atmosphere in polar oceans.

References

Bennington, K. O.: Desalination features in natural sea ice, J. Glaciol., 6, 845–857,1967.

Bock, C. and Eicken, H.: A magnetic resonance study of temperature-dependent microstructural evolution and self- diffusion of water in Arctic first-year sea ice, Ann. Glaciol., 40, 179–184, 2005.

Carte, A. E.: Air bubbles in ice, Proc. Phys. Soc., 77, 757–768, 1961.

Cole, D. M. and Shapiro, L. H.: Observations of brine drainage net- works and microstructure of first-year sea ice, J. Geophys. Res., 103, 21739–21750, 1998.

Cole, D. M., Eicken, H., Frey, K., and Shapiro, L. H.: Observations of banding in first-year Arctic sea ice, J. Geophys. Res., 109, C08012, 10.1029/2003JC001993, 2004.

Cox, G. F. N. and Weeks, W. F.: Brine drainage and initial salt entrapment in sodium chloride ice, Report 345, Cold Regions Research and Engineering Laboratory Research, Hanover, NH, 1975.

Cox, G. F. N. andWeeks,W. F.: Equations for determining the gas and brine volumes in sea-ice samples, J. Glaciol., 29, 306–316, 1983.

Cox, G. F. N. and Weeks,W. F.: Changes in the salinity and porosity of sea-ice samples during shipping and storage, J. Glaciol., 32, 371–375, 1986.

Cox, G. F. N. and Weeks,W. F.: Numerical simulations of the pro- file properties of undeformed first-year sea ice during the growth season, J. Geophys. Res.-Oceans, 93, 12449–12460, 1988.

Crabeck, O., Delille, B., Else,.B, Thomas, D. N., Geilfus, N. X., Rysgaard, S., and Tison, J. L.: First "in situ" determination of gas transport coefficients (DO2, DAr, and DN2) from bulk gas concentration measurements (O2, N2, Ar) in natural sea ice, J. Geophys. Res.-Oceans, 119, 6655–6668, 10.1002/2014JC009849, 2014a.

Crabeck, O., Delille, B., Thomas, D., Geilfus, N.-X., Rysgaard, S., and Tison, J.-L.: CO2 and CH4 in sea ice from a subarc- tic fjord under influence of riverine input, Biogeosciences, 11, 6525–6538, 10.5194/bg-11-6525-2014, 2014b.

Delille, B., Vancoppenolle, M., Geilfus, N.-X., Tilbrook, B., Lannuzel, D., Schoemann, V., Becquevort, S., Carnat, G., Delille, D., Lancelot, C., Chou, L., Dieckmann, G. S., and Tison, J.-L.: Southern Ocean CO2 sink: The contribution of the sea ice, J. Geophys. Res.-Oceans, 119, 6340–6355, 10.1002/2014JC009941, 2014.

Deutscher, R. L. and Fletcher, S.: Nucleation of Active Sites: 5. The Theory of Nucleation Rate Dispersion, J. Electroanalyt. Chem., 277, 1–18, 1990.

Duliu, O. G.: Computer axial tomography in geosciences: An overview, Earth-Sci. Rev., 48, 265–281, 1999.

Eicken, H., Lange, M. A., and Dieckmann, G. S.: SpatialVariability of Sea–Ice Properties in the Northwestern Weddell Sea, J. Geo- phys. Res., 96, 10603–10615, 1991.

Eicken, H., Bock, C., Wittig, R., Miller, H., and Poertner, H.-O.: Magnetic resonance imaging of sea-ice pore fluids: methods and thermal evolution of pore microstructure, Cold Reg. Sci. Tech- nol., 31, 207–225, 2000.

Eide, L. I. and Martin, S.: The formation of brine drainage features in young sea ice, J. Glaciol., 14, 137–154, 1975.

Feltham, D. L., Untersteiner, N., Wettlaufer, J. S., and Worster, M. G.: Sea ice is a mushy layer, Geophys. Res. Lett., 33, L14501, 10.1029/2006GL026290, 2006.

Fritsen, C. H., Lytle, V. I., Ackley, S. F., and Sullivan, C. W.: Au- tumn bloom of Antarctic pack-ice algae, Science, 266, 782–784, 1994.

Galley, R. J., Else, B. G. T., Geilfus, N.-X., Hare, A. A., Isleifson, D., Barber, D. G., and Rysgaard, S.: Imaged brine inclusion in young sea ice – Shape, distribution and formation timing, Cold Reg. Sci. Technol., 111, 39–48, 10.1016/j.coldregions.2014.12.011, 2015.

Garcia, H. E. and Gordon, L. I.: Oxygen solubility in seawater – bet- ter fitting equations, Limnol. Oceanogr., 37, 1307–1312, 1992.

Geilfus, N.-X., Carnat, G., Dieckmann, G. S., Halden, N., Nehrke, G., Papakyriakou, T., Tison, J. L., and Delille, B.: First estimates of the contribution of CaCO3 precipitation to the release of CO2 to the atmosphere during young sea ice growth, J. Geophys. Res.-Oceans, 118, 244–255, 2013.

Geilfus, N.-X., Tison, J.-L., Ackley, S. F., Rysgaard, S., Miller, L. A., and Delille, B.: Sea ice pCO2 dynamics and air–ice CO2 fluxes during the Sea Ice Mass Balance in the Antarctic (SIMBA) experiment – Bellingshausen Sea, Antarctica, The Cryosphere, 8, 2395–2407, 10.5194/tc-8-2395-2014, 2014.

Geilfus, N.-X., Galley, R. J., Crabeck, O., Papakyriakou, T., Landy, J., Tison, J.-L., and Rysgaard, S.: Inorganic carbon dynamics of melt-pond-covered first-year sea ice in the Canadian Arctic, Biogeosciences, 12, 2047–2061, 10.5194/bg-12-2047-2015, 2015.

Golden, K. M., Ackley, S. F., and Lytle, V. I.: The percolation phase transition in sea ice, Science, 282, 2238–2241, 1998.

Golden, K. M., Eicken, H., Heaton, A. L., Miner, J., Pringle, D. J., and Zhu, J.: Thermal evolution of permeability and microstructure in sea ice, Geophys. Res. Lett., 34, L16501, 10.1029/2007GL030447, 2007.

Grasshoff, K., Erhard, M., and Kremling, K.: Methods of seawater analysis, 2nd Edn., Verlag-Chemie,Weinhem, Germany, 1983.

Grenfell, T. C.: A theoretical model of the optical properties of sea ice in the visible and near infrared, J. Geophys. Res., 88, 9723– 9735, 1983.

Hamme, R. C. and Emerson, S. R.: The solubility of neon, nitrogen and argon in distilled water and seawater, Deep-Sea Res. Pt. I, 51, 1517–1528, 2004.

Hare, A. A., Wang, F., Barber, D., Geilfus, N.-X., Galley, R. J., and Rysgaard, S.: pH evolution in sea ice grown at an outdoor experimental facility, Mar. Chem., 154, 46–54, 10.1016/j.marchem.2013.04.007, 2013.

Hounsfield, G. N. : Computerized transverse axial scanning (tomography). Part 1: Description of system, British J. Radiol., 46, 1016–1022, 1973.

Hunter, M. W., Dykstra, R., Lim, M. H., Haskell, T. G., and Callaghan, P. T.: Using Earth's field NMR to study brine content in Antarctic sea ice: Comparison with salinity and temperature estimates, Appl. Magnet. Reson., 36, 1–8, 10.1007/s00723- 009-0003-9, 2009.

Iassonov, P., Gebrenegus, T., and Tuller, M.: Segmentation of X-ray computed tomography images of porous materials: Acrucial step for characterization and quantitative analysis of pore structures, Water Resour. Res., 45, W09415, 10.1029/2009WR008087, 2009.

Kapur, J. N., Sahoo, P. K., and Wong, A. K. C.: A new method for gray-level picture thresholding using the entropy of the histogram, Graph. Models Image Process., 29, 273–285, 10.1016/0734-189X(85)90125-2, 1985.

Kawamura, T.: Observations of the internal structure of sea ice by X ray computed tomography, J. Geophys. Res., 93, 2343–2350, 10.1029/JC093iC03p02343, 1988.

Killawee, J. A., Fairchild, I. J., Tison, J. L., Janssens, L., and Lor- rain, R.: Segregation of solutes and gases in experimental freezing of dilute solutions: Implications for natural glacial systems, Geochim. Cosmochim. Acta, 62, 3637–3655, 1998.

Knoll, G. F.: Radiation Detection and Measurment, John Wiley & Sons, New York, 1989.

Kotovitch, M., Moreau S., Zhou J., Vancoppenolle M., Gerhard S., Dieckmann, Evers K.-U., Van der Linden F., Thomas D., Tison J.-L., Delille B.: Air-ice carbon pathways inferred from a sea ice tank experiment, Elementa: Science of the Anthropocene, 75, 7212-7220, 10.1128/AEM.02227-09, 2016.

Kozisek, Z., Demo, P., and Sato, K.: Nucleation on active sites: Evolution of size distribution, J. Cryst. Growth, 209, 198–202, 2000.

Krembs, C., Gradinger, R., and Spindler, M.: Implications of brine channel geometry and surface area for the interaction of sympagic organisms in Arctic sea ice, J. Exp. Mar. Biol. Ecol., 243, 55–80, 2000.

Langway, C. C.: Ice fabrics and the universal stage Rep. 62, US Snow, Ice and 496 Permafrost Research Establishment, Wilmette, Illinois, 1958.

Light, B., Maykut, G. A., and Grenfell, T. C.: Effects of temperature on the microstructure of first-year Arctic sea ice, J. Geophys. Res., 108, 3051, 10.1029/2001JC000887, 2003.

Loose, B., McGillis, W. R., Schlosser, P., Perovich, D., and Takahashi, T.: Effects of freezing, growth, and ice cover on gas trans- port processes in laboratory seawater experiments, Geophys. Res. Lett., 36, L05603, 10.1029/2008gl036318, 2009.

Loose, B., Schlosser, P., Perovich, D., Ringelberg, D., Ho, D. T., Takahashi, T., Richter-Menge, J., Reynolds, C. M., McGillis, W. R., and Tison, J. L.: Gas diffusion through columnar laboratory sea ice: implications for mixed-layer ventilation of CO2 in the seasonal ice zone, Tellus B, 63, 23–39, 10.1111/j.1600- 0889.2010.00506.x, 2011.

Lubetkin, S. D.: Why is it much easier to nucleate gas bubbles than theory predicts?, Langmuir, 19, 2575–2587, 2003.

Matsuo, S. and Miyake, Y.: Gas composition in ice samples from Antarctica, J. Geophys. Res., 71, 5235–5241, 1966.

Moreau, S., Vancoppenolle, M., Zhou, J., Tison, J.-L., Delille, B., and Goosse, H.: Modelling argon dynamics in first-year sea ice, Ocean Model., 73, 1–18, 2014.

Nomura, D., Yoshikawa-Inoue, H., Kobayashi, S., Nakaoka, S., Nakata, K., and Hashida, G.: Winter-to-summer evolution of pCO_2 in surface water and air–sea CO2 flux in the seasonal ice zone of the Southern Ocean, Biogeosciences, 11, 5749–5761, 10.5194/bg-11-5749-2014, 2014.

Notz, D. and Worster, M. G.: In situ measurements of the evolution of young sea ice, J. Geophys. Res., 113, C03001, 10.1029/2007JC004333, 2008.

Obbard, R., Troderman, G., and Baker, I.: Imaging brine and air inclusions in sea ice using micro-X-ray computed tomography, correspondance, J. Glaciol., 55, 1113–1115, 2009.

Otsu, N.: A threshold selection method from gray-level histograms, IEEE Trans. Syst. Man Cybern., 9, 62–66, 10.1109/TSMC.1979.4310076, 1979.

Pal, N. R.: Minimum cross entropy threshold selection, Pattern Recog., 29, 575–580, 10.1016/0031-3203(95)00111-5, 1996.

Pal, N. R., and Pal, S. K.: Entropic thresholding, Signal Process., 16, 97–108, 10.1016/0165-1684(89)90090-X, 1989.

Perovich, D. K. and Gow, A. J.: A statistical description of the microstructure of young sea ice, J. Geophys. Res., 96, 16943– 16953, 10.1029/91JC01594, 1991.

Perovich, D. K. and Gow, A. J.: Aquantitative description of sea ice inclusions, J. Geophys. Res.- Oceans, 101, 18327–18343, 1996.

Pringle, D. J., Miner, J. E., Eicken, H., and Golden, K. M.: Pore space percolation in sea ice single crystals, J. Geophys. Res., 114, C12017, 10.1029/2008JC005145, 2009.

Raynaud, D., Delmas, R., Ascencio, M., and Legrand, M.: Gas extraction from polar ice cores: a critical issue for studying the evolution of atmospheric CO2 and ice-sheet surface elevation, Ann. Glaciol., 3, 265–268, 1982.

Rees Jones, D. W. and Worster, M. G.: A simple dynamical model for gravity drainage of brine from growing sea ice, Geophys. Res. Lett., 40, 1–5, 10.1029/2012GL054301, 2013.

Ridler, T.W. and Calvard, S.: Picture thresholding using an iterative selection method, IEEE Trans. Syst. Man Cybern., 8, 630–632, 1978.

Rosin, P. L.: Unimodal thresholding, Pattern Recog., 34, 2083– 2096, 10.1016/S0031-3203(00)00136-9,1978, 2001.

Rysgaard, S. and Glud, R. N.: Anaerobic N2 production in Arctic sea ice, Limnol. Oceanogr., 49, 86–94, 2004.

Rysgaard, S.,Wang, F., Galley, R. J., Grimm, R., Notz, D., Lemes, M., Geilfus, N.-X., Chaulk, A., Hare, A. A., Crabeck, O., Else, B. G. T., Campbell, K., Sørensen, L. L., Sievers, J., and Pa- pakyriakou, T.: Temporal dynamics of ikaite in experimental sea ice, The Cryosphere, 8, 1469–1478, 10.5194/tc-8-1469- 2014, 2014.

Semiletov, I. P., Makshtas, A., Akasofu, S. I., and Andreas, E. L.: Atmospheric CO2 balance: The role of Arctic sea ice, Geophys. Res. Lett., 31, L05121, 10.1029/2003GL017996, 2004.

Sezgin, M. and Sankur, B.: Survey over image thresholding techniques and quantitative performance evaluation, J. Electron. Imaging, 13, 146–165, 10.1117/1.1631315, 2004.

Shannon, C. E. and Weaver, W.: The mathematical theory of communication, Bell Syst. Tech. J., 27, 379–423, 1948.

Skoog, D. A., West, D. M., and Holler, F. J.: Chimie Analytique, De Boeck Univ., Paris, 1997.

Stefels, J., Carnat, G., Dacey, J. W. H., Goossens, T., Elzenga, J. T. M., and Tison, J. L.: The analysis of dimethylsulfide and dimethylsulfoniopropionate in sea ice: Dry-crushing and melting using stable isotope additions, Mar. Chem., 128–129, 34–43, 2012.

Timco, G.W. and Frederking, R. M.W.: A review of sea ice density, Cold Reg. Sci. Technol., 24, 1–6, 1996.

Tison, J. L., Haas, C., Gowing, M. M., Sleewaegen, S., and Bernard, A.: Tank study of physico-chemical controls on gas content and composition during growth of young sea ice, J. Glaciol., 48, 177– 191, 2002.

Tison, J.-L., Worby, A., Delille, B., Brabant, F., Papadimitriou, S., Thomas, D., de Jong, J., Lannuzel, D., and Haas, C.: Temporal evolution of decaying summer first-year sea ice in the West- ernWeddell Sea, Antarctica, Deep-Sea Res. Pt. II, 55, 975–987, 2008.

Tsai, D. M.: A fast thresholding selection procedure for multimodal and unimodal histograms, Pattern Recog. Lett., 16, 653–666, 10.1016/0167-8655(95)80011-H, 1995.

Tsurikov, V. : The formation and composition of the gas content of sea ice, J. Glaciol., 22, 67–81, 1979.

UNESCO: Eight report of the joint panel on oceanographic tables and standards, UNESCO Tech. Pap. Mar. Sci., Paris, France, 28 pp., 1978.

Vancoppenolle, M., Meiners, K. M., Michel, C., Bopp, L., Brabant, F., Carnat, G., Delille, B., Lannuzel, D., Madec, G., Moreau, S., Tison, J.-L., and van der Merwe, P.: Role of sea ice in global biogeochemical cycles: Emerging views and challenges, Quaternary Sci. Rev., 79, 207–230, 10.1016/j.quascirev.2013.04.011, 2013.

Weeks,W. F. and Ackley, S. F.: The growth, structure and properties of sea ice, in: The geophysics of sea ice, edited by: Untersteiner, N., Plenum Press, New York, 9–164, 1986.

Wilt, P. M.: Nucleation rates and bubble stability in water– carbon dioxide solutions, J. Colloid Interf. Sci., 112, 530–538, 10.1016/0021-9797(86)90122-0, 1986.

Worster, M. G.: The dynamics of mushy layers, in: Interactive Dynamics of Convection and Solidification, NATO ASI Ser. E219, Kluwer, Dordrecht, 113–138, 1992.

Worster, M. G.: Convection in mushy layers, Annu. Rev. Fluid Mech., 29, 91–122, 1997.

Yen, J.-C., Chang, F. J., and Chang, S.: A new criterion for automatic multilevel thresholding, IEEC Trans. Image Process., 4, 370–378, 10.1109/83.366472, 1995.

Zack, G. W., Rogers, W. E., and Latt, S. A.: Automatic measurement of a sister chromatid exchange frequency, J. Histochem. Cytochem., 25, 741–753, 1997.

Zemmelink, H. J., Delille, B., Tison, J. L., Hintsa, E. J., Houghton,L., and Dacey, J. W. H.: CO2 deposition over the multi-year ice of the western Weddell Sea, Geophys. Res. Lett., 33, L13606, 10.1029/2006GL026320, 2006.

Zhou, J. Y., Delille, B., Eicken, H., Vancoppenolle, M., Brabant, F., Carnat, G., Geilfus, N. X., Papakyriakou, T., Heinesch, B., and Tison, J. L.: Physical and biogeochemical properties in land- fast sea ice (Barrow, Alaska): Insights on brine and gas dynamics across seasons, J. Geophys. Res.-Oceans, 118, 3172–3189, 10.1002/jgrc.20232, 2013.

Chapter-VII-Conclusions

VII-1 Summary of key findings

The work presented in this thesis has opened a new avenue for advancing knowledge on gas composition, porosity, and exchange processes in sea ice. These are controlling factors for gas entrapment and transport between the ocean and atmosphere in ice-covered seas.

In chapter IV, I investigated the transport of major atmospheric gases (Ar, O_2, N_2) by diffusion and the physical state of these gases (dissolved or gaseous) in cold natural sea ice from a subarctic fjord in Greenland. The computation of bulk ice transport coefficients for Ar, N_2, and O_2, shows that diffusion is the major determinant of gas fluxes across sea ice in impermeable ice layers (V_b<5%). Diffusive transport across the porous sea ice cover is an alternative transport process for ocean–ice-atmosphere exchange of gas in the absence of convective exchange between ice and underlying seawater (i.e. brine drainage). The effective diffusivities for Ar, O_2, and N_2 were close to the aqueous diffusion rate ($10^{-5}cm^2s^{-1}$). However, based on the solubility law, it was estimated that most gases in impermeable ice layers were contained in bubbles rather than being dissolved in brine. In these estimations, I assumed no oversaturation state exists in brine meaning that gases start to nucleate once their concentrations exceed the saturation point, given that the total partial pressure of all three major atmospheric gases (Ar, O_2, N_2) is above the brine hydrostatic pressure (1 atm). Thus, the preference for

gases to exist in bubbles does not exclude an aqueous diffusion through the brine medium. This work therefore extends to natural sea ice, the hypothesis that there is a connection and exchange between air-filled porosity and liquid-filled porosity (Loose et al., 2011). In addition, some insight on parameters controlling the total gas content was provided. Specifically, our data shows that the ice was rich in low soluble gas (N_2) compared to Ar and O_2 due to the solubility partitioning effect, and that nucleation processes appeared at a saturation factor between 1.9 and 4.9.

As suggested in chapter IV, major atmospheric gases are preferentially residing in gaseous phase in bubbles instead of being dissolved in brine. Therefore, in chapter VI I focused on the air porosity and bubble distribution. I developed a non-destructive methodology using a CT-X-ray imaging system, which provides an accurate visualization and characterization of the air volume fraction at high resolution. Application of this methodology distinguishably contributes to the field, as it provides the first vertical profile of air volume fraction as well as bubble size distribution in sea ice. Substantiation of air porosity in columnar internal layers and granular top layers questions the traditional sea ice mathematical description in which the air volume fraction is currently neglected (Taylor and Feltham, 2004; Feltham et al., 2006; Notz and Worster, 2009). Moreover, the evidence of air volume fraction over 5% in granular top layers with the presence of macro bubbles, introduces new challenges for the interpretation of sea ice atmosphere gas exchange. The CT-X-ray technique was compared to two others methods: (i) the dry crushing technique, which collects both fractions of gases, the dissolved fraction in the brine and gaseous fraction in bubbles; and (ii) the density (M/V)

derived air volume fraction using the equation of Cox and Weeks (1983). Following comparison, it is clear that the density (M/V) method is unreliable in deriving the air volume fraction, and that the dry crushing technique underestimates the total gas content due to gas leakage during the sampling procedure (cutting and vacuum step). Finally, it was suggested in chapter VI that no linear dependency exists between the air volume fraction and saturation factor, challenging the preceding methodology that estimated the air volume fraction using the solubility law, as in chapter IV.

While studies in chapters IV and VI focused on major atmospheric gases, greenhouse gas content (CO_2 and CH_4) was investigated in chapter V. In order to understand how sea ice interacts with the underlying seawater and the fjord system, I used a multi-disciplinary approach which involved sampling from underlying seawater, river water, snow layer, and tracers such as $\delta^{18}O$. By using this multi-disciplinary approach, I was able to link the increase in total gas content to riverine input in the fjord, which highlights the need for a multi-disciplinary sample approach in coupling systems. Bulk ice CH_4 concentration ranged from 1.8 to 12.1 nmol L^{-1}, which corresponds to a partial pressure ranging from 3 to 28 ppmv (1.5 to 15 times the atmospheric concentration). Evidently, most of the trapped CH_4 within the ice was contained in bubbles and only a minor portion was dissolved in brine. The partial pressure of CH_4 exceeded the atmospheric CH_4 content and as such sea ice could potentially be a transient source of CH_4 for the atmosphere. During periods of sea ice cover, CH_4 can accumulate within or below the sea ice, and therefore when the ice breaks up and melts during spring and summer, large

CH_4 fluxes to the atmosphere can be expected. The bulk ice pCO_2 ranged from 60 to 330 ppmv, indicating that sea ice at temperatures above -4°C was undersaturated compared to the atmosphere (390 ppmv). This work adds to the few existing studies on CO_2 content in sea ice – knowledge on this topic is required for proper modeling and crucial for evaluating the role of coastal Arctic sea ice in the carbon cycle. The results of this studies represent an important first step in revealing how sea ice can affect CH_4 fluxes, as they reported the second measurements of bulk ice CH_4 concentration (the first originating from Zhou et al., 2014).

VII-2 Conceptual model of factors controlling gas content in first year impermeable sea ice

Gas content and fluxes in a complex medium such as sea ice are controlled by various factors as highlighted in the chapters above. However, my work has provided key data in natural and artificial sea ice on the various components of diffusional transport, gas content, and air porosity. In the following section, the various findings are integrated into a conceptual model, which illustrates the factors and processes controlling gas content in first year impermeable sea ice (cold winter ice). This model considers the ice as a three-phase medium; a solid pure ice matrix with a network of liquid brine inclusions in which air bubbles reside (Light et al., 2003).

According to our results and cited literature, the vertical distribution of gas in impermeable first year sea ice is a function of (i) the physical condition at the ice-seawater interface (Figure VII-1-(1)) and (ii) nucleation processes occurring either in the bottom layer (Figure VII-1-(1)), within the ice itself (Figure VII-1-(2))

or at the ice-atmosphere interface (Figure VII-1-(3)).

Once incorporated within the ice, gas can be further redistributed or released to the underlying seawater and to the above atmosphere by diffusion transport, convective transport, and buoyant transport (Table VII-1: Synthesis of gas transport across impermeable sea ice cover). Convective transport (i.e. brine drainage) expels dissolved gas into underlying seawater (Figure VII-1-(1)) (Zhou et al., 2013; Else et al., 2015; Crabeck et al., 2016), diffusion transport redistributes dissolved gases along a concentration gradient and governs the flux of gas at the sea ice-atmosphere interface (Figure VII-1-(2)) (Nomura et al., 2006; Loose et al., 2011; Crabeck et al., 2014a), and buoyant transport causes the upward migration of bubbles, which could ultimately lead to a release of gas to the atmosphere given that the brine is sufficiently connected (Figure VII-1-(1) and 1-(3)) (Zhou et al., 2013; Moreau et al., 2014).

Table VII-1: Synthesis of gas transport across impermeable sea ice cover in winter.

Transport	Conditions	In the vertical	Gas	Effect
Convection	-V_b>5%; Ra>5*	-Ice-seawater interface (winter condition)	Dissolved	-Rejection into the underlying seawater
Diffusion	-V_b<5%; Ra <5* -Concentration gradient	-Ice-seawater interface -Internal layer -Ice-atmosphere interface	Dissolved	-Redistribution within the sea ice cover -Released of gas to the atmosphere
Buoyant	-V_b>7 %**	-Ice-seawater interface (winter sea ice) -Ice-atmosphere interface	Air bubbles	-Local accumulation of bubbles at permeability transition -Released of gas to the atmosphere

Ra <5* (Vancoppenolle et al., 2010) or 10 (Notz and Worster, 2008) **Vb> 7% (Zhou et al., 2014) or 10 % (Moreau et al., 2014).

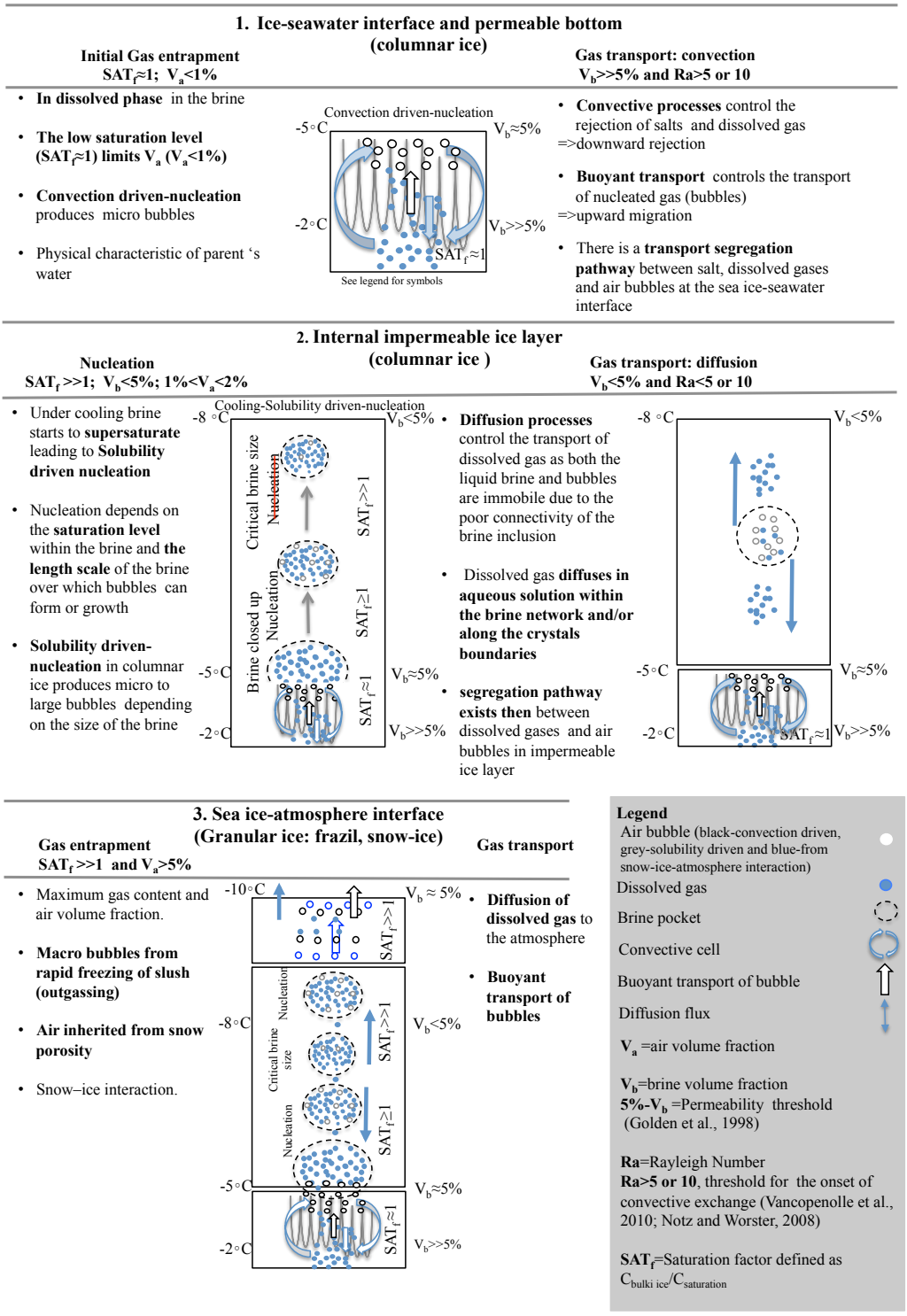

Figure VII-1: Conceptual model of factors controlling the gas entrapment and transport, and air porosity in winter impermeable sea ice.

VII.2.1 Nucleation processes

Nucleation is mostly a function of supersaturation in the brine medium. It exerts a strong control on gas content and transport, because at any given time when bubbles form (Figure VII-1, (-1),(-2) and (-3)), they are segregated from the transport pathway of dissolved salts and dissolved gas. Due to their low density, bubbles will not drain out of the ice by convection. Instead, nucleation leads to a forced upward transport and an accumulation of gas in sea ice. These bubbles are stored within the ice cover until the brine network sufficiently enlarges to allow buoyant transport to the atmosphere (Zhou et al., 2013; Moreau et al., 2014; Crabeck et al., 2014a, 2016).

Based on the solubility coefficient (i.e. Bunsen, b), the gas with the lowest solubility has the ability to partition in the gas phase more easily (Loose et al., 2011; Crabeck et al., 2014a). Thus, the level of supersaturation needed to initiate the nucleation process would be reached earlier. Consequently, the gas phase is enriched with less soluble gases; this is referred to as ‘‘solubility partitioning” (Crabeck et al., 2014a).

VII.2.2 Gas dynamics at the sea ice-seawater interface (V_b>5%, Ra>5) (Figure VII-1-(1))

As can be expected, gas entrapment depends on the amount of gas initially present in the seawater. The presence of freshwater under growing sea ice impacts total gas volume since the solubility of gas increases in freshwater compared to seawater (Crabeck et al., 2014b). In addition, currents and turbulences at the growing interface will positively impact the gas content as well (Tison et al., 2002;

Crabeck et al., 2014b). Finally, a higher freezing rate will result in greater gas content, since the gases have less time to be transported away from the growing interface (Killawee et al., 1998; Tison et al., 2002; Loose et al., 2009, 2011). Altogether, this highlights that physical and chemical characteristics of sea ice are directly dependent on the chemical and physical properties of the water mass from which it forms and the physical conditions at the sea ice-seawater interface.

In the bottom permeable layer, gas incorporation preferentially occurred in the dissolved state (V_a<1%) (Tison et al., 2002; Zhou et al., 2013; Crabeck et al., 2014a, 2016). The main transport mechanism in the bottom layer is brine drainage, given that the brine volume is commonly greater than the percolation threshold of 5 % -V_b (Golden et al., 1998), and that the Rayleigh number (Ra) exceeds the threshold for the onset of convection (Ra_c of 5 or 10 according to Vancoppenolle et al. (2010) and Notz and Worster (2008), respectively). Brine convection (i.e. brine drainage) is the main desalination process. Despite only being active in the bottom permeable layer in winter, it is responsible for the decrease of the average salinity in growing sea ice (Untersteiner, 1968; Lake and Lewis, 1970; Eide and Martin, 1975; Niedrauer and Martin, 1979; Weeks and Ackley, 1986; Oertling and Watts, 2004; Notz and Worster, 2009). Conceivably, brine drainage also causes the loss of dissolved gas (Zhou et al., 2013; Else et al., 2015; Crabeck et al., 2016); its capacity to do so depends on the partitioning of gas between the fraction present in bubbles and dissolved in brine. Within the bottom layer where gases are mostly dissolved in brine, the rejection of dissolved gas into the underlying seawater by brine convection contributes to maintain a low saturation level (Crabeck et al., 2016).

These convective cells simultaneously trigger the formation of micro bubbles (Crabeck et al., 2016). Due to their buoyancy, these bubbles will not drain out of the ice and instead accumulate at the upper limit of the convecting layer (bottom layer). The upper limit of the convective bottom layer is defined by the 5% brine volume contour modulating the permeability (V_b=5%). Therefore, since brine convection leads to an augmentation of the vertical extent of the lower salinity central zone (C-shaped profile) in growing sea ice, it is responsible for the formation of a bubbly layer above the permeable bottom. The vertical extent of this bubbly layer will grow thicker as the ice thickens (Crabeck et al., 2016).

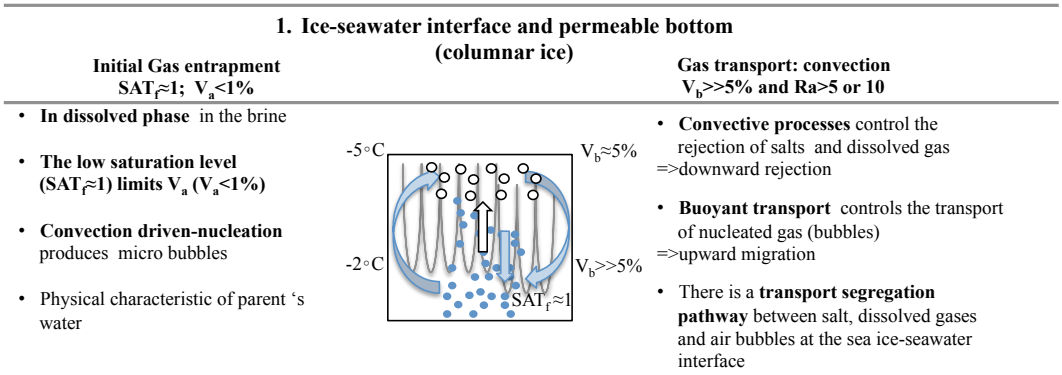

Figure VII-1-(1): Conceptual model of factors controlling the gas entrapment and transport, and air porosity in winter impermeable sea ice at the ice-seawater interface and permeable bottom.

VII.2.3 Gas dynamics in columnar impermeable ice layers (V_b<5%; Ra<5) (Figure VII-1-(2))

During ice growth, the brine initially at the warm water interface is further exposed to colder temperature causing the freeze up of some water molecules at the brine boundaries. Consequently, the brine, which was previously connected to the underlying seawater is slowly enclosed into the sea ice matrix and concentrates most of the sea ice impurities (salts and gases). Under such cooling conditions, the

closed brine inclusions start to supersaturate (SAT_f D 1.9 to 4.7 and 2.5 to 5 for natural and artificial, respectively), leading to solubility-driven nucleation (Crabeck et al., 2014a, 2016). This process drives the partition of the total gas content between the fraction of gas remaining in the dissolved phase and the fraction forming air bubbles within the brine. Considering that the air volume fraction does not linearly increase with the saturation level of the brine, these nucleation processes are limited by the size of the brine inclusion. Indeed, bubbles in sea ice brine inclusions are constrained by the length, scale, or volume over which they can form or growth (Crabeck et al., 2016).

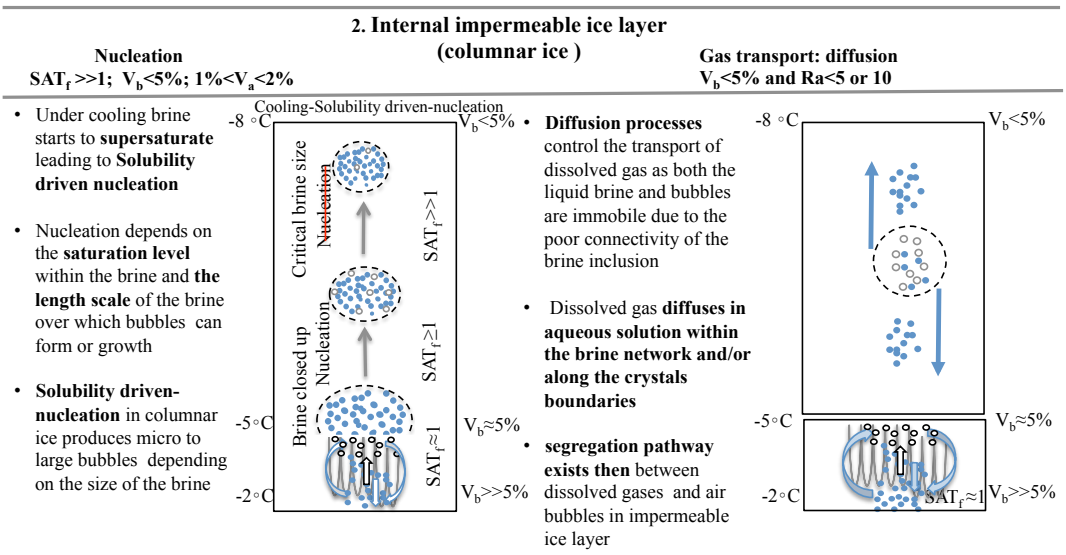

Figure VII-1-(2): Conceptual model of factors controlling the gas entrapment and transport, and air porosity in winter impermeable sea ice in the internal impermeable layer.

In impermeable layers, convective exchange is prevented (V_b<5% and Ra<5or 10 according to Vancoppenolle et al. (2010) and Notz and Worster (2008), respectively), and buoyant transport of bubbles is unlikely to occur due to the poor

connectivity of the brine inclusions. Therefore, the liquid brine and air bubbles are mostly immobile. However, dissolved gases can still be transported by diffusion along a concentration gradient through the brine medium and/or along the crystal boundaries (Loose et al., 2011; Crabeck et al., 2014a). Conceivably, the gases contained in bubbles can be exchanged with the brine and diffuse into the aqueous phase (Loose et al., 2011; Crabeck et al., 2014a).

VII.2.4 Gas dynamics at the sea ice-atmosphere interface (granular ice layer)(Figure VII-1-(3))

At the ice-atmosphere interface, the air volume fraction can exceed 5%. Frazil ice naturally contains more gas than congelation ice (columnar), since air is directly trapped from the atmosphere. Snow-ice and superimposed-ice formation can inherit air from snow, which due to its porosity has a greater air content than ice (Perovich and Gow, 1996; Cole et al., 2004; Crabeck et al., 2016). Despite similar supersaturation level in columnar and granular ice, the rapid freezing of slush at the ice surface can lead to the formation of larger bubbles because the medium is less constrained compared to columnar layer (Crabeck et al., 2016).

In the present work, I did not discuss the modality of exchange processes occurring at the ice-atmosphere interface. However, fluxes are likely to occur as a result of diffusive processes between the brine and the atmosphere, and depending on the sea ice permeability, buoyant transport of bubbles (Nomura et al., 2006, Moreau et al., 2014; Kotovitch et al., 2016).

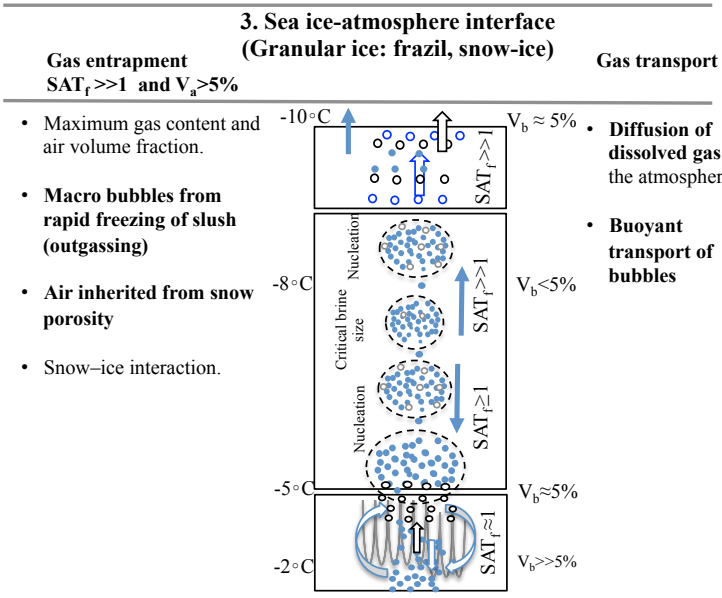

Figure VII-1-(3): Conceptual model of factors controlling the gas entrapment and transport, and air porosity in winter impermeable sea ice at the sea ice –atmosphere interface.

VII-3 Future work directions for gas dynamics and air porosity in first year sea ice

To accurately simulate the fate of climate-active gases in ice covered areas, we need to increase our understanding of the incorporation and transport of gases in sea ice. The detection and characterization of major gas profiles is a clear knowledge gap, with the only complete set of major atmospheric gas profiles (Ar, O_2 and N_2) in sea ice produced by Zhou et al. (2013, 2014a). To address this gap, efforts should be taken to develop a long-term monitoring program that focuses on the collection of ice cores across varying spatial and temporal scales. In particular, simultaneously sampling underlying seawater, brine, snow layers, ice texture, and tracer, such as $\delta^{18}O$, will improve our understanding of the interactions of sea ice with the pelagic zone and the sea ice-snow-atmosphere interface. To effectively

interpret results, the integration of new imaging techniques into traditional gas content measurements will ensure accuracy and create a greater understanding of gas dynamics, in particular the dynamics of air volume fraction. Not only this data will improve our understanding of the factors controlling the air volume fraction, but also it will assist us in establishing a link between air volume fraction and the thermohaline structure of sea ice.

As demonstrated by our work, micro and macro bubbles are present within sea ice cover. Since there is no analytical method to assess the partitioning of gas between dissolved and gaseous forms in sea ice brine, the next step is to develop a method for measuring gas composition and concentration in theses bubbles (i.e. what is in the bubbles?). Planar luminescent sensors (optodes) represent an *in situ* technique, which offers high potentiality and applicability to the study of gas within the microenvironments of brine inclusions in microcosm experiment. This approach has contributed to the development of conceptual and quantitative findings on biogeochemical cycle occurring in porous sediments, including processes controlling the pH level and redox conditions, and the distribution of key biogenic gases (O_2 and CO_2), nutrient compounds and contaminants (Glud et al., 1996; Hulth et al., 2002; Zhu et al., 2006; Santner et al., 2015). Following the generation of a complicated calibration protocol, this technology is suited for sea ice environments (Rysgaard et al., 2007). The planar optodes can provide high quality resolution of either O_2 saturation or pCO_2 using 2D imaging with a pixel resolution less than 100μm (exact resolution dependent upon sensor film thickness) (Santner et al., 2015). Therefore, in a controlled microcosm experiment, combining

the 2D images of O_2 saturation/pCO_2 and 2D images of sea ice microstructure, given that O_2 saturation/pCO_2 is different between brine and bubbles, we might infer the amount of O_2/pCO_2 trapped in bubbles (Figure VII-2). The *in situ* collection of planar optode measurements is highly advantageous as it does not disturb the system, conserving the sea ice temperature gradient and the sea ice-seawater interaction. Therefore, this technique presents the opportunity to link the impact of *in situ* temperature gradient to sea ice gas dynamics and investigate particular processes occurring at the sea ice-seawater and sea ice-snow-atmosphere interfaces.

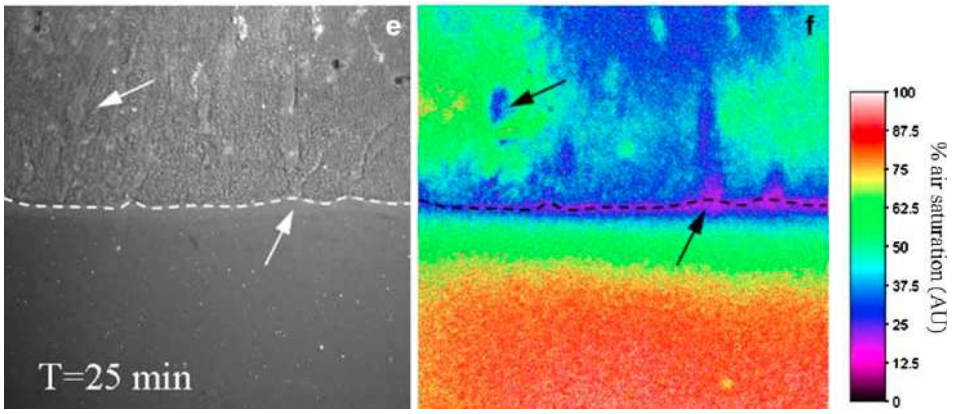

Figure VII-2: Black-and-white images along with simultaneously obtained 2D O_2 images of the ice-seawater interface during ice melt. The gradual thawing induces O_2 depletion in brine (see arrows). As the sensor is temperature-sensitive, and that there is no information on temperature micro-distribution, the O_2 images cannot be fully calibrated. Scale images across are 45 mm (from Rysgaard et al., 2007).

A recent modeling study by Kotovitch et al. (2016) inferred that the buoyant transport of bubbles within sea ice is likely a significant contributor to air-ice CO_2 flux in young growing sea ice. Thus, evaluating the experimental role of transporting CO_2 through bubbles out of the sea ice cover is of prime interest.

Particular attention should be given to the ice-atmosphere interface, as evidence of a larger air volume fraction and macro bubbles in granular layers and snow-ice imply that air porosity may play an important role in regulating sea ice-atmosphere exchange. At the ice-atmosphere interface, the current description of flux is based on molecular diffusion: a flux depends on the difference of partial pressure between brine and the atmosphere, which is moderated by the fraction of brine at the interface and wind speed (Nomura et al., 2006; Moreau et al., 2014). Further studies should analytically investigate the existence of an air bubble ice-atmosphere pathway that regulates the exchange of gas at the ice-atmosphere interface. This requires further investigation into the air permeability threshold and the bubble rise velocity. Such work requires determining the bubble connectivity, as well as bubble size and the interactions between air bubbles and brine pockets sidewalls, i.e. viscous drag. Improving our knowledge of sea ice tortuosity is important since some bubbles could be stored within an interconnected brine network and anfractuosities, which could slow down the transport of air bubbles to the atmosphere (Moreau et al., 2014).

Current sea ice physics literature assumes that the air volume fraction is very low compared to the brine volume, causing it to be ignored in the mathematical description of sea ice permeability and mushy layer theory (Feltham et al., 2006; Nots and Worster, 2009). These models approximate that ice is a two-phase media, pure ice matrix and liquid brine, free of air inclusions. This is especially true in the bottom permeable layer of sea ice (V_a<1%); however, our results indicate the presence of micro bubbles where air volume fraction was less than 2% and the brine

volume fraction was less than 5%. To address this discrepancy, future research should evaluate the impact of neglecting air volume fraction on the transfer of heat, mass and solute in mushy layer theory equation, focusing also on the effect of air volume on sea ice liquid permeability and brine percolation threshold.

In order to simulate bubble distribution within sea ice, current models, such as those by Moreau et al. (2014) and Kotovitch et al. (2016), apply only the gas solubility law as in chapter IV of this work. This reasoning assumes that air bubbles form once the dissolved gas concentration exceeds the saturation point given that the total partial pressure of all three major atmospheric gases (Ar, O_2, N_2), is above the brine hydrostatic pressure, which is also assumed to be 1 atm:

$$C_{saturation}=K_H \times P \qquad \text{(Eq.- VII-1)}$$

$$C_{nuc} \geq C_{saturation}$$

Where P is the partial pressure of a given gas directly above the solution, $C_{saturation}$ is the concentration of the gas dissolved in the solution (the aqueous phase), and K_H, Henry's law constant, which is a function of temperature and salinity.

Our results show that the air volume fraction is not a linear function of the saturation state. Supersaturation may occur in brine because of the work (free energy barrier) required to form a bubble. In the case of heterogonous nucleation, this energy barrier is low, but not null. It is argued that the nucleation observed in most instances occurs at low levels of supersaturation of 5 or less (Jones et al., 1999; Lubtetkin., 2003).

Gas nucleation could be trigged when the concentration exceeds a critical saturation concentration, C_{nuc}, as defined by Super Henry's Law (Bowers et al., 1996):

$$C_{nuc}=(K_H \times P)+C \qquad \text{(Eq.- VII-2)}$$

According to our results, the critical nucleation concentration is between 1.9 and 4.7 times greater than the concentration at saturation, which is in agreement with previous literature (Killawee et al., 1998; Jones et al., 1999; Tison et al., 2002).

Despite the unlikeliness, we observed high gas content and high saturation factor but surprisingly low air volume fraction in an internal ice layer (where V_b is at its smallest). We explained (see conceptual model) the low air volume fraction in these high saturated brine by the fact that the bubbles may have had insufficient room to form or grow in these small brine inclusions. However, the answer may be more complex and is worth discussing. Even if the brine is supersaturated, a bubble may shrink in size or disappear due to impacts of surface tension. The surface tension (γ) increases the bubble's inner pressure by an amount equal to the Laplace pressure. The Laplace pressure describes the pressure difference between the inside and the outside of a curved surface (bubble) that forms at a gas-liquid interface (Butt, 2013, p.6-12):

$$P_{solution}-P_{bubble}=\frac{2\gamma}{R} \qquad \text{(Eq.- VII-3)}$$

Where $P_{solution}$ is the partial pressure of gas in solution and P_{bubble} is the partial pressure of gas in the bubble, γ is the surface tension of the liquid and R is the radii of the bubble. Therefore, a bubble at Henry's equilibrium (in absence of surface

tension) will no longer be in equilibrium with the surrounding liquid if you consider the increase of inner pressure driven by surface tension (C^*):

$$C_{saturation}=K_H \times P \qquad \text{(Eq.- VII-4)}$$

$$C^*=K_H \times \left(P+\frac{2\gamma}{R}\right) \qquad \text{(Eq.- VII-5)}$$

The higher gas pressure in the bubble causes the surrounding solution to be slightly undersaturated ($C^*>C_{saturation}$), driving the outward bulk diffusion of gas into the liquid (Epstain Plesset, 1950; Vreme et al., 2015).

Because the surface tension increases with decreasing temperature (Vargaftik and Voljak, 1983) and increasing salinity (Nasr El Din et al., 2005; Barnes and Gentle, 2010, p.69-70), cooling brine results of an increase in surface tension. Therefore, despite the supersaturation of brine, the surface tension may reduce nucleation processes. The surface tension effect may also explain why Light et al. (2003) observed that under cooling conditions (-2°C to -25°C) not only did inclusions shrink in size, but also the smallest air inclusions disappeared. Note that surface tension impacts only small bubbles (∅ in ηm and in μmm) since its effects become negligible for bubbles with diameters greater than 1 mm (Figure VII-3).

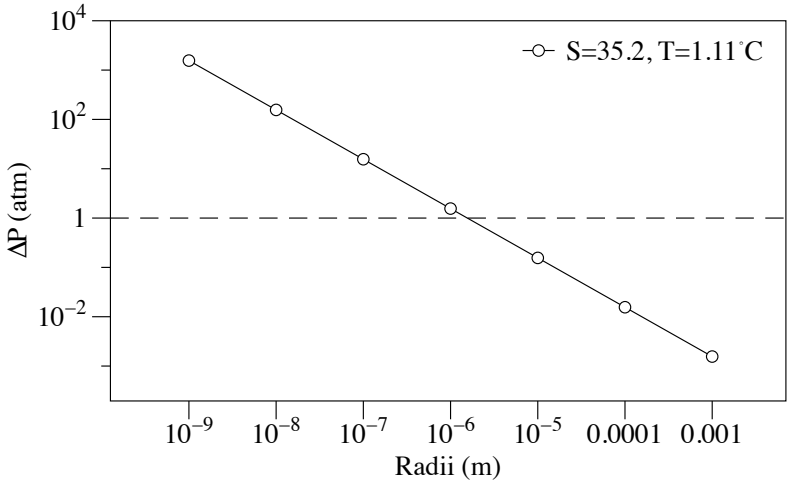

Figure VII-3: Relationship between bubble radii and Laplace pressure for seawater at 1.11 °C (S=35.2) , γ =0.076307 Jm^{-2}.

We assumed that brine is always at atmospheric pressure (1 atm); however, we can reasonably expect that during the freezing of brine inclusions, the internal pressure of brine increases due to the liquid volume reduction. Since the solubility of gases increases with increasing pressure, the brine would no longer be supersaturated and nucleation could reduce by some amount. Therefore, our theoretical computation of saturation may overestimate the saturation level in the brine. This overestimation could account for the high gas content and low air volume fraction in the internal ice layer, as well as the disappearance of the smallest inclusion during the cooling sequence experiment of Light et al. (2003). If during cooling the internal pressure increases, further formation of cracks and/or internal melting will trigger a depressurization of the brine inclusion. As a result, the brine inclusion might act as a champaign bottle until the solution is no longer supersaturated.

As demonstrated above, there is a lack of understanding related to nucleation of bubbles in sea ice brine. It is likely that nucleation processes within sea ice are highly dependent on the sea ice temperature gradient, which exerts control on the brine size, gas solubility, and surface tension. Nucleation processes should also vary both within the vertical profile of the sea ice cover and seasonally throughout the course of growth and melt. Future work should investigate the effects of changing temperatures on the behaviour of bubbles in brine at varying temporal and spatial scales.

Medical CT-scan demonstrated promising results when characterizing air volume fraction of complete ice cores at high spatial resolutions. Despite promising results, the spatial resolution of current medical CT-scanner (97µm X 97µm x 600µm) inadequately resolved micro bubbles and did not distinguish between ice and brine, limiting our understanding of nucleation processes within brine. Micro CT-scan with a voxel size of 3µm X 3µm X 3µm is an available alternative to simultaneously visualize the brine and air porosity. Moreover micro CT-scanner is a transportable system that can be placed in a cold lab allowing various scanning temperatures and recovery of the *in situ* sea ice temperature (Figure VII-4). To improve our interpretation of nucleation processes within the brine medium, future studies should evaluate the effects of freezing and melting on air inclusions within columnar and granular sea ice by using a micro CT-scanner. However, using a micro CT-scanner would create another trade-off between the resolution and sample size. Micro CT-scanner like the Bruker SkyScan 1174, for example, require additional scan time (>1h; medical CT-scan time <1min); which increases internal

operating temperature compromising the stability of sea ice microstructure, and can only analyze samples no larger than 3 x 3 cm. This much smaller subsample size creates problems as the calculation of air/brine volume fraction would likely be heavily biased by the occurrence of bubbles/brine > 1mm in diameter in each 3 x 3 cm subsample. Thus, combining medical CT-scan results with results from numerous micro-CT subsamples is in our best interest.

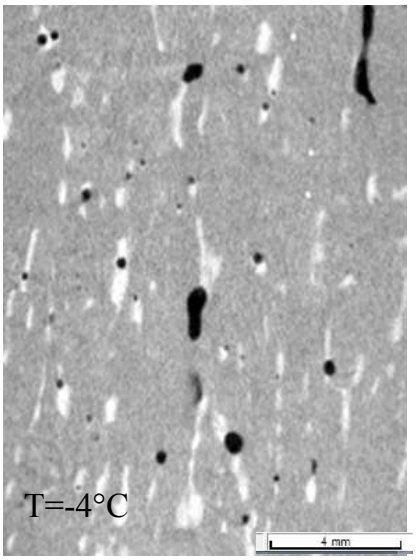

Figure VII-4: Raw micro CT-image produced with Bruker SkyScan 1174; brine (white) and bubbles (black) in a columnar ice matrix (Grey) at -4 ºC (scan time 3h, cold lab temperature =-8°C) .

Finally, Scanning Electron Microscopy (SEM) produces images based on the interaction between a beam of focused electrons and the atoms of a sample. This produces various signals (secondary electron, backscattered electron, and X-ray detection) that contain information about the sample's chemical composition and surface topography at nanometer scale. Numbers of studies have already applied low temperature scanning electron microscopy (LTSEM) to identify salt

precipitates and particulate impurities in both snow and ice (e.g. Wolf et al., 1988; Barnes et al., 2003; Obbard et al., 2003; Spaulding et al., 2011; Bartels-Rausch, 2014). Similar techniques have been used to image snowflakes and metamorphosed snow (Werghin and Erbe, 1995; Rango et al., 2000). These images are highly detailed and could introduce new qualitative structural information about the nature of the brine-air-ice interface (Figure VII-5).

Figure VII-5: Dendritic snow crystal, imaged at 2 kV with LTSEM vertical field width = 2.9 mm (Wergin and Erbe, 1995).

VII-4 Recommendations for clarifying the role of sea ice as potential interface for storage and transformation of CH_4 in the Arctic

When compared to Ar, an inert gas, our results show that CH_4 is accumulated within and under the sea ice cover. I did not find any evidence of potential methane sources (biological production) or sinks (aerobic or anaerobic oxidation process) within sea ice cover. Consequently, I explained that the excess of CH_4 resulted from physical processes related to bubble entrapment. Similarly, Zhou et al., (2014) investigated the processes controlling CH_4 concentrations in sea ice cover, and suggest that the sea ice CH_4 content is mainly regulated by physical processes rather than biological activities. Given that both CH_4 oxidation and production are probably slow (and/or inhibited) in sea ice (see discussion below) and that their impact may not be quantifiable on the bulk properties, reporting the bulk ice CH_4 concentration over 4 days is clearly insufficient to pinpoint biochemical processes.

VII.4.1 Future research strategy

In Figure VII-6, I report the different sources, and potential CH_4 production and transformation pathways that should be investigated in future research.

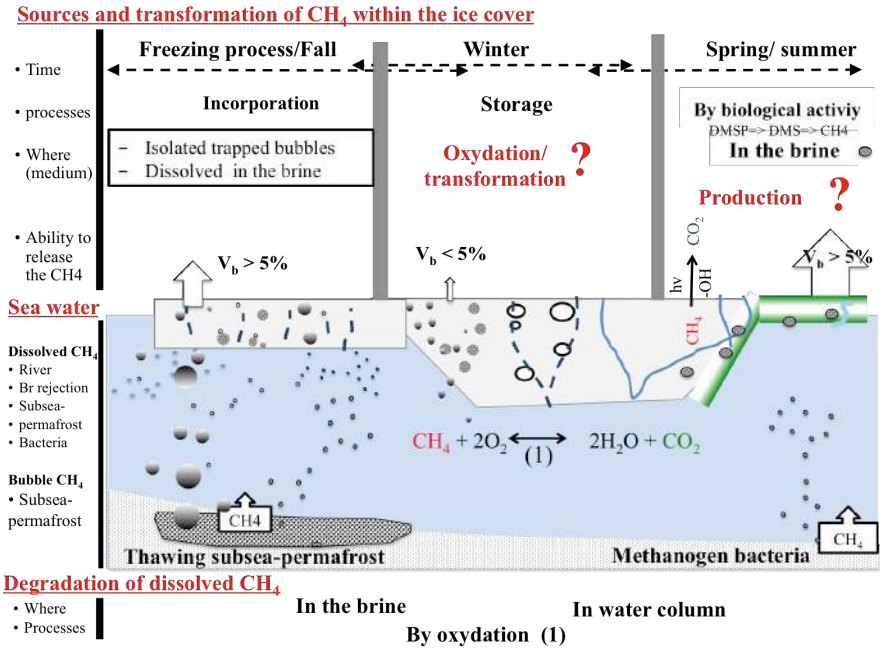

Figure VII-6: Sea ice as a potential interface for CH_4 storage and transformation. During the freezing process, CH_4 from sediments and subsea-permafrost could be trapped within the sea ice. Since the ice is permeable during the early stage of growth, CH_4 could be released to the atmosphere. Through the winter, the ice become impermeable and CH_4 is locked within the sea ice and under the sea ice cover. During this residential time, CH_4 could be oxidized both in brine and in the seawater underneath however it is a slow processes and may be insignificant in sea ice. During the spring and summer, the sea ice is warming up and become permeable again, so that CH_4 could be released to the atmosphere and photo-oxidize. During the algal bloom, the degradation of the DMSP in DMS could be responsible for CH_4 production.

Firstly, we can expect a release of CH_4 rich brine into underlying seawater and a CH_4 flux to the atmosphere when sea ice becomes permeable over the spring. Further studies should focus on the deployment of chamber and/or eddy correlation systems in order to estimate CH_4 fluxes at both interfaces. Secondly, research should investigate the potential origins of methane, marine sediment (bacterial), subsea-permafrost (thermogenic), and riverine input (bacterial from wetlands), using natural CH_4 isotopes ($\delta^{13}C$-CH_4 and $\delta^{2}H$-CH_4). Diagram plots of paired

measurements of $\delta^{13}C\text{-}CH_4$ versus $\delta^{2}H\text{-}CH_4$ can be used to infer origins from broad categories, such as thermogenic and bacterial. Moreover, these paired diagrams can be useful when investigating potential CH_4 transformation and/or production, since their plots infer trajectories resulting from isotope fractionation during oxidation, production, and transport (Reeburgh et al., 2007). If paired diagram can assist the detection of CH_4 production and oxidation pathways, to truly evidence biogenic CH_4 production and/or oxidation, incubations using isotope decay tracers should be carried out. Additionally, genome studies should be conducted to detect the presence of methanogen and oxidizing bacteria.

VII.4.2 Potential sources and sinks of CH_4 in sea ice

The *in situ* production of CH_4 in sea ice is not likely to occur because it requires a strictly anoxic environment, however, past studies have suggested the potential existence of anoxic brine inclusions (Rysgaard and Glud, 2004, Rysgaard et al., 2007). Production of CH_4, through methanogenis is the last step in the remineralization of complex of organic matter in anaerobic system (O_2>NO_3^- >Mn(IV)>Fe(III)>SO_4^{2-}>CO_2). Moreover, early studies by Martens (1977) and Crill and Martens (1983) indicate that methanogenis does not occur until sulfates are nearly exhausted and the sulfate reduction rate of marine sediment decreases. This is not only due to the energy yield constraints above, but also because sulfate reducers are very effective in their uptake in of H_2 and are capable of maintaining H_2 at concentrations too low for methanogens to function (Reeburgh et al., 2007).

Potential sinks of CH_4 by either aerobic or anaerobic oxidation pathways, are unlikely to occur in first year sea ice. Aerobic CH_4 oxidation, which is the fastest of the two processes, is very slow or even inhibit at the observed sea ice CH_4 concentration (nmolar concentration) (Ward., 1990; Valentine et al., 2001). The rate of oxidation of CH_4 in the water column exceeds 1 year when the CH_4 concentration in the seawater is nmolar (Griffiths et al., 1982; Ward et al., 1992; Valentine et al., 2011), taking much longer than the growth and melt rates of first year sea ice.

A more realistic source of *in situ* CH_4 production could be from the decomposition of dimethyl sulfide propionate (DMSP) and dimethyl sulfur (DMS). Methanogenic archaea have been identified to have the ability to metabolize dimethylsulfoniopropionate (DMSP) and its degradation products (DMS) by producing CH_4 (Oremland, 1989; Kiene et al., 2000). Damm et al. (2015) detected a CH_4 hotspot in the surface water where sea ice was melting in western Fram Strait during summer 2008. They postulate that DMSP released from sea ice acted as the precursor of CH_4 production via methylotrophic methanogenesis. Through modeling they prove that anaerobic methanogenis occurs inside of a bacterial cell despite high oxygen saturation levels in its surroundings. Similar reasoning has been discussed in past literature to explain CH_4 supersaturation in aerobic surface water ("Ocean Methan paradox") (Holmes et al., 2000; Karl et al., 2008; Damm et al., 2010). Earlier studies provided evidence of the presence of methanogenic bacteria in fish and plankton samples as well as in marine snow and fecal pellets ('Microenvironment') (Sieburth et al., 1987; Tilbrook et al., 1995).

Since aerobic and anaerobic oxidation is unlikely to occur in sea ice, the most plausible sink for trapped CH_4 in sea ice is the photo- oxidation by hydroxyl radical, -OH. It has been shown that sunlit snow and ice play an important role in processing atmospheric species. Multiple studies proved that a large amount of radical -OH is released into snow and ice during the photochemical oxidation of NO (Dibb et al., 2002; Mauldin et al., 2004; Grannas et al., 2007; Sjostedt et al., 2007). Radical -OH is known to be the most important sink of atmospheric CH_4 (Wuebbles and Hayhoe, 2002). As a result, CH_4 could be rapidly photo-chemically degraded into CO_2 in the snowpack and at the ice-atmosphere interface. Photo-chemical reaction at the ice-snow-atmosphere interface is still an emerging field and concerted research is needed to improve our understanding of these processes.

References

Barnes, P. R., Wolff, E. W., Mallard, D. C., and Mader, H. M.: SEM studies of the morphology and chemistry of polar ice, Microscopy research and technique, 62, 62-69, 2003.

Barnes, GT, Gentle IR.: Interfacial science. 2st ed. Oxford University Press,10-98, 2011.

Bartels-Rausch, T.; Jacobi, H.-W.; Kahan, T. F.; Thomas, J. L.; Thomson, E. S.; Abbatt, J. P. D., Ammann, M., Blackford, J. R., Bluhm, H.; Boxe, C.:. A Review of Air-Ice Chemical and Physical Interactions. Atmos. Chem. Phys, 14, 1587−1633, 2014.

Bowers, P. G., Bar-Eli, K., and Noyes, R. M.: Unstable supersaturated solutions of gases in liquids and nucleation theory, J. Chem. Soc., Faraday Trans., 92, 2843-2849, 1996.

Butt H-J, Graf K, Kappl M. Thermodynamics of interfaces, Weinheim, Germany: Wiley-VCH Verlag GmbH & Co. KGaA, 6-12, 2013.

Cole, D. M., Eicken, H., Frey, K., and Shapiro, L. H.: Observations of banding in first-year Arctic sea ice, Journal of Geophysical Research: Oceans, 109, 2004.

Cox, G. F. N., and Weeks, W. F.: Equations for determining the gas and brine volumes in sea-ice samples, Journal of Glaciology, 29, 306 - 316, 1983.

Crabeck, O., Delille, B., Rysgaard, S., Thomas, D. N., Geilfus, N.-X., Else, B., and Tison, J.-L.: First "in situ" determination of gas transport coefficients (DO2, DAr, and DN2) from bulk gas concentration measurements (O2 , N2 , Ar) in natural sea ice, Journal of Geophysical Research: Oceans, 14pp, 10.1002/2014JC009849, 2014a.

Crabeck, O., Delille, B., Thomas, D., Geilfus, N. X., Rysgaard, S., and Tison, J. L.: CO2 and CH4 in sea ice from a subarctic fjord under influence of riverine input, Biogeosciences, 11, 6525-6538, 10.5194/bg-11-6525-2014, 2014b.

Crabeck, O., Galley, R., Delille, B., Else, B., Geilfus, N. X., Lemes, M., Roches, M. D., Francus, P., Tison, J. L., and Rysgaard, S.: Imaging air volume fraction in sea ice using non-destructive X-ray tomography, Cryosphere, 10, 1125-1145, 10.5194/tc-10-1125-2016, 2016.

Crill, P. M., and Martens, C. S.: Spatial and temporal fluctuations of methane production in anoxic coastal marine sediments, Limnology and Oceanography, 28, 1117-1130, 1983.

Damm, E., Helmke, E., Thoms, S., Schauer, U., Nöthig, E., Bakker, K., and Kiene, R. P.: Methane production in aerobic oligotrophic surface water in the central Arctic Ocean, Biogeosciences, 7, 1099-1108, 10.5194/bg-7-1099-2010, 2010.

Damm, E., Thoms, S., Beszczynska-Miller, A., Nathig, E. M., and Kattner, G.: Methane excess production in oxygen-rich polar water and a model of cellular conditions for this paradox, Polar Science, 9, 327-334, 10.1016/j.polar.2015.05.001, 2015.

Else, B. G. T., Rysgaard, S., Attard, K., Campbell, K., Crabeck, O., Galley, R. J., Geilfus, N. X., Lemes, M., Lueck, R., Papakyriakou, T., and Wang, F.: Under-ice eddy covariance flux measurements of heat, salt, momentum, and dissolved oxygen in an artificial sea ice pool, Cold Regions Science and Technology, 119, 158-169, 10.1016/j.coldregions.2015.06.018, 2015.

Epstein, c. e. P., and Plesset, M. S.: On the stability of gas bubbles in liquid-gas solutions, The Journal of Chemical Physics, 18, 1505-1509, 1950.

Feltham, D. L., Untersteiner, N., Wettlaufer, J. S., and Worster, M. G.: Sea ice is a mushy layer, Geophysical Research Letters, 33, 4-7, 10.1029/2006GL026290, 2006.

Glud, R. N., Ramsing, N. B., Gundersen, J. K., Klimant, I., and Gludl, R. N.: Planar optrodes: a new tool for fine scale measurements of two-dimensional O2 distribution in benthic communities, Marine Ecology Progress Series, 140, 217-226, 10.3354/meps140217, 1996.

Golden, K. M., Ackley, S. F., and Lytle, V. I.: The percolation phase transition in sea Ice, Science, 282, 2238-2241, 10.1126/science.282.5397.2238, 1998.

Grannas, A., Jones, A. E., Dibb, J., Ammann, M., Anastasio, C., Beine, H., Bergin, M., Bottenheim, J., Boxe, C., and Carver, G.: An overview of snow photochemistry:

evidence, mechanisms and impacts, Atmospheric Chemistry and Physics, 7, 4329-4373, 2007.

Holmes, M. E.: Methane production, consumption, and air-sea exchange in the open ocean: An evaluation based on carbon isotopic ratios M. Elizabeth Holmes, 1 Francis J. Sansone, Terri M. Rust, and Brian N. Popp, Global Biogeochemical Cycles, 14, 1-10, 2000.

Hulth, S., Aller, R. C., Engström, P., and Selander, E.: A pH plate fluorosensor (optode) for early diagenetic studies of marine sediments, Limnology and Oceanography, 47, 212-220, 10.4319/lo.2002.47.1.0212, 2002.

Jones, S., Evans, G., and Galvin, K.: Bubble nucleation from gas cavities—a review, Advances in colloid and interface science, 80, 27-50, 1999.

Kiene, R. P., Linn, L. J., and Bruton, J. A.: New and important roles for DMSP in marine microbial communities, Journal of Sea Research, 43, 209-224, 2000.

Killawee, J. A., Fairchild, I. J., Tison, J. L., Janssens, L., and Lorrain, R.: Segregation of solutes and gases in experimental freezing of dilute solutions: Implications for natural glacial systems, Geochimica et Cosmochimica Acta, 62, 3637-3655, 10.1016/S0016-7037(98)00268-3, 1998.

Kotovitch, M., Moreau S., Zhou J., Vancoppenolle M., Gerhard S., Dieckmann, Evers K.-U., Van der Linden F., Thomas D., Tison J.-L., Delille B.: Air-ice carbon pathways inferred from a sea ice tank experiment, Elementa: Science of the Anthropocene, 75, 7212-7220, 10.1128/AEM.02227-09, 2016.

Lake, R. A., and Lewis, E. L.: Salt rejection by sea ice during growth, Journal of Geophysical Research, 75, 583 - 597, 1970.

Light, B., Maykut, G. A., and Grenfell, T. C.: Effects of temperature on the microstructure of first-year Arctic sea ice, Journal of Geophysical Research-Oceans, 108, 3051, 10.1029/2001jc000887, 2003.

Loose, B., McGillis, W. R., Schlosser, P., Perovich, D., and Takahashi, T.: Effects of freezing, growth, and ice cover on gas transport processes in laboratory seawater experiments, Geophysical Research Letters, 36, L05603, L05603 10.1029/2008gl036318, 2009.

Loose, B., Schlosser, P., Perovich, D., Ringelberg, D., Ho, D. T., Takahashi, T., Richter-Menge, J., Reynolds, C. M., McGillis, W. R., and Tison, J. L.: Gas diffusion through columnar laboratory sea ice: implications for mixed-layer ventilation of CO2 in the seasonal ice zone, Tellus Series B-Chemical and Physical Meteorology, 63, 23-39, 10.1111/j.1600-0889.2010.00506.x, 2011.

Lubetkin, S.: Why is it much easier to nucleate gas bubbles than theory predicts?, Langmuir, 19, 2575-2587, 2003.

Martens, C. S., and Berner, R. A.: Interstitial water chemistry of anoxic Long Island Sound sediments. 1. Dissolved gases, Limnol. Oceanogr, 22, 10-25, 1977.

Mauldin, R., Kosciuch, E., Henry, B., Eisele, F., Shetter, R., Lefer, B., Chen, G., Davis, D., Huey, G., and Tanner, D.: Measurements of OH, HO 2+ RO 2, H 2 SO 4, and MSA at the south pole during ISCAT 2000, Atmospheric Environment, 38, 5423-5437, 2004.

Moreau, S., Vancoppenolle, M., Zhou, J., Tison, J.-L., Delille, B., and Goosse, H.: Modelling argon dynamics in first-year sea ice, Ocean Modelling, 73, 1-18, 10.1016/j.ocemod.2013.10.004, 2014.

Nasr-El-Din, H., Al-Otaibi, M., Al-Aamri, A., and Ginest, N.: Surface tension of completion brines, SPE International Symposium on Oilfield Chemistry, 2005,

Niedrauer, T. M., and Martin, S.: An experimental study of brine drainage and convection young sea ice, Journal of Geophysical Research, 84, 1176, 10.1029/JC084iC03p01176, 1979.

Nomura, D., Yoshikawa-Inoue, H., and Toyota, T.: The effect of sea-ice growth on air-sea CO2 flux in a tank experiment, Tellus, Series B: Chemical and Physical Meteorology, 58, 418-426, 10.1111/j.1600-0889.2006.00204.x, 2006.

Notz, D., and Grae Worster, M.: In situ measurements of the evolution of young sea ice, Journal of Geophysical Research: Oceans, 113, 10.1029/2007JC004333, 2008.

Notz, D., Haumann, A., Haak, H., Jungclauss, J. H., and Marotzke, J.: Arctic sea ice evolution as modeled by Max Planck Institute for Meteorology's Earth system model, Journal of Advances in modeling Earth Systems, 5, 1-22, 10.1002/james.20016, 2013.

Obbard, R., Iliescu, D., Cullen, D., Chang, J., and Baker, I.: SEM/EDS comparison of polar and seasonal temperate ice, Microscopy research and technique, 62, 49-61, 2003.

Oremland, R. S., Hollibaugh, J. T., Maest, A. S., Presser, T. S., Miller, L. G., and Culbertson, C. W.: Selenate reduction to elemental selenium by anaerobic bacteria in sediments and culture: biogeochemical significance of a novel, sulfate-independent respiration, Applied and Environmental Microbiology, 55, 2333-2343, 1989.

Perovich, D. K., and Gow, A. J.: A quantitative description of sea ice inclusions, Journal of Geophysical Research, 101, 18327, 10.1029/96JC01688, 1996.

Rango, A., Wergin, W., Erbe, E., and Josberger, E.: Snow crystal imaging using scanning electron microscopy: III. Glacier ice, snow and biota, Hydrological sciences journal, 45, 357-375, 2000.

Reeburgh, W. S.: Oceanic Methane Biogeochemistry, Chemical Reviews, 107, 486-513, 10.1021/cr050362v, 2007.

Rysgaard, S., and Glud, R. N.: Anaerobic N2 production in Arctic sea ice, Limnology and Oceanography, 49, 86-94, 10.4319/lo.2004.49.1.0086, 2004.

Rysgaard, S., Glud, R. N., Sejr, M. K., Blicher, M. E., and Stahl, H. J.: Denitrification activity and oxygen dynamics in Arctic sea ice, Polar Biology, 31, 527-537, 10.1007/s00300-007-0384-x, 2007.

Santner, J., Larsen, M., Kreuzeder, A., and Glud, R. N.: Two decades of chemical imaging of solutes in sediments and soils – a review, Analytica Chimica Acta, 878, 9-42, 10.1016/j.aca.2015.02.006, 2015.

Sieburth, J. M.: Contrary habitats for redox-specific processes: methanogenesis in oxic waters and oxidation in anoxic waters, Microbes in the Sea, 11-38, 1987.

Sjostedt, S., Huey, L. G., Tanner, D., Peischl, J., Chen, G., Dibb, J. E., Lefer, B., Hutterli, M., Beyersdorf, A. J., and Blake, N. J.: Observations of hydroxyl and the sum of peroxy radicals at Summit, Greenland during summer 2003, Atmospheric Environment, 41, 5122-5137, 2007.

Spaulding, N., Meese, D., and Baker, I.: Advanced microstructural characterization of four East Antarctic firn/ice cores, Journal of Glaciology, 57, 796-810, 2011.

Taylor, P. D., and Feltham, D. L.: A model of melt pond evolution on sea ice, Journal of Geophysical Research-Oceans, 109, 10.1029/2004jc002361, 2004.

Tilbrook, B. D., and Karl, D. M.: Methane sources, distributions and sinks from California coastal waters to the oligotrophic North Pacific gyre, Marine Chemistry, 49, 51-64, 1995.

Tison, J.-L., Haas, C., Gowing, M. M., Sleewaegen, S., and Bernard, A.: Tank study of physico-chemical controls on gas content and composition during growth of young sea ice, Journal of Glaciology, 48, 177-191, 10.3189/172756502781831377, 2002.

Untersteiner, N.: Natural desalination and equilibrium salinity profile of perennial sea ice, Journal of Geophysical Research, 73, 1251 - 1257, 1968.

Valentine, D. L.: Emerging topics in marine methane biogeochemistry., Annual review of marine science, 3, 147-171, 10.1146/annurev-marine-120709-142734, 2011.

Vancoppenolle, M., Goosse, H., De Montety, A., Fichefet, T., Tremblay, B., and Tison, J. L.: Modeling brine and nutrient dynamics in Antarctic sea ice: The case of dissolved silica, Journal of Geophysical Research: Oceans, 115, 10.1029/2009JC005369, 2010.

Vargaftik, N., Volkov, B., and Voljak, L.: International tables of the surface tension of water, Journal of Physical and Chemical Reference Data, 12, 817-820, 1983.

Vreme, A., Pouligny, B., Nadal, F., and Liger-Belair, G.: Does shaking increase the pressure inside a bottle of champagne?, Journal of Colloid and Interface Science, 439, 42-53, 10.1016/j.jcis.2014.10.008, 2015.

Ward, B., and Kilpatrick, K.: Relationship between substrate concentration and oxidation of ammonium and methane in a stratified water column, Continental Shelf Research, 10, 1193-1208, 1990.

Ward, B.: The subsurface methane maximum in the Southern California Bight, Continental Shelf Research, 12, 735-752, 1992.

Weeks, W. F., and Ackley, S. F.: The Growth, Structure, and Properties of Sea Ice, in: The Geophysics of Sea Ice, edited by: Untersteiner, N., Springer US, Boston, MA, 9-164, 1986.

Wergin, W. P., Rango, A., and Erbe, E. F.: Observations of snow crystals using low-temperature scanning electron microscopy, Scanning, 17, 41-50, 1995.

Wolff, E., Mulvaney, R., and Oates, K.: The location of impurities in Antarctic ice, Ann. Glaciol, 11, 194-197, 1988.

Wuebbles, D. J., and Hayhoe, K.: Atmospheric methane and global change, Earth-Science Reviews, 57, 177-210, 2002.

Zhou, J., Delille, B., Eicken, H., Vancoppenolle, M., Brabant, F., Carnat, G., Geilfus, N. X., Papakyriakou, T., Heinesch, B., and Tison, J. L.: Physical and biogeochemical properties in landfast sea ice (Barrow, Alaska): Insights on brine and gas dynamics across seasons, Journal of Geophysical Research: Oceans, 118, 3172-3189, 10.1002/jgrc.20232, 2013.

Zhou, J. Y., Tison, J. L., Carnat, G., Geilfus, N. X., and Delille, B.: Physical controls on the storage of methane in landfast sea ice, The Cryosphere, 8, 1019-1029, 10.5194/tc-8-1019-2014, 2014.

Zhu, Q., Aller, R. C., and Fan, Y.: Two-dimensional pH distributions and dynamics in bioturbated marine sediments, Geochimica et Cosmochimica Acta, 70, 4933-4949,10.1016/j.gca.2006.07.033, 2006.

Annexe 1: Additional contribution to the peer reviewed literatures

In addition to the three manuscripts presented in this thesis, I also participated as co-author on six peer reviewed publications listed in Table AI-1.

Table AI-1: Contribution to the scientific literature as co-author.

Scientific questions	**Contribution to the literature as co-author**
Related to 1	Else, B. G. T., Rysgaard, S., Attard, K., Campbell, K., Crabeck, O., Galley, R. J., Geilfus, N.-X., Lemes, M., Lueck, R., Papakyriakou, T., and Wang, F.: Under-ice eddy covariance flux measurements of heat, salt, momentum, and dissolved oxygen in an artificial sea ice pool, Cold Reg. Sci. Technol., 119, 158–169, 2015.10.1016/j.coldregions.2015.06.018, 2015.
Related to 2	Rysgaard, S., Wang, F., Galley, R. J., Grimm, R., Notz, D., Lemes, M., Geilfus, N.-X., Chaulk, A., Hare, A. A., Crabeck, O., Else, B. G. T., Campbell, K., Sørensen, L. L., Sievers, J., and Papakyriakou, T.: Temporal dynamics of ikaite in experimental sea ice, The Cryosphere, 8, 1469–1478, 10.5194/tc-8-1469-2014, 2014.
	Geilfus, N.-X., Galley, R. J., Crabeck, O., Papakyriakou, T., Landy, J., Tison, J.-L., and Rysgaard, S.: Inorganic carbon dynamics of melt-pond-covered first-year sea ice in the Canadian Arctic, Biogeosciences, 12, 2047–2061, 10.5194/bg-12-2047-2015, 2015.
	Geilfus, N.-X., Galley, R. J., Else, B. G. T., Campbell, K., Papakyriakou, T., Crabeck, O., Lemes, M., Delille, B., and Rysgaard, S.: Estimates of ikaite export from sea ice to the underlying seawater in a sea ice–seawater mesocosm, The Cryosphere, 10, 2173-2189,10.5194/tc-10-2173-2016, 2016.
Indirectly related to the thesis topic	Dmitrenko I, Sergev K, Rysgaard S, Barber DG, Babb D, Toudal L, nv K, Wieter B, Crabeck O and Mortensen J.: Polynya impacts on water properties in a Northeast Greenland fjord. Estuarine, Coastal and Shelf Science, 153, 10-17, 10.1016/j.ecss.2014.11.027, 2015.
	Galley, R. J., Babb, D., Ogi, M., Else, B. G. T., Geilfus, N.-X., Crabeck, O., Barber, D. G., and Rysgaard, S.: Replacement of multiyear sea ice and changes in the open water season duration in the Beaufort Sea since 2004, Journal of Geophysical Research: Oceans, 123, 1806-1823, 10.1002/2015JC011583, 2016.

I was a contributing author to a publication (Else et al., 2015) related to my first scientific question concerning the physical processes controlling gas content. In this manuscript, I participated to the data collection (SERF, January 2013) and contributed to the redaction of the manuscript:

In Else et al. (2015), we reported new methodological improvement for measuring O_2 fluxes at the ice-seawater interface. We examined the potential to measure under-ice turbulent exchanges of heat, salt, momentum, and dissolved oxygen using eddy covariance in an experimental sea ice facility. We identified bubble formation and dissolution as one possible cause for the observed high fluxes of dissolved oxygen.

The following three publications; Rysgaard et al. (2014), Geilfus et al. (2015, 2016), were directly related to my second scientific question and addressed the fate of CO_2 in the Arctic carbon cycle. For each manuscript, I participated with data collection (Resolute Bay, June 2012 for Geilfus et al. (2015) and SERF, January 2013 for Rysgaard et al. (2014) and Geilfus et al. (2016) and contributed to the redaction:

In Geilfus et al. (2015), we reported on the CO_2–carbonate chemistry of melting sea ice, as well as the impact of pond formation on both the direction and magnitude of CO_2 fluxes at the surface of first-year landfast sea ice in Resolute Passage, Nunavut, June 2012. Recently, ikaite crystals have been found in sea ice, and it has been suggested that their precipitation may play an important role in air–sea CO_2 exchange in ice-covered seas. In Rysgaard et al. (2014), we presented the spatial and temporal dynamic of ikaite in sea ice, while in Geilfus et al. (2016), we

reported the impact of ikaite precipitation and export on underlying seawater carbonate chemistry.

Finally, I was a contributing author to two publications (Dmitrenko et al., 2015; Galley et al., 2016), which are indirectly linked to my thesis topic. In the fifth manuscript (Dmitrenko et al., 2015), I participated to the data collection during the leg 1 of the Young Sound Campaign (Young Sound, Greenland, May 2014) and contributed to the redaction of the manuscript, and the sixth study (Galley et al., 2016), I contributed to the editing of the final manuscript:

In Dmintrenko et al. (2015), we provided the only long-term record of a coastal polynya (Young Sound, northeast Greenland) and the impact on water mass circulation and chemistry. This research is highly relevant since recent publications have shown that polynyas characterized by rapid ice formation and high biological productivity enhance the air-sea gas exchange and potentially increases the oceanic CO_2 uptake (e.g. Anderson et al., 2004; Else et al., 2011).

In Galley et al. (2016), we reported the evolution and trends of sea ice concentration and the duration of the open water season since 2004 in the Beaufort Sea. We also provided a sea ice climatologically analysis for the western Arctic region by sea ice stage-of-development. Monitoring long-term variation of sea ice concentration is important to both the assessment of current climate trends and of the impact of these trends on the carbon cycle and greenhouse gas fluxes in ice-covered area.

References

Anderson, L. G., Falck, E., Jones, E. P., Jutterstrom, S., and Swift, J. H.: Enhanced uptake of atmospheric CO_2 during freezing of seawater: A field study in Storfjorden, Svalbard, Journal of Geophysical Research-Oceans, 109, 2004.

Else, B. G. T., Papakyriakou, T. N., Galley, R. J., Drennan, W. M., Miller, L. A., and Thomas, H.: Wintertime CO_2 fluxes in an Arctic polynya using eddy covariance: Evidence for enhanced air-sea gas transfer during ice formation, Journal of Geophysical Research: Oceans, 116, 9-10, 10.1029/2010JC006760, 2011.